Old Dominion University

ODU Digital Commons

Electrical & Computer Engineering Theses & Dissertations

Electrical & Computer Engineering

Fall 1998

Modeling and Simulation of High-Field, High-Temperature SiC Devices

Sanjay Pathak
Old Dominion University

Follow this and additional works at: https://digitalcommons.odu.edu/ece_etds

 Part of the Electrical and Computer Engineering Commons

Recommended Citation

Pathak, Sanjay. "Modeling and Simulation of High-Field, High-Temperature SiC Devices" (1998). Doctor of Philosophy (PhD), Dissertation, Electrical & Computer Engineering, Old Dominion University, DOI: 10.25777/gmgr-8k59
https://digitalcommons.odu.edu/ece_etds/184

This Dissertation is brought to you for free and open access by the Electrical & Computer Engineering at ODU Digital Commons. It has been accepted for inclusion in Electrical & Computer Engineering Theses & Dissertations by an authorized administrator of ODU Digital Commons. For more information, please contact digitalcommons@odu.edu.

MODELING AND SIMULATION OF HIGH FIELD, HIGH TEMPERATURE SiC DEVICES

by

Sanjay Pathak
B.Tech. G. B. Pant University, Pantnagar, INDIA
M.Tech. Indian Institute of Technology, Kanpur, INDIA

A Dissertation submitted to the Faculty of
Old Dominion University in Partial Fulfillment
Of the Requirement for the Degree of

DOCTOR OF PHILOSOPHY

ELECTRICAL ENGINEERING

OLD DOMINION UNIVERSITY
Oct, 1998

Approved by:

Ravindra P. Joshi (Director)

Linda L. Vahala (Member)

John J. Swetits (Member)

Lee A. Belfore II (Member)

Reproduced with permission of the copyright owner. Further reproduction prohibited without permission.

ABSTRACT

MODELING AND SIMULATION OF HIGH FIELD, HIGH TEMPERATURE SiC DEVICES

Sanjay Pathak
Old Dominion University, 1998
Director: Dr. Ravindra P. Joshi

With superior properties such as a large band gap, high thermal conductivity, and large electron drift velocity, SiC is expected to give a new dimension to high power, high temperature electronic devices used in power applications, microwave circuits, and for the space and automobile industries. SiC possesses an inherent advantage over its other large bandgap competitors in terms of inherited processing and device technology from Si. However, there is inadequate understanding of SiC device and its parameters. Simple extrapolations from Si are known to be inadequate. The aim of this dissertation, therefore, is to produce better understanding of SiC devices using drift-diffusion numerical simulations and the extraction of SiC material parameters using Monte Carlo codes.

Results of this study show that despite favorable material characteristics, there are inherent problems associated with SiC. Many parameters obtained using Monte Carlo simulations are new additions to the SiC literature. These have also been used in simulation of device behavior. These SiC parameters were explained and compared with available experimental data. Results show that electron mobility in MOSFET structures suffers due to surface roughness. Deep levels have been shown to play a significant role in p-n diode transient response, and can cause persistent conductivity. Device geometry has been shown to play a major role in device stability. Finally, the influence of deep levels on charge injection at the contacts has been demonstrated, and could be used to improve device stability in MSM diodes.

Co-Directors of Advisory Committee: Dr. Linda L. Vahala
Dr. John J. Swetits
Dr. Lee A. Belfore II

Reproduced with permission of the copyright owner. Further reproduction prohibited without permission.

Dedicated To My Wife "Neeta"

Reproduced with permission of the copyright owner. Further reproduction prohibited without permission.

ACKNOWLWDGEMENTS

I would like to express my sincere appreciation to my Advisor, Professor R. P. Joshi for his valuable guidance and encouragement throughout the course of this study, which proved to be invaluable to me. I would also like to thank my research guidance committee members Dr Linda L. Vahala, Dr. John J. Swetits and Dr. Lee A. Belfore for their help in the completion of this research work.

I am also obligated to my family (my wife and daughter Juhi) for making my life so wonderful during the course of my doctoral program. Also my parents and sisters whose faith in me and my ambition still pursue me for my great achievements. I can certainly not forget the contribution of my dearest friends Gopal and Indu whose presence and wonderful company always kept me bringing me back to Norfolk again and again. Also thanks to all my friends and anybody who did any help in the completion of this work.

Reproduced with permission of the copyright owner. Further reproduction prohibited without permission.

TABLE OF CONTENTS

Reproduced with permission of the copyright owner. Further reproduction prohibited without permission.

Reproduced with permission of the copyright owner. Further reproduction prohibited without permission.

LIST OF TABLES

Reproduced with permission of the copyright owner. Further reproduction prohibited without permission.

LIST OF FIGURES

Reproduced with permission of the copyright owner. Further reproduction prohibited without permission.

Reproduced with permission of the copyright owner. Further reproduction prohibited without permission.

Reproduced with permission of the copyright owner. Further reproduction prohibited without permission.

Reproduced with permission of the copyright owner. Further reproduction prohibited without permission.

Reproduced with permission of the copyright owner. Further reproduction prohibited without permission.

Reproduced with permission of the copyright owner. Further reproduction prohibited without permission.

CHAPTER 1

INTRODUCTION

1.1 BRIEF BACKGROUND AND MOTIVATION

After over five decades of technological development, semiconductor based devices have become the mainstay of modern solid state electronic circuits. In this area, Silicon technology is the most well developed, and yields low cost, extremely reliable devices. About 90 percent of the solid state devices manufactured worldwide today, are based on silicon material. However, despite its popularity and success, there are a number of disadvantages associated with silicon technology. The primary drawback stems from its relatively small bandgap of about 1.12 eV. The small bandgap leads to higher intrinsic carrier densities, fuels large "dark currents" for detector systems, increases noise, and makes devices intolerant to high temperature operation. This material cannot be used for many applications involving high temperature operation as the intrinsic carrier density increases in an exponentially rapid manner with temperature. The problem is worsened by the fact that the thermal conductivity of Si is not very high. This presents an inherent limitation to efficient device cooling through heat removal. This can become a very important issue for microelecrtronics as the packing density continues to increase. With increased densities, severe localized on-chip heating is expected during device operation. This makes it very important to ensure efficient heat dissipation for smooth and stable service.

In addition, due to the low bandgap of silicon, the energy threshold for band-to-band impact ionization and subsequent device breakdown is fairly small compared to the other materials such as GaAs that are being considered in the semiconductor industry. As a result, devices made of Si impact ionize relatively easily and are unable to withstand high values of electric fields and external voltages. This limits the upper range of voltage operation, and

---

Format for references in this work is taken from Journal Of Applied Physics

Reproduced with permission of the copyright owner. Further reproduction prohibited without permission.

makes Si based technology unsuited for high-power, high-voltage applications. The low threshold for impact ionization also implies that the material is not "radiation hard" and will deteriorate relatively quickly under the influence of external ionizing radiation. Such external radiation will, for example, be encountered in space applications. Given many of the above listed shortcomings, the existing Si semiconductor technology is not adequate or sufficient. It becomes necessary and essential, therefore, to find and develop other suitable materials for many of the high-temperature, high-voltage applications. Ideally, such materials should also have the favorable property of "survivability" through radiation hardness.

In terms of the potential industrial, military, and space applications, the need for electronic devices capable of operating at high electric fields, with the ability to withstand elevated temperatures and harsh environments has been increasing dramatically [1-3]. This has given rise to the recent surge of research activity in wide-band-gap semiconductors. For example, pollution control and the monitoring of toxic gases in the environment is becoming an important task both for industry and the government. In particular, the measurement and control of toxic gas emissions from automobile exhausts and airplane jet engines is a vital issue. With concerns of global warming and the need for environmental protection, such monitoring is gaining importance. However, for efficient space-effective monitoring and control of the emissions, the sensors need to be positioned close to the hot engines. Proximity placement eliminates the need for costly fiber optic links, and greatly helps reduce overhead space for compactness. Weight reduction is also an important related consideration, especially for aircraft and space applications and hence favors compact semiconductor devices. The development of such an emissions sensor for the above application will require a semiconductor based device for compactness, capable of operating at elevated temperatures. Another potential application of high-temperature electronic devices, capable of operating under harsh environments, is for circuits used in spacecrafts and armored vehicles for the military. In the former case, the harsh environment would arise from cosmic

Reproduced with permission of the copyright owner. Further reproduction prohibited without permission.

rays and other high energy particles in space, while the possibility of electromagnetic pulses on the battlefield would present adverse conditions in the latter situation. Finally, in regards to high-power and high-voltage applications, the need to generate high power microwaves and communication electronics for radar, would drive the need for developing a suitable semiconductor. Apart from military and space applications, there is also a demand for high power electronic components and semiconductor devices in the commercial sector. The power companies and utilities need to develop compact switching devices capable of manipulating electric distribution and changing power factor loads to optimize performance and reduce the power losses. Apart from the power handling capacity, the semiconductor devices for such applications need to be reliable under rugged conditions.

Of the various semiconductor materials known today, SiC, GaN and diamond seem to be the likely candidates for such high temperature, high-power applications. They all have relatively large bandgaps and good thermal conductivities. Diamond however, is not a very promising contender because it has been difficult technologically to dope the material n-type. The problem partially arises from the small atomic radius of the constituent carbon atoms, and the strong sp^3 bonding. It is therefore not energetically favorable to break the carbon bonds and replace the host atoms with external impurities. To date, partial success has been achieved with the use of Lithium. This is related to the small atomic mass of Lithium which makes it easier to replace the carbon host. However, on balance, the fabrication and development of p-n junctions or other bipolar devices operating on the basis of electron flow, has not been successful. Devices based on the flow of holes alone are not very useful because their speeds tend to be quite low. This arises from the sluggish response of the holes which have a larger effective mass relative to the more mobile electrons. Furthermore, at the present time diamond is a very difficult material to grow, and the processing is very expensive. These drawbacks, virtually eliminate diamond as a competitive material for semiconductor devices.

GaN, a direct bandgap material, is being pursued as a possible candidate. However,

Reproduced with permission of the copyright owner. Further reproduction prohibited without permission.

there are a number of problems that remain to be overcome in terms of growing good electronic quality, defect-free material [4,5]. Furthermore, GaN does not have a native oxide, and hence reliable production is more difficult to control. Its thermal conductivity is about four times lower than SiC, and hence may not be as useful for high temperature applications. It is, however, being studied as a potential blue laser and even as an optical source at ultra-violet wavelengths.

Properties of SiC, on the other hand, offer a variety of advantages over the other semiconductors. These include a wider band-gap E_g, higher critical electric field capability, larger thermal conductivity, and the higher saturation velocity of carriers in SiC. The high higher breakdown electric field allows for the fabrication of smaller devices for a given value required value of the applied voltage. The smaller active device lengths not only help in increasing the density, thus lowering the manufacturing cost per chip, but also reduce the device "ON-resistance" value. A lower "ON resistance" is important for increased speed through the reduced internal "RC" time constants and higher power transfer efficiency. Besides, SiC has a natural native oxide, and hence is easier to grow in a controlled manner. The oxide allows for device passivation against possible contaminents, and makes it possible to fabricate Metal Oxide Semiconductor Transistor (MOSFET) structures. The lattice mismatch with Si is not very large, and hence SiC can be grown on Si substrates that are readily available at inexpensive prices.

SiC exists in many forms defined as polytypes depending on the staking sequence of the bonded Si-C bilayers. 3C and 2H are the two basic structures of SiC and are known as cubic and hexagonal respectively. All of the remaining polytypes are the combination of 3C and 2H-SiC. Important electronic properties of some of the common semiconductors are given in Table 1.1 for a quick comparison.

Much progress has recently been made in SiC for high temperature and high power device applications as a result of development work in the growth of high-quality SiC

Reproduced with permission of the copyright owner. Further reproduction prohibited without permission.

substrates, advances in chemical-vapor-deposition (CVD) technique. growth of epitaxial structures, and ability to dope the material easily with both n- and p-type atoms [7,8]. SiC

Table 1.1. Comparison of important semiconductor properties [6].

property	Si	GaAs	GaP	3C-SiC (6H-SiC)	Diamond	GaN
Band gap (eV) at 300 K	1.1	1.4	2.3	2.2 (3.0)	5.5	3.39
Maximum operating temperature (K)	600	760	1250	1200 (1580)	1400	
Melting point (K)	1690	1510	1740	Sublimes >2100	Phase change	
Physical stability	Good	Fair	Excellent	Very good	Good	Good
Electron mobility RT, cm^2/Vs	1400	8500	350	1000 (600)	2200	900
Hole mobility RT, cm^2/Vs	600	400	100	40	1600	150
Breakdown voltage E_b, $10^6V/cm$	0.3	0.4	_	4	10	5
Thermal conductivity c_T, W/cm	1.5	0.5	0.8	5	20	1.3
Sat. C. elec. drift vel. v(sat), $10^7cm/s$	1	2	_	2	2.7	2.7
Dielectric const. K(0)	11.8	12.8	11.1	9.7	5.5	9

processing technology has an added advantage due to its similarity in processing with Si, which already has a successful history and a well developed infrastructure. Many devices on SiC have been fabricated and tested successfully at the present time. Examples of such devices include: blue light emitting diodes [9], UV photodiodes [10] p-n junction devices and Schottky diodes [11,12], field effect and bipolar transistors [12,13], heterojunction

Reproduced with permission of the copyright owner. Further reproduction prohibited without permission.

bipolar transistors [14,15], high efficiency solar cells [16], and thyristers [17]. The SiC material processing and device fabrication has been beset with many problems, which are gradually being overcome. Though these problem areas for SiC technology are briefly discussed in the following section, it may be pointed out that the principle difficulty from a fabrication standpoint has been the occurrence of "micro-pipe" defects [18]. Electrically, these micro-pipes function as effective short-circuit elements, thereby destroying the useful device operation. The micro-pipes also act as effective recombination centers, and tend to severely limit the lifetime of the mobile charge carriers. Given the presence of such micro-pipes, most SiC test structures fabricated to date, have not been large area devices. Their performance, therefore, has not been optimal, or to its full possible potential. In some cases, special geometry structures had to be devised to overcome the practical difficulties of fabricating defect-free SiC devices. An example of this is the recent successful fabrication of UMOSFETs which are similar to the usual MOSFETs of Si technology, but use a recessed gate structure. Some of the SiC devices and their structures [19] are shown in Fig. 1.1 for completeness. On the theoretical development side, analyses of the SiC transport properties and simulations of simple SiC-based devices have only recently begun to emerge [20-23]. However, most of the analysis has been restricted to the 3C- and 4H-polytypes as they have been experimentally studied over a slightly longer time. However, the 6H-SiC polytype is the most important technologically because of its largest bandgap. Studies of 6H-SiC are not available in the literature to date, and have been carried out in this current research.

1.2 ADVANTAGES OF SiC AND ITS DEVICES

SiC has a major advantage over other wide-band-gap materials, as it has an established infrastructure for material growth and processing. This occurs because SiC is very similar to Si. Since Si has the most advanced processing technology today among all the semiconductors, it is expected that the SiC technology would have a natural headstart.

Reproduced with permission of the copyright owner. Further reproduction prohibited without permission.

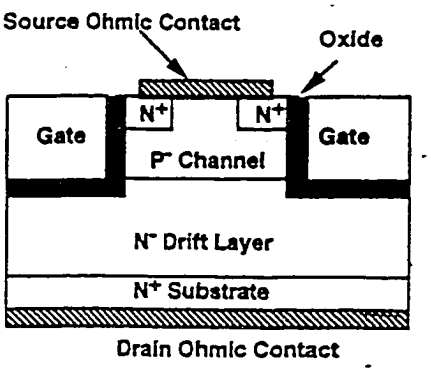

Fig 1.1 a SiC UMOSFET

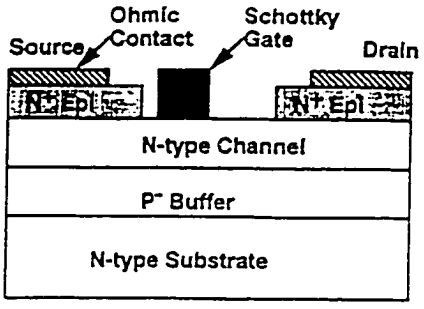

Fig 1.1 b SiC MESFET

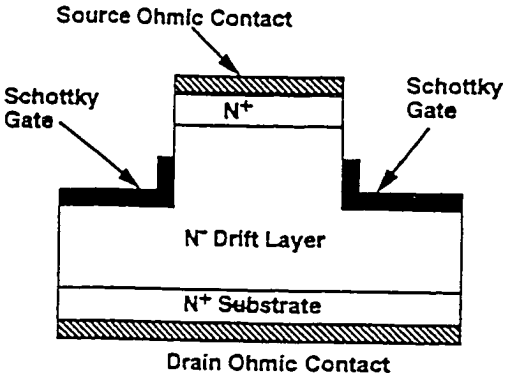

Fig 1.1 c SiC static induction transistor (SIT)

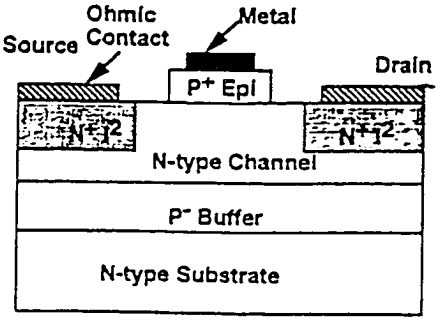

Fig 1.1 d 6H-SiC JFET

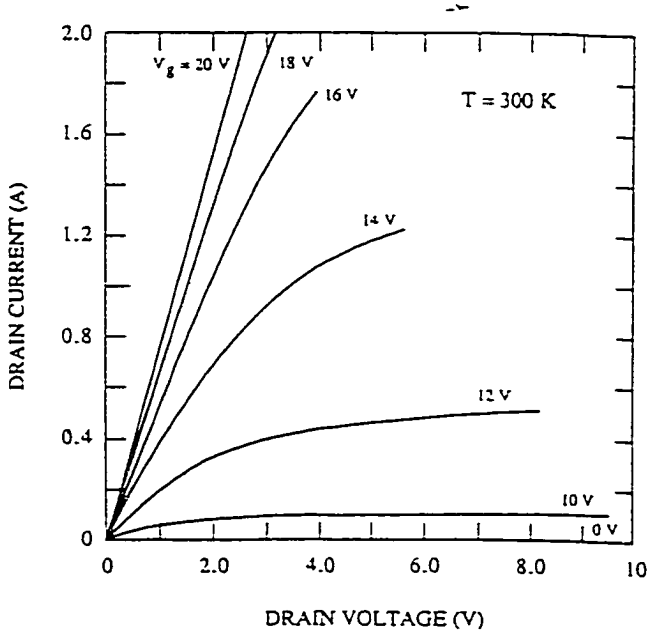

Fig 1.1 e I-V curve of a large area (0.01 cm2) 4H-SiC vertical UMOS power FET

Reproduced with permission of the copyright owner. Further reproduction prohibited without permission.

Some of the potential drawbacks of Si were mentioned in the previous section. SiC, with its large bandgap, excellent thermal conductivity, and high breakdown strength should yield superior electronic devices that have many advantages over the Si counterparts [1]. A brief list of the potential benefits is given below. These potential benefits demonstrate the need for focusing on an in-depth study of SiC material, its electronic parameters, and related device response.

(i) Due to the good thermal conductivity and hence better thermal management, the current handling capacity of SiC devices is expected to be superior. This should lead to compactness and higher on-chip packing densities.

(ii) Low noise and extremely small leakage currents should make SiC an excellent material for the fabrication of high energy detectors.

(iii) The high field electron drift velocity is predicted to be higher than most other semiconductor materials such as GaAs, InP, GaN, Diamond and Si. This should lead to inherently high switching speeds and superior cut-off frequency values. Hence, SiC based transistors would be very useful for signal amplification for high power microwaves.

(iv) Due to the low leakage currents, SiC Schottky diodes can be expected to be very efficient, and could have applications such as non-linear rectification of power signals, heterodyning and signal mixing, and multiple frequency generation. The low leakage current across a Schottky barrier implies that SiC is likely to be a good candidate for JFET and MESFET devices. These unipolar transistors could be used for amplification of power microwave signals.

(v) The large bandgap of SiC will allow for higher doping levels than in Si. This should help reduce the "on-state resistance" leading to smaller power losses and faster "RC" time constants.

Reproduced with permission of the copyright owner. Further reproduction prohibited without permission.

(vi) The high breakdown electric field will allow the fabrication of thinner layers at higher doping levels for a given voltage than Si or GaAs devices. This should reduce the physical device size without adversely affecting the internal resistance. Power MOSFET and BJT structures should benefit.

(vii) Power thyristors and high voltage electronic switching is another area in which SiC material would be very useful. The high blocking voltage would increase the holdoff capability.

1.3 PROBLEM OVERVIEW AND DEFINATION OF OBJECTIVES

Silicon Carbide (SiC) is a relatively new material for semiconductor devices and not much research has been done in this area. Though the material has not been fully explored, the trends show promise. Many of the predicted advantages of SiC have yet to be fully realized. The material has also not been fully characterized and modeled, and most of the merits of SiC devices are based on guesses, estimates and extrapolations from the Si material properties. A detailed understanding of this material and its properties has not yet fully emerged. However for realistic projections and performance outlook, it becomes necessary to correctly model and understand the electrical response behavior of SiC before venturing into costly fabrication. This research is a step in this direction. The primary aim of this study is to evaluate many of the important transport parameters of the material that govern the electrical characteristics. Monte Carlo type first principles calculations will be used for this purpose. The simulation predictions will be carefully compared with available experimental data. Finally, the electrical transport parameters of SiC so obtained will be used to predict the transient switching behavior of SiC diodes under high biasing voltages.

Research carried out on SiC so far identifies several important issues. These issues have a broad scope and cover many areas which include processing technology and crystal growth, material characterization, the evaluation of intrinsic SiC properties, device physics,

Reproduced with permission of the copyright owner. Further reproduction prohibited without permission.

electronic transport behavior, and predictions of the electrical response characteristics. However, this research will focus on only a small part related to electrical transport and predictions of the transient SiC diode response. The main issues and research objectives are given below. For completeness, some of the other interesting problems and research areas are also briefly discussed.

(i) The first issue concerns an accurate evaluation of the electrical transport parameters for the SiC polytypes that are of technological interest. Such parameters include: (a) The electron and hole mobilities; (b) field dependent carrier drift velocities including its non-linear behavior and saturation; (c) the precise nature of the anisotropies which arise due to a lack of inversion symmetry within the basic crystal structure; and (d) values of the impact ionization coefficients and their behavior on electric field. The parameters indicated above apply to bulk situations in which it is possible for carriers to move unrestricted throughout the material in all three directions, or to confining "quantum" geometries in which motion may be forbidden due to potential barriers along at least one of the directions. In semiconductor electronics both types of situations can occur. For example, most of the common devices such as PN junctions, bipolar transistors, and thyristors allow for bulk conduction. However, others such as the metal-oxide-semiconductor field effect transistor (MOSFET) are based on a restricted flow of carriers within a narrow channel. These changes in the degree of freedom affect the values and qualitative trends of the transport parameters given above, depending on the type of conductive flow allowed. Hence, bulk parameters can be quite different from the corresponding values for a restricted geometry due to the "quantization" effects. Given this change in the parameter set with geometry, and the technological importance of both bulk and MOSFET type devices, it is necessary to obtain transport parameters for both types of situations. Accordingly, both situations will be examined in this research. Furthermore, suitable comparisons with available experimental

Reproduced with permission of the copyright owner. Further reproduction prohibited without permission.

data will be necessary to understand the role of the individual physical processes and their relative contributions. For example, the mobility in SiC MOSFET structures is currently observed to be much lower than for the bulk material. The physical reasons are not well understood. It is therefore an important challange to examine and understand the differences and their origins.

(ii) Another important issue concerns the behavior of deep levels in SiC. There is an important difference between this material and the better known Si or GaAs systems. The deep levels can arise from two sources: (a) extrinsic impurities such as donor and acceptor atoms that have been deliberately incorporated into the device material, and (b) unintentional defects and traps that arise during the processing phase. In both cases, the energies associated with the levels are much larger than encountered in the more common semiconductors such as Si and GaAs. For example, the Nitrogen and Phosphorus donors in SiC are about 50-60 meV below the conduction band, as compared to values of about 15 meV for Silicon. Recent experimental studies have shown that defects in SiC are fairly common and can have large energies ranging from 0.4-1.2 eV [24]. This implies that while one would have complete donor and acceptor impurity ionization in Si, only a small fraction of the impurities would be ionized in SiC. Furthermore, almost all defect states would remain completely unionized. This presence of *unionized* donor and/or acceptor sites at room temperature inherently creates a latent supply of mobile charge. Upon the application of an external field, this charge can become mobile and create an unwanted increase in the device current. In the extreme case, at high electric fields this supply of mobile carriers can lead to impact ionization and subsequent device failure. Furthermore, it is expected that these deep levels will exhibit a significant temperature dependent ionization. This temperature change in the level occupancy and ionization state could lead to uncontrolled generation of free-carriers within the device and eventual device breakdown. The internal thermal generation could be due to either a hot

Reproduced with permission of the copyright owner. Further reproduction prohibited without permission.

environment (as in high temperature sensing applications) or might be produced by internal Joule heating at high fields.

(iii) In the usual semiconductor materials, band-to-band impact ionization is the main cause of breakdown. However, for SiC the band-to-band impact ionization rate is not expected to be very high, unless the electric fields became excessively large. However, the presence of unionized impurity atoms in SiC as discussed above, would raise the possibility of trap-to-band ionization. This process requires much less ionization energy, and hence is expected to be non-negligible for SiC material containing filled traps. This trap-to-band ionization process is not an important phenomenon in the conventional semiconductors since the impurity levels in those materials are mostly shallow and hence largely empty. The trap-to-band process could act as an internal source of carriers and lead to an internal instability.

(iv) Another issue concerns the transient response and the breakdown behavior of SiC devices. As a general rule for any conventional device, the breakdown voltage is higher in the pulse mode of operation, than for a continuous applied bias. This higher tolerance to a pulsed voltage is due to the much lower amounts of energy deposited into the system under a pulsed biasing mode. Strangely, however, in some recent experiments on SiC p-n diode structures at NASA Lewis, the breakdown voltage under the pulses mode was found to be *lower than the breakdown voltage in the continuous mode* [25]. This occurrence is as yet unexplained, and leads to a area of investigation for obtaining a better understanding of the underlying physics.

(v) Finally, this study will attempt to examine the limits on the rate of voltage switching across the SiC devices containing unionized impurity charge. Ordinarily, the application of an external biasing voltage leads to device current due to the flow of mobile carriers.

Reproduced with permission of the copyright owner. Further reproduction prohibited without permission.

However, in SiC material, if most of the impurities are not ionized, there is likely to be a very low supply of mobile charge prior to the application of an external biasing voltage. As a result, if the voltage ramping rate exceeds the thermal generation rate, then much of the device current will arise from a displacement component since sufficient mobile charge will not have been generated from the unionized impurities. This is likely to set up large internal electric fields within the device. At later times, the slow release of carriers from the unionized impurities might serve to fuel impact ionization across the regions of high electric fields. Thus, there appears to be a detrimental effect of a imposing fast voltage ramps in the SiC devices, as they may lead to ionization breakdown.

The focus of this research is based on all of the issues that have been described above. The main goal is to first ascertain the underlying transport parameters that would dictate and govern the electrical response in SiC material. This evaluation of the transport parameters will be done based on microscopic Monte Carlo methods. Furthermore, the parameters will be evaluated and analyzed for both bulk SiC and the MOSFET type confining geometries. Careful comparisons with experiments should help reveal the importance of various internal processes. An understanding and identification of the detrimental processes would help in the eventual elimination through technological and processing innovations. Next, the parameters will be used to study the electrical response of pn junction diodes under high power conditions to simulate and understand the available experimental data [25]. The analysis carried out here includes the effect of temperature changes caused by internal heating and the role of deep level dopant atoms. The transient high field response of the diodes has also been simulated to examine trapping/detrapping effects. In summary, the following tasks have been performed during this research:

a) Evaluation of SiC transport parameters for high temperature operation. The Monte Carlo technique was used for this purpose. Both bulk and "quantum

Reproduced with permission of the copyright owner. Further reproduction prohibited without permission.

confined" situations were examined. Though the focus was on the technologically important 6H-SiC, bulk results were obtained for the 3C- and 4H-SiC polytypes as well.

b) A numerical analysis of a 6H-SiC diode response based on the drift-diffusion approach. Inclusion of non-uniform spatial temperature distributions in the numerical drift-diffusion device models was achieved.

c) Analysis of the role of deep levels on the device performance under high temperature and electric field conditions.

d) Inclusion of the impact ionization process in SiC device modeling.

e) Simulations of the ultrafast p-n junction diode response to reverse biasing pulses, and a detailed analysis of its transient behavior. The p-n junction diode was chosen because of its simplicity, and because some experimental data is already available for comparison. Besides, many of the device applications being proposed rely on the simple diode structure as the basic building block.

Most of the other research issues in the SiC area pertain to crystal growth, processing, material characterization and device testing. For example, it has been observed that most forms of SiC have a relatively high density of defects and "micropipes." The occurrence of micropipes is not well understood, but thought to arise from lattice imperfections during growth [26]. Substrate mismatch, and the requirement of high entropy during the high temperature processing sequence are thought to be some of the contributing factors. It has therefore been a challenge to produce large pieces of good electronic quality, defect-free SiC. Similarly, the material grown so far has not been well characterized. The range of defect levels or their densities is not well known. Characterization of the contact resistances and their properties under high temperature operating conditions, bonding and robustness of the

Reproduced with permission of the copyright owner. Further reproduction prohibited without permission.

metallization remain to be adequately done. However, most of these issues are experimental in nature and process related, and will not be addressed in this dissertation.

1.4 SUMMARY

In summary, SiC material is a new emerging technology which shows promise of superior performance for high temperature, high field, radiation hard applications. However, it is as yet not well developed, the material and related devices have not been well characterized, and the electrical parameters and device response are not well understood. Consequently, this dissertation attempts to make a contribution in understanding and evaluating the electrical response characteristics of SiC material. In particular, numerical modeling and simulation work has been carried out to evaluate and predict the electron transport parameters that are at present unavailable in the literature, and the transient behavior of a simple p-n junction diode subject to ultrafast reverse biasing pulses. The SiC p-n junction was chosen as the typical device structure for the numerical modeling effort for two reasons. First, it is the simplest structure and so can be easily understood. It also forms the basic building block of more complex device structures, and so evaluating the response characteristic of the diode is an essential building block. Second, some experimental results are also available for comparison.

The numerical modeling is based on a combination of the Monte Carlo and drift-diffusion models. Chapter 2 presents a brief literature review to present the current status on both the experimental and theoretical sides. This is followed by a description of the numerical scheme and modeling effort for the SiC simulations in Chapter 3. The various results obtained from the current simulations are discussed in detail in Chapter 4. Appropriate comparisons with available experimental data are also included. Finally, Chapter 5 summarizes the main results and contributions. Some discussions of possible future modeling work have also been given for completeness.

Reproduced with permission of the copyright owner. Further reproduction prohibited without permission.

CHAPTER 2

LITERATURE REVIEW AND BACKGROUND

2.1 INTRODUCTION

A brief review of the SiC literature is given in this chapter. Some of the important electronic and structural properties of SiC are first discussed. This brings out the complexity associated with the material band structure and the large number of polytypes. Though there over ten polytypes, the 6H- and 3C-SiC are the two most important technologically. The growth and processing techniques for the others are not as well developed, though 4H-SiC is beginning to emerge as an important material for high speed devices. A discussion of the current fabrication and processing in SiC status is presented after a brief review of the SiC electronic properties. This is followed by a section on the experimental results of bulk electron mobilities that have been measured in actual SiC devices to date. Details of the MOSFET results and channel mobility data are also discussed. Since mobility modeling results will be presented in chapter 4, such experimental information has direct relevance. Next, a section on bulk devices that have been fabricated and tested to date is included for completeness. This includes published reports on the device performance levels. Finally in closing, detailed experimental results on simple p-n junction diodes fabricated at NASA Lewis are presented. These devices were tested under high voltage pulsed conditions, and their transient response was observed. These results shed light on the high field electrical transient and the possibility of breakdown failures under ultrafast voltage ramps. This actual data thus provides a basis for comparing the simulations results, and highlights aspects of the SiC device physics that needs to be better understood.

2.2 ELECTRICAL PROPERTIES OF SiC

A comparison of the electronic properties of SiC with respect to the most popular semiconductors (Si and GaAs), and other competitive large bandgap semiconductors (GaN,

Reproduced with permission of the copyright owner. Further reproduction prohibited without permission.

GaP and diamond) was shown in Table 1.1 of Chapter 1. Several favorable material properties such as a large bandgap, high thermal conductivity, a large break down voltage, and superior saturation velocity make SiC a potential candidate for high-power, high temperature electronics. The excellent physical stability which results from the strong covalent atomic bonding, allows higher operating temperature of the device. Due to the large bandgap and strong resistance to harsh chemical environments, the material shows great potential for radiation hardened device as well as a low noise amplifier.

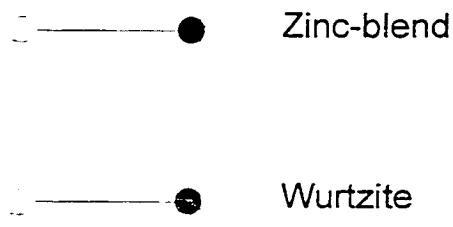

Fig. 2.1 Zinc-blend and wurtzite bonding between Si and C atoms in adjacent planes.

In nature, SiC crystal exhibits a one-dimensional polymorphism called polytypism. The SiC polytypes are differentiated by the stacking sequence of the tetrahedrally bonded SiC bilayers. Local atomic environments of the atoms are identical and the overall symmetry of the crystal is determined by the stacking periodicity of these bilayers. These bilayers have a tetrahedral bonding scheme with the bonding between Si and C atoms in the adjacent bilayer displaying either of a Zinc-blend (cubic) or wurtzite (hexagonal) nature as shown in Fig. 2.1. The SiC bilayers can be positioned in three possible situations with respect to the lattice named A, B and C. The arrangement of these classified A, B and C layer determine the crystal structure of SiC lattice.

Two forms of the stacking sequences as ABCABC..., and ABAB... yield the two basic structures, which are purely cubic zinc-blend and purely hexagonal wurtzite in nature,

Reproduced with permission of the copyright owner. Further reproduction prohibited without permission.

and are referred to as 3C-SiC and 2H-SiC, respectively. All other kinds of structure are the combination of these two basic structure. 4H-SiC and 6H-SiC are among the other common polytypes with more complex stacking sequences. 4H-SiC has equal elements of cubic and hexagonal structures, while 6H-SiC has one third hexagonal and two thirds of the cubic element. Irrespective of the cubic element contained in their structure, each polytype has an overall hexagonal crystal symmetry. 3C, 4H and 6H-SiC are the most common polytypes and have widely ranging physical properties. Among them are: the highest electron mobility and electron saturation velocity of 3C-SiC, the lowest band-gap for 3C-SiC and a maximum "E_g" for 4H-SiC as indicated in Figs. 2.2-2.4.

Although some of the electronic properties of SiC were investigated in the 1960's, most of the work on SiC has been done in the last 4-5 years. This is due to the advances in processing technology which have now made it possible to grow good, electronic-quality material. Initial interest in this material arose from its potential for high temperature, corrosion resistant semiconductor manufacture. Recent studies in this area have been driven by the need for electronic devices capable of operation at high power levels, high temperatures, and caustic environments. There is also a separate need for robust optical

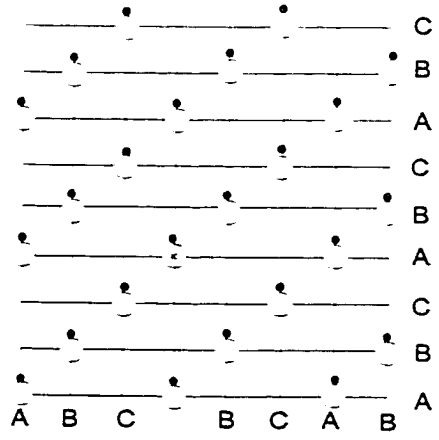

Fig. 2.2 Crystal structure of the purely cubic 3C-SiC polytypes. Each lattice site (k, representing the cubic symmetry) is equivalent.

Reproduced with permission of the copyright owner. Further reproduction prohibited without permission.

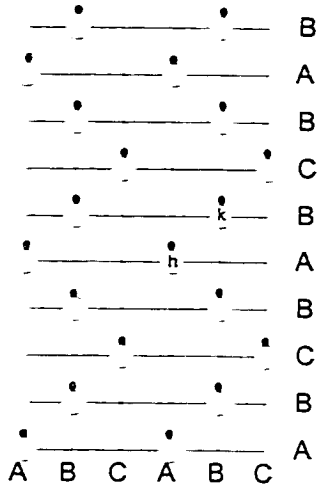

Fig. 2.3 Crystal structure of the 4H-SiC polytype. h and k are hexagonal and cubic site respectively.

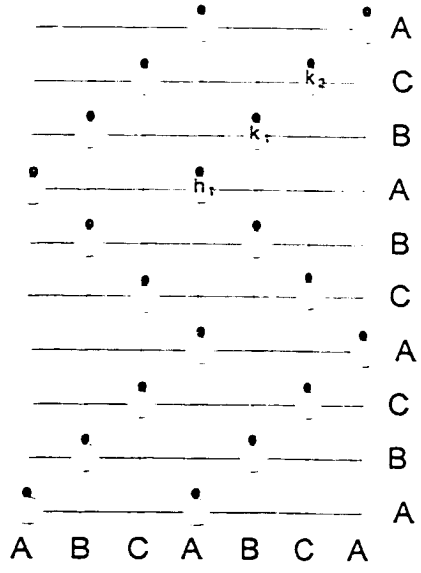

Fig. 2.4 Crystal structure of 6H-SiC polytypes, the most prevalent polytype.

The lattice is two third cubic (k_1 and k_2) and one third hexagonal (h_1).

material, especially emitters, which are active in the blue and ultraviolet wavelengths. SiC and other wide-band-gap semiconductors are not so well studied as Si and GaAs.

6H-SiC is a hexagonal symmetric crystal and is one of the most widely used polytypes. Though 3C-SiC is also readily available, the 6H material is favored because of its

Reproduced with permission of the copyright owner. Further reproduction prohibited without permission.

much larger bandgap. It has cigar shaped constant energy surfaces in its first Brillouin zone as shown in Fig. 2.5. Due to cigar shaped equi-energy surfaces, the effective mass of the electron is different along the x-, y-, and z- directions. In first Brillouin-zone, minimum energy point lie between M and L for 6H-SiC as indicated in Fig. 2.6 [27].

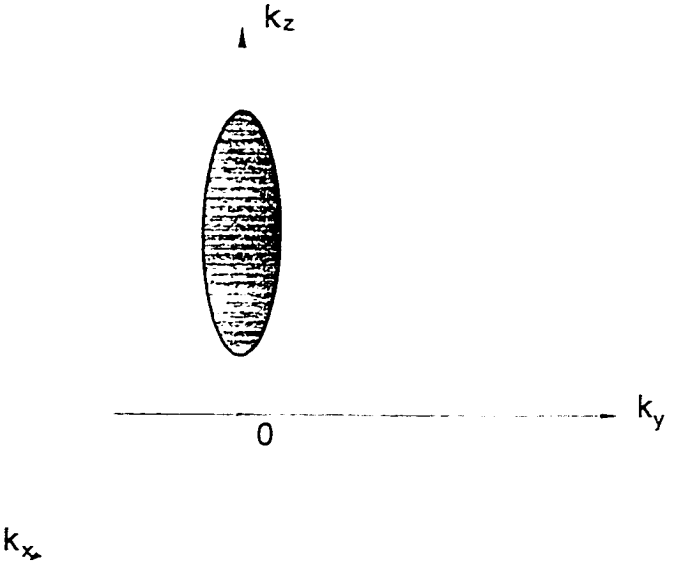

Fig. 2.5 Ellipsoidal equi-energy surface in k-space.

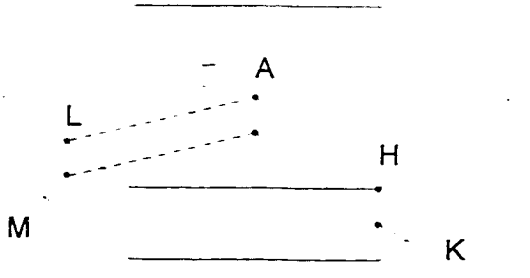

Fig. 2.6 Hexagonal Brillouin zone of 6H-SiC. Between M and L is the minimum energy point for 6H-SiC.

Reproduced with permission of the copyright owner. Further reproduction prohibited without permission.

Due to the hexagonal symmetry of 6H-SiC crystal, effective mass and hence the mobility are both anisotropic parameters [28-30]. N.T. Son et al. have obtained effective mass values of $m_{\perp}^{*}=(0.42\pm0.02)m_0$ and $m_{\parallel}^{*}=(2.0\pm0.2)m_0$ using optical detected cyclotron resonance techniques [2.2]. The transverse and parallel components are associated with directions that are transverse and parallel to the c-axis of the hexagonal crystal. Suttrop et al. obtained the effective mass as $m_{\perp}^{*}=0.24m_0$ and $m_{\parallel}^{*}=0.34m_0$ for 4H-SiC [30]. Anisotropy has been observed in the directional dependent measurements of the Hall mobility. Hall's measurements for the various combination of current and magnetic field direction revealed a 1:5 ratio of the minimum and maximum mobilities [29]. This ratio was also temperature dependent. In another study, the ratio of electron conductivity along the [1-100] and [0001] directions was found to be 5:1 [31]. Schaffer et al. have recently obtained a set of parametric values to fit an empirical Caughey-Thomas relation for the basal plane mobilities in 6H-SiC [31]. Breakdown voltage values for 6H-SiC as a function of doping concentration have also been measured for one-sided abrupt junctions by various workers and reveal a decrease with doping concentration [11,32,33]. M. Ruff et al. have considered the effect of anisotropy on the impact ionization rate in their calculations for the breakdown voltage. Their results for the breakdown voltage show good agreement with an averaged set of experimental values [19].

The electron velocity verses field characteristics of SiC have shown [6] that higher electron saturation velocities can be attained as compared to GaAs, Diamond and GaN materials. This clearly demonstrates that SiC can function well and yield a fast device response at much higher electric fields on the order of 10^5-10^7 V/cm. However, the effective masses and details of the energy-band structure have only recently become available. Hence, an updated calculation of the velocity-field characteristics for SiC via the Monte Carlo method was performed to yield the latest data [22, 23]. This Monte Carlo generated data was subsequently used in the drift-diffusion modeling work.

Reproduced with permission of the copyright owner. Further reproduction prohibited without permission.

2.3 FABRICATION AND PROCESSING

SiC has a major advantage over other wide-band-gap materials, as it has an established infrastructure for material growth and processing. This occurs because SiC is very similar to Si. Since Si has the most advanced processing technology today among all the semiconductors, it is expected that the SiC technology would have a natural headstart.

6H-SiC substrates can be prepared by three methods, namely: thermal decomposition, the CZ method using carbon-enriched Si melts, and sublimation [34-36]. Usually the SiC substrates are of high purity and quality, but suffer from the problem of micropipe formation. Micropipes are defects that nucleate at the seed crystal and propagate as hexagonal cross sectional voids through the entire crystal. Some efforts have been made to remove micropipes by preparing seed crystals in which epitaxial layers are grown on the A face prior to bulk crystal sublimation growth [37]. However, progress in the growth and fabrication techniques have contributed significantly to the reduction in the micropipe density. Over the last five years, micropipe densities have come down from over 1,000 /cm^2 to about 50-70 /cm^2.

SiC can be grown epitaxially by liquid-phase epitaxy (LPE) and chemical vapor deposition (CVD). CVD is more popular technique and growth of high purity 4H and 6H-SiC has been reported [31]. The CVD can be done either by low-pressure or by atmospheric-pressure. Usually atmospheric-pressure CVD is preferred since it is better for small diameter and provides good uniformity. Gas-source-molecular-beam epitaxy (GSMBE) has also been tried for the growth of SiC epitaxial layers.

The presence of Si in SiC and the occurrence of a native oxide, gives SiC a distinct advantage over other wide-band-gap materials. The thermally grown oxide is used as a mask for doping, ion implanting, etching and metallization during device fabrication. Another advantage of the native oxide on SiC is that the large bandgap reduces the minority-carrier generation rate to a very low level, effectively rendering an "infinitely" large charge retention

Reproduced with permission of the copyright owner. Further reproduction prohibited without permission.

time in metal-oxide-semiconductor devices. This is very useful for memory storage applications, and would eliminate the need for periodically refreshing the stored information in MOS-type memory devices. An increase in the chip life expectancy and reliability of MOS devices is thus expected.

Oxidation of SiC starts at 900 C at atmospheric-pressure and proceeds via diffusion in a surface limited process [38,39]. Oxidation of SiC can be modeled in a manner similar to silicon [40] :

$$X^2+AX=B(t+T_0), \tag{2.1}$$

where X is the oxide thickness, t the time of oxidation, a process constant. with A and B being temperature-dependent rate constants.

Etching of SiC is fairly difficult due to its strong bonding. Though Si atoms are easy to etch, the C atoms present greater difficulty. Reactive ion etching (RIE) is the most popular technique and can be used with SF_6 ,$CBrF_3$, and CHF_3 mixtures with O_2. Two basic reaction mechanisms of the etching are:

$$Si+4F \Rightarrow SiF_4, \tag{2.2}$$

$$C+xO \Rightarrow CO \text{ or } CO_2. \tag{2.3}$$

A process selectivity of about 1:3.6 between SiC and SiO_2 has been observed by using CHF_3 + 80% O_2 [41].

Large Schottky barrier heights ranging from 1.3 to 1.7eV, which are independent of the choice of metal due to the Fermi level pinning, have been known to lead to poor Ohmic contact resistances in SiC devices. The best values achieved to date have been about $0^{-4}\Omega cm$ and $10^{-3}\Omega cm^2$ for moderately doped n-type and p-type SiC, respectively. Most metal-SiC contact seems to be physically unstable and degrade with time and high temperature. At present poor metal-SiC contact schemes are one of the limiting factors for high temperature operation.

Reproduced with permission of the copyright owner. Further reproduction prohibited without permission.

Doping of the wide-band-gap material is another limiting factor for the wide-band-gap semiconductor technologies. Most of the commonly known dopants do not form a shallow level in an energy band diagram. Nitrogen (N) and aluminum (Al) are the most popular dopant for SiC as n-type and p-type, respectively. By incorporating N during growth, carrier concentrations of about $10^{18} cm^{-3}$ have been achieved. Efforts to further increase the carrier concentration by incorporating a higher density of nitrogen results in the formation of poly-crystalline material. Formation of SiN_X is expected to be one of the reasons for the poly-crystalline growth.

It has been observed that for n-type doping, the dopant atom has a different binding energy at the cubic site than at the hexagonal sites as shown in Table 2.1 [42]. The relative abundance of the various N dopants corresponds to the ratio of the available binding site for a given polytype. Thus, 4H SiC has an equal number of donor atoms at the cubic and hexagonal sites. As indicated in Table 2.1, various different values of the nitrogen energy levels have been reported. These range from 45meV to 85.5meV for the hexagonal site, and from 125 meV to 137meV for the cubic site. For aluminum, only one level has been reported with a value between 200meV and 225meV [2,19,43,44]. Finally, no useful shallow level impurity levels have been found in SiC.

Table 2.1 Ionization energy of the various types of SiC.

Type of SiC	h	k_1(meV)	k_2(meV)
3C-SiC	48	-	-
4H-SiC	85.5	125	125
6H-SiC	45	100	100

It is more difficult to obtain p-type doping because all of the acceptor impurities that have been investigated so far (e.g. Al, B, Ga and Sc); all form deep levels and are difficult to activate. Another disadvantage of these deep acceptor levels is that the p-concentration is

Reproduced with permission of the copyright owner. Further reproduction prohibited without permission.

strongly dependent on temperature, which can lead to severe complications in device modeling and design. So far Al has been the most common dopant, yielding a maximum p-type concentration in the $^{19}-10^{20}cm$ range [2]. Doping of Al in SiC yield ionization energy of about 200 meV for each of the three most common SiC polytypes.

Ion-implantation is a good doping technique for SiC because of the physical stability of SiC. The excellent physical stability of SiC lends itself well to the heat treatment which is required to anneal out the ion-implantation damage. Both post annealing and in-situ annealing can be utilized to "cure" the ion-implantation damage [45].

2.4 MOBILITIES IN BULK AND MOSFET STRUCTURES

Experimental data on electron mobilities in SiC continues to be obtained by various groups. The mobility is an important parameter to monitor since it controls the low field drift velocity, electron transit times and hence the device switching speeds, the frequency response and the 3 dB cut-off values. The mobility is dependent on the internal scattering mechanisms, and is a very good indicator of the overall crystalline quality of the material. For example, material that is polycrystalline in nature or has a large density of defects and dislocations will tend to scatter electrons quite heavily. This will lead to unacceptably low values of the mobility, and such devices would have poor utility. The mobility parameter thus serves as a crude check for the processing quality.

The mobility values obtained in bulk SiC material have shown the following features: (a) The magnitudes have typically been in the 300-400 $cm^2\ V^{-1}\ s^{-1}$ range, and hence much lower than the corresponding values in Si or GaAs. This is largely due to a higher effective electron mass which reduces the low field mobility. However, since SiC material can withstand much larger electric fields, it is expected that the overall drift velocity which depends on both the mobility and the applied field, would be higher than Si. (b) A strong anisotropy has been observed, with different mobility values being measured for electric

Reproduced with permission of the copyright owner. Further reproduction prohibited without permission.

fields applied along two mutually perpendicular directions. This is most strongly observed in the 6H-polytype which has the greatest anisotropy. (c) A strong temperature dependence is seen with the mobility decreasing at high temperatures. This is indicative of the phonon-dominated scattering in the material. (d) Finally, the mobility values in MOSFET structures have been found to be rather small, roughly around 50 $cm^2 V^{-1} s^{-1}$. These low mobility values are not well understood at present, and are believed to be due to the additional scattering mechanisms that are present in MOSFET structures. The presence of an oxide charge is one of the potential scattering processes that could lower the mobility. In this research, it is shown that though ionized impurity scattering due to impurities present in the oxide can occur, the interface roughness at the SiC-SiO_2 junction plays an even more important role.

Figure 2.7 shows the variation of experimental mobility with temperatures for various samples of 6H-SiC [46]. The samples were doped n-type by introducing Nitrogen with densities ranging from 10^{16} cm^{-3} to 10^{19} cm^{-3}. The highest mobilities were obtained for the low-doped samples since ionized impurity scattering was effectively eliminated at these concentrations. Thus, Fig. 2.7 does demonstrate the wide variation possible based on the processing conditions and purity of the sample. The possible anisotropy and the dependence on the applied electric field direction is shown in Fig. 2.8 based on the data of Schaffer et al. [47]. The fields were applied parallel and perpendiclar to the longitudinal c-axis of the hexagonal closed packed structure of 6H-SiC. As seen from the data, higher mobilities will result for an electric field orientation perpendicular to the c-axis in SiC. This is due to the anisotropy in the bandstructure and effective mass, and would be the preferred direction of applying external voltages in actual devices fabricated from SiC. Variations with doping density as seen in Fig. 2.7 were observed for both electric field orientations, but have not been shown in Fig. 2.8 for simplicity. Electron mobility data measured by Palmour et al. [48] for the 4H-polytype is shown in Fig. 2.9. This result underscores differences in mobility that can arise with changes in the polytypes, and variations in the degree of anisotropy.

Reproduced with permission of the copyright owner. Further reproduction prohibited without permission.

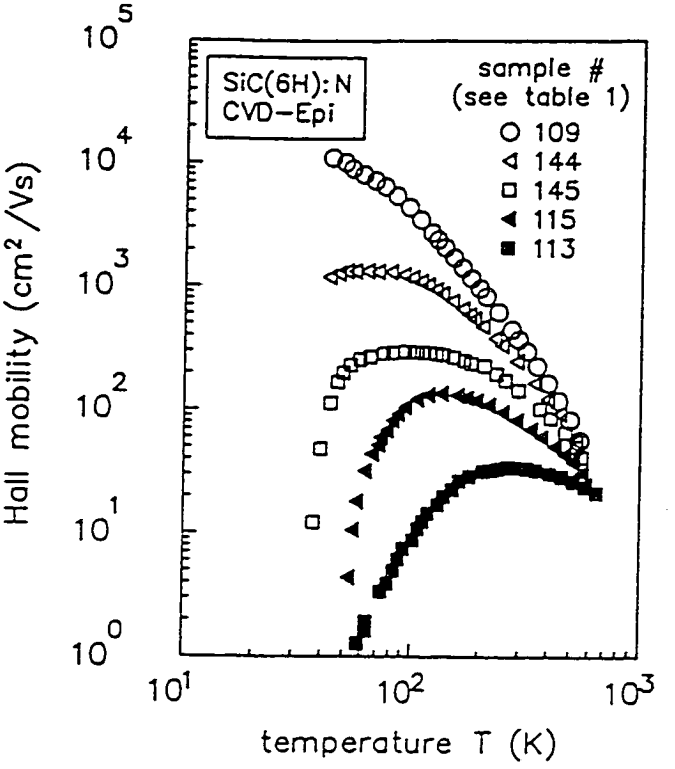

Fig. 2.7 Experimental electron mobility variation with temperature in 6H-SiC [46].

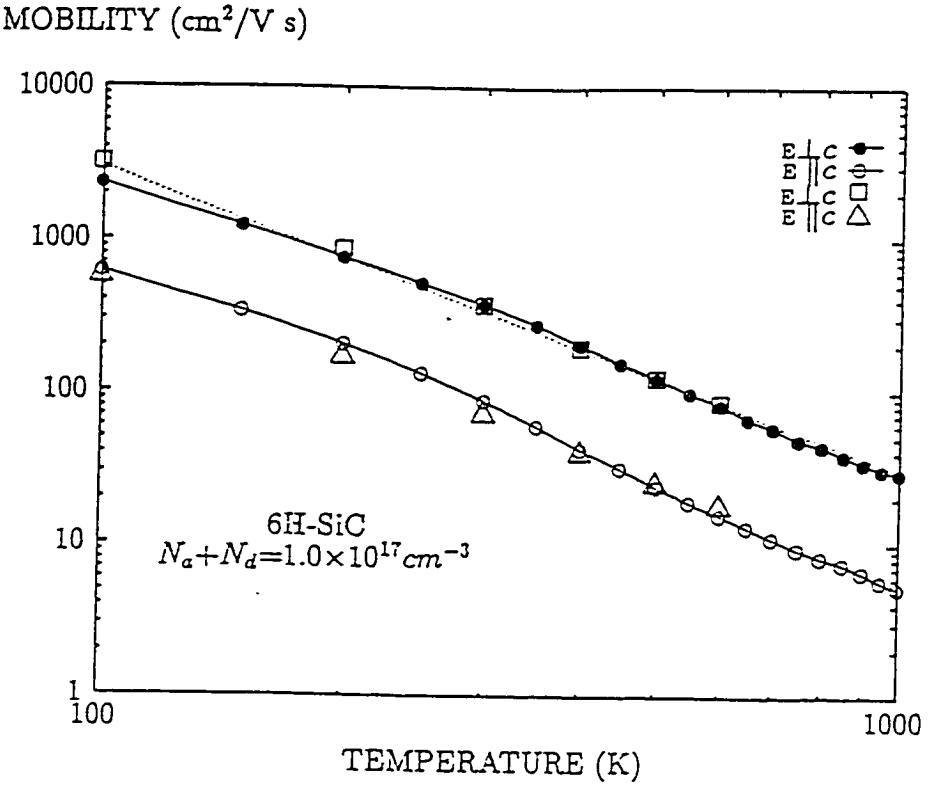

Fig. 2.8 Experimental electron mobility data for 6H-SiC showing anisotropy [47].

Reproduced with permission of the copyright owner. Further reproduction prohibited without permission.

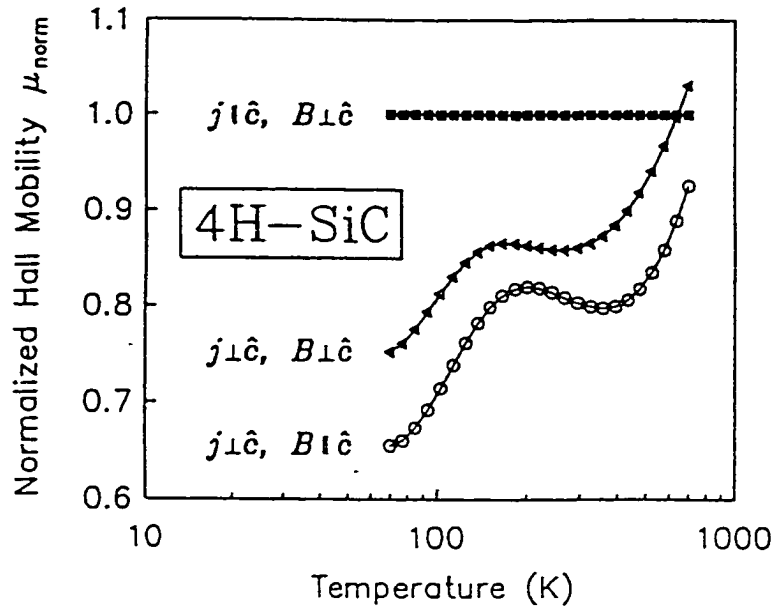

Fig. 2.9 Experimental electron mobility data for 4H-SiC [48].

Finally, the mobility data available to date on MOSFET structures is presented next. This represents a slightly different physical system, since the electrons are confined by the electric field at the gate to move in only two of the three directions. Such channel mobilities are, therefore, a result of a two-dimensional electron flow close to the interface between SiC and the oxide. The test results seem to indicate that the mobility values that have been obtained for such "quantum structures" in SiC are much lower than those in bulk devices. The origin of this difference is not well understood at present, and is examined in this work. In any case, the measured room temperature mobility as a function of the applied gate field in a 6H-SiC MOSFET structure with the c-axis perpendicular to the oxide interface [49] is shown in Fig. 2.10. The results show a mobility decrease with applied transverse field, and the relatively low values ranging around 50 $cm^2 V^{-1} s^{-1}$.

2.5 SiC DEVICES AND THEIR CAPABILITIES

SiC has shown great potential for a variety of electronic applications ranging from microwave radar and communications, radiation hard circuitry, high-temperature sensing, and high-power devices. 6H-SiC has been the most frequently studied polytype due to the

Reproduced with permission of the copyright owner. Further reproduction prohibited without permission.

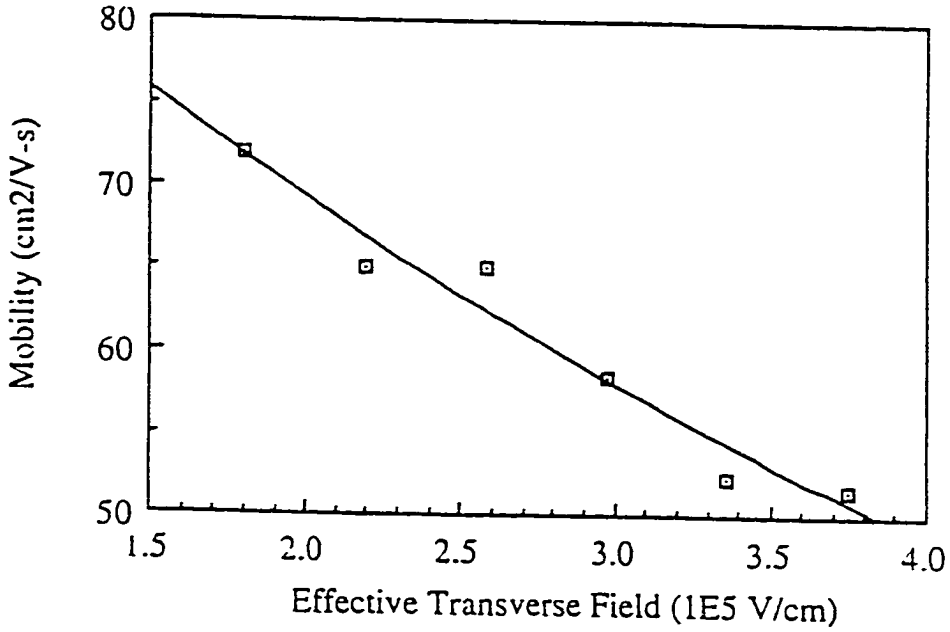

Fig. 2.10 Electron mobility data for a 6H-SiC MOSFET at room temperature [49].

ease of fabrication. Extremely low leakage currents, large break down voltages, and high temperature operation have been observed for the various devices fabricated to date [4,50,51].

SiC MOSFETs have been fabricated with the capability for high-field operation [1,52]. Variations of the basic structure to yield vertical UMOS transistors have also been realized [53]. JFETs have been fabricated from both 3C and 6H-SiC. A 3C SiC buried gate JFET grown on a 6H substrate achieved transconductance as large as 20ms/mm [43]. Similar devices fabricated from homoepitaxial 6H-SiC achieved a maximum transconductance of 17ms/mm, and could be completely pinched off at a gate voltage of -40V [54]. 6H-SiC MESFETs fabricated on 6H substrate have shown a transconductance of 25ms/mm and the high frequency power gain of 14dB at 1.0GHz limited largely by the Ohmic contact resistance [52,55].

Relatively less work has been done on SiC bipolar transistors (BJTs). In a simulated study, the high power, high frequency performance of SiC BJTs were found to be limited by the ohmic contact resistance. Another factor attributed to the weak device performance was

Reproduced with permission of the copyright owner. Further reproduction prohibited without permission.

the low hole concentrations attainable in the p-type base region. This has led to small current gains in the 10-15 range thus far.

Wide band-gap semiconductors are very desirable for ultra violet (UV) detection applications because of their insensitivity to the longer wavelengths, their ability to withstand hostile environments (for space applications, for instance), and their low dark currents. Considerable improvements have been made in reducing the device dark current to values as low as 10^{-11} A at -1V and 200C [56]. Besides, the SiC detectors are potentially capable of high sensitivity. In a recent experiment, a SiC photodiode yielded a sensitivity four times larger than that of a comparable Si UV detector [55]. Attempts are also being made to further reduce the wavelength capability, by capping the detectors with SiO_2 passivation layers to alleviate the surface recombination problem [44].

Due to its superior thermal conductivity and power handling capacity, SiC is an ideal material for high voltage rectifiers. Up to 1.1 KV operation at 400C has shown good characteristic with a low on-resistance [57]. In another experiment, a low 2 Volts forward voltage drop was attained in a Schottky rectifier designed to support 3 KV bias [50]. Forward currents of 500mA are being routinely achieved [58]. Reverse leakage currents as low as 10^{-5} A/cm^2 under voltages of 1.3 kV have been achieved at 350° C [53]. These devices have successfully passed reliability tests with continuous operation over 1000 hours. Thyristors operating at elevated temperatures as high 400° C have also been demonstrated. As with BJTs, the high specific on-resistance of about 15 mOhm cm^2 beyond the breakover voltage due to the low doping within the p-region, has presented a problem. Performance enhancements are being attempted through the use of mesa structures.

Finally, SiC-based LEDs and lasers are being tested as potential candidates to fill the present gap in blue color display technology. Since SiC is a indirect band-gap material, the overall efficiency is not expected to be very high. However, in principle, this difficulty can partially be compensated by driving the SiC LED devices at higher currents. The LED

Reproduced with permission of the copyright owner. Further reproduction prohibited without permission.

development has been partially successful, and a recent device has shown pure blue emission centered at 470nm with 18.3μW power output at a 25mA (3V) forward bias, with a spectral half width of 69nm [2].

2.6 HIGH VOLTAGE SWITCHING IN SiC DIODES

High voltage testing and pulsed measurements to determine the reliability and power handling capability of SiC material has mainly been carried out so far in p-n junction diodes. This choice is related to the simplicity of the device which makes it easier to test, analyze and interpret experimental data. Besides, the diode structure forms the basic building block for other more complicated devices such as thyristors, and hence needs to be well characterized and understood before developing other electronic components. In the experimental work carried out mainly at NASA Lewis, the forward characteristics of SiC diodes were found to be very well behaved, exhibiting saturation current densities below 10^{-20} A/cm^2 with ideality factors close to 2.0 [59]. The ideality factor value is indicative of a strong recombination current component, and hence of traps and recombination centers within the SiC device. The measured forward resistance has been on the order of 0.3 Ohm cm^2. The true test of high voltage operation and power handling capacity can be gauged in the reverse biased mode. The most recent diodes tested [59] have exhibited a dc reverse blocking voltage of 2200 Volts for a 24 μm thick n-region. The devices were immersed in Fluorinert to prevent arcing and surface discharges. This values crudely translates into an electric field of about 1 MV/cm.

Despite the high voltage holdoff capability under the dc mode, results from pulsed measurements at NASA Lewis have been quite different. Strangely, much lower hold-off voltages have been observed in response to a fast reverse biased voltage ramp with rise times of less than 1 ns [25]. The basic 4H and 6H-SiC diodes used in the NASA Lewis high voltage experiments for the breakdown and transient characteristics were n^+-n-p^+ structures

Reproduced with permission of the copyright owner. Further reproduction prohibited without permission.

as shown in Fig. 2.11. The samples was prepared by CVD growth over a p-type substrate. The dc current-voltage (I-V) characteristics of these 4H and 6H-SiC diodes shown in Fig 2.12, indicate that the dc reverse breakdown voltage was over 140 Volts for a 0.8 μm n-layer. The cause of the reverse breakdown was also studied, and found to be the result of micropipe defects. As such, three types of defects were seen to be present in the NASA SiC material. All or some of these defects can be expected to contribute to the device breakdown. These defects were: (a) Triple defects, (b) Droplet defects, and (c) Micropipe defects. However, their study finally revealed that triangle defects and droplet defects have very little or almost no measurable impact on the p^--n junction I-V characteristic. The main cause of failure were

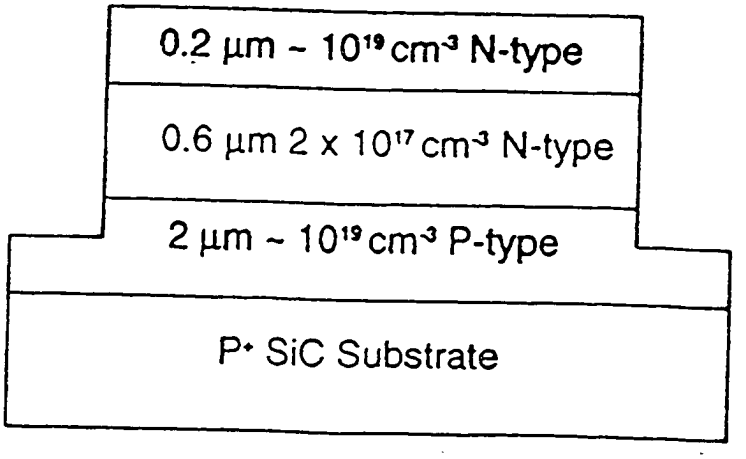

Fig. 2.11 Structure of the SiC device used for the experiment. [59]

the micropipes defects. Such defects are expected to cause recombination and trapping within SiC. Hence, their role in influencing the breakdown characteristics can be studied through numerical simulations. The defect density, energy, and rate constants for such research could then be chosen as variable parameters for performance predictions.

For observations under pulsed voltage conditions, it was found that the breakdown voltage for 4H-SiC diode was lower for pulse widths on the order of 200 ns and having

Reproduced with permission of the copyright owner. Further reproduction prohibited without permission.

risetimes on the ordere of 1 ns, as compared to the breakdown voltage value obtained from continuous mode measurements. This is shown in Fig. 2.13. Such behavior is unusual and is not well understood at present. The physics of this phenomena has been investigated in this research, and will be analyzed through the numerical drift-diffusion simulations.

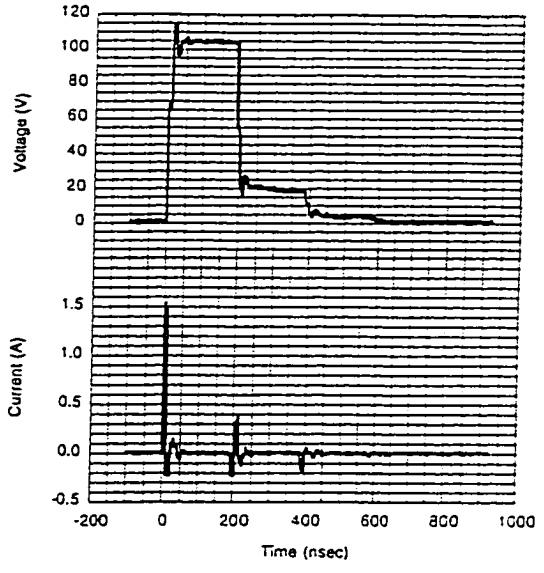

Fig. 2.12 Reverse biased IV characteristics of 4H-SiC diode. [59]

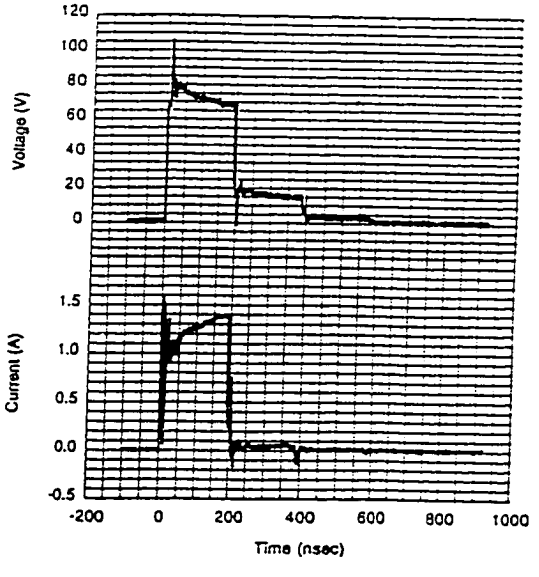

Fig. 2.13 Breakdown of 4H-SiC diode during reverse biased pulsed input voltage [25].

Reproduced with permission of the copyright owner. Further reproduction prohibited without permission.

CHAPTER 3

DETAILS OF THE NUMERICAL SIMULATIONS

3.1 INTRODUCTORY OVERVIEW OF SIMULATION APPROACHES

The principal goal of semiconductor device simulations is to determine the behavior of terminal current and device voltage in response to an applied stimulus. The stimulus could either be an external bias, an optical excitation, or a thermal perturbation as a function of time. The mathematical model to be used for device analysis should, in general, include the dynamics of free carriers within the bulk semiconductor, apply appropriate boundary conditions to different semiconductor sections, and account for the time dependent behavior at the contacts and surfaces and any applicable thermal exchanges within the semiconductor system. The simplest approach for describing the transport behavior in semiconductors is classical. This methodology is called the **Kinetic Approach**, since it uses the kinetics of an "average particle" with a simple treatment of collisions to describe its equation of motion [60]. In its simplest form, the semiconductor band structure is considered parabolic, leading to a constant effective mass, and particle is considered to be non-interacting. This implies low concentrations leading to a non-degenerate Maxwell-Boltzmann carrier distribution. Frequency-dependent response is analyzed for the time periods larger then the relaxation time. Though this approach reasonably describes macroscopic properties of the semiconductors, all of the off-equilibrium effects are largely excluded.

In the **Boltzmann Transport Approach** which represents a higher level of sophistication, a governing integro-differential equation is obtained for the equation of motion for the distribution function $f(r,p;t)$ of particle ensemble [61]. This distribution function f is the probability of finding a particle with the momentum p at a position r at time t. The Boltzmann Transport Equation (BTE) incorporates all of the internal scattering effects taking place over time, and is thus able to describe non-equilibrium,

Reproduced with permission of the copyright owner. Further reproduction prohibited without permission.

transient effects correctly provided the scattering relationship can be characterized. Usually, a time-dependent perturbation theory based on the Fermi Golden rule is used to ascertain the scattering relationships. However, the Boltzmann transport approach is usually restricted to inherent assumptions, such as a simplified treatment of the band structure and distribution functions. This approach fails, however, in cases where simplified distributions do not exist such as in very short dimensional structure or during ultrashort transient time intervals. However, this is a popular scheme given its advantage of not being very computationally intensive.

In order to correctly simulate semiconductor structures having very small dimensions, for phenomena involving ultrashort time scales, or when the assumptions of the BTE become unacceptable, another approach called the **Monte Carlo Approach** is used for greater accuracy [62]. In the stochastic Monte Carlo approach, individual particles are randomly selected and their motion followed in space and time. The average ensemble behavior is subsequently determined by collecting enough information about the particles. The biggest advantage of this method is that no fitting parameter is required. However, the approach is very intensive computationally since a large number of particles are required for simulation.

The next level of mathematical complexity involves the **Quantum Transport Approach** which describes electronic behavior in situations where the quantum nature of the states and kinetics becomes dominant [63]. Such a treatment becomes necessary in problems where the spatial and temporal extents are similar to the de Broglie wavelength and the duration of scattering respectively. It is the only technique that can account for the wave-like nature of electrons and describe the related interference phenomena. All variations of the quantum transport approaches are very complex, and are presently needed in only a few of the devices of interest.

Boltzmann transport equation, under several assumptions, can be simplified down into a relatively straight-forward expression, known as the Drift-Diffusion equation. For this

Reproduced with permission of the copyright owner. Further reproduction prohibited without permission.

research, such a **Drift-Diffusion Transport Approach** will be employed for diode simulations given its relative simplicity and modest computational requirements. Furthermore, since the device dimensions ($\approx 10\mu m$) are not restrictively small and the time scale of interest are relatively large being higher than 10 ns, the more complex approaches will not be necessary. The results obtained from the drift-diffusion scheme are therefore expected to be adequate. However, many of the transport parameters that need to be used in the drift-diffusion approach can only be obtained accurately from a more basic Monte Carlo type approach. Hence, here both the Monte Carlo and the Drift-Diffusion schemes will be used. The Monte Carlo will serve to supply an accurate set of transport parameters for the drift-diffusion model.

3.2 CONSIDERATIONS OF MICROSCOPIC TRANSPORT SIMULATIONS

The study of charge transport in semiconductors is of fundamental importance both from the point of view of basic physics and for its application to electronic devices. Charge transport is in general a tough problem, from both the mathematical and physical points of view. Calculations of transport properties in semiconductors have most commonly been approached by attempting to solve the Boltzmann Transport Equation (BTE). The BTE describes the dynamic evolution of the distribution function, f, under non-equilibrium conditions and the approach is well defined in the litrature. The total rate of change of distribution function f can be expressed as [64]:

$$\frac{\partial f}{\partial t} = -\mathbf{v}.\nabla_r f - \frac{eF}{\hbar}.\nabla_k f + \left[\frac{\partial f}{\partial t}\right]_{collisions} \qquad (3.1)$$

where **F** is the applied external field, **v** is the drift velocity, and the last term is the change in occupancy "f" due to collisions and scattering. The first and second terms of the equation describe the effects of the density gradient and of the external electric field, respectively on

Reproduced with permission of the copyright owner. Further reproduction prohibited without permission.

the distribution function. The collision term in the equation involves an integral. This yields a complicated integro-differential form for the BTE, which does not offer simple (or even complicated) analytical solutions except for very few cases, and these cases usually are not applicable to real systems. Furthermore, since transport quantities are derived from the averages over many physical processes whose relative importance is not known a priori, the formulation of reliable microscopic models for the physical system under investigation is difficult [64].

Approximate analytical solutions involve either approximations regarding the form of the scattering rates, or assumptions on the distribution function. The two most used techniques are the Legendre polynomial expansion [65] and the displaced Maxwellian approximation [66]. In most cases of interest the approximations are so drastic that it is no longer clear whether the features of interest in the results are due to the microscopic model or to mathematical approximations.

To circumvent the problems associated with analytical solution of the Boltzmann transport equation, numerical techniques have been developed to obtain an exact solution for the distribution function. With the aid of modern large and fast computers, exact numerical solutions of the BTE can be obtained for microscopic physical models of considerable complexity in a relatively short computer execution time. The two most important numerical techniques are the iterative method [67] and the Monte Carlo technique [68]. The Monte Carlo technique is by far the more popular of the two. This technique is easy to implement and offers the following advantages:

- The microscopic interpretation of the physical details is quite transparent.
- Stochastic calculation is achieved at a minimum level of difficulty while incorporating memory effects.

Reproduced with permission of the copyright owner. Further reproduction prohibited without permission.

- Temperature gradients and fields (both electric and magnetic) can all be comprehensively included.
- Time and space dependent phenomena can be easily simulated.
- No arbitrary assumption regarding the distribution function needs to be made.
- System memory effects are easily included and hence all non-Markovian behavior.
- Arbitrary shapes and geometries, as well as complicated boundary conditions can be analyzed with ease.

Monte Carlo is a statistical numerical method used for solving mathematical problems. It was born well before its application to the transport problems, and has been applied to a number of scientific fields. In the case of charge transport, however, the Monte Carlo approach to the solution of the Boltzmann equation proves to be a direct simulation of the dynamics of charge carriers inside the crystal, so that, while the solution of the equations is being built up, any physical information required can be easily extracted. This method was first applied to transport in semiconductors by Kurosawa [68] to study steady-state hole transport in Ge through the inclusion of a "self-scattering" scheme. Fawcett et al. [69] extended this method for use in GaAs where different scattering processes and band structures were incorporated.

3.3 THE MONTE CARLO METHOD

The Monte Carlo method, as applied to charge transport in semiconductors, consists of simulation of the motion of one or more electrons inside the crystal, subject to the action of external forces due to applied electric and magnetic fields and a set of appropriate scattering mechanisms. In the frame of semiclassical approximation, the motion consists of a sequence of free flights interrupted by instantaneous scattering events. The approach is semi-classical in the sense that the particles are treated as classical point-like objects, but the

Reproduced with permission of the copyright owner. Further reproduction prohibited without permission.

scattering rates are determined using quantum mechanical theory. During the free flight, electrons obey classical laws of motion and drift in the electric field. The free flight time, the type of scattering event, and the final state of the electron after the scattering are random quantities which are selected stochastically in accordance with some given probabilities. The probability distributions for these random quantities can be expressed in terms of the transition rates due to the various processes and the strength of the electric field. This technique was proposed in 1966 and has been used extensively [64]. The details described in this and the following sections are taken from reviews by Jacobin and Reggiani. In practice, the physical distributions may be quite complex and difficult to manipulate even with a computer. The manipulation can be simplified by mapping the complex distributions on to a simple pseudo-random distribution [70]; the most convenient pseudo-random distribution is the uniform distribution, which is readily available on most computer systems. In general, if p(q) and p(r) are the respective probability densities, associated with q in the physical distribution and r in the pseudo-random distribution, then [64]:

$$\int_0^q p(q')\,dq' = \int_0^r p(r')\,dr' \quad . \tag{3.2}$$

In a uniform distribution p(r) = 1, so we get:

$$r = \int_0^q p(q')\,dq' \quad . \tag{3.3}$$

Hence, provided that this integral can be evaluated in a simple closed analytic form, inversion will yield a random value for the physical variable q in terms of the uniformly distributed random number r. As a consequence, any Monte Carlo method relies on the generation of a sequence of uniformly distributed random numbers corresponding to various random processes involved in the phenomenon of interest.

Reproduced with permission of the copyright owner. Further reproduction prohibited without permission.

When the purpose of analysis is the investigation of a steady-state, homogeneous phenomenon, it is sufficient in general to simulate the motion of one single electron; from ergodicity we may assume that a sufficiently long path of this simple electron will give information on the behavior of the entire electron gas. When, on the contrary, the transport process is not homogeneous or stationary, it is necessary to simulate the motion of an ensemble of charge carriers and evaluate over the time the ensemble average of the physical quantities of interest. The method is known as Ensemble Monte Carlo (EMC) method. and the structure of the program is summarized below.

3.3.1 DEFINITION OF THE PHYSICAL SYSTEM

The starting point of the program is the definition of the physical system of interest, which includes the parameters of the material and the values of physical quantities. such as lattice temperature and electric field. The parameters that control the simulation are also defined, such as the number of electrons simulated, duration of each subhistory. total time of simulation, the desired precision of results, and so on. The next step in the program is a preliminary calculation of the scattering rates as a function of electron energy. The scattering rates are normalized and stored in a tabulated form.

3.3.2 INITIAL CONDITIONS

This step involves choosing the initial position, momentum, and energy of the electrons. Uniformly distributed random numbers are used to select the initial position and direction of motion of the electrons, if required. The valley of the electrons in the conduction band is also chosen. Usually, the electrons all reside in the lowest valley and are assumed to be in a state of initial thermal equilibrium. For simulations involving photoexcitation, the initial state lies in the lowest direct valley with an energy equal to the excess energy of the external excitation. The momentum at this initial energy is usually distributed randomly.

Reproduced with permission of the copyright owner. Further reproduction prohibited without permission.

However, in situations involving electrical carrier injection from a contact, the distributions would be suitably modified. For example, electronic energies associated with injection from a contact would correspond to a heated Maxwellian with a semi-hemispherical momentum distribution.

3.3.3 FLIGHT DURATION

The next step is to determine the free flight time for each electron. The flight time depends on the scattering probability. Each process that can scatter the electron at the end of a free flight is characterized by a transition rate $S_n(K,K')$. from the momentum state $\hbar K$ to $\hbar K'$. Here the subscript n denotes an individual scattering process and can take values n = 1,2 .... N if there are N possible processes. The total scattering rate from the state k, because of the n^{th} process, is given by:

$$\lambda_n(k) = \int S_n(kk')dk'' \quad . \tag{3.4}$$

Hence, the total scattering rate, due to all processes,as explained in [64] is

$$\lambda(k) = \sum^{N} \lambda_n(k) \quad , \tag{3.5}$$

where k is a function of time. In practice the total scattering rates are only functions of |k|, so $\lambda(k)$ can be easily transformed to $\lambda(E)$. Thus, if $\lambda(k)$ dt is the probability that an electron in the state k suffers a collision during the interval dt, the probability that an electron suffered a collision at time t=0 has not yet suffered another collision after a time "t" is:

$$\exp(-\int_0^t \lambda[k(t')]dt') \quad . \tag{3.6}$$

Reproduced with permission of the copyright owner. Further reproduction prohibited without permission.

Consequently, the probability the electron will suffer its next collision during interval dt around t is given by [64]:

$$P(t)dt = \lambda[k(t)]\exp(-\int_0^t \lambda[k(t')]dt')dt \quad . \tag{3.7}$$

The probability density P(t) is, therefore:

$$P(t) = \lambda[k(t)]\exp(-\int_0^t \lambda[k(t')]dt') \quad . \tag{3.8}$$

Using eq. (3.8) and eq.(3.3), a uniformly distributed random number r can be used to describe the process, which gives:

$$r = 1 - \exp(-\int_0^t \lambda[k(t')]dt') \quad . \tag{3.9}$$

Eq.(3.9) is very complicated and cannot, for practical scattering mechanisms. be solved analyticaly for t. Numerical integration can be performed to produce r and tin tabular form for each value of electron energy, but this approach is time consuming and rather impractical.

A new technique for circumventing this difficulty has been found [71,72]. It involves supplementing the real scattering processes with a virtual scattering process that does not affect the state of the electron. This scattering mechanism is usually referred to as "self scattering" or "null collision." The virtual scattering rate $\lambda_V(k)$ is chosen such that total scattering rate becomes a constant. Thus, total scattering rate for the electron which includes the virtual process is simply:

$$\lambda_T(k) = \lambda(k) + \lambda_V(k) = \Gamma_{max} \quad . \tag{3.10}$$

Eq.(3.8) now reduces to the elementary form

Reproduced with permission of the copyright owner. Further reproduction prohibited without permission.

$$r = 1 - e^{-\Gamma_{max} t} \quad . \tag{3.11}$$

Solving for t gives:

$$t = -\frac{1}{\Gamma_{max}} \ln(1-r) = -\frac{1}{\Gamma_{max}} \ln(r) \tag{3.12}$$

Flight time "t" can thus be determined form the uniformly distributed random number r. Γ_{max} is chosen to be the maximum value of $\lambda(k)$ in the region of k space of interest. This is done to avoid negative values for $\lambda_v(k)$. If an electron undergoes a self scattering. its state k after the collision is taken to be equal to its state k before the collision. so that in practice the electron path continues unperturbed as if no scattering at all had occurred. The computer time wasted in taking care of self scattering events is more than compensated for by the simplification of the calculation of the free flight time.

3.3.4 FREE FLIGHT WITHIN THE MONTE CARLO

The electrons are allowed to drift freely under the influence of the electric field. During the free flight, the electron wave vector k changes continuously according to Newton's law of motion for the frictionless regime in the absence of magnetic fields or any thermal gradients:

$$\hbar \frac{\partial k}{\partial t} = eE \quad . \tag{3.13}$$

The flight is terminated after the free flight time with a scattering event. Parameters of interest (eg. electronic position, momenta and energy) are recorded at the end of free flight.

Reproduced with permission of the copyright owner. Further reproduction prohibited without permission.

3.3.5 CHOICE OF THE SCATTERING MECHANISM

The scattering rates of the various mechanisms are tabulated as function of energy and normalized to Γ . Thus for a given E, the normalized probability $P_j(E)$ for the scattering mechanism j is $\lambda_j(E)/\Gamma$. The selection of scattering mechanism is made by generating a random number r between 0 and 1. If $\sum_{i=1}^{i=j-1} P_i(E) < r < \sum_{i=1}^{i=j} P_i(E)$ .then the j^{th} scattering mechanism is selected. if $r > \sum_{i=1}^{N} P_i(E)$, where N is the total number of scattering mechanisms, then self scattering occurs. The inequality

$$r < \sum_{i=1}^{m} P_i(E) \tag{3.14}$$

is tested for all possible values of m, starting from 1 and going up to N. and scattering process m is selected once the inequality is satisfied.

3.3.6 CHOICE OF STATE AFTER SCATTERING

Once the scattering mechanism that caused the end of the flight has been determined, the new state after the scattering of the electron, k' must be chosen. If a self scattering has occurred, k' is taken equal to k. The flight is not terminated, and a new flight time Δt is chosen and added to t. This goes on until a real scattering event is selected. When a real scattering event occurs, k' is chosen stochastically according to the differential cross-section of that particular mechanism. The energy of the electron is altered if an inelastic process such as polar optical, or intervalley scattering has occurred. On the other hand, for ionized impurity scattering or acoustic scattering, the final energy equals the initial energy because of the elastic nature of the collision. A change in momentum will always occur; however, the scattering mechanism could be either a momentum randomizing (acoustic, intervalley scattering) or non-momentum randomizing (polar optical, ionized impurity scattering) process. Optical phonons add or extract a constant quanta of energy "$h\omega$" through emission

Reproduced with permission of the copyright owner. Further reproduction prohibited without permission.

or absorption. Such a fixed energy quanta is a direct consequence of the ω-k dispersion curves for optical phonons in semiconductor materials. The determination of the new wave vector k after the phonon scattering requires further generation of random numbers. These random numbers are used to determine the azimuthal angle θ and angle ϕ according to the angular dependence of the selected scattering mechanism. The angle ϕ after the scattering can take any value between 0 to 2π with equal probability. So ϕ is chosen using a random number r as:

$$\phi = 2\pi r \tag{3.15}$$

On the other hand, the angle θ depends on the nature of the scattering process. For momentum randomizing processes, θ is given by:

$$r = \frac{1}{2}(1-\cos\theta) \tag{3.16}$$

For other scattering mechanisms, that have directional dependence P(θ), one can select θ by generating a random number and mapping the distribution P(θ) to a uniform distribution [71].

After the scattering event, the momentum and energy of the electron are updated. The electron position remains unchanged as the collisions are considered to be instantaneous. The electron begins its next flight and drift-scatter mechanism repeats until the end of the simulation.

3.5 SCATTERING MECHANISMS IN SiC

Calculation of scattering rates is an important step in the Monte Carlo method. It requires knowledge of quantum mechanics behind each scattering mechanism involved. The aim is to determine the various scattering probabilities as a function of electron energy. This

Reproduced with permission of the copyright owner. Further reproduction prohibited without permission.

section contains a brief discussion of the scattering mechanisms and the underlying quantum mechanics. A detailed treatment of the issue can be found elsewhere [64].

3.5.1 GENERAL SCATTERING THEORY

The transitions of interest for electron transport in semiconductors can be classified as intervalley, if both initial and final states of the electron lie in the same valley, or intravalley, if the final state lies in a valley different from that of the initial valley. The transitions are induced by different scattering sources present in the crystal, of which the most important are phonons, impurities and other electrons.

In the Born approximation, the scattering process only consists of a transition between two definite momentum states for the electron involved. The transition probability per unit time for scattering from a state k to k' , due to a perturbation Hamiltonian H, is given by the Fermi Golden rule

$$S(k,k') = \frac{2\pi}{\hbar}|\langle k|H'|k'\rangle|^2\delta(E'-E) \qquad (3.17)$$

where $|\langle k|H'|k'\rangle|^2$ is the matrix element of H' between the initial and final states and the delta-function expresses the conservation of energy, E and E' being the eigenenergies of the initial and final states, respectively. For a transition due to a phonon with wavevector q and frequency ω, we have:

$$E' - E = \pm\hbar\omega \quad , \qquad (3.18)$$

$$k - k' \pm q = 0 \quad , \qquad (3.19)$$

Reproduced with permission of the copyright owner. Further reproduction prohibited without permission.

By integrating over all possible final states k', the total scattering rate out of state k is obtained.

$$\Gamma(k) = \frac{2V}{8\pi^3}\int dk' \int d\phi \int d\theta S(k,k')k'^2 \sin\theta \quad , \tag{3.20}$$

where V is the volume of the crystal, θ is the angle between k and k', and ϕ is the azimuthal angle. The factor of "2" comes from the spin-degeneracy of the electronic states. The angular dependence of the scattering is obtained directly from the angular dependence of S(k.k'). The matrix element in eq.(3.17) can be written as [64]

$$|\langle k|H'|k'\rangle|^2 = V(q)G(k,k') \quad , \tag{3.21}$$

so that the transition rate is

$$S(k,k') = \frac{2\pi}{\hbar}V(q)G(k,k')\delta(E'-E) \quad , \tag{3.22}$$

where V(q) contains the dependence upon q = k' - k of the square Fourier transform of the interaction potential. The manner in which V(q) depends on the momentum transfer depends on the nature of scattering.

Now we consider the different scattering mechanisms individually. The electron-phonon interaction is due to the deformation associated with phonon vibrations, of the otherwise perfect crystal. In covalent semiconductors it is described in the framework of the deformation-potential method [73] for both acoustic and optical phonons. As regards impurities, they can be ionized or neutral. In the former case the interaction is of long-range Coulomb type, while in the latter, the interaction is of much shorter range. The overall effect of neutral impurities is, in general, much weaker. Hence the neutral impurities are not included in the present Monte Carlo calculations. The electron-electron collisions are also

Reproduced with permission of the copyright owner. Further reproduction prohibited without permission.

not considered for the simulation process since their effect is also very limited at the low carrier densities being considered here.

3.5.2 ACOUSTIC PHONON SCATTERING

The energy change in acoustic phonon scattering is negligible and it is treated as an elastic process. However, for nonlinear transport problems in low fields or temperature, the small energy dissipation is needed to establish a smooth distribution function. The squared matrix element V(q) (eq. 3.21) is given by:[64]

$$V(q) = \frac{E_a^2 \hbar q}{\rho s}(N_q + \frac{1}{2} \pm \frac{1}{2}) \quad , \tag{3.24}$$

with the plus (minus) sign above referring to phonon emission (absorption) process. E_a is the acoustic deformation potential, ρ the crystal density, s the speed of sound, and N_q the Bose-Einstein distribution given by:

$$N_q = (\exp[\frac{\hbar\omega}{kT}] - 1)^{-1} \quad , \tag{3.25}$$

where $\hbar w$ is the phonon energy. The acoustic phonon scattering rate can be determined by substituting V(q) in eq.(3.22) and using eq.(3.20) for integrating over all k'.

3.5.3 POLAR OPTICAL SCATTERING

In optical phonon mode of vibration, the two oppositely charged unit cells oscillate out of phase. The displacement during the oscillation sets up a polarization field that scatters the electron. The square of the matrix element for this process is given by:[64]

Reproduced with permission of the copyright owner. Further reproduction prohibited without permission.

$$V(q) = \frac{\pi e^2}{\hbar \epsilon_0 q^2} \frac{\hbar\omega}{2} \left[\frac{1}{\epsilon(\infty)} - \frac{1}{\epsilon(0)}\right] \left(N_q + \frac{1}{2} \pm \frac{1}{2}\right) \quad , \qquad (3.26)$$

where $\epsilon(\infty)$ and $\epsilon(0)$ are the high frequency and static dielectric constants respectively. N_q is again given by the Bose-Einstein distribution.

3.5.4 NON-POLAR OPTICAL PHONON SCATTERING

The non-polar optical phonons generate a short range potential that causes a shift in the electronic band states. In the long wavelength optical mode of vibration. one set of atoms moves as a body against the second set of atoms which creates a strain in the lattice. The scattering of electrons by this strain is known as deformation potential scattering. The square of matrix element is given by:

$$V(q) = \frac{D_0^2 \hbar^2}{2\rho\hbar\omega} \left(N_q + \frac{1}{2} \pm \frac{1}{2}\right) \quad , \qquad (3.27)$$

where D_0 is the deformation optical potential.

3.5.5 INTERVALLEY PHONON SCATTERING

The transitions between different valleys involve a large amount of momentum transfer so that the polar interactions play a negligible role since its matrix element is dominated by low wavevector phonons. The wave-vector "q" of the phonons causing the transitions is nearly the same as the distance between the minima of the initial and final valley in the Brillouin zone is fixed. This fixes q for a given pair of valleys, so that the energy change in these transitions is constant for a given phonon mode. Consequently, the

Reproduced with permission of the copyright owner. Further reproduction prohibited without permission.

intervalley transitions can also be treated using the deformation potential concept. The squared matrix element is given by:

$$V(q) = \frac{D_{ij_0}^2 \hbar^2}{2\rho\hbar\omega_{ij}}(N_q + \frac{1}{2} \pm \frac{1}{2}) \quad , \tag{3.28}$$

where D_{ij} is the deformation potential for scattering from the i^{th} valley to the j^{th} valley induced by a phonon of energy $\hbar\omega$.

3.5.6 IONIZED IMPURITY SCATTERING

The ionized impurity scattering is elastic in nature. The squared matrix element in the Brooks-Herring formulation case is given by: [76]

$$V(q) = \frac{NZ^2e^4}{(4\pi\epsilon)^2(q^2+\beta^2)^2} \quad , \tag{3.29}$$

where Z is the number of unit charge in the impurity, and β is a constant screening parameter.

3.6 SCATTERING WITH ELECTRON QUANTIZATION

The above discussion assums that electrons are capable of unimpeded motion in all three directions within the semiconductor bulk. However, for analyzing electron motion and their mobilities in MOSFET structures, one needs to include the effect of constrained motion in one of the three directions. This occurs because the electrons in a MOSFET move laterally from the source to drain within a very narrow inversion channel that is formed at the semiconductor-oxide interface. This channel is typically on the order of 10-20 nm, which on the order of the typical deBroglie length of a "free electron." The thickness of the channel is dependent on the transverse field set up by the applied gate voltage, and can reduce the

Reproduced with permission of the copyright owner. Further reproduction prohibited without permission.

channel width at higher gate voltages. In such a situation, the electron can no longer be described as a free particle, and its "plane-wave" description has to be modified. This is usually done by treating its lateral motion parallel to the interface as a usual classical particle, but incorporating "quantization effects" along the third direction. Such electron quantization has been discussed in detail [74]. Briefly it leads to the following effects:

(a) Modification of the wavefunction from a three dimensional "electron plane wave" to a two-dimensional "electron plane wave" modulated by an envelope function along the constraining direction. Thus, the wavefunction changes from:

$$\Psi(x,y,z) = \frac{1}{\sqrt{(V)}} \exp[-ik_x\, x] \exp[-ik_y\, y] \exp[-ik_z\, z] \quad , \tag{3.30}$$

to:

$$\Psi(x,y,z) = \frac{1}{\sqrt{(A\ L_z)}} \exp[-ik_x\, x] \exp[-ik_y\, y]\ F_j(z) \quad , \tag{3.31}$$

where $F_j(z)$ is a suitable envelope function for electrons in the j^{th} subband. As a result, the modified wavefunction needs to be used in the calculation of all the scattering rates. The matrix elements also change since the initial and final states are now described by two dimensional wavefunctions. The two-dimensional wavefunction given by (3.31) have to satisfy the Schrodinger wave equation. Now for the MOSFET device, the interface can be represented by a potential barrier at $z = 0$ due to the discontinuity between the conduction band of SiC and SiO_2. In addition, the applied gate voltage produces a perpendicular field along the longitudinal z-direction. This gives rise to a potential that varies linearly with distance away from the interface and into the SiC material. A good analytical approximation for the envelope function F(z) based on the above potential has been worked out [77,78], and yields:

Reproduced with permission of the copyright owner. Further reproduction prohibited without permission.

$$F_1(z) = \sqrt{\frac{b_o^3}{2}}\, z \exp[-\frac{b_o z}{2}] \quad ,$$

$$\text{where} \quad b_o = \frac{33\, m^* e^2}{8\, \varepsilon\, \hbar^2} \left[n_s + \frac{32}{11} N_b\right]^{1/3} , \tag{3.32}$$

$$F_2(z) = \sqrt{\frac{3b_1^5}{2[b_o^2 - b_o b_1 + b_1^2]}} \left[z - \frac{(b_o + b_1) z^2}{6}\right] \exp[-\frac{b_1 z}{2}] , \tag{3.33}$$

with $b_1 = 0.754\, b_o$, N_b the background MOSFET doping, and ns = inversion channel density.

(b) Another effect is the quantization of the electron energies and the formation of a set of discrete "subbands". The subbands result from the quantization, just as full three-dimensional quantization in an atom leads to discrete electron energies. The difference though, is that instead of complete energy discretization, a continuum of energies results in the two directions in which motion is allowed, while a discrete subband level forms due to the quantized along the z-direction. Thus, the total energy E(k) as a function of the electron wavevector "k" becomes:

$$E(k_x, k_y, k_z) = \frac{\hbar^2 (k_x^2 + k_y^2)}{2m} + E_{oj} \quad , \tag{3.34}$$

where E_{oj} is the discrete energy of the jth subband. According to the model given above [77,78], the subband energies are given in terms of the longitudinal electric field "F_g" due to the gate voltage as:

$$E_{oj} = \left[\frac{\hbar^2}{2m}\right]^{1/3} \left[\frac{3}{2} e \pi F_g \left(j + \frac{3}{4}\right)\right]^{2/3} . \tag{3.35}$$

Reproduced with permission of the copyright owner. Further reproduction prohibited without permission.

(c) Finally, due to quantization and the formation of subbands, the scattering becomes somewhat more complicated. In addition to scattering processes within each subband due to either phonon emission or absorption events, or ionized impurities, one also needs to consider intersubband scattering. For intrasubband processes, the initial and final energy states of an electron lie within the same j^{th} subband. However, for an intervalley scattering event, the electron transitions from the jth initial state to a new state in the i^{th} subband. This, in principle, is not more difficult but simply requires a more complicated tracking based on a larger scattering table. A second, an additional "interface roughness scattering" process needs to be included. This scattering mechanism is arises because the inversion electrons in a MOSFET move in close proximity to the interface. Undulations at the atomic level due to variations in the positioning of SiC and SiO_2 atoms at the boundary produce a "scattering potential." Such interface roughness scattering can be especially important at high gate voltages, since the inversion electrons are then tightly clustered close to the interface.

The details of the various scattering rates for treating such two-dimensional electron quantization have been worked out in the literature [79-82]. The formulae and equations given in the various references has been applied to Si MOSFET structures, but **not** to SiC devices. Here, the available results [79-82] were used and suitable parameter changes made for simulations of SiC MOSFETs. As given in the next chapter, such simulations predicted electrical characteristics that were in very good agreement with experimental data. Furthermore, some important process related parameters were extracted by curve fitting the MOSFET Monte Carlo results with available data under specific conditions. This will enable predictions of MOSFET characteristics to great accuracy under a variety of operating conditions.

Reproduced with permission of the copyright owner. Further reproduction prohibited without permission.

3.7 THE DRIFT-DIFFUSION TRANSPORT APPROACH

The governing Drift-Diffusion equation is given as:

$$J=nqv_n+pqv_p-qD_n(\frac{dn}{dx})+qD_p(\frac{dp}{dx}) \tag{3.36}$$

where J is the current density, n and p are the electron and hole densities, D_n and D_p are the electron and hole diffusion coefficients, v_n and v_p are the electron and hole drift velocities and q is the electronic charge. This equation is derived from the Boltzmann transport equation under the following assumptions:

a) An isotropic and parabolic single band.

b) Inherent assumption of the relaxation time approximation.

c) Absence of degeneracy with no hot carrier effects.

d) A homogeneous collision time. For example, a single energy-independent relaxation time τ_p is assumed for mobility calculations. The carrier mobility μ is then given in terms of the effective mass m^* through the following expression:

$$\mu=\frac{q\tau_p}{m^*}. \tag{3.37}$$

The validity of the drift-diffusion scheme also requires that the scattering time τ_p be significantly smaller then the simulation time scale of interest.

e) No strong off-equilibrium effects, and

f) An assumption that the length scales for spatial variation of the electric field and impurity concentrations are much longer than the carrier mean free path.

In order to adequately include high frequency and transient effects, the displacement current which is observed as a capacitive effect in the external circuit, needs to be incorporated in

Reproduced with permission of the copyright owner. Further reproduction prohibited without permission.

the drift-diffusion model. The overall current transport is then an aggregate of particle current and displacement current given as:

$$J=nqv_n+pqv_p-qD_n(\frac{dn}{dx})+qD_p(\frac{dp}{dx})+\epsilon\frac{dE}{dt} \quad (3.38)$$

where E is the electric field and ϵ is the permitivity of material. The details of the underlying transport model used in this research and its numerical implementation are presented in the following section. In summary, it may be noted that the model developed has the following salient features:

- It is based on the one-dimensional (1D) drift-diffusion scheme.
- It yields the self-consistent transient analysis, as well as the final steady-state response.
- The model is bipolar in nature, and can treat both electron and hole transport on an equal footing.
- An important component of the model consists of rate equations which describe the transient dynamics of the free-carrier generation, trapping and recombination.
- An external circuit has been incorporated in the model.
- The model takes into account the distributed capacitance of the device in the form of an internal displacement current.
- An added feature of the model is the inclusion of impact ionization at high electric fields. Both band-to-band and band-to-trap impact processes are considered.
- Finally, the numerical implementation includes heat generation within the device. A diffusive heat flow model is included, and changes in the transport parameters with any resulting temperature rise taken into account.

Reproduced with permission of the copyright owner. Further reproduction prohibited without permission.

3.7.1 GOVERNING EQUATIONS AND NUMERICAL DRIFT-DIFFUSION IMPLEMENTATION

The 1D Drift-diffusion equation (3.32) which includes the displacement current is the basic equation for charge transport. The free carrier densities in (3.32) are a function of position and time, and need to be updated continuously in time. Time dependent changes in their densities occur not only due to the physical flows arising from on-going carrier drift and diffusion, but also arise from the internal generation/recombination processes. The local charge density change due to physical flow of charge is calculated on the basis of the standard current continuity equation. The role of the generation/recombination mechanisms is described in terms of the following rate equations:

$$\frac{dn}{dt} = e_n N_{D0} - nN_D^+ \sigma_n v_{th}^n - \frac{(np-n_{ie})}{\tau_p(n+n_{ie}) + \tau_n(p+n_{ie})} -$$

$$- (C_p p + C_n n)(np - n_{ie}^2) + \alpha_n n|v_n| + \alpha_p p|v_p| + \alpha_n' n|v_n| \,, \qquad (3.39)$$

$$\frac{dp}{dt} = e_p N_{A0} - pN_A^- \sigma_p v_{th}^p - \frac{(np-n_{ie})}{\tau_p(n+n_{ie}) + \tau_p(p+n_{ie})} -$$

$$- (C_p p + C_n n)(np - n_{ie}^2) + \alpha_p p|v_p| + \alpha_n n|v_n| \,, \qquad (3.40)$$

where e_n and e_p are the emission coefficients, σ_n and σ_p are the capture cross sections N_{D0} and N_{A0} are the unionized dopant concentrations and N_D^- and N_A^- are ionized donor and acceptor concentrations. C_n and $_pC$ are the Auger recombination coefficients, α_n *and* α_p are the band-to-band impact ionization coefficients, α_n' is the band-to-trap

Reproduced with permission of the copyright owner. Further reproduction prohibited without permission.

impact ionization coefficient, v_{th}^{n} and v_{th}^{p} are the thermal velocities and n_{ie} is the intrinsic carrier density. The first two terms of the equations (3.33) and (3.34) are the trap-to-band thermal generation and recombination, respectively, while the next two terms correspond to the Shockley-Reed-Hall [83] and Auger recombination-generation [21] processes. The second last term of eqn. (3.33) and last term of eqn. (3.34) are the band-to-band impact ionization terms for electrons and holes respectively, and the last term of 3.33 is the trap-to band impact ionization term for electrons. The lifetimes τ_n and τ_p of electrons and holes. for the SHR process depend on the doping level, and have been described by the Scharfetter relations [21] given below:

$$\tau_n = \frac{\tau_{n0}}{1+\left(\frac{N_D+N_A}{N_n^{SRH}}\right)^{\gamma_{ns}}} \tag{3.41}$$

for electrons, and for holes,

$$\tau_p = \frac{\tau_{p0}}{1+\left(\frac{N_D+N_A}{N_p^{SRH}}\right)^{\gamma_{ps}}} \tag{3.42}$$

where N_D and N_A are the donor and acceptor concentrations, and N^{SRH}, and $\gamma_{ns,ps}$ are some constant parameters. The generic parameter values for SiC used in this research are given in Table 3.1. These values have been taken from the literature and are based on curve fitting to experimental data. The rate coefficients for band to band Auger recombination in SiC are similarly tabulated. In must be emphasized that the mobility and field dependent velocity values, however, were obtained from Monte Carlo simulations carried out in this research.

The impact ionization coefficients α_n and α_p given in the rate equation, determine the strength of the impact ionization process and are in general field-dependent. An empirical

Reproduced with permission of the copyright owner. Further reproduction prohibited without permission.

relation [21] for the electron and hole impact ionization rates has been used in this research. given by :

$$\alpha_n = a_n \exp(-\frac{b_n}{|E|}) \ , \ and \ \alpha_p = a_p \exp(-\frac{b_p}{|E|}) \ . \qquad (3.43)$$

Table 3.1. List of the parameters used in the research.

parameters	for electron	for hole
$\sigma_{n,p}$ (m^{-2})	$2x10^{-19}$	$2x10^{-19}$
$\tau_{n0,p0}$ (sec)	$5x10^{-9}$	$1x10^{-9}$
$C_{n,p}$ (m^6/sec)	$2.8x10^{-31}$	$9.9x10^{-32}$
$\gamma_{ns,np}$	0.3	0.3
$N_{n,p}^{RSH}$ (m)	$3x10^{-23}$	$3x10^{-23}$
$v_{sn,sp}$ (m/sec)	$2x10^5$	$1x10^5$
$\beta_{n,p}$	0.2	0.2
$E_{d,a}$ (meV)	45	200
n_i (m^{-3})	1.6	1.6
$\rho(Kg/m^3)$	$3.166x10^3$	$3.166x10^3$
C_p'(J/mol/K)	36	36
K(W/cm/deg)	$4.9x10^2$	$4.9x10^2$

In the above, "a_n", "b_n", "a_p" and "b_p" are fitting parameters, and have been given in the Table 3.1. The ionization corresponding to the trap-to-band process is modeled here as :

$$\alpha_n' = N_{D0} a_n' \exp(-\frac{b_n'}{|E|}) \qquad (3.44)$$

The velocities $v_n(x)$ and $v_p(x)$ needed for the calculations in (3.33), are usually obtained in terms of the local electric field "E". At low values, the velocity is linearly related to the local electric field. However, at larger fields non-linear affects become dominant, and

Reproduced with permission of the copyright owner. Further reproduction prohibited without permission.

the velocity is modeled in terms of a field-dependent mobility. In this framework, the low-field drift mobility can be modeled by the Caughey-Thomas equation [21] as :

$$\mu_{n,p} = \mu_{n,p}^{min} + \frac{\mu_{n,p}^{\delta}}{1+\left(\frac{N_D+N_A}{N_{n,p}^{\mu}}\right)^{\gamma_{n,p}}}\left(\frac{T}{300K}\right) . \tag{3.45}$$

Table 3.2. Fitting parameter for the Caughey-Thomas equation.

Material	$\mu_{n,p}^{\delta}$ (cm^2/Vs)	$\mu_{n,p}^{min}$ (cm^2/Vs)	N_{ref} (cm^{-3})	γ
N:4H SiC	947	0	1.94×10^{17}	0.61
N:6H SiC	415	0	1.11×10^{18}	0.59
Al:4H SiC	108.1	15.9	1.76×10^{19}	0.34
Al:6H SiC	92.2	6.8	2.10×10^{19}	0.31

Based on experimental Hall mobility data obtained from SiC samples at 300 K, the parameters given in Table 3.2 were obtained as the best fits to the Caughey-Thomas equation. These values matched the results of the bulk Monte Carlo rather well, and so were largely unmodified.

At high electric fields, the drift velocity v_n and v_p of the carrier begins to saturate. This can be described by the following field dependent mobility model:

$$\mu_n^E = \mu_n\left[\frac{1}{1+\left(\frac{E\mu_n}{v_{sn}}\right)^{\beta_n}}\right]^{1/\beta_n} \quad and \quad \mu_p^E = \mu_p\left[\frac{1}{1+\left(\frac{E\mu_p}{v_{sp}}\right)^{\beta_p}}\right]^{1/\beta_p} \tag{3.46}$$

and,

$$\overline{v_n} = \mu_n^E \overline{E} \quad and \quad \overline{v_p} = \mu_n^E \overline{E} \tag{3.47}$$

Reproduced with permission of the copyright owner. Further reproduction prohibited without permission.

for electrons and holes, respectively. Where $v_{sn,sp}$ is the drift saturation velocity of carriers β is a constant parameter and μ_n^E *and* μ_p^E are the high field electron and hole mobilities respectively. The fitting parameters used for 6H-SiC based on a curve fitting procedure to the Monte Carlo results are again given in Table 3.1.

Since 6H-SiC exhibits a substantial anisotropy, directionally dependent effective masses need to be used. Cyclotron resonance measurement on 6H-SiC has yielded a high effective mass m_l^* along the c-axis of $2m_0$, and a transverse effective mass m_t^* equal to $0.42m_0$ [84]. The effective mass tensor and conductivity masses for SiC can be obtained based on the above values, and are used in this research. The energy gap E_g of 6H-SiC, as with other semiconducting material, is a function of temperature. The following relation is used here based on absorption measurement data obtained for SiC at temperature T [83] :

$$E_g(T)=3-3.3*10^{-4}(T-300)\ \ eV. \tag{3.48}$$

In order to compute the occupancy and ionized density of the donors and acceptors as given in (3.32), their energy levels need to be specified. For SiC these were chosen to be located at 45 meV and 200 meV from the conduction and valance bands. This corresponds to experimentally measured values for the nitrogen and aluminum dopant impurities in 6H-SiC.

Finally, in order to describe the internal device temperature T(x,t) of the simulated SiC devices, a one-dimensional diffusive heat flow equation has been used. The density ρ, thermal conductivity k, and specific heat capacity C_p' were all assumed to be fixed constants, independent of the temperature. The heat flow equation then reduces to :

$$k\,\frac{\partial^2 T(x,t)}{\partial x^2} + g(x,t) = \rho\, C_p'\,\frac{\partial T(x,t)}{\partial t}\ . \tag{3.49}$$

Here g(x,t) is the power generation rate per unit volume. The constant values for the above equation are given in Table 3.1. For numerical implementation, the above equation was

Reproduced with permission of the copyright owner. Further reproduction prohibited without permission.

discretized and solved using the implicit Crank-Nicholson technique. The heat generation term was set equal to the internal Joule heating and was computed as a function of spatial position and time.

The effect of changing temperature appears in the following parameters, saturation velocity, mobility, life time and emission coefficients of carriers [83], given as:

$$\mu_{n,p} = \mu_{n,p\,RT}\left(\frac{T}{T_{RT}}\right) \quad , \tag{3.50}$$

$$v_{s_{n,p}} = \frac{v_{s_{n,p}\,RT}}{1+0.8\exp\left(\frac{T}{T_{RT}}\right)} \quad , \tag{3.51}$$

$$e_{n,p} = e_{n,p\,RT}\left(\frac{T}{T_{RT}}\right)^2 \exp\left[\frac{-E_{D,A}}{kT}\left(1-\frac{T}{T_{RT}}\right)\right] \quad , \tag{3.52}$$

$$\tau_{n,p} = \tau_{n,p\,RT}\left(\frac{T}{T_{RT}}\right) \quad , \tag{3.53}$$

where T is the operating temperature and T_{RT} is the room temperature equal to 300K (subscript RT in the above equations stands for values at room temperature). In the last equation, the effect of temperature on all the associated terms needs to be included.

7.3.2 TUNNELING

At the metal semiconductor boundry, a large electric field reduces potantial barrier width and electrons can tunnel through the barrier. This causes a large supply of electrons in the semiconductor from the contact. Tunneling current can be expressed as:

Reproduced with permission of the copyright owner. Further reproduction prohibited without permission.

$$J = E^2 \exp(-\frac{4\sqrt{2m^*}(q\Phi_B)^{3/2}}{3qh\bar{E}_{00}}) \quad (3.54)$$

7.3.3 TWO DIAMENSION EXTENSION OF THE EQUATIONS

All the governing equations with some modification in equations 3.36 can be used in the simulation of a 2D structure. Following are the modifications:

$$J=nqv_{xn}+nqv_{yn}+pqv_{xp}+pqv_{yp}-qD_n(\frac{dn}{dx})-qD_n(\frac{dn}{dy})+qD_p(\frac{dp}{dx})+qD_p(\frac{dp}{dy}) \quad (3.55)$$

3.7.4 SiC MODEL IMPLEMENTATION AND SIMULATION SCHEME

For numerical implementation of the device model, the device was spatially divided into N boxes each with a spatial extent of 20 nm as shown in Fig. 3.1. The density of free carriers, ionized/unionized donors and acceptors, the average internal electric field, and device temperature were all represented by discrete values at the center of each box. Thus the above parameters were assumed to be fixed within each box, but to vary from box to simulation box.

The temporal scale was also discretized into time intervals of magnitude Δt. This time step Δt was chosen to satisfy the requirement of being greater than both the relaxation time and the internal collision times. In order to obtain numerical stability of the space-time discretization, the well known "Courant-Fredericks-Lewy" inequality condition was used to put a constraint on the upper limit on the value of the time step 'Δt'. The limit for the maximum value of 'Δt' is related to the size of the box 'Δx' as:

$$\Delta t_{max} \leq \frac{\Delta x}{2v_{max}}. \quad (3.56)$$

The SiC device structure used for the simulation was a n^--n-p^- diode with dimensions of $0.2\,\mu m$, $0.6\,\mu m$ and $2.0\,\mu m$ respectively. The chosen spatial resolution of 20 nm, yields

Reproduced with permission of the copyright owner. Further reproduction prohibited without permission.

a total of 140 discretized boxes for the device simulations. The circuit resistance, device area, and doping parameters used were as shown in Fig 3.1.

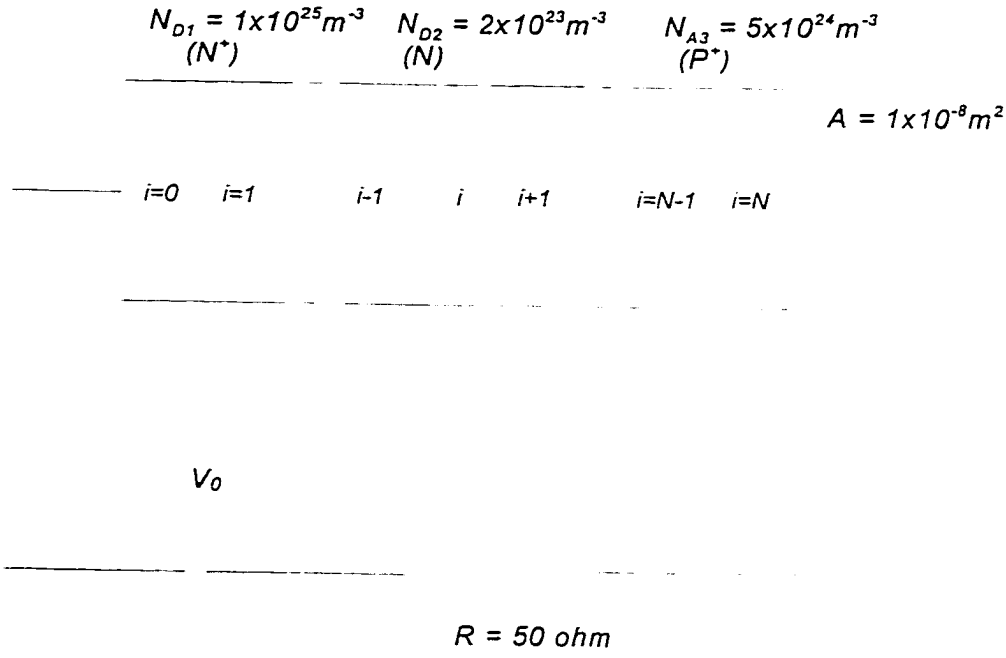

Fig. 3.1 Circuit diagram of the device used for simulation.

Reproduced with permission of the copyright owner. Further reproduction prohibited without permission.

CHAPTER 4

SIMULATION RESULTS AND DISCUSSION

4.1 INTRODUCTION

This chapter presents all of the results obtained from the numerical simulations. First, the Monte Carlo predictions of electron transport are discussed, and compared with available experimental data. These results yield accurate transport parameters that have subsequently been used for the drift-diffusion analysis. This process of using some of the Monte Carlo results as input to the drift-diffusion simulator yields improved accuracy. Also the lack of experimental data on the transport parameters makes it necessary to generate the required parameters for SiC through an accurate, microscopic scheme such as the Monte Carlo.

Following a discussion of the Monte Carlo results, predictions of the transient electrical behavior of simple SiC diode structures based on the drift-diffusion scheme are presented. These results reveal some useful trends, and confirm the potential for an instability in SiC containing deep levels or defects. Finally, the two-dimensional, time-dependent simulations are presented, and the role of contact injection on the device stability discussed.

4.2 MONTE CARLO RESULTS FOR TRANSPORT IN SiC MATERIAL

Results of the temperature and field dependent electron transport parameters based on the Monte Carlo simulations are first discussed. A simple curve fitting procedure was then used to obtain analytical expressions for the drift-diffusion analysis.

4.2.1 TEMPERATURE AND FIELD DEPENDENT 4H-SiC PARAMETERS

Of the various polytypes, 4H-SiC is predicted to have the highest mobility associated with the smallest effective electronic masses. Cyclotron resonance measurements on 4H material, have yielded a low anisotropy, with a lower longitudinal mass m^*_L of 0.29 m_o and $m^*_T = 0.42\ m_o$. Although, the 4H material promises to be important technologically, there has

Reproduced with permission of the copyright owner. Further reproduction prohibited without permission.

not been much theoretical work to analyze its electrical transport properties. Here, Monte Carlo simulations have been performed to compute the electron mobilities, drift velocities and diffusion coefficients for 4H-SiC for the first time. The calculations explicitly include the crystal anisotropy, and results were obtained for electric field orientations both parallel and transverse to the c-axis of the hexagonal structures. The electron transport parameters were calculated for a range of operating temperatures and electric fields. Suitable comparisons with existing experimental data highlight the accuracy of the simulation results presented here.

The present simulations of electronic transport were based on the Monte Carlo approach described in Chapter 3. Very briefly, a single equivalent isotropic valley model was used with a nonparabolicity factor of 0.323 eV^{-1}. The transverse and longitudinal effective electronic masses $m_{T,L}$ were taken to be 0.42 and 0.29 for 4H-SiC respectively, in keeping with the cyclotron resonance data. Acoustic deformation potential scattering, polar-optical phonon interactions, ionized impurity processes, and impact ionization were considered for electronic scattering. In addition, two different equivalent-intervalley phonon processes representing a first-order and a zero-order interaction [85] were also included. The coupling constants for the intervalley phonons and the acoustic deformation potential were the same as used previously for 3C material [85], which had been determined by fitting the static velocity-field characteristics to measured data. The Brooks-Herring formula was used for ionized impurity scattering. Impact ionization was neglected here since the fields taken here were not very large. Most of the other SiC parameters were chosen from available data [86].

Monte Carlo simulations were performed with 10,000 particles. The results for the electron mobility as a function of temperature in 4H-SiC are shown in Fig. 4.1. A partially compensated n-type material with $N_A = 10^{16}$ cm^{-3} and $N_D = 6 \times 10^{16}$ cm^{-3} was assumed for the calculations. These densities are similar to actual concentrations found in experimental samples [48]. The two curves shown represent values obtained with the electric field applied

Reproduced with permission of the copyright owner. Further reproduction prohibited without permission.

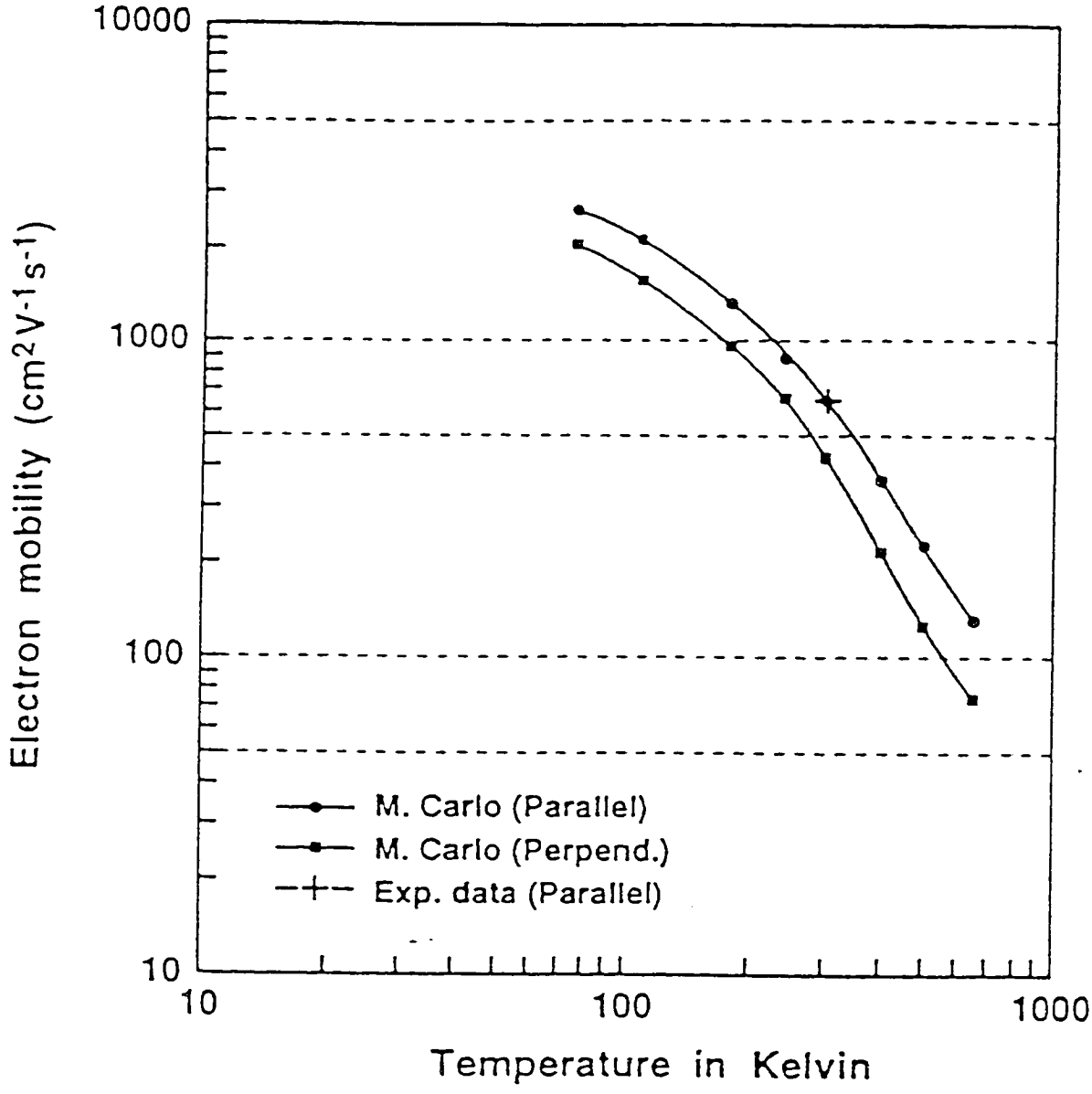

Fig. 4.1 Electron mobility in 4H-SiC as a function of temperature for electric fields parallel and perpendicular to the c-axis. Experimental data point taken from reference 48.

Reproduced with permission of the copyright owner. Further reproduction prohibited without permission.

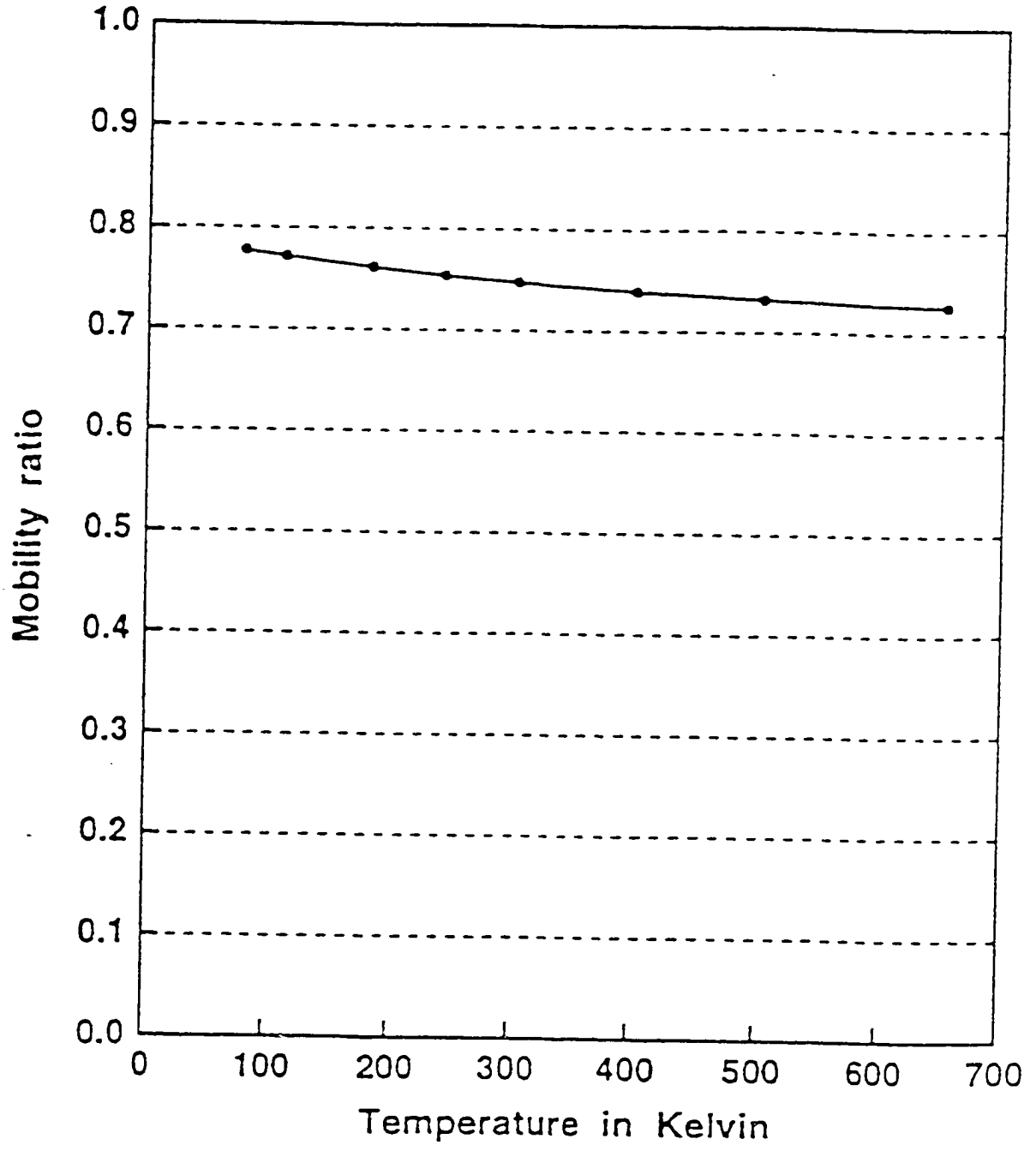

Fig. 4.2 Temperature dependence of the mobility anisotropy in 4H-SiC. The mobility ratio was obtained from the corresponding values shown in Fig. 4.1.

Reproduced with permission of the copyright owner. Further reproduction prohibited without permission.

parallel and perpendicular to the c-axis. A value of the measured mobility at 300 Kelvin [48] is also shown on the figure for comparison. The mobilities are seen to be higher for the parallel orientation, in keeping with previously reported experimental data. The calculated values also agree very well with a recent measurement [48]. The corresponding temperature dependence of the mobility ratio "R" between the two field orientations is shown in Fig. 4.2. The plot reveals the role of energy dependent momentum relaxation and ionized impurity scattering as discussed below.

Theoretically, under the relaxation time approximation, the mobility ratio "R" presented in Fig. 4.2 is given as: $R = \mu_T/\mu_L = [S_L m_L/(S_T m_T)]$ where $S_{L,T}$ are the effective momentum relaxation rates for the parallel and transverse field orientations. If polar optical phonon scattering were to be dominant, S(E) would increase monotonically with energy, and exhibit a slight discontinuity at the phonon emission threshold energy. Consequently, S_L would be greater than S_T, since the ensemble average energy of the electrons would be higher for fields oriented parallel to the c-axis. For such a case then, the mobility ratio "R" can be expected to exceed the ratio of the effective masses, which is 0.6904 for 4H-SiC. This is borne out in Fig. 4.2. The temperature dependence seen in the figure results from changes in the momentum relaxation rates due to a broadening of the electronic distribution. Basically, with increasing temperature, S_T increases more rapidly as compared to S_T since a larger fraction of the electrons begin to acquire energies above the phonon emission threshold. The ratio S_L/S_T therefore, decreases, and so does "R" in Fig. 4.2. The results presented here are thus indicative of the dominance of phonon scattering over the ionized impurity interactions. If ionized impurity scattering were to have been dominant on the other hand, an opposite effect would have been observed. In such a case, S(E) would decrease with energy, at least at small energies, and the phonon emission related threshold effect would be greatly reduced. Consequently, with increasing temperature the ratio S_L/S_T would *increase*, as S_T would decrease more rapidly in comparison to S_L. Such an increasing trend is not seen

Reproduced with permission of the copyright owner. Further reproduction prohibited without permission.

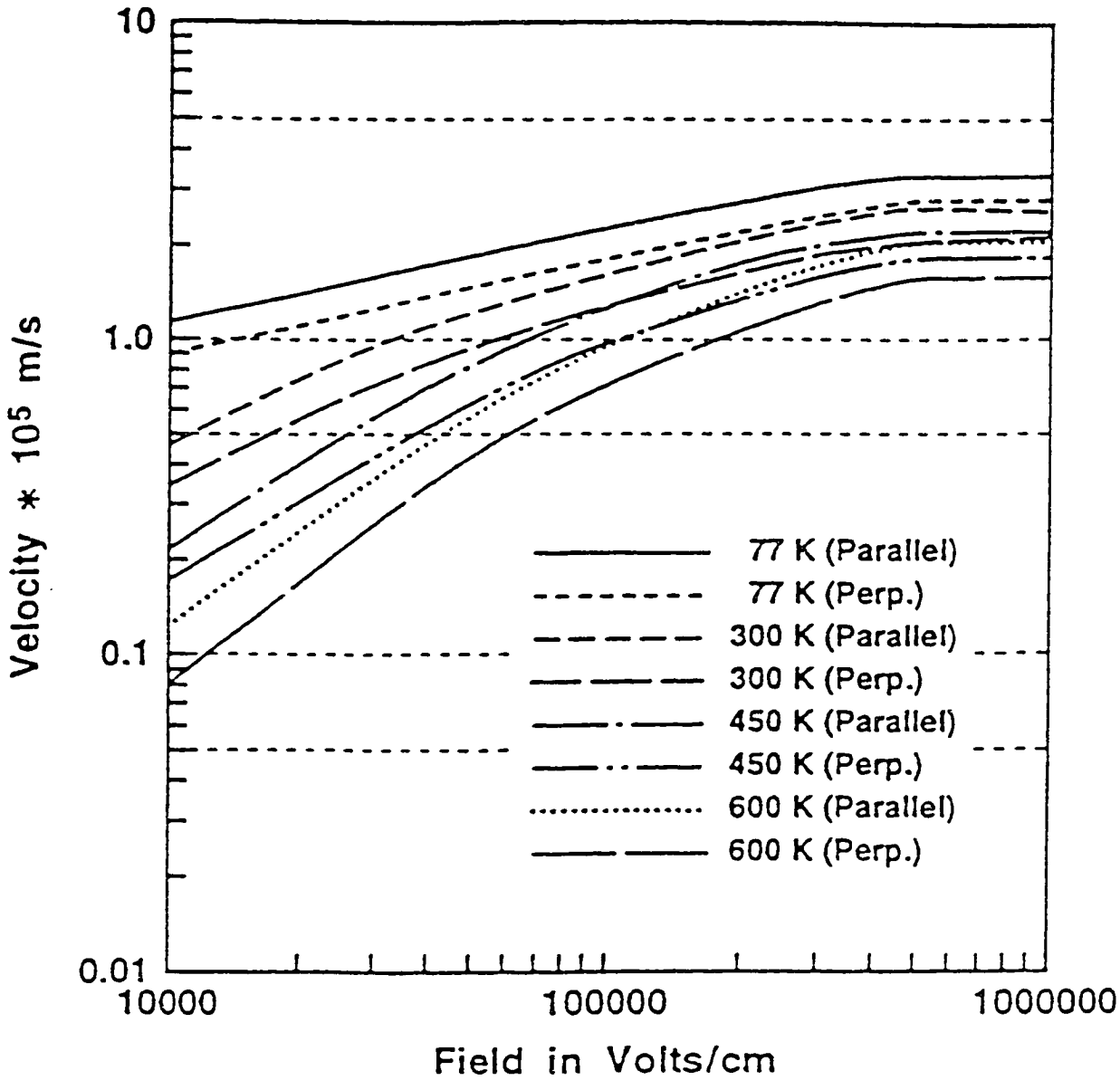

Fig. 4.3 Electronic drift velocity for 4H-SiC as a function of the electric field for orientations parallel and perpendicular to the c-axis.

Reproduced with permission of the copyright owner. Further reproduction prohibited without permission.

here in the simulations, since a relatively low impurity density of 7×10^{16} cm^{-3} was chosen for our SiC simulations. However, for much higher density values, a monotonic increase of the anisotropy ratio with temperature is predicted. Such an increase as anticipated here has actually been observed in recent experiments at impurity concentrations of 1.2×10^{17} cm^{-3} [48].

Results for the electron drift velocity for 4H-SiC as a function of the applied electric field are presented in Fig. 4.3 for the same two orientations of the electric field with $N_A = 10^{16}$ cm^{-3} and $N_D = 6 \times 10^{16}$ cm^{-3}. The lattice temperature was the variable parameter. The room temperature drift velocity is seen to have a value of 2.7×10^5 cm s^{-1}. This is higher than the previously reported value for 3C-SiC [85]. The anisotropy is also evident in the curves. Also, for a given electric field, there is a spread in velocity with temperature due to the temperature dependence of phonon scattering. As may be expected, the spread decreases at higher fields. This is because changes in the lattice temperature no longer have as significant an impact at the higher fields since the electrons are already quite "hot."

Finally, field dependent values of the diffusion coefficients D(E) for the 4H polytype were obtained from Monte Carlo simulations. Due to crystal anisotropy, the diffusion coefficient $D_{ij}(E)$ is, in general, a field dependent tensor. Based on the effective masses, values of the diffusion coefficients for 4H-SiC can be expected to be larger along the c-axis than those along the transverse directions. As is well known [87,88], numerical values for the diffusion coefficients under non-equilibrium conditions can be obtained from the second central moment of the carrier distribution as :

$$D_{ij}(E,t) = \frac{1}{2}\frac{d}{dt}\langle (x_i(t) - \langle x_i(t)\rangle)(x_j(t) - \langle x_j(t)\rangle)\rangle \quad . \qquad (4.1)$$

The above expression is a function of time "t," with $x_i(t)$ being the time-dependent electronic position coordinate along the i^{th} direction.The steady state value for $D_{ij}(E)$ results by carrying

Reproduced with permission of the copyright owner. Further reproduction prohibited without permission.

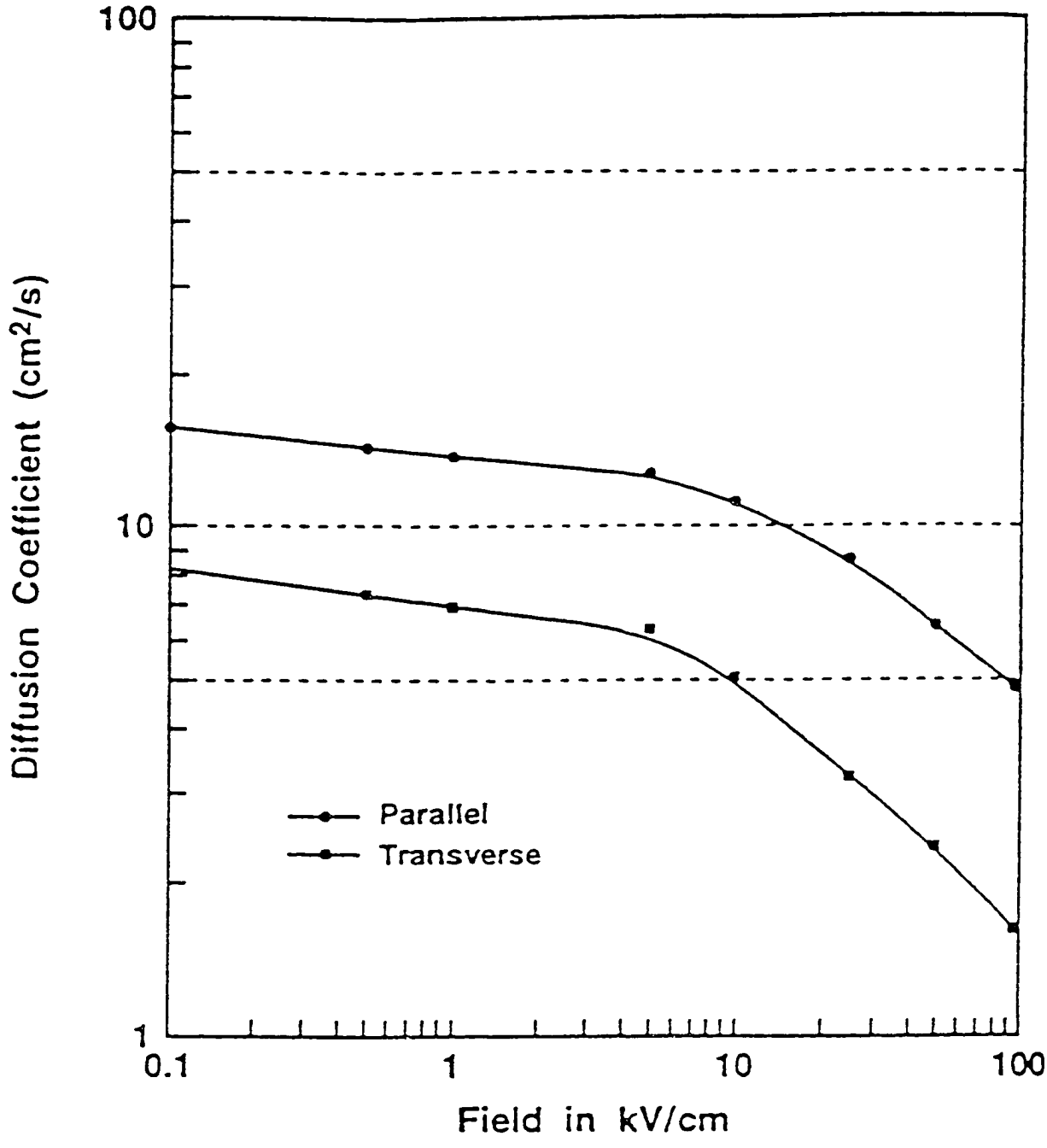

Fig. 4.4 Field dependence of the parallel and transverse diffusion coefficients in 4H- SiC at 300 K. The field was taken to be parallel to the c-axis.

Reproduced with permission of the copyright owner. Further reproduction prohibited without permission.

the simulations long enough until steady state. Results obtained from our Monte Carlo simulations at 300 K for the longitudinal and transverse diffusion coefficients $D_{11}(E)$ and $D_{22}(E)$ respectively, are shown in Fig. 4.4. The electric field was taken to be along the principal c-axis. The values obtained here should serve as important input parameters for the drift-diffusion simulation schemes commonly used in device modeling. The results show that the diffusion coefficients have highest values at the lowest fields. Furthermore, Einstein's relation is roughly seen to hold at the lowest fields. With the increasing field, the Einstein relation fails, and both $D_{11}(E)$ and $D_{22}(E)$ decrease monotonically. This behavior is expected, since internal scattering increases with the applied field and leads to higher fluctuations in the carrier velocity. Enhanced fluctuations decrease the velocity auto-correlation, and hence the diffusion coefficients, in accordance with the fluctuation-dissipation theorem [88].

Finally, the diffusion coefficients of Fig. 4.4 are seen to exhibit a relatively sharper decrease for fields beyond 8 kV/cm. This soft threshold effect is associated with the LO phonon emission, and arises for the following reason. For 4H-SiC, the LO phonons involved in polar-optical scattering have a relatively large energy quanta of about 120 meV. Consequently for 300 K operation, the polar-optical emission process remains negligible at low fields, since the average electron energies are below the emission threshold. With the increasing field, however, the electrons begin to acquire energies above the 120 meV LO phonon emission threshold. The onset of this process thus increases the overall scattering, and leads to a sharper reduction in the diffusion coefficients. In our simulations of Fig. 4.4, such a field dependent threshold effect on the diffusion coefficients is seen to occur at about 8 kV/cm. It may be noted that such an effect is not discernable in either Si or GaAs because of the relatively small phonon energies for these materials.

4.2.2 MONTE CARLO SIMULATIONS FOR BULK 6H-SiC

The Monte Carlo simulations were used to obtain both the transient and steady-state

Reproduced with permission of the copyright owner. Further reproduction prohibited without permission.

electronic velocities at various temperatures and dc electric fields. Calculations of the small signal ac mobility which is of great interest to microwave devices and high frequency power amplifiers, were also computed. The Monte Carlo simulations were performed with 10,000 particles for a 1.0 μm bulk SiC semiconductor. The applied electric field was taken to be the variable parameter. Results of the transient electronic velocity thus obtained at 300 K and 900 K are shown in Figs. 4.5a and 4.5b, for three different values of the electric fields. As expected, the electronic velocities are lower at 900 K due to the higher internal phonon scattering. At the highest field of 5×10^5 V/cm, a velocity overshoot is predicted to occur at both the temperatures. This occurrence is similar to the well known phenomena in silicon, and is associated with differences between the energy dependent momentum and energy relaxation rates. With increasing temperature however, the overshoot effect diminishes for two reasons. First, the disparity between the energy and momentum relaxation times begins to reduce. This occurs because optical phonon interactions begin to dominate, and swamp out the elastic scattering contributions of the acoustic phonons. In addition, the effectiveness of elastic ionized impurity scattering also diminishes with temperature. Second, at the higher temperature of 900 K, the energy of carriers re-injected from the contacts are much higher, and can easily exceed the typical LO phonon quanta. This effectively reduces the "dead-zone" for energy relaxation near the injecting cathode, and contributes to increasing average energy relaxation within the device.

Based on the transient simulations at different temperatures, the steady state velocity-field curves at 300 K, 600 K and 900 K were obtained. The results are shown in Fig. 4.6. The velocity at 900 K does not show saturation, and has a value slightly in excess of 10^7 cm/s at a field of 5×10^5 V/cm. An upper bound of 5×10^5 V/cm was used for the electric field, to avoid complications from impact ionization which has been shown to occur beyond this limit [20]. Since otherwise, by exceeding the 5×10^5 V/cm threshold, the Monte Carlo simulation procedure would have had to account for the production and subsequent dynamics of all

Reproduced with permission of the copyright owner. Further reproduction prohibited without permission.

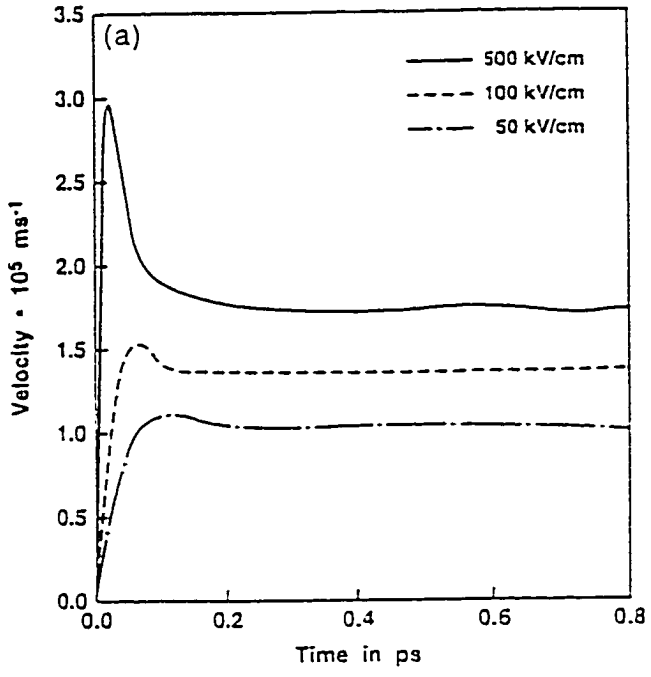

Fig. 4.5a Transient electron velocity at 300 K for three different electric fields.

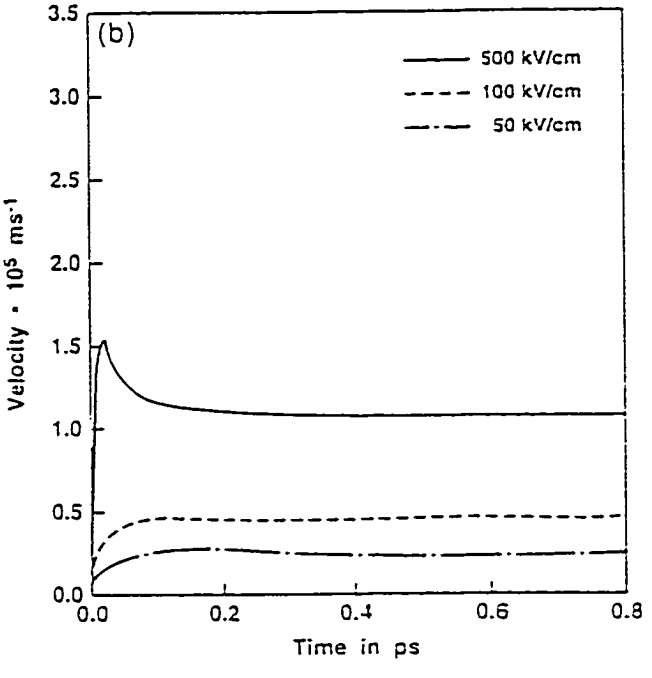

Fig. 4.5b Transient electron velocity at 900 K for three different electric fields.

Reproduced with permission of the copyright owner. Further reproduction prohibited without permission.

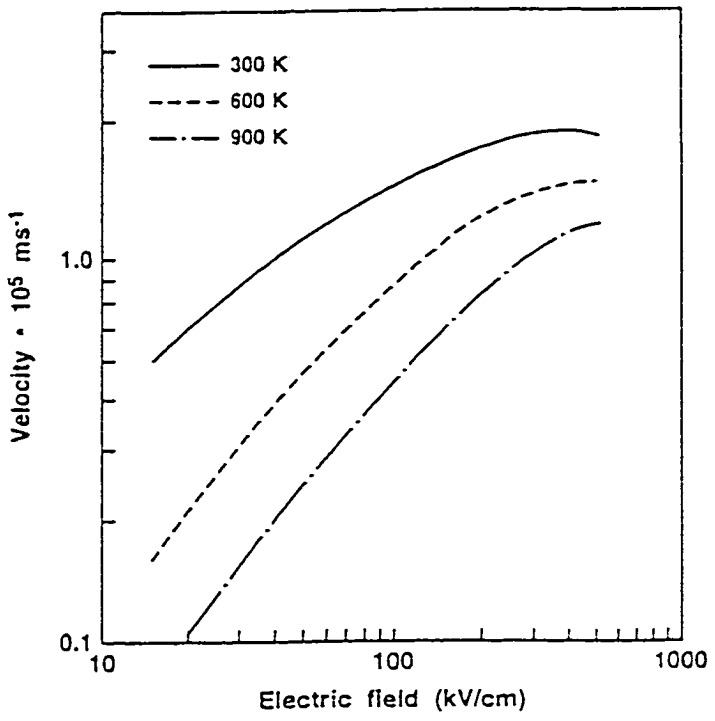

Fig. 4.6 Steady state electron drift velocity curves at 300 K, 600 K and 900 K.

secondary electrons. At 300 K, the drift velocity displays a gentle peak with a value of about 1.9×10^7 cm/s, and is close to the experimentally obtained value in 6H-SiC [48].

Finally, the effect of contact injection and its role in affecting the transient velocity through changes in the carrier distribution functions was examined. Smaller devices at low temperatures are expected to be most strongly influenced in this regard, due to the injection of cold electrons at the cathode which would increase the average drift times. Results comparing the low-frequency electronic ac mobilities of β-SiC for five different traversal lengths are shown in Fig. 4.7. The lengths were varied from 0.1 μm to 1.0 μm, with the simulations being performed at 300 K and 900 K. The low frequency ac mobility values were obtained as: $\mu_{ac}(F_o) \approx [v_o(F_o)/F_o]$. An overall reduction of about 50 per cent is seen at both temperatures, but the effects are most significant below 0.3 microns. This also implies that the steady state velocities are greatly reduced as the dimensions get smaller. This detrimental effect occurs because electrons in a smaller device cannot gain as much energy for a given

Reproduced with permission of the copyright owner. Further reproduction prohibited without permission.

electric field. It may also be mentioned that though velocity transients have not been shown here, the overshoot effect was seen to be much stronger at 0.1 μm because of a lower steady state velocity. The results indicate that reducing the device dimensions beyond a certain point to decrease the transit times at a given field could be counter-productive. The gain-bandwidth product of the device could fall if the transport was dominated by effects of contact injection. Possible alternatives for overcoming this drawback, might include schemes for high energy electronic injection across heterojunctions or devising structures that provide built-in fields through doping variations.

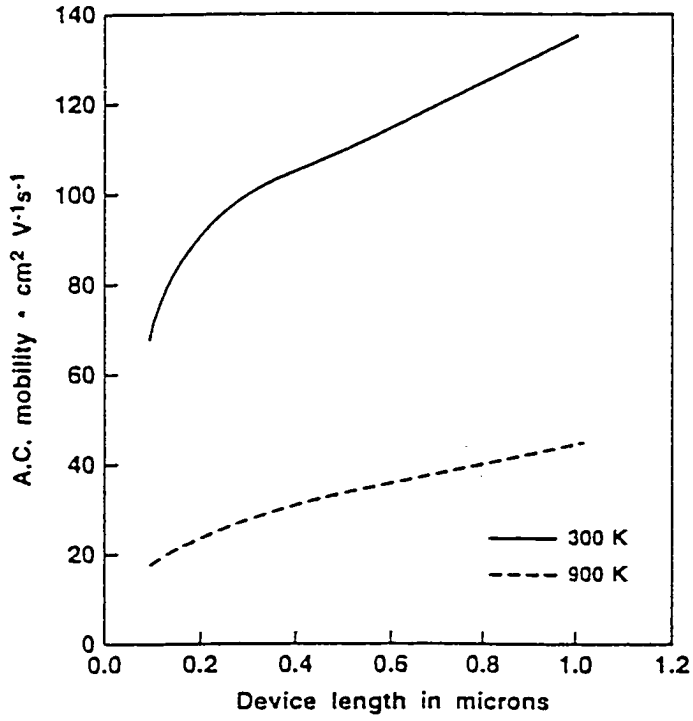

Fig. 4.7 Results, at two different temperatures, comparing the electronic ac mobilities for different device lengths. The lengths were varied between 0.1 μm and 1.0 μm.

Reproduced with permission of the copyright owner. Further reproduction prohibited without permission.

4.2.3 INVERSION ELECTRON MOBILITIES IN 6H-SiC MOSFETS

The ability to grow thermal oxides on SiC appears to extend its utility to the realm of metal oxide semiconductor (MOS) devices and integrated circuits [49]. However, it is important to note that despite rapid advances in material fabrication and the growth of superior oxides with low interface defects, experimental values of the electron channel mobilities in such SiC MOS structures have been quite discouraging. For instance, data on 6H-SiC material has yielded channel mobilities as low as 40-50 cm^2/Vs, compared to about 400 cm^2/Vs in bulk samples. It is conceivable that the low mobilities result from excessive oxide and interface charge, and could eventually be reduced significantly through improved processing. On the other hand, the low mobility may be a direct consequence of other inherent electron transport processes within the SiC inversion layer.

Here, we have performed Monte Carlo simulations for electronic transport in the inversion layer of a 6H SiC MOS structure in an attempt to address and resolve the above question. The 6H-polytype is used here instead of 3C- or 4H-SiC. Also, the effect of electron quantization as discussed in chapter 3 has explicitly been taken into account. Except for one recent report [89], no other simulation studies have, to the best of our knowledge, included electron quantization aspects in SiC. However, the work of reference [89] was on 3C-SiC, and did not include any experimental comparisons. Furthermore, though interface roughness scattering had been considered based on a Gaussian model, the roughness parameters were not specified. In the absence of quantitative values, the mobility predictions are difficult to duplicate, nor can meaningful comparisons be made with actual data. The salient features of this SiC study include: (i) Simulations for 6H-SiC as it is technologically more important than the cubic polytype. (ii) Direct comparisons with actual experimental data available at 300 K for 6H SiC MOS structures. (iii) An evaluation of interface roughness scattering, and its role on limiting electron channel mobility. (iv) Predictions of the mobility limits in the absence of interface ion scattering, at a few different temperatures of interest.

As is well known [90], inversion layer confinement at the SiC-oxide interface has the

Reproduced with permission of the copyright owner. Further reproduction prohibited without permission.

following consequences: (i) Electron quantization with subband formation leading to a two-dimensional flow. (ii) Changes in the transverse wavefunctions that slightly lower the electron-phonon scattering rates, but increase the number of inter- and intra-subband processes. (iii) A relative decrease in the influence of remote ion, oxide charge and depletion dopant ion scattering due to the increased physical separation. (iv) The inclusion of an additional interface roughness scattering which imparts a strong transverse electric field dependence to the channel mobility, as first shown by Sabnis and Clemens [91] for Si. Such a field dependence has also been observed in recent tests on 6H SiC MOS devices [49] and must be accounted for very carefully in any numerical modeling. Physically, higher transverse fields enhance the electronic confinement, drawing them closer to the interface which leads to greater interface roughness scattering and lower mobility. The details, however, are complicated since the relative subband occupancy and spatial electron distribution within each subband shifts with transverse field by different amounts. Furthermore, as channel densities are enhanced with the transverse field, free carrier screening increases and should work to lower the effects of polar and Coulombic interactions, thereby moderating the mobility reductions. The interface roughness scattering has been treated in Si material based on Gaussian [90] and exponential [92] models. The best-fit values of the correlation length "L" and root-mean-square (rms) roughness fluctuation height Δ have been found to be roughly around 22 Å and 2.0 Å [93,94]. The corresponding parameters for SiC are not known, but one expects "L" to be nearly unchanged from Si. However, "Δ" can be expected to be larger due to the longer c-axis lattice constant in 6H-SiC.

In keeping with experiments, the c-axis was taken to be perpendicular to the SiC-oxide interface resulting in a single transverse effective mass and one set of subbands. Fang and Howard [95] variational wavefunctions were used for computations of the scattering rates. A six valley, two-subband Monte Carlo model was used, and included electron

Reproduced with permission of the copyright owner. Further reproduction prohibited without permission.

interactions with acoustic modes via the deformation potential, polar optical phonon interactions, zero and first-order intervalley deformation potential scattering [96], interface roughness [93] and interface ion interactions [90]. Finally, both the intra- and interband transitions were accounted for in the numerical transport simulations.

As already stated, material parameters for 6H-SiC are not well known.The best fit parameters thus obtained are given in Table 4.1, and were subsequently used for the inversion layer problem. Simulations were next carried out at 300 K for various combinations of interface ion density and roughness parameter "Δ" as a function of the transverse electric field. Recent experiments [49] suggest that the interface ion density is typically in the 4 x 10^{11} - 10^{12} cm^{-2} range. However, no measurements are available on the interface roughness characteristics. In the absence of such data, the interface roughness correlation length "L" was set equal to 22 Å, a value that has been measured for Si MOS structures. Though, some corrections may be necessary after experimental data becomes available, we believe minor adjustments will not affect the mobility significantly since interface scattering rate has a weak dependence on "L". A much stronger dependence results from the parameter "Δ", which is the measure of the rms height of the interface roughness fluctuations. Here, this parameter was varied from 2 Å to 7.5 Å.

Results of the electron channel mobility at 300 K for various combinations of "Δ" and ion density values are shown in Fig. 4.8. The available experimental data [49] is also shown. Clearly, the lowest two curves for Δ = 7.5 Å and interface ion densities of 4 x 10^{11} and 10^{12} cm^{-2} track the experimental data rather well. However, values of "Δ" below 7.5 Å do not yield good agreement with experimental data, and exhibit an incorrect trend with the transverse field. Basically, for low values of "Δ", interface roughness scattering is not as dominant in comparison to the interface ion process. The latter process leads to *higher* electron mobilities with increasing transverse fields due to enhanced screening. Since such a trend is contrary to measured data, the simulations reveal the dominance of interface

Reproduced with permission of the copyright owner. Further reproduction prohibited without permission.

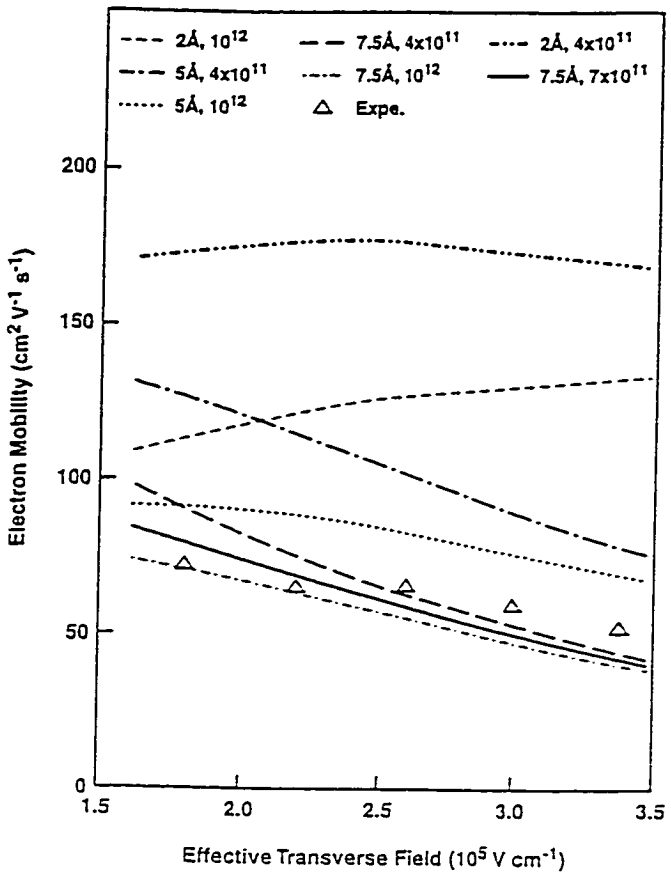

Fig. 4.8 Simulation results and experimental data for the MOSFET electron mobilities as a function of transverse electric field.

roughness scattering and the relatively large value of about 7.5 Å necessary to match the experimental mobilities. It may be noted that the deformation interaction has a weak $n_s^{-1/3}$ dependence on the electron density "n_s" arising from the wavefunction overlap factor, and this process does not significantly contribute to the transverse field dependence.

Finally, based on the above value of 7.5 Å, simulations were carried out to predict the electron channel mobility at various temperatures in the absence of interface ion scattering. This represents a theoretical mobility limit in a 6H-SiC MOS structure, if all interface states and impurity charges could be eliminated. The curves of Fig. 4.9 show a mobilities approaching 40 $cm^2 V^{-1}s^{-1}$ at 900 K and about 130 $cm^2 V^{-1}s^{-1}$ at 300 K. Values, however, are still much lower than those in bulk material. In conclusion, electron mobility in 6H-SiC MOS

Reproduced with permission of the copyright owner. Further reproduction prohibited without permission.

structures has been analyzed and important transport parameters extracted for the first time. Our data fits available experimental data very well, and underscores the dominance of interface roughness scattering in the current MOS devices. Based on a similar reasoning, one might expect rather low mobility values in 4H-SiC MOS structures as well.

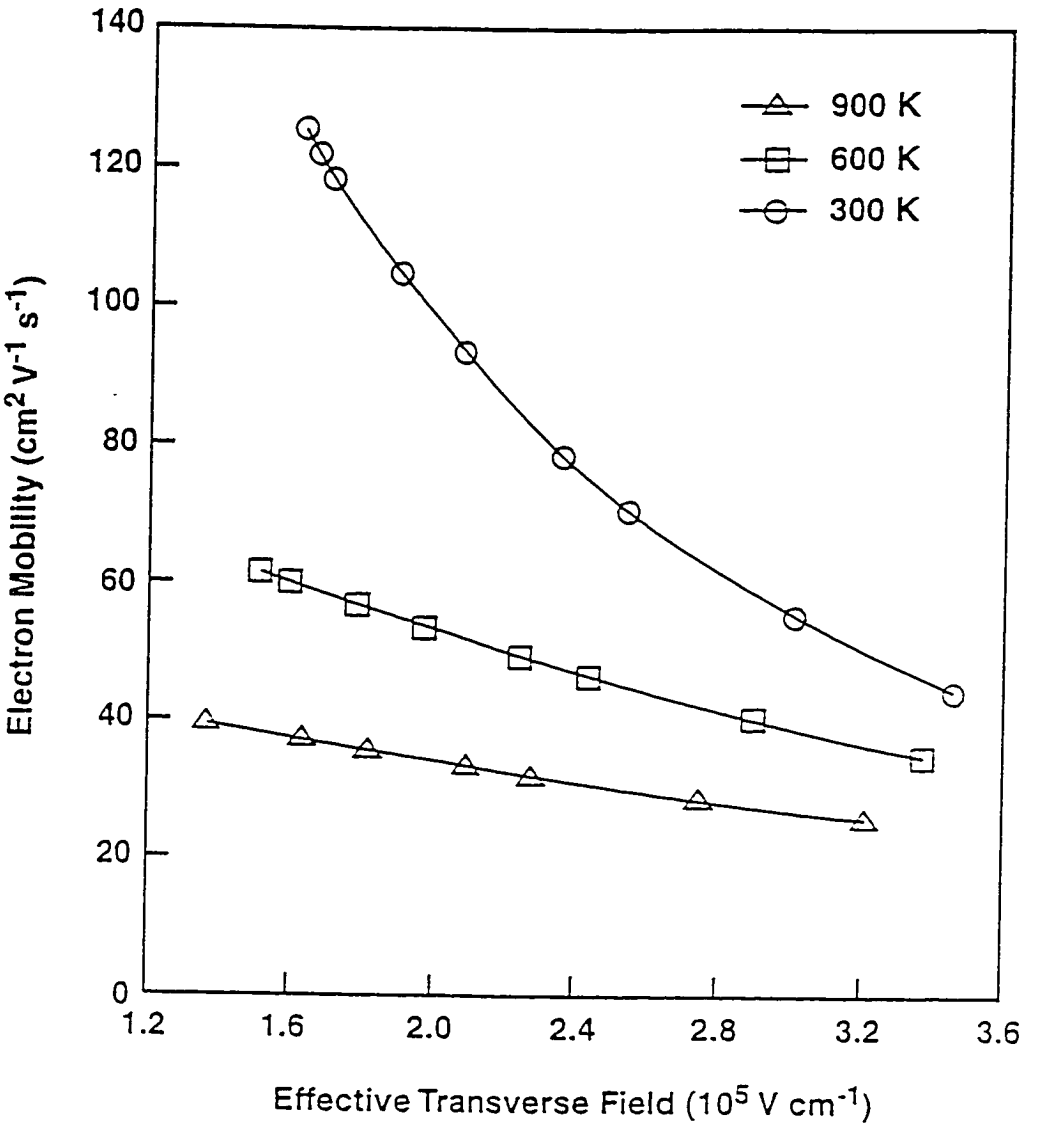

Fig. 4.9 Predicted mobility at three temperatures in absence of interface ions.

Reproduced with permission of the copyright owner. Further reproduction prohibited without permission.

Table 4.1 Parameters Used For Electron Transport In 6H-SiC

PARAMETER	VALUE
Longitudinal effective mass (m^*_L)	0.42
Transverse effective mass (m^*_T)	2.20
Density (g/cm^3)	3.166
Band nonparabolicity (eV^{-1})	0.25
Relative permittivity (High frequency)	6.62
Relative permittivity (Static)	9.66
Acoustic velocity (cm/s)	1.3×10^6
Acoustic deformation potential (eV)	17.3
Effective polar field (V/cm)	1.08×10^5
Polar optical phonon energy (meV)	119.8
Zero order intervalley coupling constant (eV/cm)	8×10^8
First order intervalley potential (eV)	5.6
Zero order intervalley phonon energy (meV)	79.7
First order intervalley phonon energy (meV)	40.0
Interface roughness correlation length (Angstroms)	22.0

4.3 DRIFT-DIFFUSION RESULTS FOR SiC DIODE

This section provides the results of all the numerical simulations performed at the elevated temperature of 673° K, along with pertinent discussions. Five different cases were simulated based on the one-dimensional, numerical drift-diffusion model for a SiC diode. The objectives in carrying out these five sets of simulations were to: (i) To obtain a physical understanding of the diode behavior under rapid voltage inputs, and to determine the effect of variations in the voltage pulse magnitude on the electrical response. Two voltage pulses having magnitudes of 30 Volts and 160 Volts were used to represent typical low and high external voltage situations. (ii) For each of the two external voltage pulses, four different sets

Reproduced with permission of the copyright owner. Further reproduction prohibited without permission.

of dopant energy levels were chosen for the diode response simulations. This was done to ascertain the role of deep levels and the possible effect of partial ionization on the overall device characteristics. Since SiC material is known to have deep levels as opposed to Si, this aspect has to be explored in the context of SiC based devices.

The simulation results obtained for each of the various parameter sets are presented and discussed next.

4.3.1 ONE-DIMENSIONAL RESULTS AND ANALYSIS: CASE I

The SiC device was taken to comprise of N^+-N-P^+ SiC material with uniform doping densities of 10^{19} cm^{-3}, 2 x 10^{17} cm^{-3}, 10^{19} cm^{-3}. These values were chosen as they correspond to the doping levels used in the actual SiC diodes at NASA Lewis [7]. The spatial extent of the N^+-region was taken to be 0.4 μm, the central N-region was 1.20 μm, and the P^+-region was 0.6 μm, roughly in keeping with the experimental conditions. The donor level was set at 50 meV while the acceptor level was taken to be at 180 meV. This is in keeping with the typical values reported for SiC material in the literature. The externally applied voltage pulse was taken to have the following shape: Zero volt initial value for the first 5 ns. followed by a rapid 0.5 ns ramp to 160 Volts, and a subsequent constant voltage magnitude at 160 Volts. A 50 Ohm series resistor was included to model effects of the external circuit. Fig. 4.10 shows the voltage transient characteristics. The device voltage is seen to have an initial nonzero value corresponding to the open-circuit built-in potential. During the first 5 ns, the applied voltage is zero, and represents a short circuit. This allows for current flow and the movement of mobile carriers (both electrons and holes) within the SiC diode. As a result, the device potential drops and tends towards a "zero steady state value" characteristic of an electrical short circuit. Just after 5 ns, a voltage ramp is rapidly applied which takes the external voltage from 0 to 160 Volts. The device voltage, in response, begins to increase and so does the circuit current as shown in Fig. 4.11. The peak device voltage of about 48 volts is predicted.

Reproduced with permission of the copyright owner. Further reproduction prohibited without permission.

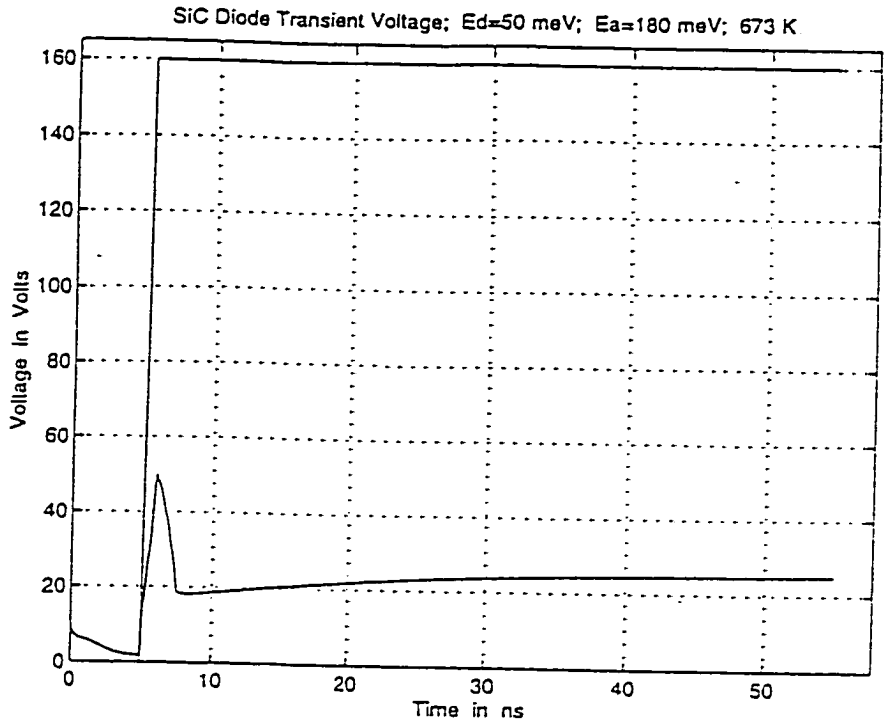

Fig. 4.10 SiC Diode Transient Voltage Response to a 160 Volt, 0.5 ns Voltage Ramp.

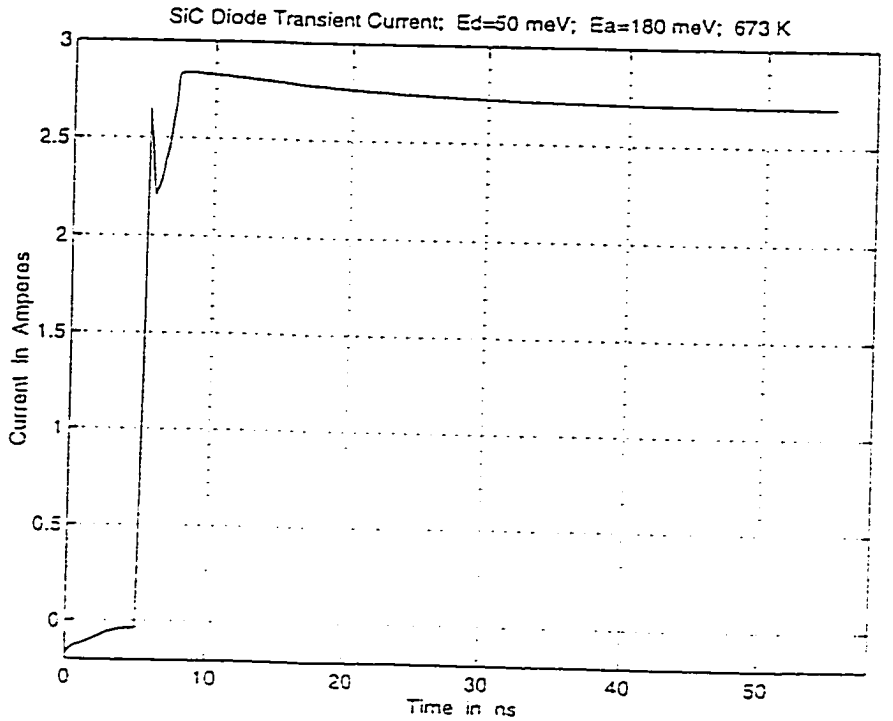

Fig. 4.11 Transient Current Response to a 160 Volt, 0.5 ns Voltage Ramp.

Reproduced with permission of the copyright owner. Further reproduction prohibited without permission.

volts is predicted. Fig. 4.10 shows a decrease in the device voltage following its initial rise, and can be understood as the collective effect of the following factors. First, the increased circuit current due to the external voltage ramp enhances the voltage drop across the 50 Ohm resistor and leads to a reduction in the device potential. From a microscopic standpoint, the drop in device voltage represents a build up of internal polarization due to the separation of mobile electrons and holes from each other and from their host impurity atoms. The end of the external voltage ramp also contributes to a negative "displacement current," and prevents any increases in the device fields and voltages. The drop across the device is seen to approach a "semi-stable" value of roughly 19 volts within about 7.5 ns. This represents a quasi-stationary state and the cessation of internal dielectric relaxation. The response behavior following these times is mainly controlled by the gradual movement of mobile charge and its slow removal from the device volume. During this stage, the device dynamics and transient voltage evolution are controlled mainly by the diffusion phenomena and the process of carrier detrapping from the deep gap states.

The details of the corresponding current transient shown in Fig. 4.11. An initial circuit current having a negative value is predicted during the first 5 ns, and represents the short circuit current driven and sustained by the diode built-in voltage. The external voltage ramp beyond 5 ns forces a steep rise in the current, much of which is a "displacement current" in response to development of internal electric fields. The slight drop in current following the initial rapid rise is associated with the "negative displacement current" upon culmination of the voltage ramp. The reduction in the device voltage between 6.0 and 7.5 ns as seen in Fig. 4.10, contributes to a current increase as is necessary to create a larger voltage drop across the resistor.

Figs. 4.12-4.15 show the internal profiles of the electric field and carrier density just prior to the onset of the voltage ramp. The electric field in Fig. 4.12 is substantial near the left boundary of the N^- region, at the N-P^- junction, and at the right boundary within the P^-

Reproduced with permission of the copyright owner. Further reproduction prohibited without permission.

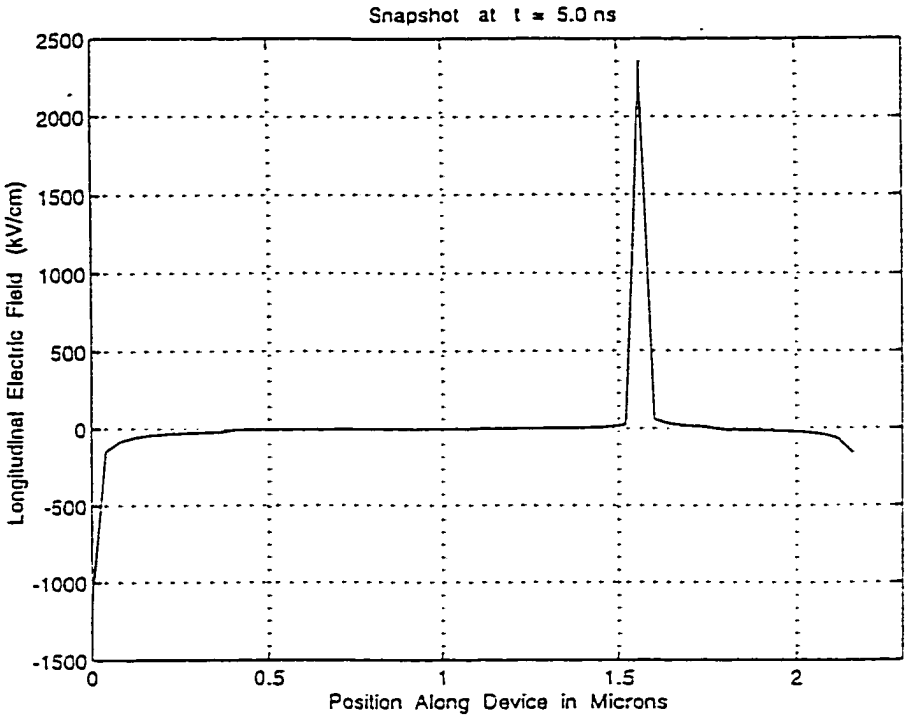

Fig. 4.12 The Internal Electric Field Profile At 5.0 ns.

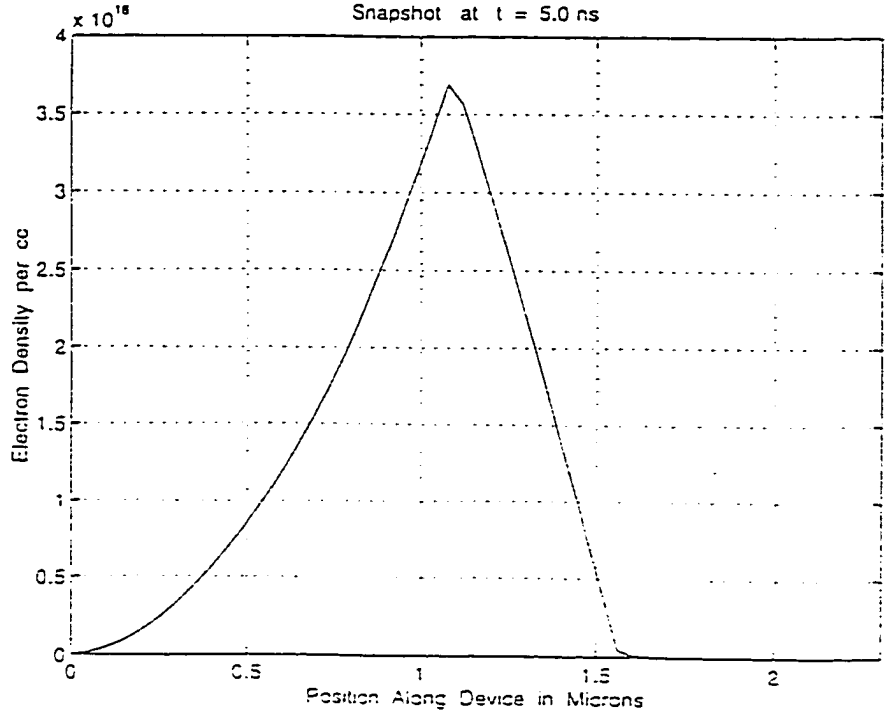

Fig. 4.13 Electron Density Distribution At 5.0 ns.

Reproduced with permission of the copyright owner. Further reproduction prohibited without permission.

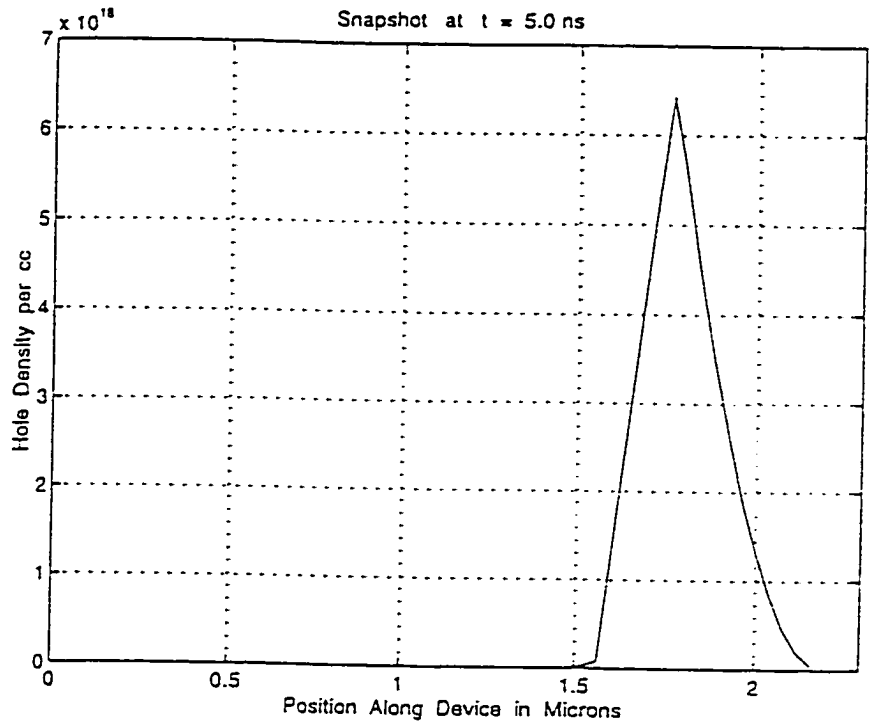

Fig. 4.14 Spatial Distribution of Hole Density At 5.0 ns.

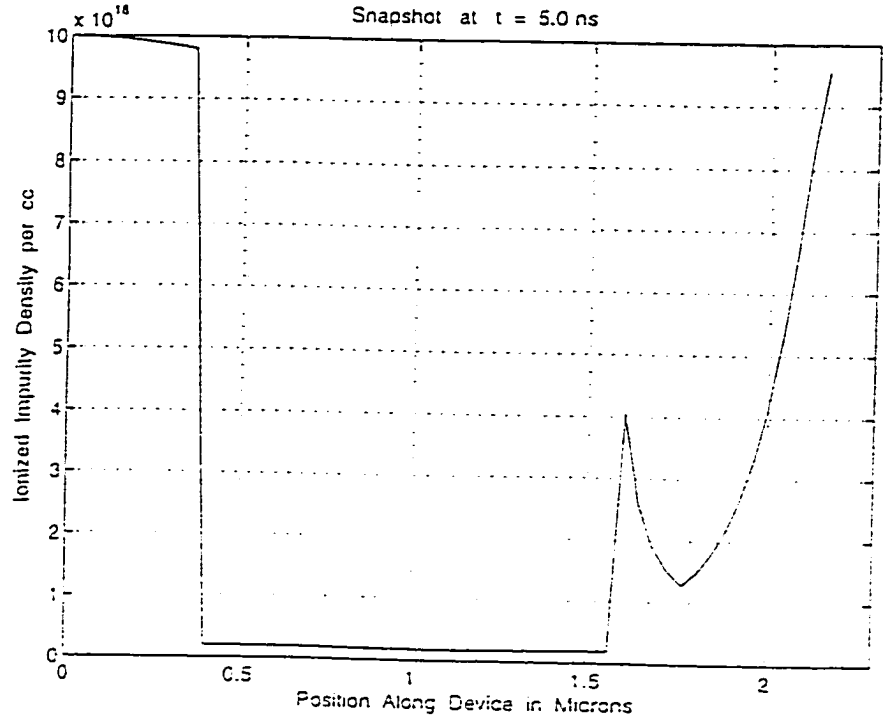

Fig. 4.15 Snapshot of the Ionized Impurity Distribution At 5.0 ns.

Reproduced with permission of the copyright owner. Further reproduction prohibited without permission.

regions. This electric field is built up due to carrier diffusion, and the necessity to maintain total current continuity. At the left boundary, mobile electrons within the N^- region diffuse away into the metal leaving behind positive immobile charge. In a similar fashion, diffusion of holes from the P^- boundary on the right also create a negative built-in electric field. At the N-P^- junction the movement is primarily that of holes, which creates a positive field having a peak value of about 2.3 MV cm^{-1}. It may be mentioned in this regard, that the electric field distribution does resemble the profile that can roughly be expected on the basis of a simple "depletion approximation." The carrier density profiles are shown in Figs. 4.13 and 4.14. The rapid diffusion of electrons from the N^-, and of holes from the P^- region is obvious. Finally, the distribution of ionized acceptor and donor states is shown in Fig. 4.15. The 50 meV ionization energy of the donors is relatively "smaller" than the 180 meV value for the acceptors. As a result, the donors are all nearly ionized, while the acceptors are ionized only at locations near the N-P^- junction and towards the extreme right boundary where the hole densities are low. This illustrates the occurrence of partial ionization, as over the central portion of the P^- region at around 1.7 μm. Complete ionization can only occur if the region gets depleted of holes leading to an increase of the local quasi-Fermi level.

Snapshots of the time evolution of the internal electric field, carrier densities and impurity occupancy are next shown at various times. Figs. 4.16-4.19 reveal the internal spatial distributions at 8.06 ns. The peak field in Fig. 4.16 is seen to have increased dramatically to a value beyond 3600 kV cm^{-1}. The spatial width is quite narrow, and most of the high field occurs over a small region at the N-P^- junction of the high field regions. In comparing Fig. 4.16 with Fig. 4.12, the quenching of the negative field at the two extreme boundaries due to the application of the external bias is obvious. The field distribution also indicates that a potential for impact ionization does exist at the N-P^+ boundary. However, the density of charge (both electron and hole) on either side of the high field region is too insignificant to lead to strong carrier growth and amplification. The electron density profile

Reproduced with permission of the copyright owner. Further reproduction prohibited without permission.

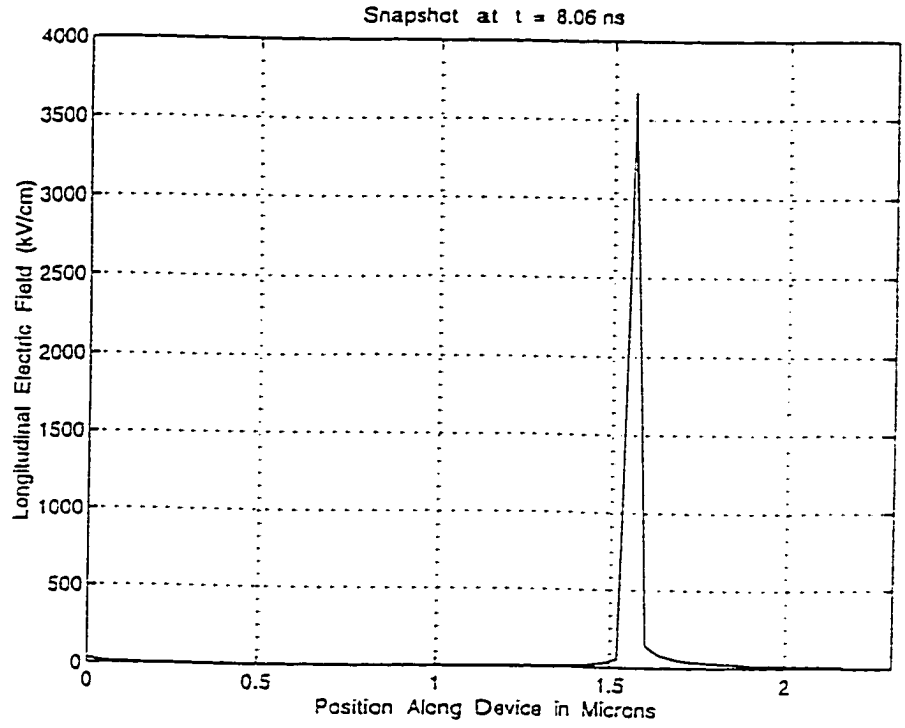

Fig. 4.16 Electric Field Distribution At 8.06 ns.

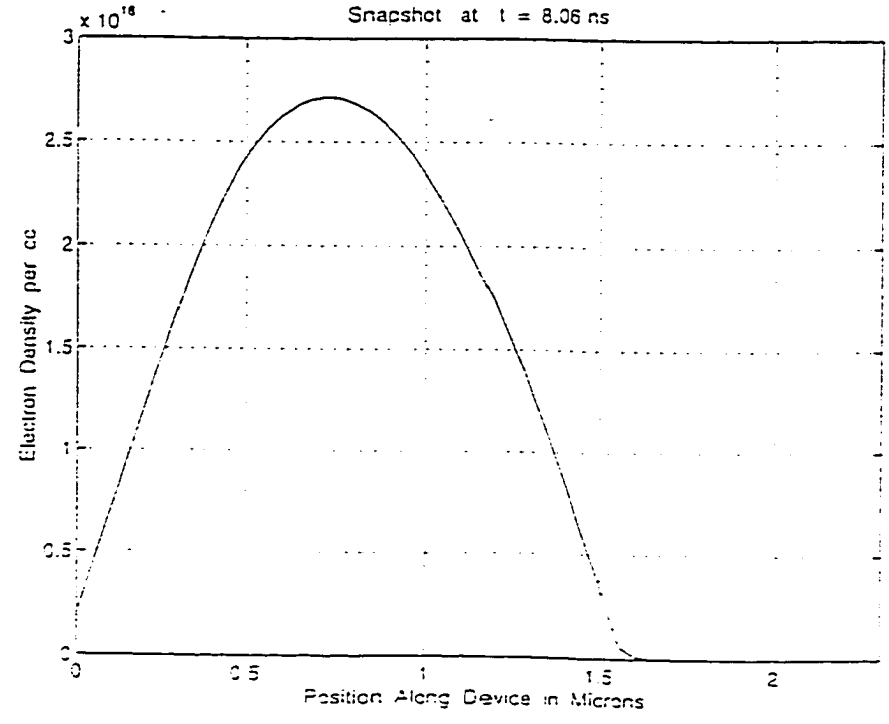

Fig. 4.17 Profile of the Electron Density Distribution At 8.06 ns.

Reproduced with permission of the copyright owner. Further reproduction prohibited without permission.

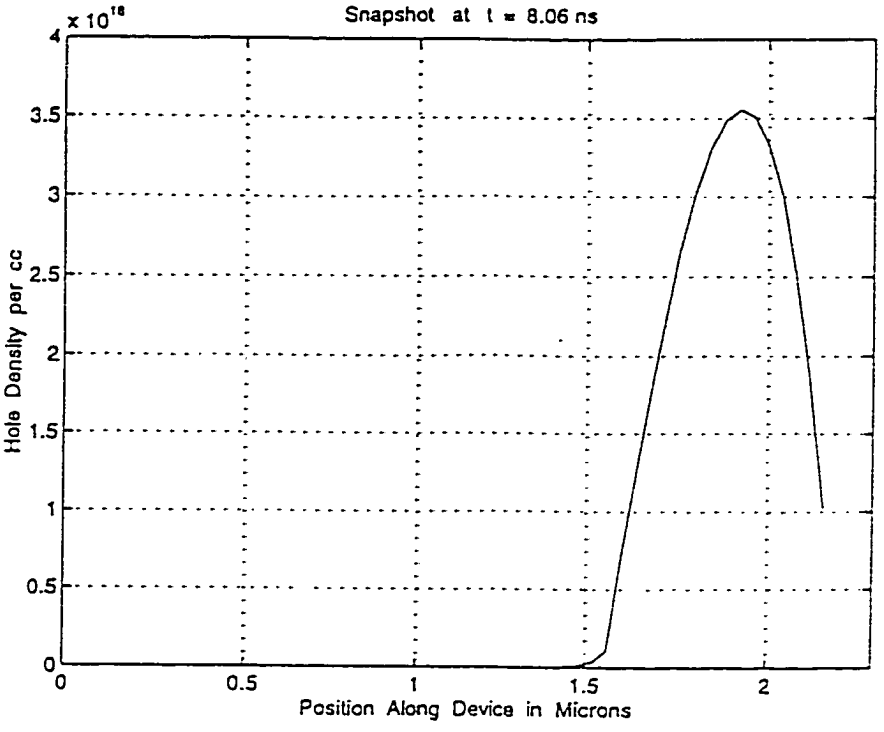

Fig. 4.18 Hole Distribution Within the Diode At 8.06 ns.

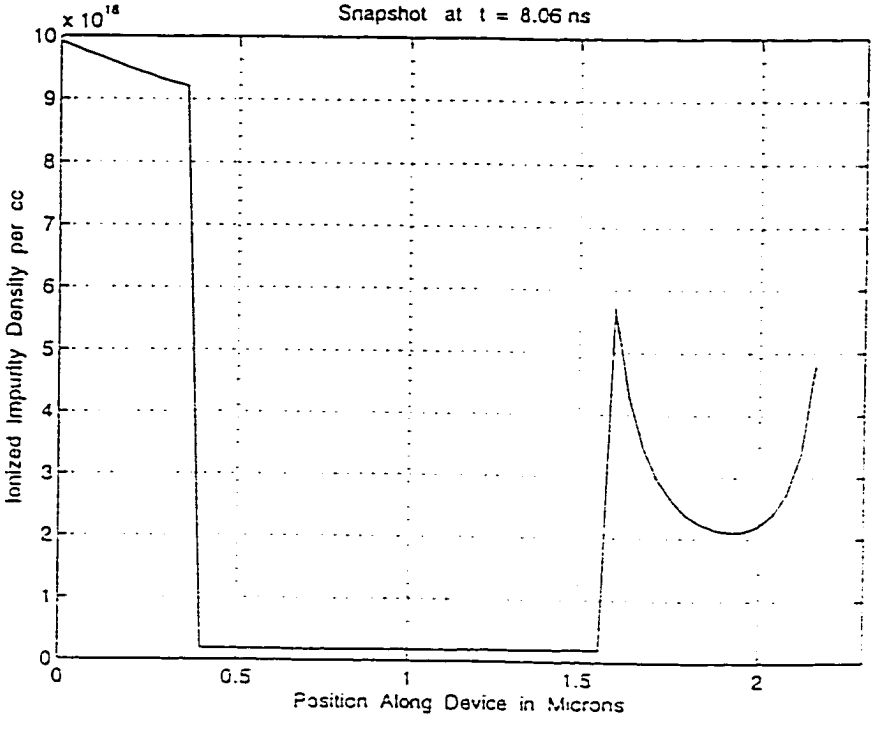

Fig. 4.19 Charged Impurity State Profile At 8.06 ns.

Reproduced with permission of the copyright owner. Further reproduction prohibited without permission.

shown in Fig. 4.17 at t = 8.06 ns, shows two distinct features. First, the electronic charge, on an average is seen to have moved and drifted towards the anode on the left. Second, the amplitude is decreased due to constant carrier removal from the left boundary. The process of diffusion, which is fairly strong at the elevated 673° K temperature, helps retain a smooth and continuous profile. The holes similarly, move towards the cathode on the right. and are seen to have a reduced average density in Fig. 4.18. However, their peak magnitude and average density is larger than that for the electrons. This results from two factors: (i) The slower diffusion coefficient of holes which reduces carrier loss, and (ii) The deep energy level of the acceptor and its partial ionization at the beginning. As the holes move towards the left, the acceptor sites gradually begin to get ionized and thus contribute to a localized hole generation process. This is clearly expected to become even more dominant for deeper lying acceptor levels. The occupancy of the donor and acceptor levels shown in Fig. 4.19 reveals the lack of complete ionization, especially for the acceptors. This is to be expected, given the deeper 180 meV level assumed here as compared to the shallow 50 meV donor.

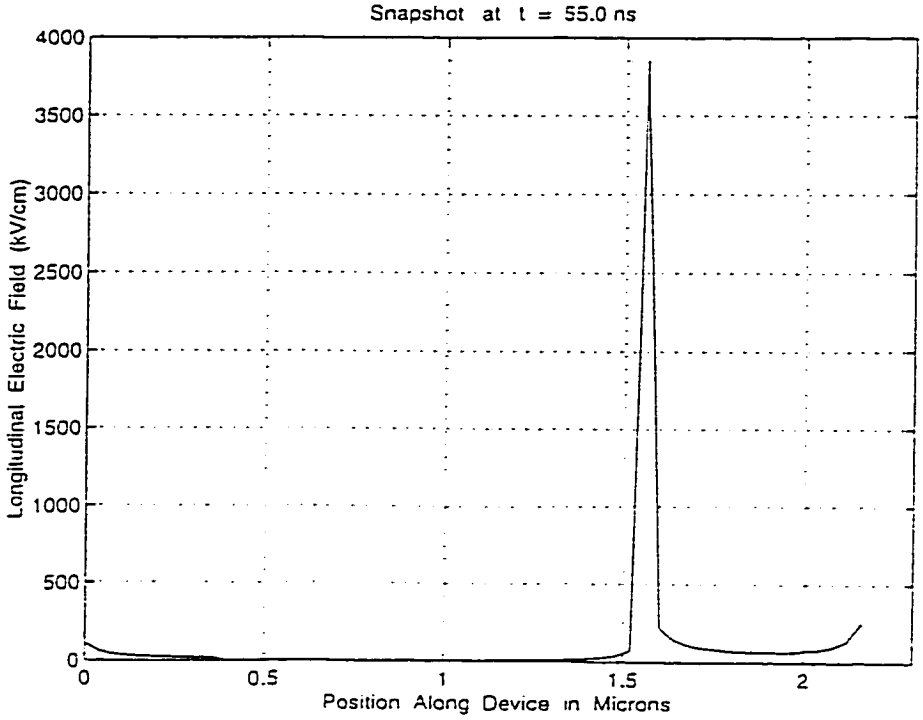

Fig. 4.20 Electric Field Distribution At 55.0 ns.

Reproduced with permission of the copyright owner. Further reproduction prohibited without permission.

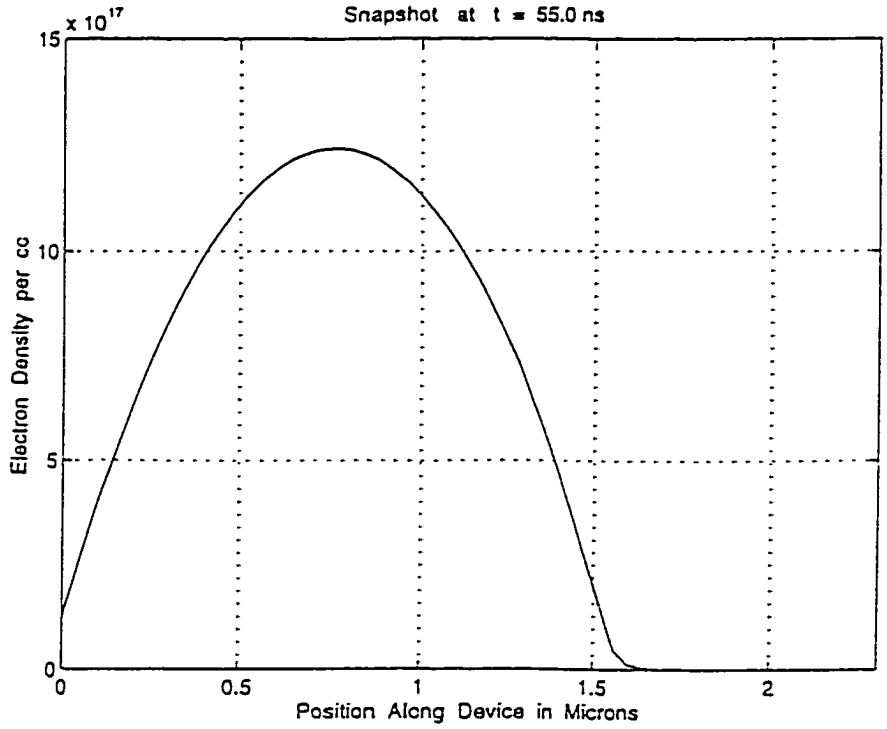

Fig. 4.21 Electron Density Profile At 55.0 ns.

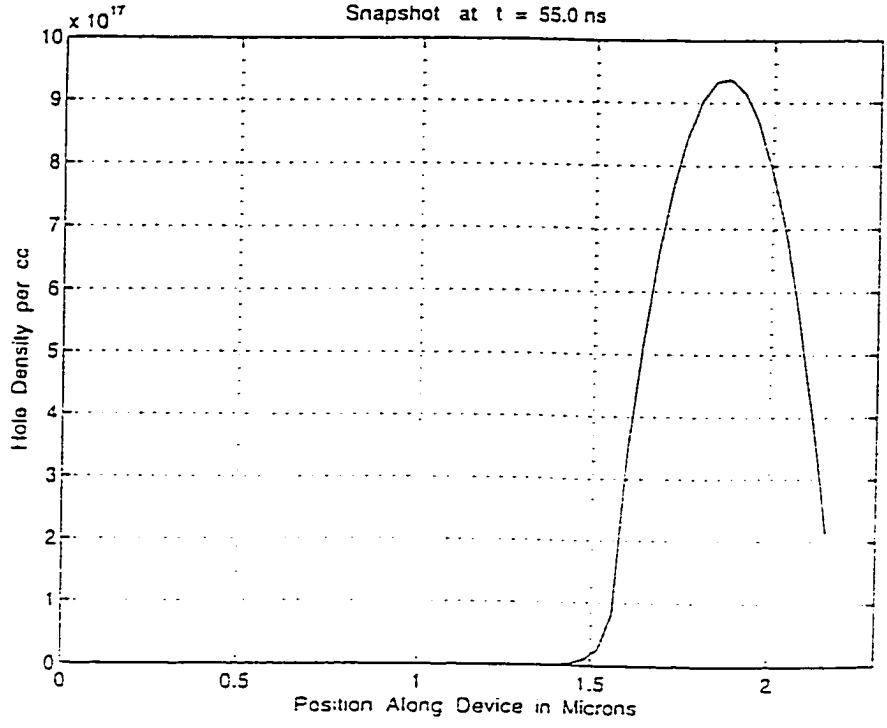

Fig. 4.22 Hole Density Distribution At 55.0 ns.

Reproduced with permission of the copyright owner. Further reproduction prohibited without permission.

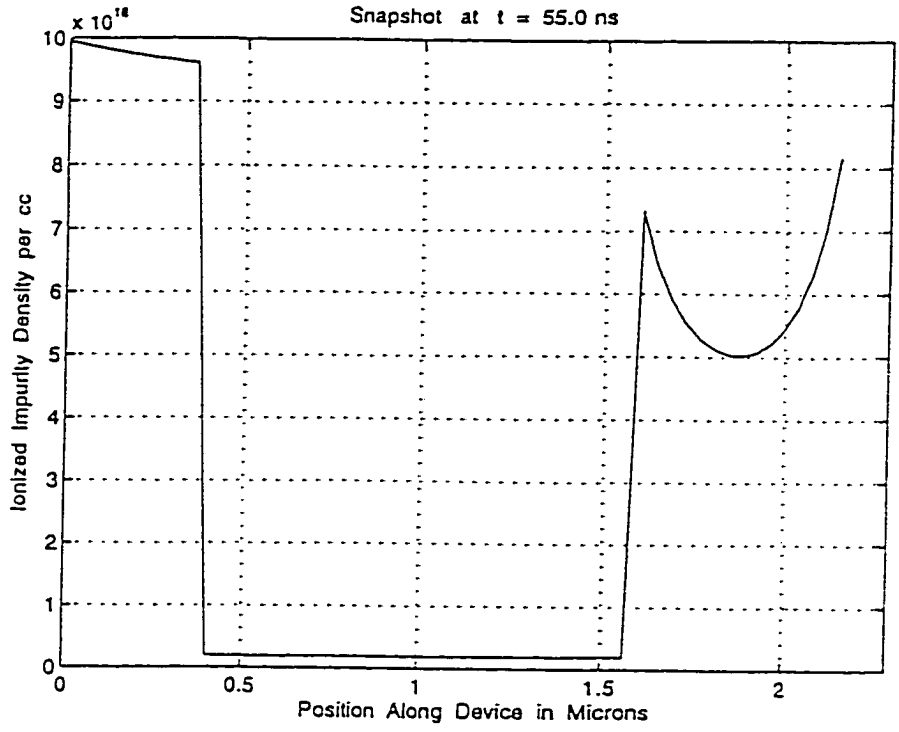

Fig. 4.23 Ionized Impurity Profile In The Diode At 55.0 ns.

Finally, the situation at 55.0 ns has been shown. Fig. 4.20 for the electric field profile is almost the same as Fig. 4.16, except for a marginal increase in the value near the cathode boundary on the right. This is associated with the gradual loss of holes which reduces the conduction current. As a result, the electric field is forced to enhance to provide a "displacement current" for maintaining total current continuity. The electron and hole profiles in Figs. 4.21 and 4.22 show a slow change, with holes densities reducing at a slightly faster rate. This is associated with electronic injection from the contacts. As the contacts were assumed to be emitters of electrons and not holes, the recombination process for the holes in the device is slightly larger. The reduction in magnitude is sluggish, and consequently the transition of the diode into a high resistant state takes place over a long time scale. The presence of traps and defect states in an actual device would hasten the carrier removal process and lead to quicker build up of the device voltage. Finally, the occupancy

Reproduced with permission of the copyright owner. Further reproduction prohibited without permission.

of the donor and acceptor levels is shown in Fig. 4.23. Comparing this plot with that of Fig. 4.19 at 8.06 ns demonstrates a gradual increase in the fractional ionization. This slow but steady increase provides an internal supply of holes into the device, and retards the rate of transition into a highly resistive state.

In summary, the 1D transient results obtained for the 160 V ramp with both acceptor and donor levels lying relatively deep shows: (i) Relatively slow decay in the device current. This is due to the slow release of carriers from the deep levels. (ii) The SiC device so operated would have a high potential for internal thermal heating, leading to possible second breakdown. Though, a thermal heating effects were not included in this simulation, the presence of a relatively large circuit current in excess of 2 Amperes, clearly demonstrates the possibility. (iii) Finally, in comparing to available data, the value of the currents over the first 55.0 ns obtained here matches rather well, thus indirectly confirming the adequacy of the 1D approach.

4.3.2 ONE-DIMENSIONAL RESULTS AND ANALYSIS: CASE II

Next, similar simulations to determine the transient response to a 160 Volt voltage ramp were carried out, but a shallow 5 meV donor and a 8 meV acceptor were assumed. The same SiC diode structure was used, and the parameters were all identical, except for the energy level of the donor and acceptor states. Though, in reality such shallow dopant levels do not exist for SiC, the hypothetical scenario was nonetheless used to gauge differences due to variations in the energy levels. Silicon, for example, would have such shallow levels.

Fig. 4.24 shows the voltage transient characteristics. The initial development of the device voltage up to about 15 ns is similar to that of Fig. 4.10. However, beyond this time, the device voltage is predicted to dramatically increase and nearly approach the external bias value.The corresponding current transient shown in Fig. 4.25 is again similar to that of Fig. 4.11 for the first 15 ns. Subsequently, the circuit current begins to monotonically decrease,

Reproduced with permission of the copyright owner. Further reproduction prohibited without permission.

and is seen to tend towards a near-zero value at large time. Having a negative value is predicted during the first 5 ns, and represents the short circuit current driven and sustained

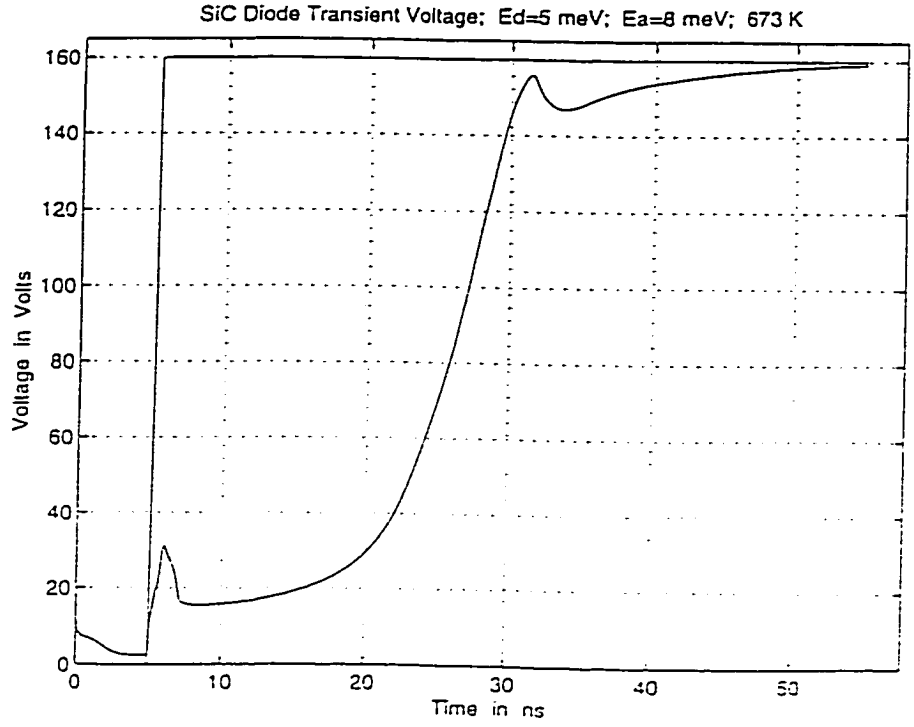

Fig. 4.24 Simulation results of the transient voltage response.

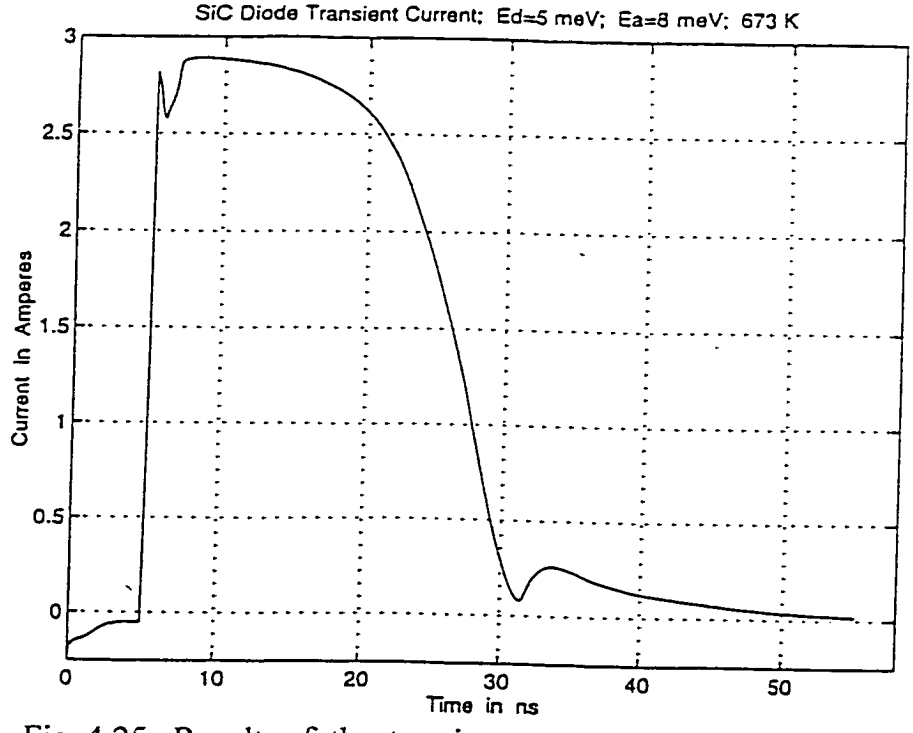

Fig. 4.25 Results of the transient current response characteristics.

Reproduced with permission of the copyright owner. Further reproduction prohibited without permission.

by the diode built-in voltage. The external voltage ramp beyond 5 ns forces a steep rise in the current, much of which is a "displacement current" in response to development of internal electric fields. The slight drop in current following the initial rapid rise, is associated with the "negative displacement current" upon termination of the voltage ramp.

The internal spatial distributions at 10.0 ns are shown in Figs. 4.26-4.28. The peak field in Fig. 4.26 is seen to be at about 3.5 MV cm^{-1}. As with the previous case, just after the voltage ramp, the spatial width is quite narrow and occurs over a small region at the $N\text{-}P^{-}$ junction. The electron density profile, shown in Fig. 4.27, shows an appreciable movement towards the anode, and the decrease in the average density. Since the donors prior to the onset of the voltage ramp were all nearly ionized, unlike the previous case, there is no continued electron supply into the conduction band. This leads to a faster decrease in the average concentration of mobile carriers. The holes in Fig. 4.28 undergo a phenomena similar to that of electrons. The situation at 30 ns, shown through Figs. 4.29-4.32 reveals a

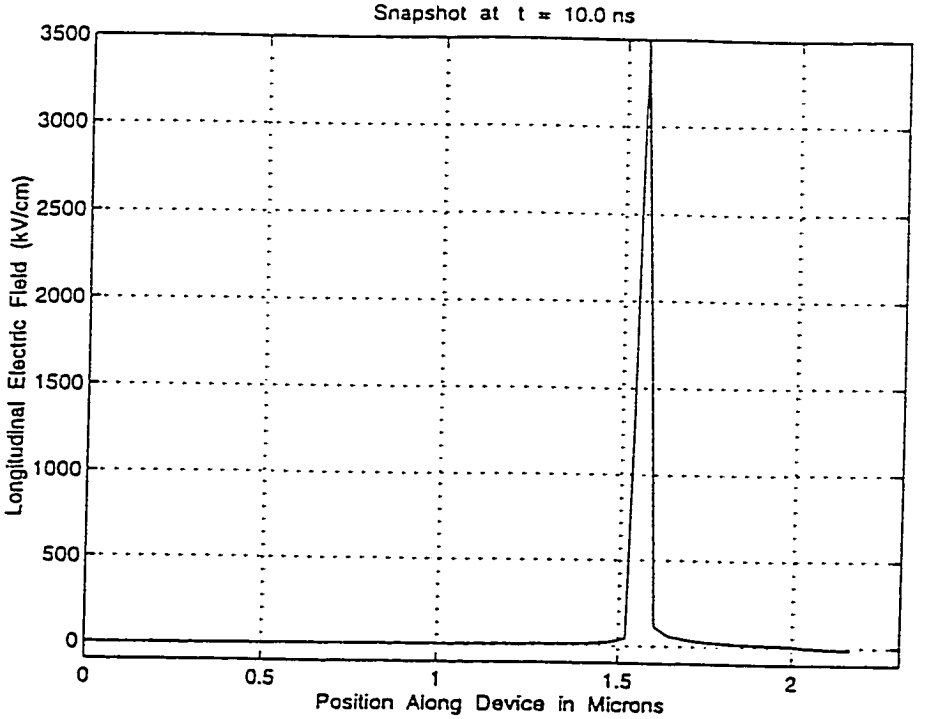

Fig. 4.26 Internal Electric Field Distribution at 10.0 ns.

Reproduced with permission of the copyright owner. Further reproduction prohibited without permission.

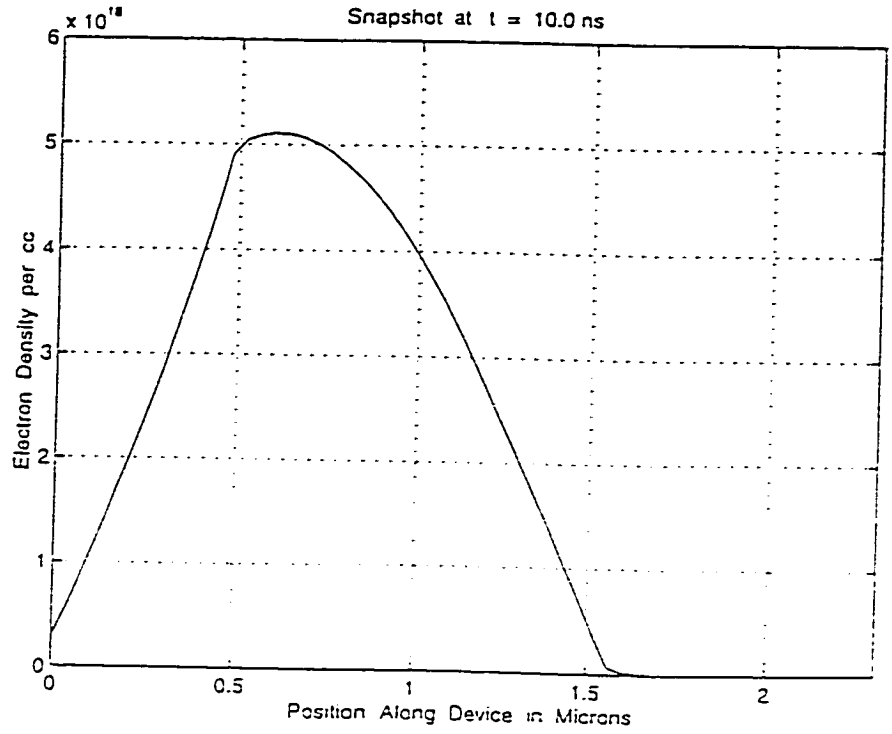

Fig. 4.27 Electron Density Profile at 10.0 ns.

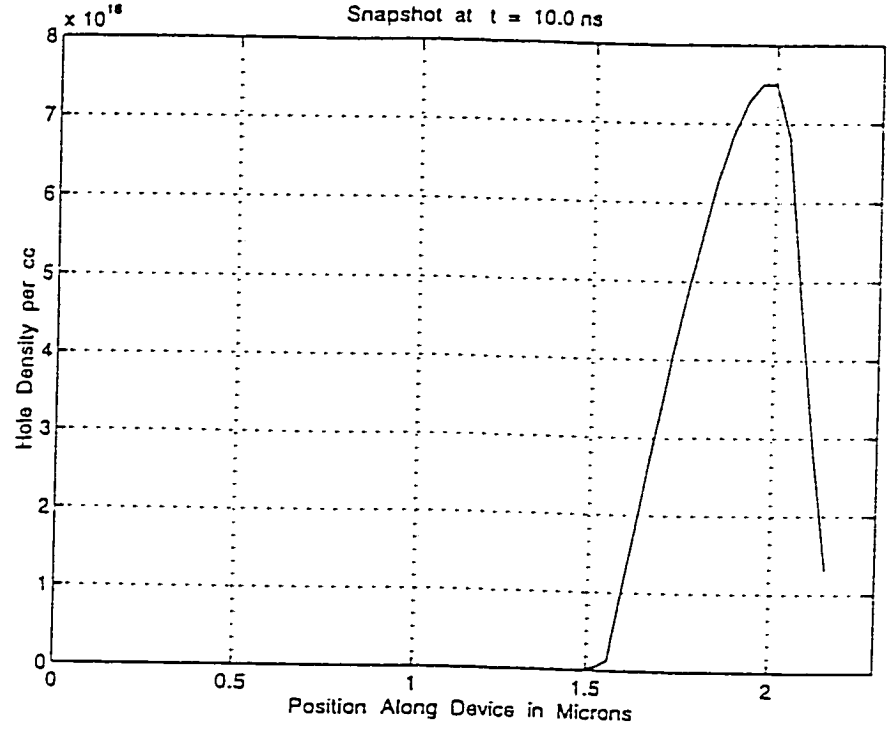

Fig. 4.28 Hole Density Profile at 10.0 ns.

Reproduced with permission of the copyright owner. Further reproduction prohibited without permission.

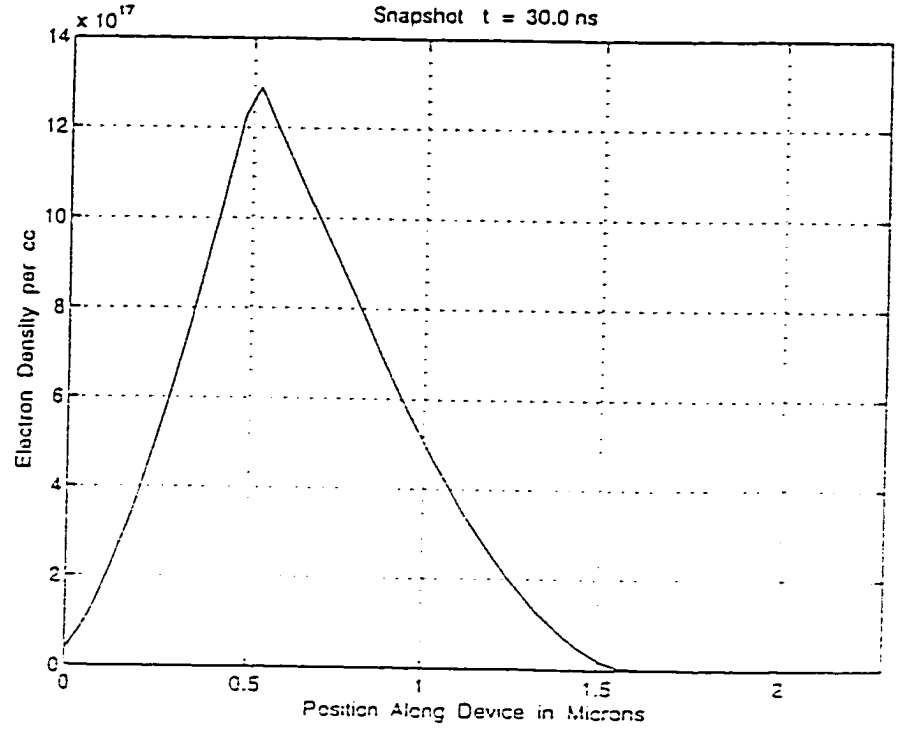

Fig. 4.29 Spatial Electron Distribution at 30.0 ns.

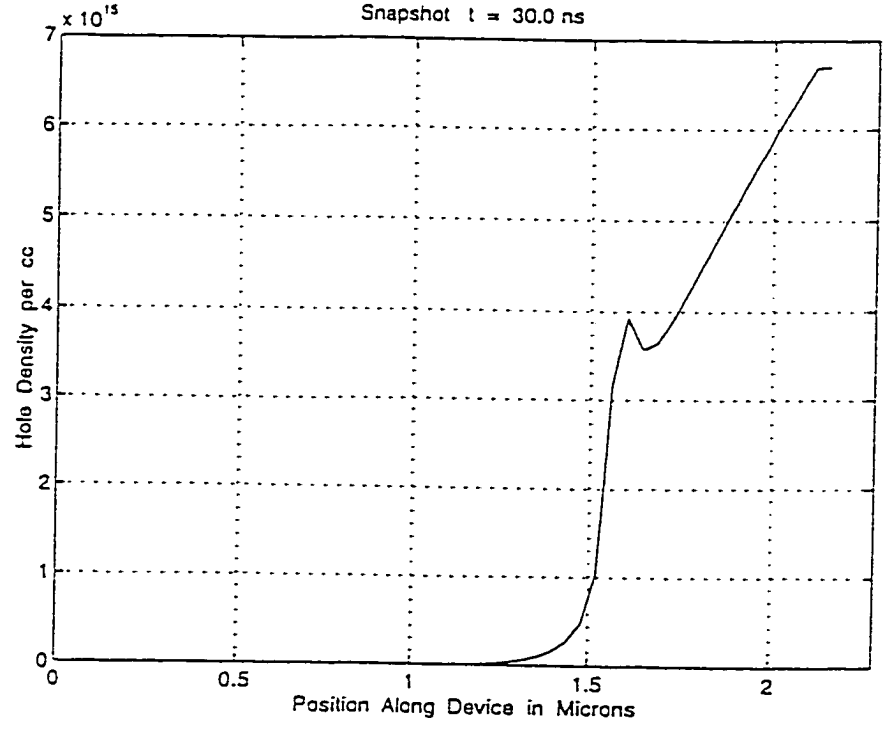

Fig. 4.30 Hole Density Profile at 30.0 ns

Reproduced with permission of the copyright owner. Further reproduction prohibited without permission.

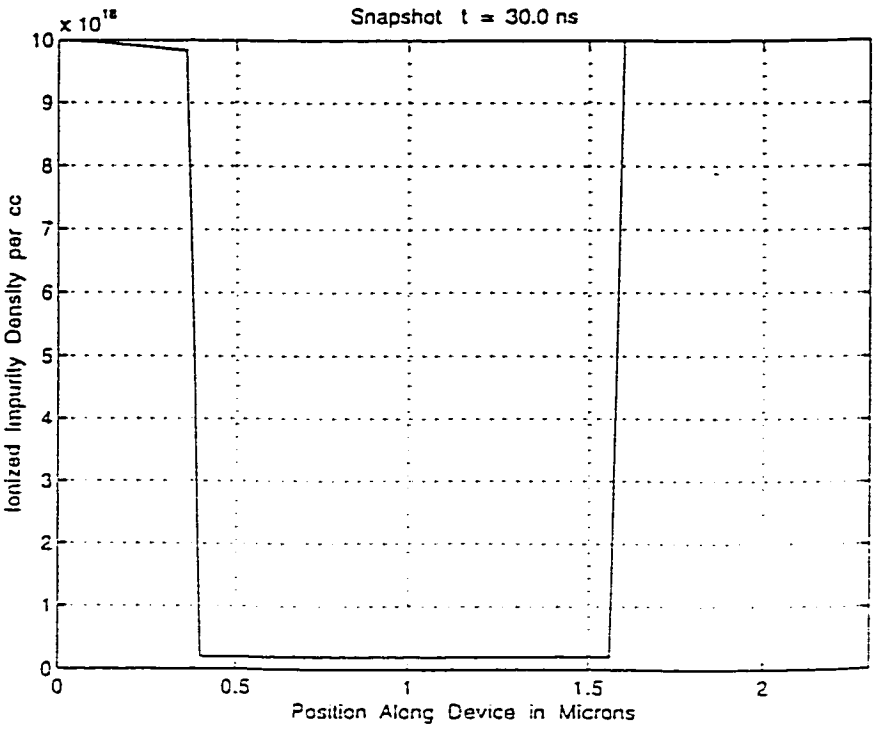

Fig. 4.31 Ionized Impurity Level Occupancy Profile at 30.0 ns.

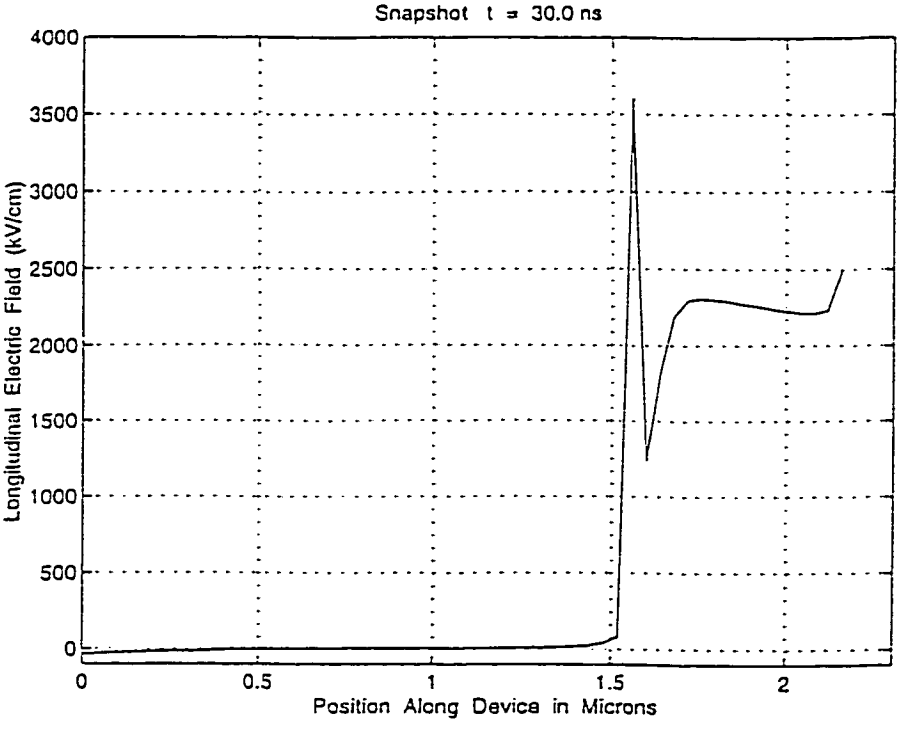

Fig. 4.32 Electric Field Distribution at 30.0 ns.

Reproduced with permission of the copyright owner. Further reproduction prohibited without permission.

significant decay in the internal mobile charge, and the development of internal fields. The electron spatial density, as shown in Fig. 4.29, is seen to have been reduced by about an order of magnitude. Hole densities, on the other hand, are reduced even more significantly over this time interval. The peak value for holes is only about 6.7 x 10^{15} cm^{-3} in Fig. 4.30. This rapid reduction results from a combination of carrier outflow, recombination with electrons injected from the cathode on the right, and the lack of hole refurbishment from the partially ionized acceptor states. In fact, the impurity level occupancy shown in Fig. 4.31 demonstrates almost complete ionization throughout the volume. This is in contrast to Fig. 4.22 at the end of 55.0 ns for case I. The small "bump" in the hole density near 1.6 μm is due to impact ionization contributions due to the high fields at the N-P^- boundary. This contribution is clearly not very large, since it produces hole densities that are on the order of 10^{15} cm^{-3}. The effect of this weak ionization could not be discerned in the previous case, as the density of background holes remaining within the P^- region was much larger. Finally, the plot of the internal field is shown in Fig. 4.32. The main features are the existence of a relatively high field at the N-P^- boundary, and the slow and steady growth within the P region. Finally, results of the internal profiles at 55.0 ns are shown in Figs. 4.33-4.36. Basically, the moving high field domain from the right side of the P^- region merges with that near the N-P^- junction boundary as given in Fig. 4.33. This effectively increases the field and hence the hole drift velocity. This drives up the conduction current, causes a redistribution of the internal fields within the device, and moves the localized high density clump of holes near 1.6 μm towards the cathode. As a result, the hole density becomes smoother as shown in Fig. 4.35.

4.3.3ONE-DIMENSIONAL RESULTS AND ANALYSIS: CASE III

After having probed the transient response characteristics at a high applied voltage, simulations were next carried out to analyze the electrical behavior at a low voltage. Case III pertains to a discussion of SiC diode having donor and acceptor impurities at 50 meV and

Reproduced with permission of the copyright owner. Further reproduction prohibited without permission.

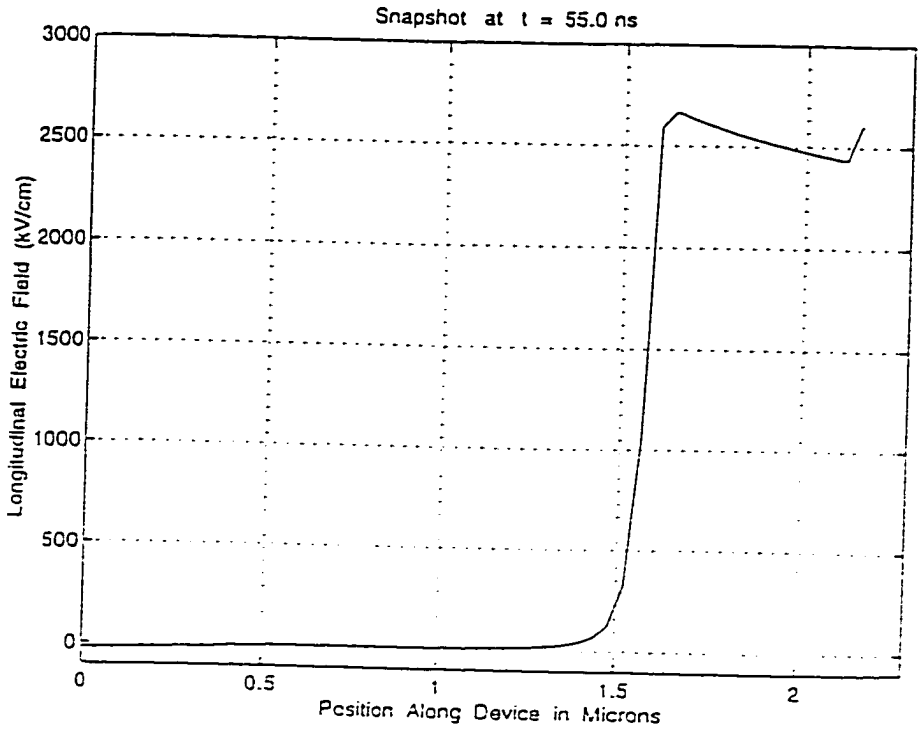

Fig. 4.33 Electric Field Distribution at 55.0 ns.

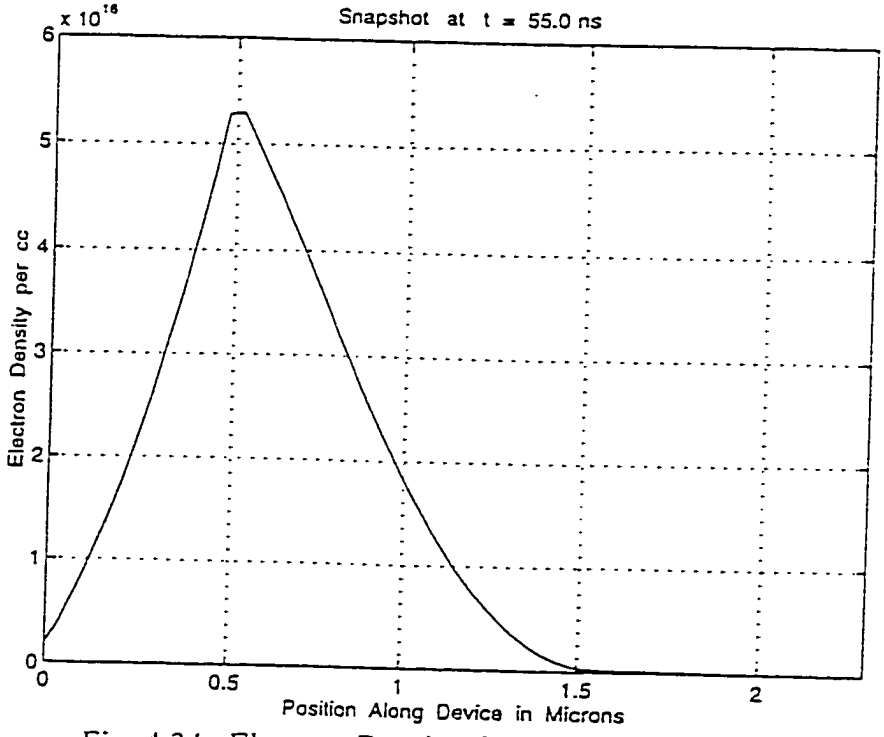

Fig. 4.34 Electron Density Distribution at 55.0 ns.

Reproduced with permission of the copyright owner. Further reproduction prohibited without permission.

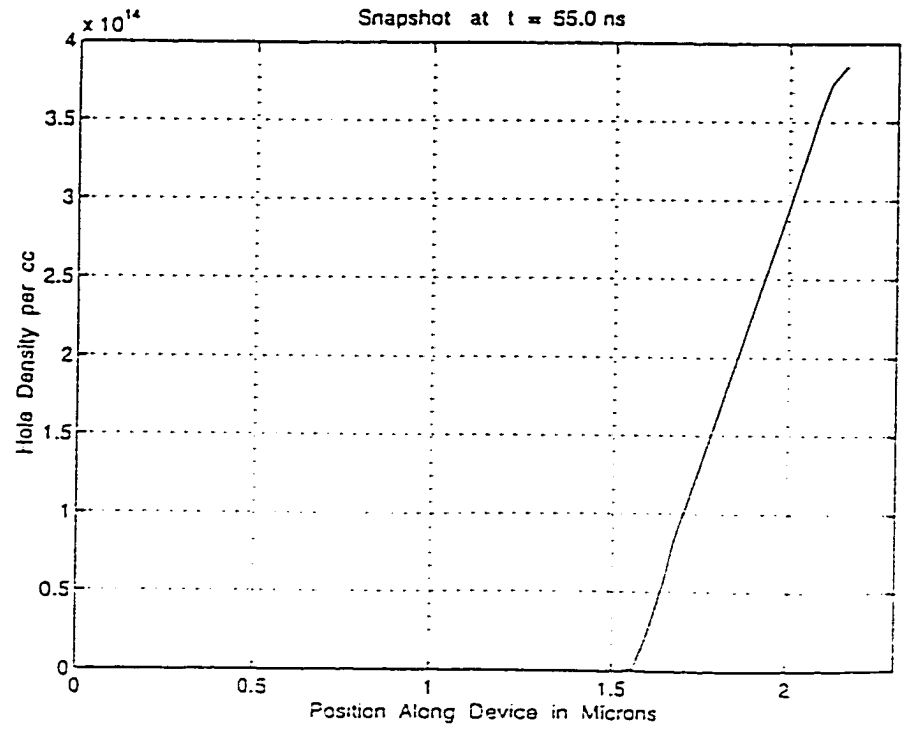

Fig. 4.35 Hole Density Profile at 55.0 ns.

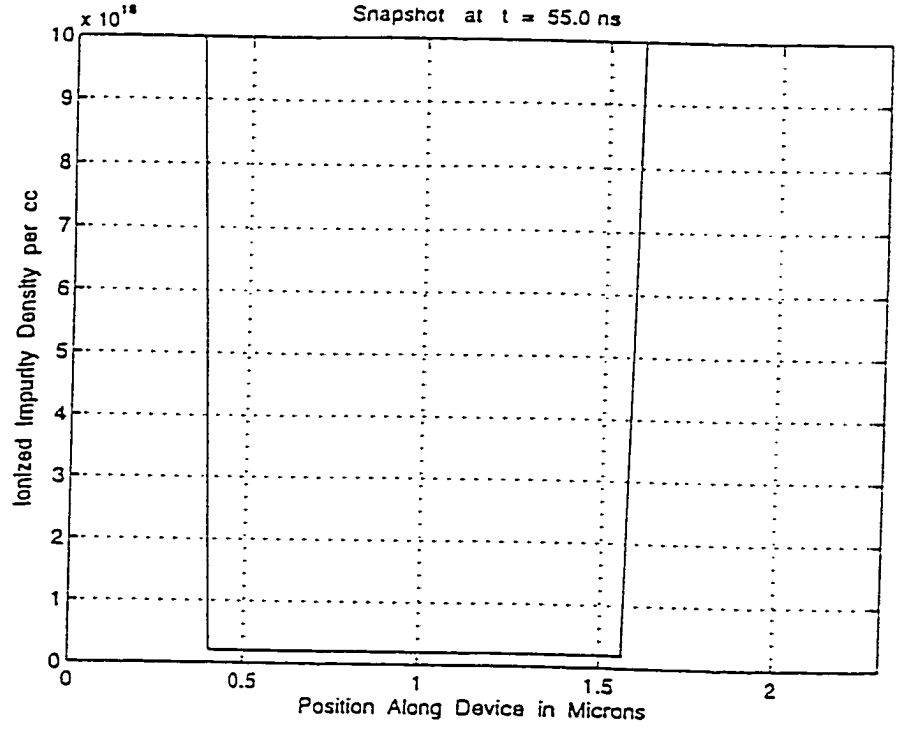

Fig. 4.36 Ionized Impurity Distribution at 55.0 ns.

Reproduced with permission of the copyright owner. Further reproduction prohibited without permission.

180 meV energies, respectively, for a voltage ramped from zero to 30 Volts. Fig. 4.37 shows the simulation results for the voltage transients at 673° K. In this situation, as for case I, the device voltage was seen to increase initially in response to the applied voltage ramp. However, the subsequent time evolution was relatively slow and had not reached the maximum 30 volt even after 55.0 ns. The transient current of Fig. 4.38 reflects the slow internal time constant of the system, with a decrease from a peak value of about 0.37 Ampere to 0.26 Ampere at 55 ns. The magnitude of the current, though, is substantially less than the 160 Volt case. Consequently, one would not expect as much device heating, or for internal thermal effects to lead to potential "second breakdown" conditions. The sluggish transition is due to slow changes in the internal field and carrier density distributions. Figs. 4.39-4.42 present the internal distributions at 9.025 ns. The plots are similar in nature to those obtained for case I during the initial stages. Figs. 4.47-4.50 show the situation at 55 ns. The electric field retains the same shape while marginally increasing in magnitude. The carrier densities reduce, though not dramatically, and move towards the contacts primarily through

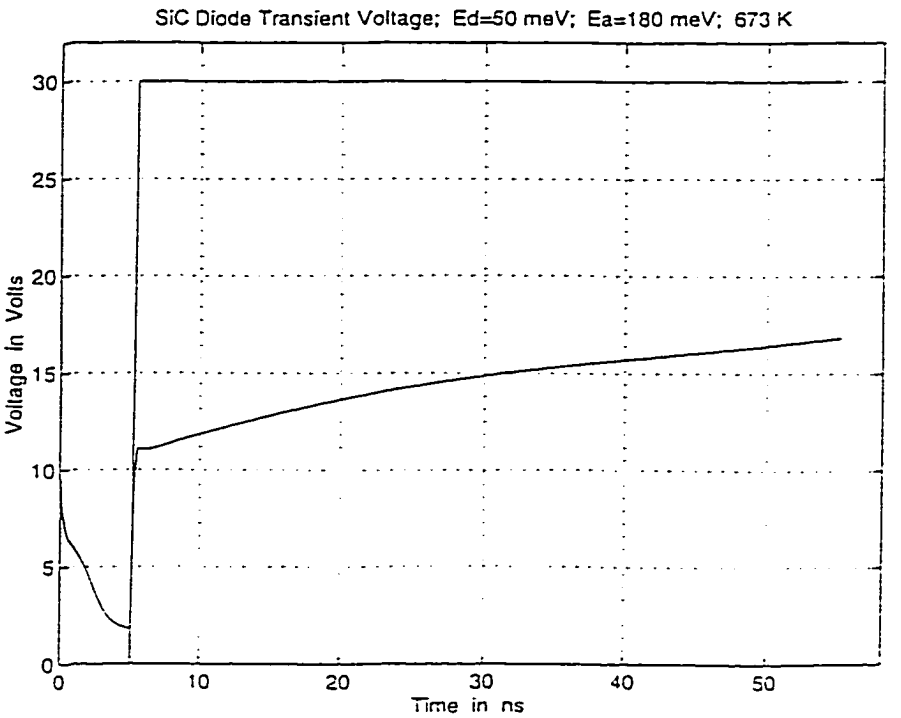

Fig. 4.37 Transient Voltage Response to a 0.5 ns, 30 V Ramp.

Reproduced with permission of the copyright owner. Further reproduction prohibited without permission.

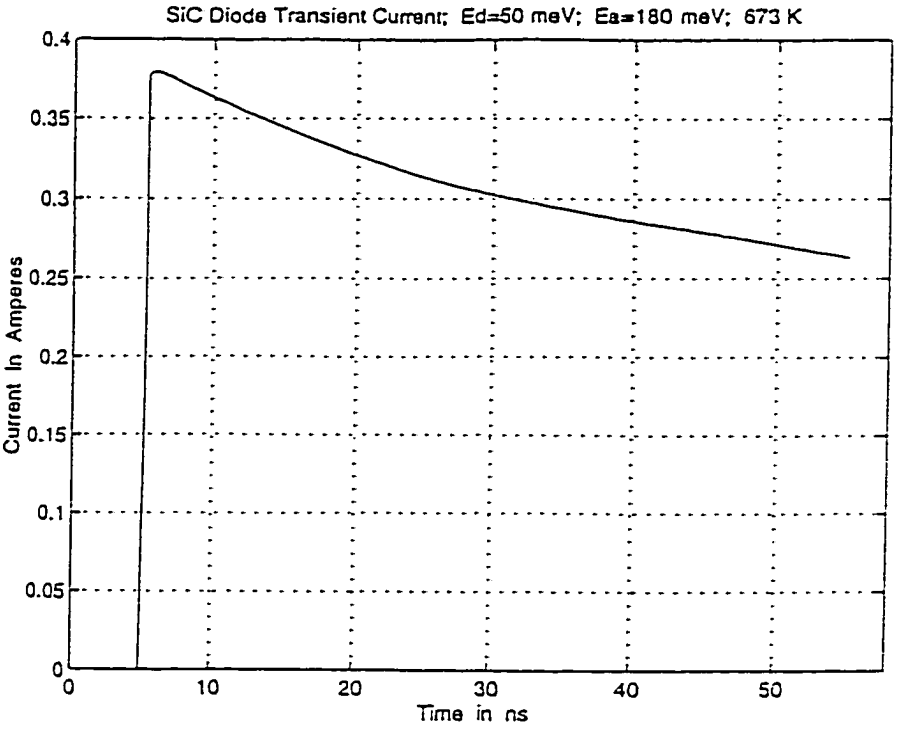

Fig. 4.38 Current Transient Response to a 30 Volt Fast Ramp.

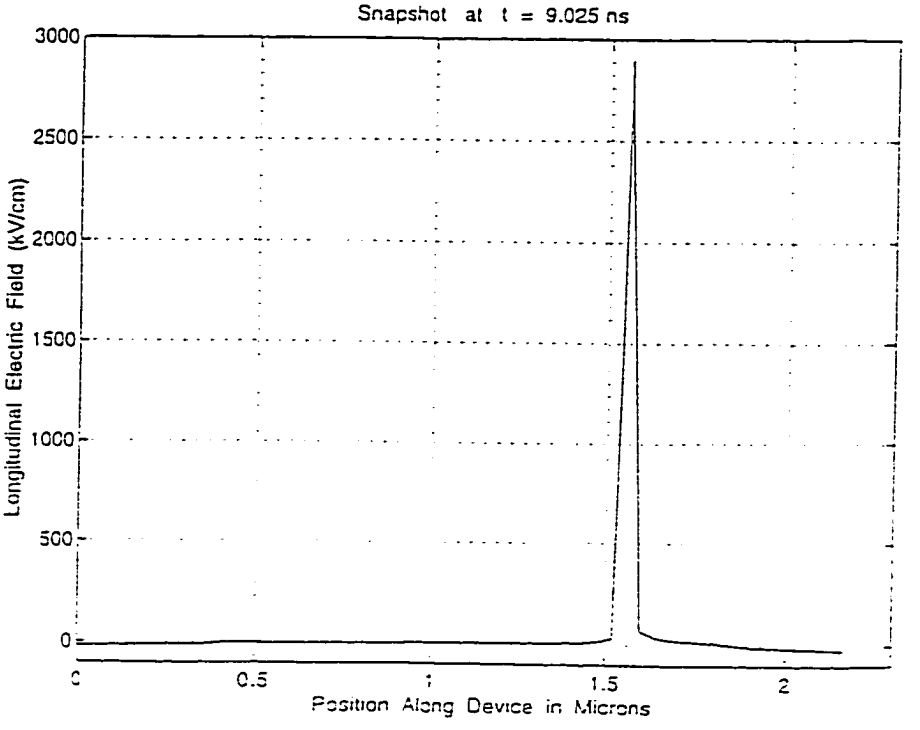

Fig. 4.39 Internal Electric Distribution at 9.025 ns.

Reproduced with permission of the copyright owner. Further reproduction prohibited without permission.

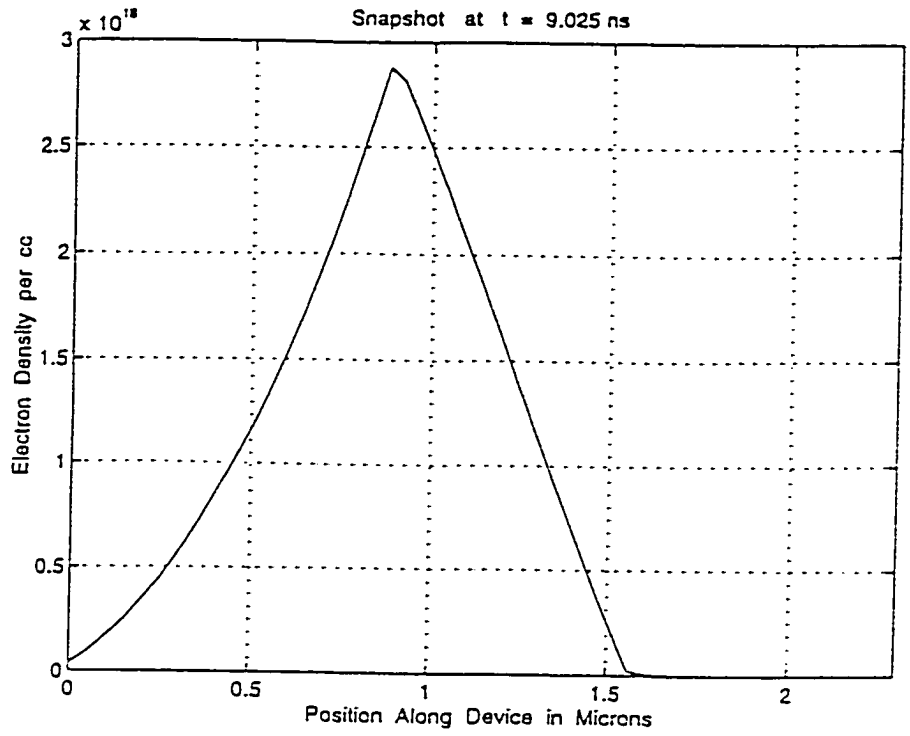

Fig. 4.40 Spatial Electron Distribution at 9.025 ns.

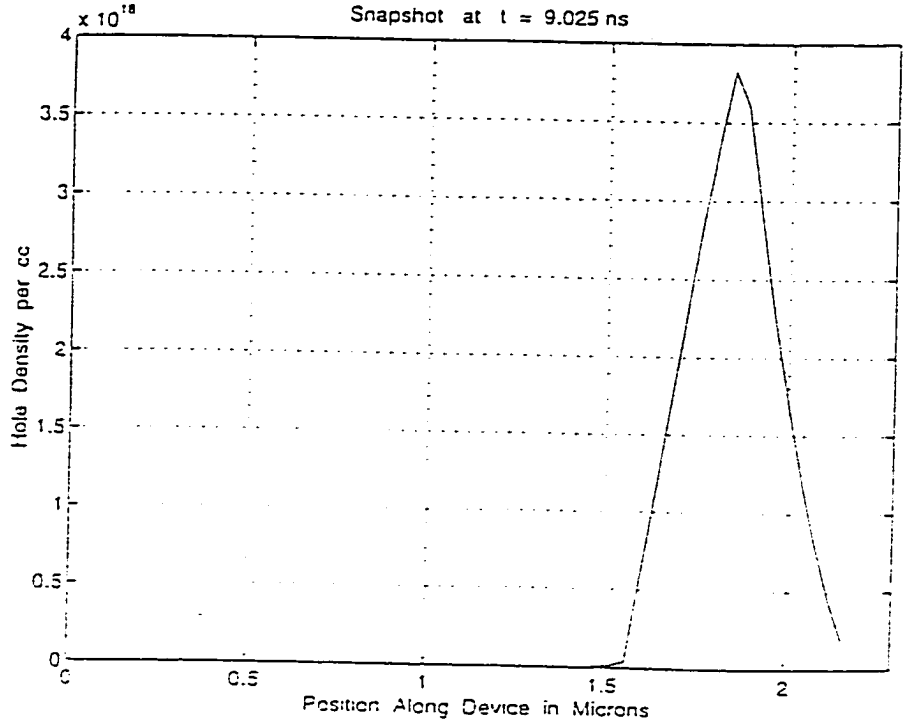

Fig. 4.41 Spatial Hole Distribution at 9.025 ns.

Reproduced with permission of the copyright owner. Further reproduction prohibited without permission.

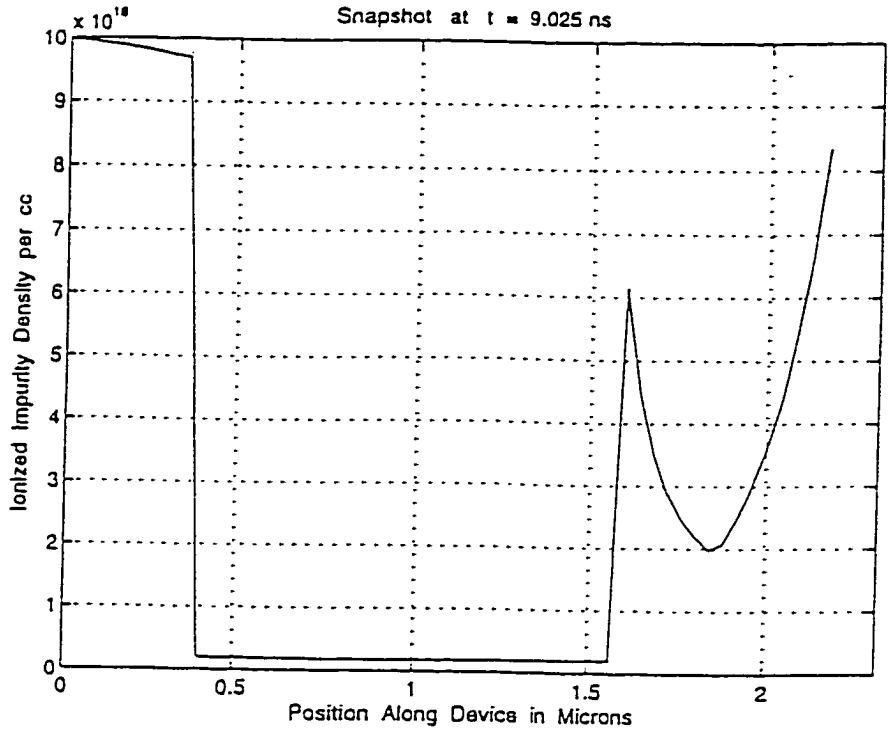

Fig. 4.42 Ionized Impurity Distribution at 9.025 ns.

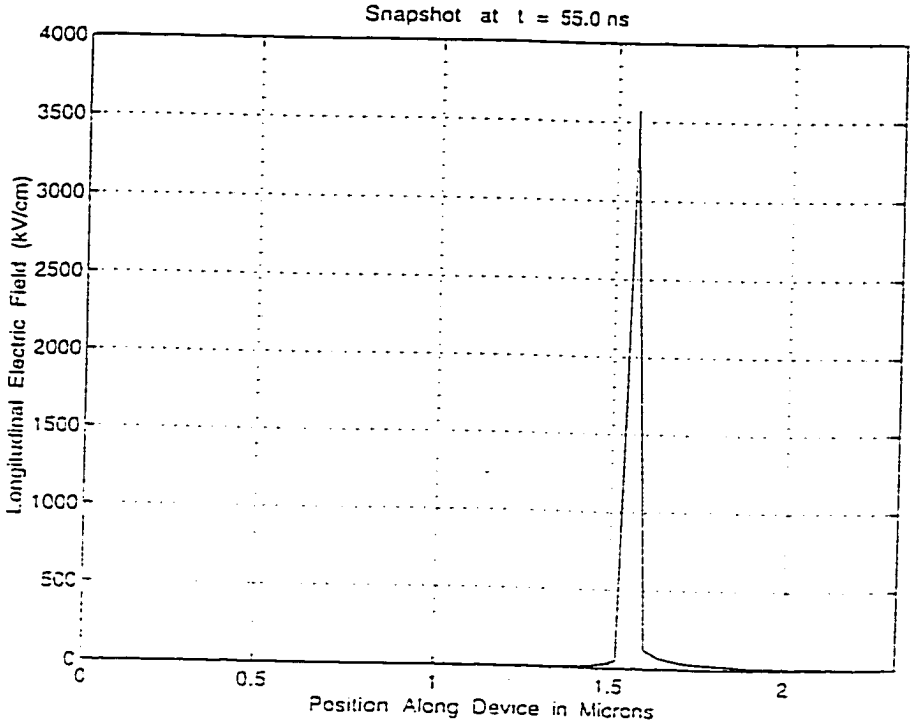

Fig. 4.43 Electric Field Profile at 55.0 ns.

Reproduced with permission of the copyright owner. Further reproduction prohibited without permission.

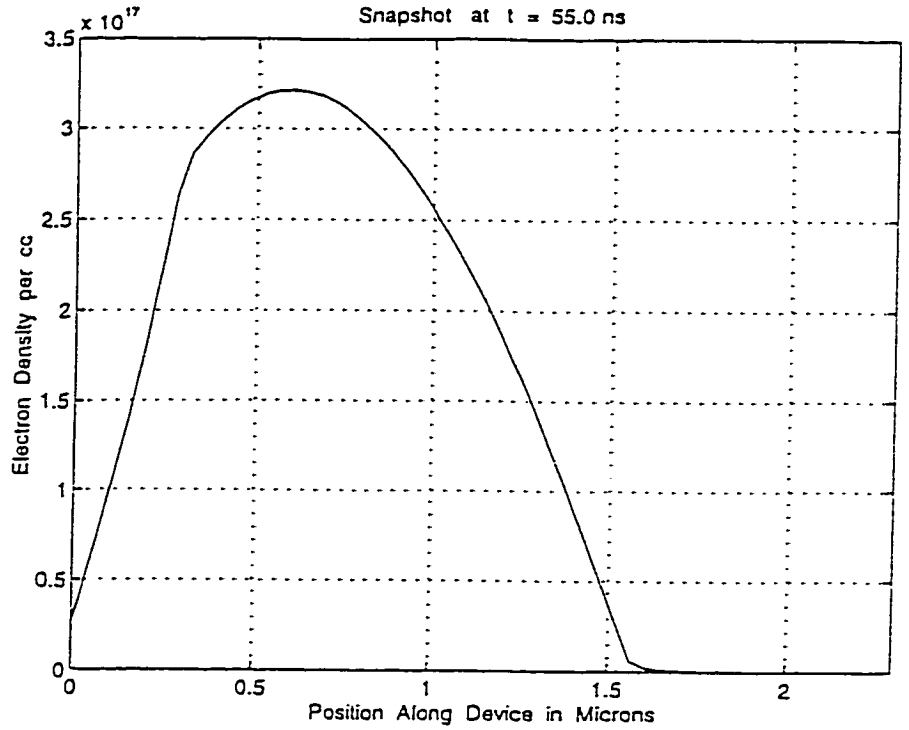

Fig. 4.44 Internal Electron Density Distribution at 55.0 ns.

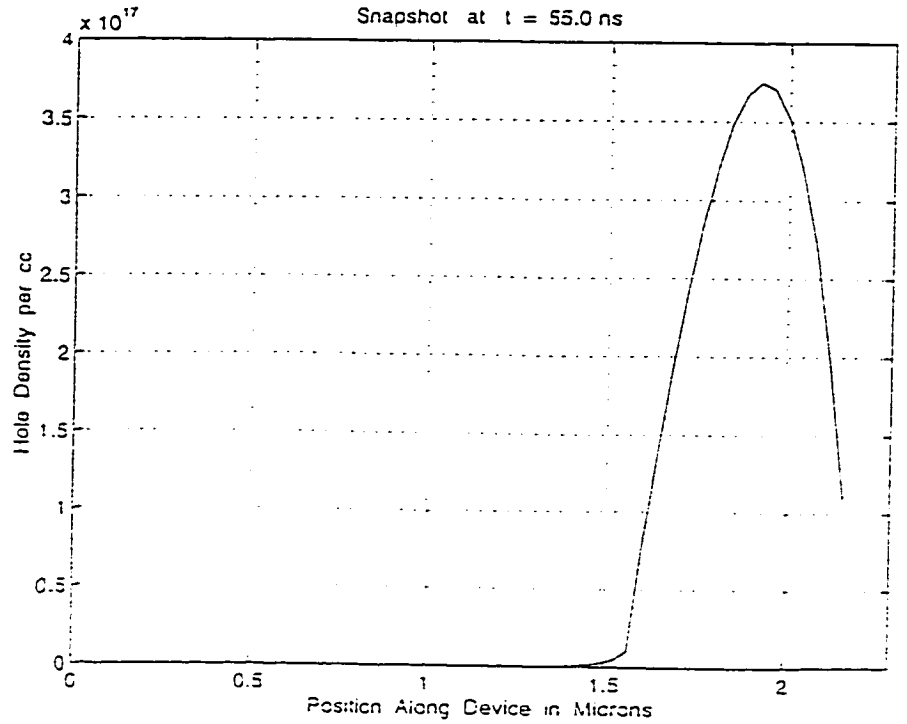

Fig. 4.45 Internal Hole Profile at 55.0 ns.

Reproduced with permission of the copyright owner. Further reproduction prohibited without permission.

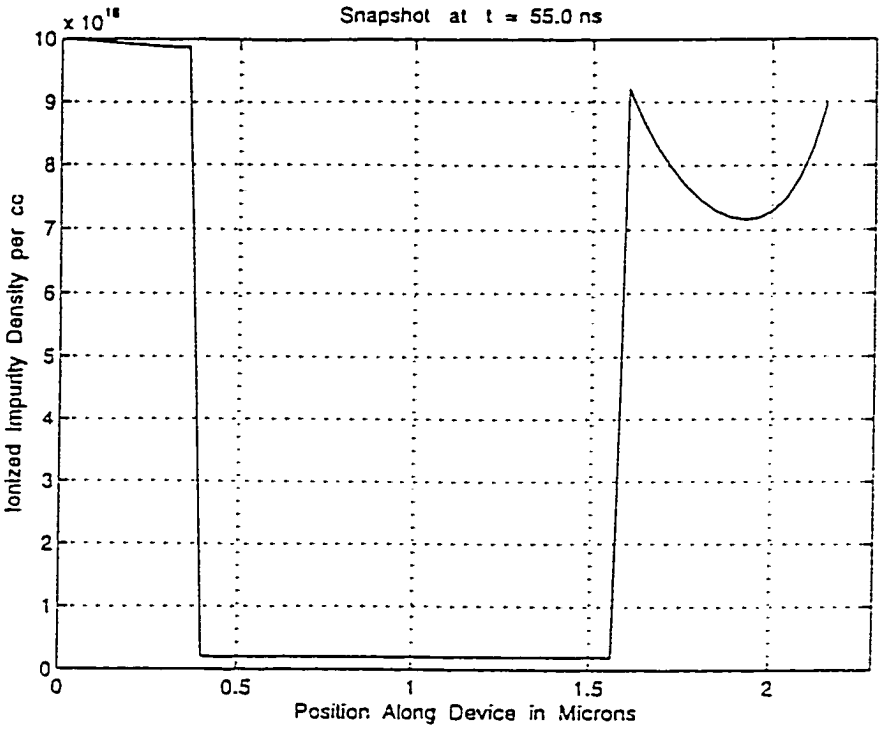

Fig. 4.46 Results for the Ionized Impurity Distribution at 55.0 ns.

the process of diffusion. The occupancy of the acceptors, however, is seen to change significantly from a low level to a large percentage. This deep level is responsible for supplying holes into the valence band which sustains currents for a relatively long time.

4.3.4 ONE-DIMENSIONAL RESULTS AND ANALYSIS: CASE IV

The transient response characteristics for a 30 Volt ramp for "shallow" impurity states are shown next. As in case II, the donors were taken to have a value of 5 meV and the acceptors 8 meV. In this case, the device voltage and transient current shown in Figs. 4.47 and 4.48 roughly track the evolution of Figs. 4.37 and 4.38 over the first 15 ns. However, after that the SiC diode is predicted to make a fast recovery and transition into a high conducting state. The current would then fall to near-zero level within the 55 ns time frame.

Reproduced with permission of the copyright owner. Further reproduction prohibited without permission.

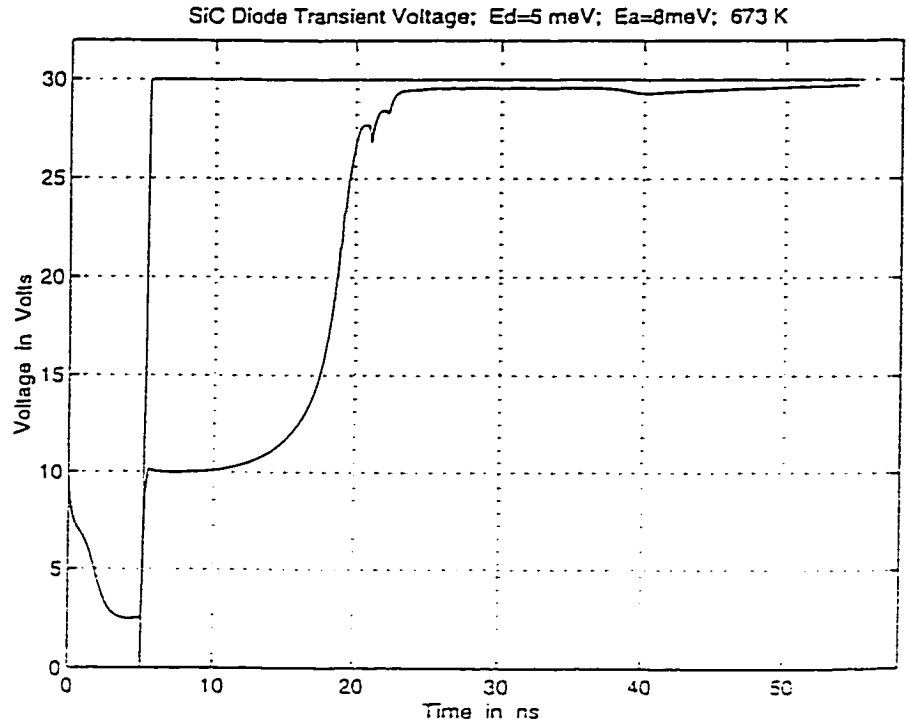

Fig. 4.47 Results for the Voltage Transient for Case IV.

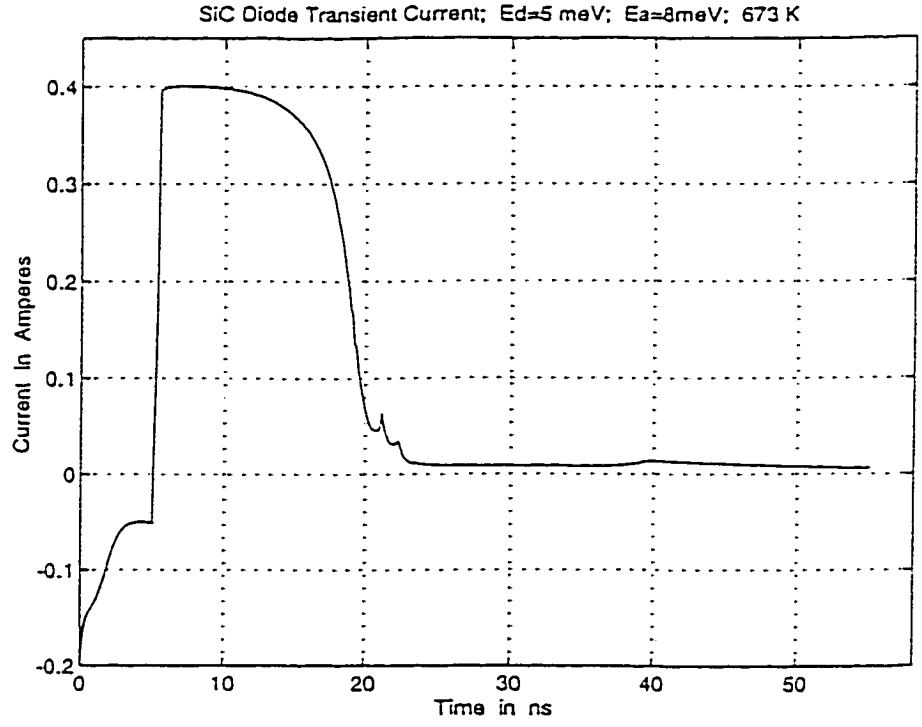

Fig. 4.48 Results for the Transient Diode Current Response for Case IV.

Reproduced with permission of the copyright owner. Further reproduction prohibited without permission.

The reasons for this behavior are identical to that of case II. The shallow levels do not provide for a continuous supply of carriers, especially holes into the valance band. Since the currents are neither large nor sustained, minimal heating effects would be expected in this case.

4.3.5 ENERGY LEVEL AND EMISSION RATE CORRELATION

In the results so far, the transient response dynamics were seen to be governed by the energy level of the impurity states. At higher energies, the degree of partial ionization would be higher, leading to a slow supply of mobile charge. The emission process from the impurity controls the rate of carrier release, and is dependent on the energy difference between the impurity state and the continuum. In order to estimate the time scales associated with the emission process, a quick evaluation of the emission rate was carried out as a function of impurity energy. Fig. 4.49 shows the emission rate for a single impurity level in SiC at 673 ^{c} K. The emission rate for electrons assumes the presence of donors (or electron traps), and that for holes is due to acceptors (or hole traps). The two main points seen from the figure are: (i) The electron emission rates are predicted to be always higher than those for holes. This is associated with the smaller electronic effective mass. (ii) Next, the emission rate would change by orders of magnitude if the energies were to vary from the 5 meV range to about 0.6 eV. The low 5 meV level has already been used to generate the transient response characteristics. The emission rates for energies around 5 meV are higher than 10^{11} s^{-1}. Consequently, impurity ionization and detrapping phenomena should proceed very fast on time scales that are much less than a nanosecond. On the other hand, for values around 180 meV (as was assumed for the deep acceptors so far in cases I and III), the characteristic time constants are on the order of a nanosecond. These longer time scales were seen to lead to persistent current in the SiC diode. However, for even deeper levels on the order of 0.6 eV, the time constants from Fig. 4.49 are predicted to be a few hundred nanoseconds. Such deep levels, should then contribute even more significantly to persistent device currents and lead

Reproduced with permission of the copyright owner. Further reproduction prohibited without permission.

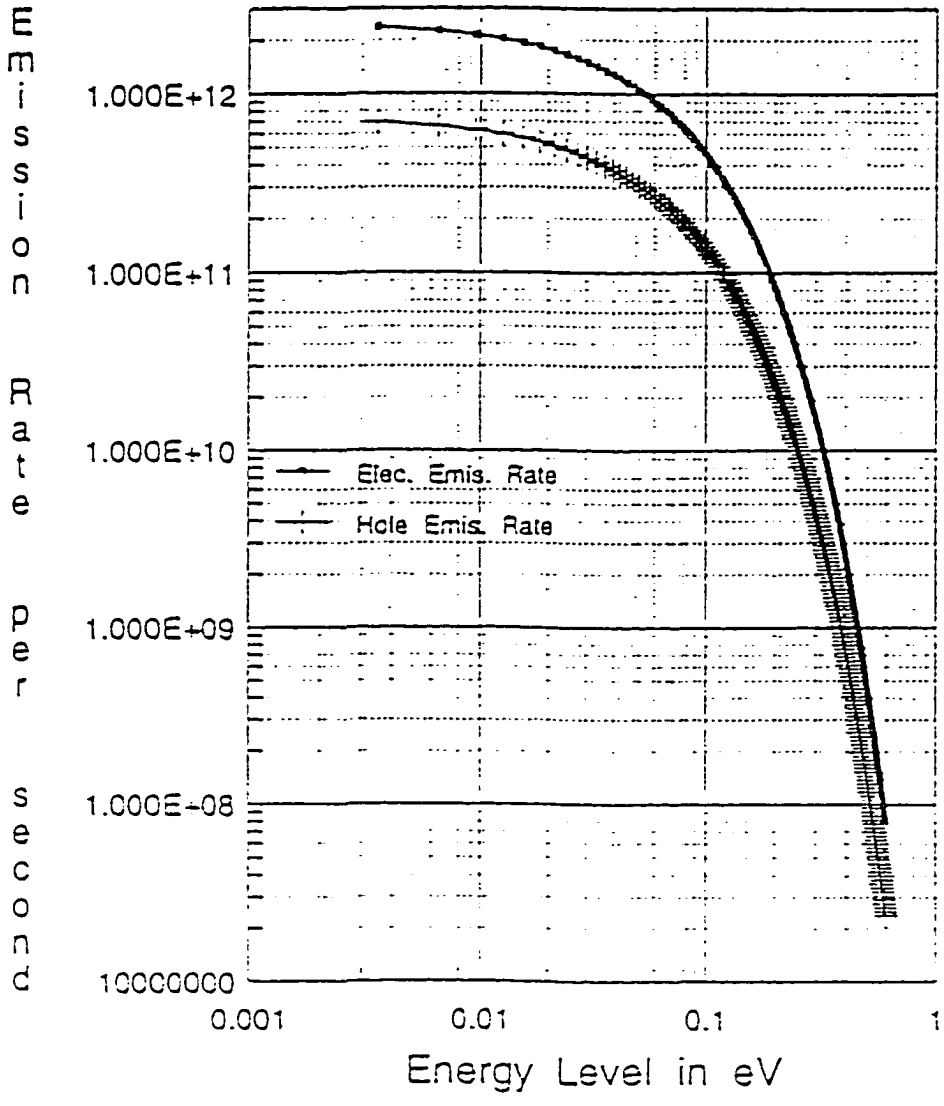

Fig. 4.49 Variation of the Emission Rate with Impurity Energy Level at 673° K.

to internal heating. The possibility of such deep levels in SiC material is actually possible as has been shown recently through experimental deep-level transient spectroscopy [24]. A state lying at an energy of about 0.6 eV was found in the P-region of a SiC diode structure. Based on the experimental evidence and the implications of Fig. 4.49, it was logical to examine the

Reproduced with permission of the copyright owner. Further reproduction prohibited without permission.

possible electrical response of a SiC diode containing deeper impurities. Towards this end then, one more simulation was performed for the same N^+-N-P^+ diode structure with the donor level fixed at 50 meV (as in cases I and III), but for a much deeper acceptor state. A fast voltage ramp was again assumed, with a maximum value of 160 Volts.

4.3.6 ONE-DIMENSIONAL RESULTS AND ANALYSIS: CASE V

Simulations results of the transient response to a 160 Volt ramp for a 50 meV donor impurity state and a "deep" 0.6 eV acceptor level are shown in Figs. 4.50 and 4.51. The overall device conductance for this case is very low, due to the extremely deep acceptor level chosen. This level remains virtually unionized as will be shown, and the device is, therefore, not capable of producing large currents. Consequently, the device voltage tends to track the applied bias over the first 7 ns. times and the potential drop across the 50 Ohm resistor is negligible. The minor "dip" in the voltage at around 8 ns is associated with a conduction current contribution from the electrons as they begin moving towards the anode in response to the fields build up within the device. Fig. 4.51 for the transient current, portrays the picture more clearly. The initial current spike at around 5 ns is mainly due to the displacement current. The secondary current increase at around 8 ns is due to electronic motion in response to the creation of internal electric fields. However, the initiation of this conduction current component leads to a quenching of the local fields to maintain total current continuity. The result is a decrease in the electron component, and the redistribution of internal fields towards the low conductivity p-type region containing the deep acceptors. Finally, the gradual process of hole movement towards the cathode on the right, creates a depletion region within the p-material. This initiates the slow generation of holes via the thermal emission process. However, the time constant associated with such hole emission, as already shown in Fig. 4.49, is slow. The device conductivity therefore, can only increase at a slow pace as mobile holes are channeled into the valance band from the deep acceptor sites.

Reproduced with permission of the copyright owner. Further reproduction prohibited without permission.

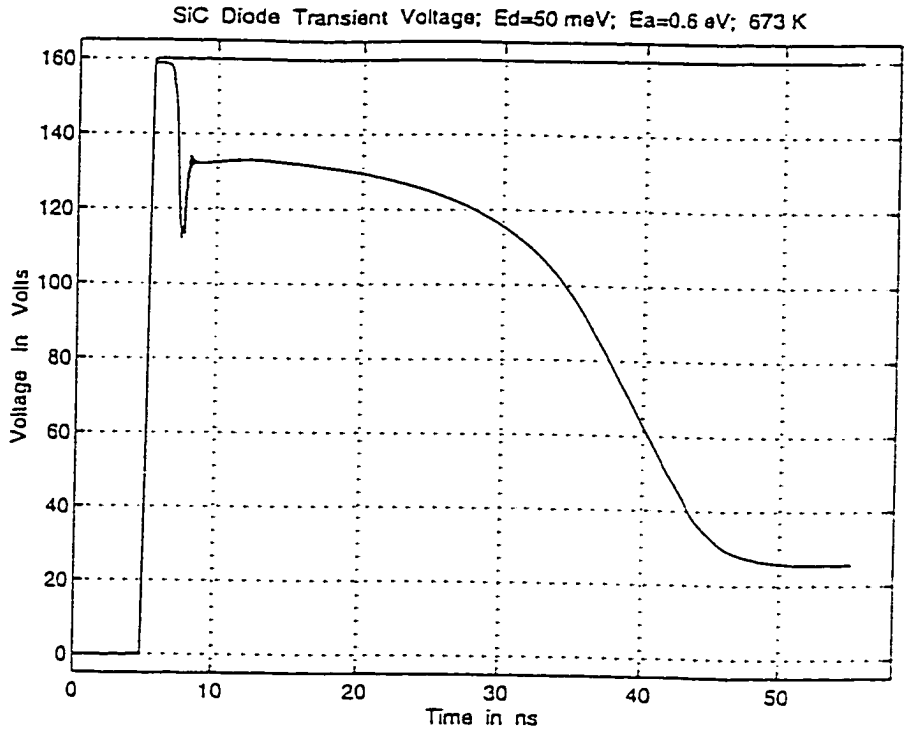

Fig. 4.50 Results for the Transient Diode Voltage Response for Case V.

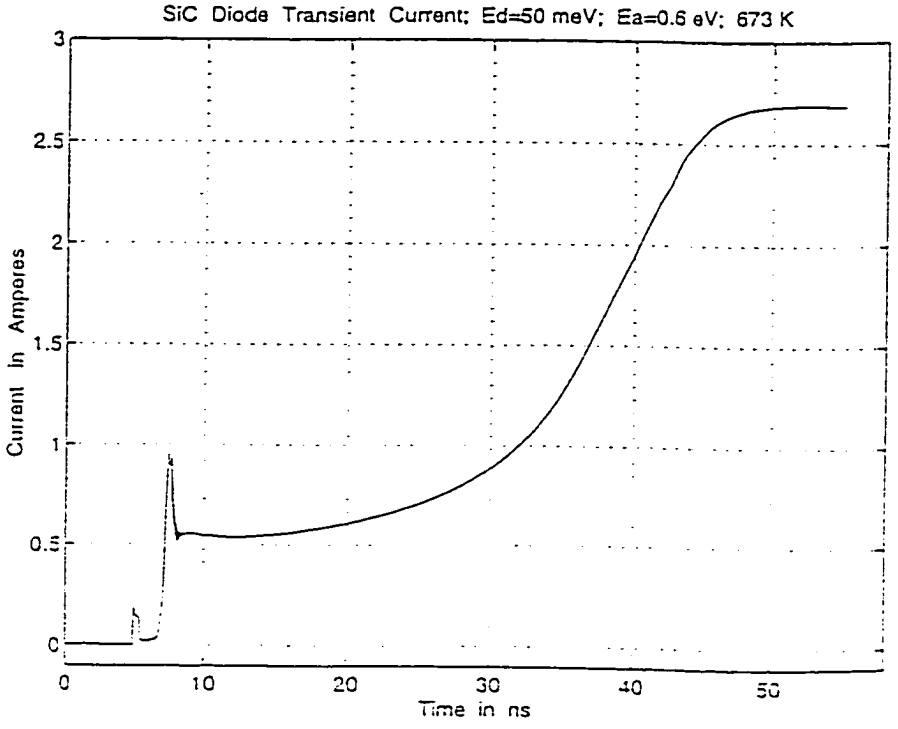

Fig. 4.51 Results of the Transient Diode Current for Case V.

Reproduced with permission of the copyright owner. Further reproduction prohibited without permission.

The overall current in Fig. 4.51 is seen to reach a saturating level of about 2.6 Amperes after about 55 ns. level of about 2.6 Amperes after about 55 ns. The two significant points regarding the simulation results can therefore be made: (i) The device current has been shown to *increase with time in keeping with recent experimental data* [25]. (ii) The rise time obtained here is indeed in the nanosecond range, and roughly coincides with the experimental value of about 100 ns. Our numerical predictions are in very good quantitative agreement with actual data. The experimental devices, however, were believed to have a deep level at about 0.73eV [24,25] instead of the 0.6 eV energy used here. Hence, it is natural to expect the experimental time constant to be slightly higher than that predicted here. (iii) Finally, the spikes in the current transient simulation data of Fig. 4.51 also appear to correlate well with those in the experiments. This suggests that the actual SiC diode probably contained multiple levels which were activate at different times. For instance, only one deep acceptor level at 0.6 eV was considered for case V. However, there could be two or more levels present, such as a deep level at around 0.6-0.7 eV, and another at around 180-240 meV. For such a situation, the current may rise quickly to begin with, and then decrease as the shallow levels quickly released and "lost" all their carriers. The deep level would then take over after the initial transient. (iv) Last, but not least, the present work indicates that the slow rising current waveform may predominantly be due to the slow release of carriers from the deep traps, rather than a result of internal heating. It is quite conceivable though, that internal heating could make a contribution eventually and propel the device towards a "second breakdown."

The internal profiles for case V are discussed next. The electric field shown in Fig. 4.52 at 7.413 ns, appears to have a broader spread than in all of the previous cases. The low density of holes in the p-region creates higher fields as most of the applied voltage in dropped across this low conductivity region. Most of the N^- region has a low field except for the left contact which is similarly deficient of mobile carriers. Fig. 4.53 for the electron profile, shows drift towards the anode and gradual sweep-out. Hole concentrations of Fig.

Reproduced with permission of the copyright owner. Further reproduction prohibited without permission.

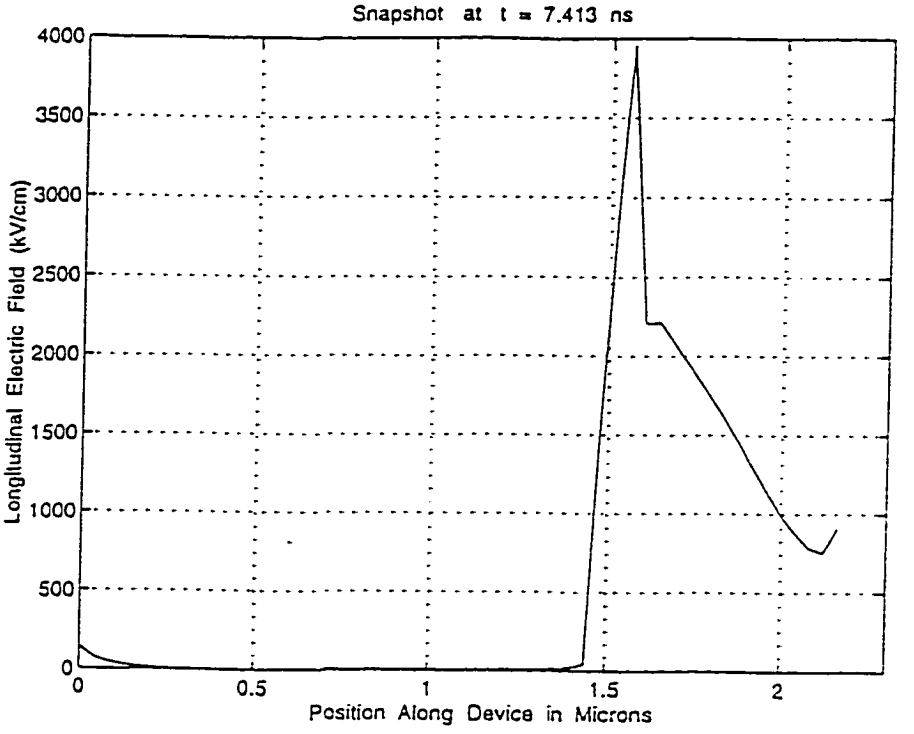

Fig. 4.52 The Internal Electric Field Profile at 7.413 ns

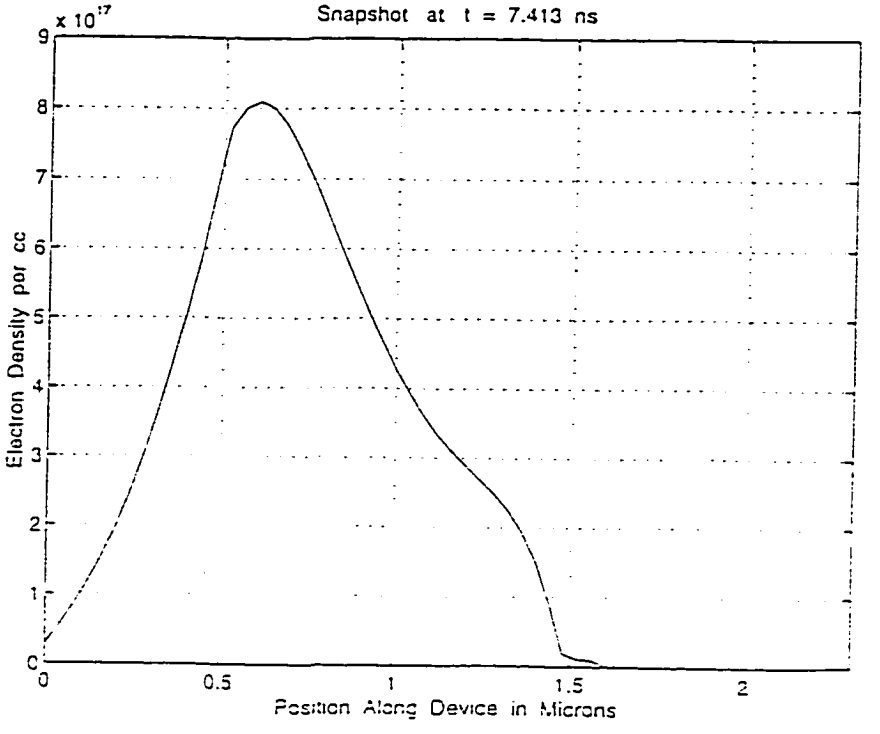

Fig. 4.53 Spatial Distribution of the Electron Density at 7.413 ns

Reproduced with permission of the copyright owner. Further reproduction prohibited without permission.

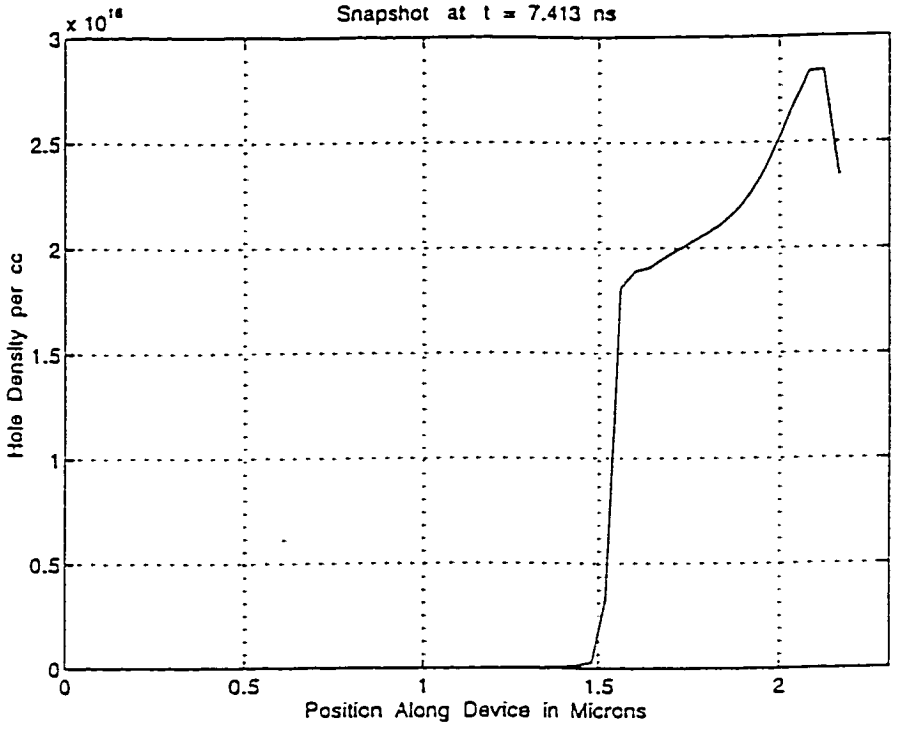

Fig. 4.54 Hole Profile for Case V at 7.143 ns

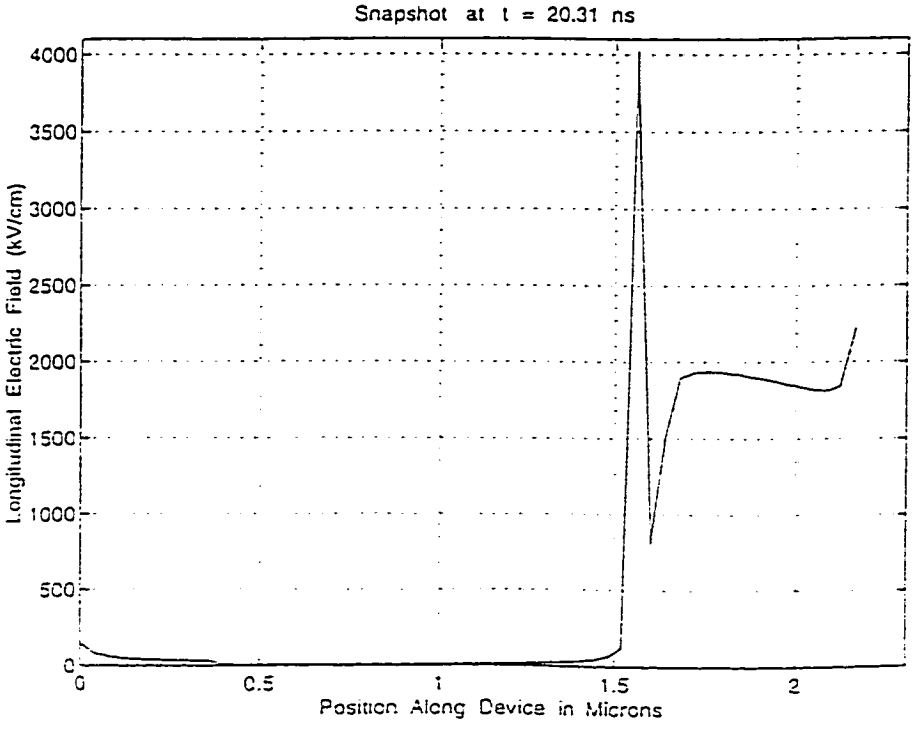

Fig. 4.55 Device Electric Field Distribution at 20.31 ns

Reproduced with permission of the copyright owner. Further reproduction prohibited without permission.

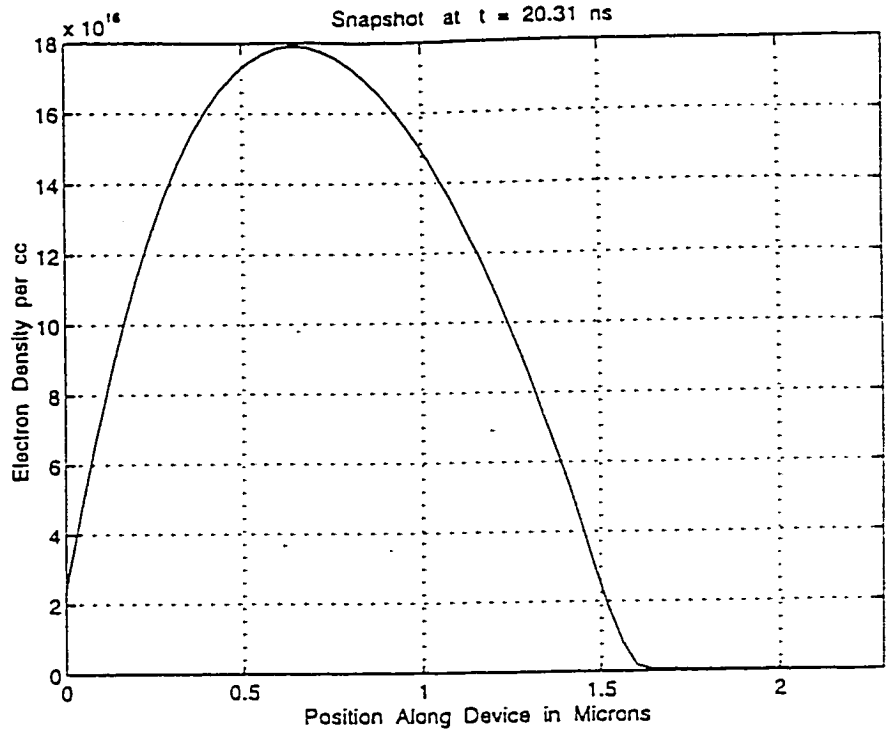

Fig. 4.56 Snapshot of the Electron Profile at 20.31 ns

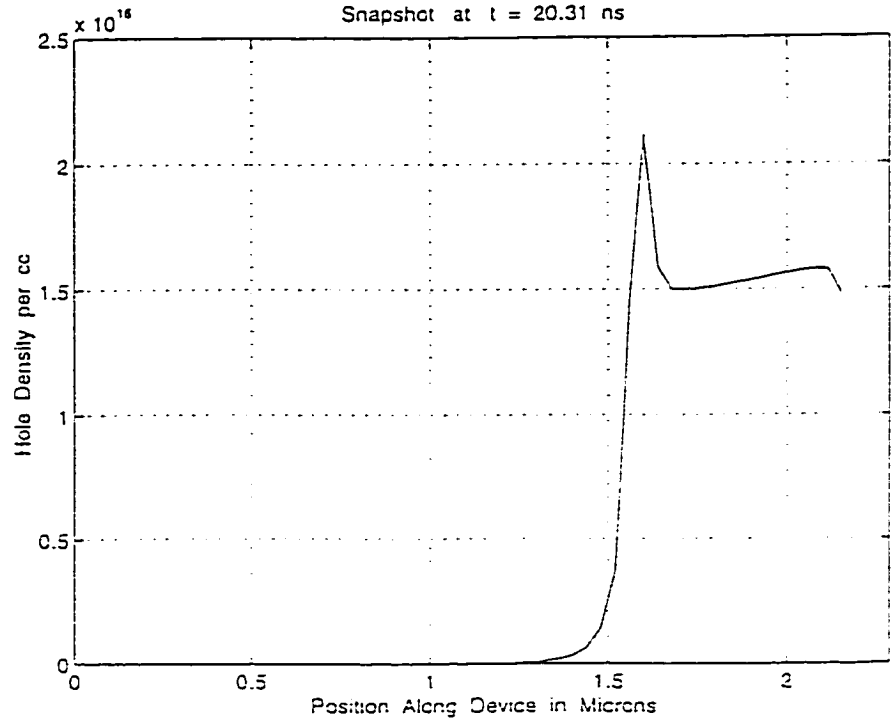

Fig. 4.57 Results for the Spatial Hole Profile at 20.31 ns

Reproduced with permission of the copyright owner. Further reproduction prohibited without permission.

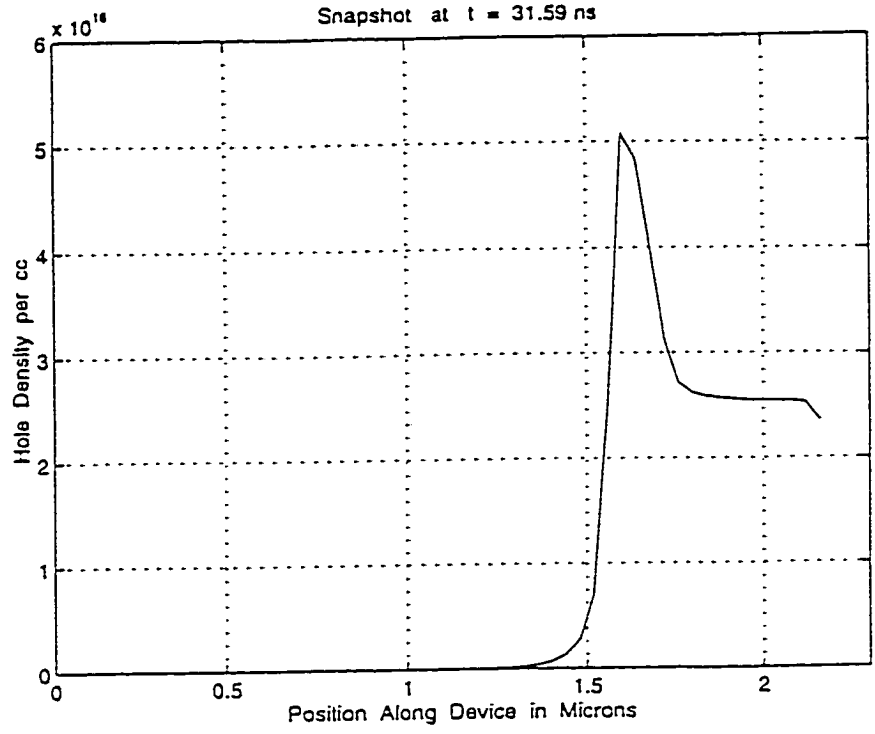

Fig. 4.58 Hole Density Profile at 31.59 ns

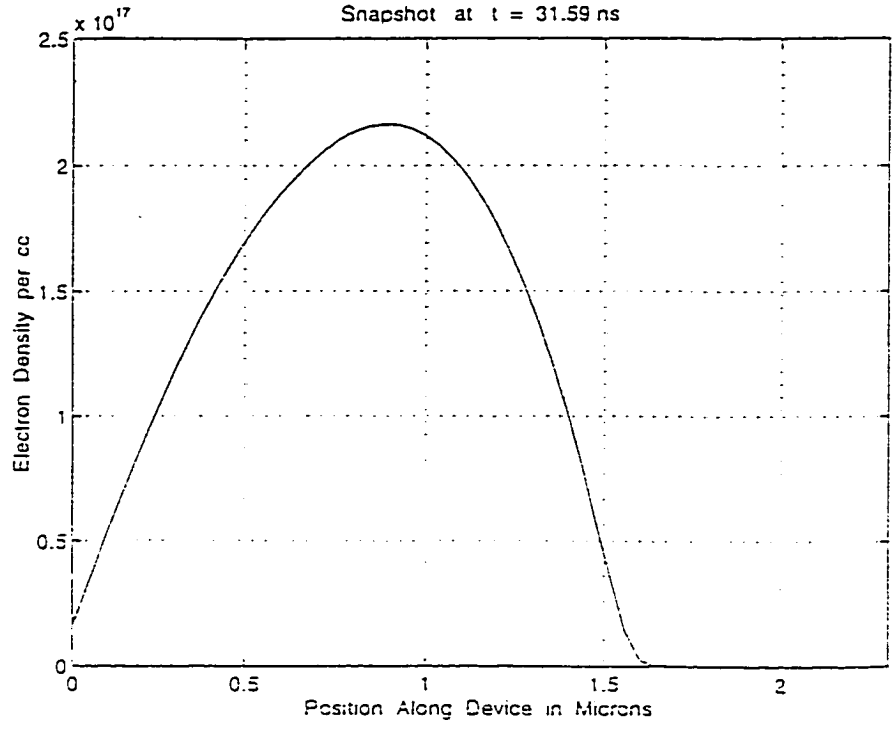

Fig. 4.59 Electron Distribution at 31.59 ns

Reproduced with permission of the copyright owner. Further reproduction prohibited without permission.

4.54 show a similar decrease in density and a shift towards the cathode on the right. The snapshots at time 20.31 ns show most of the evolution to be occurring within the p-region. The plot of Fig. 4.55 shows the electric field to be building up at the cathode boundary as mobile holes move out of the device. This increase, in part, augments the device drift current. The peak value still occurs at the N-P^- boundary due to the strong depletion region. The electron profile shown in Fig. 4.56 at 20.31 ns continues the outflow with a resulting density decrease. The hole density, on the other hand, is seen to *increase in Fig. 4.57 in the region near the N-P^- junction*, compared to its value at 7.413 ns. Between Figs. 4.54 and 4.57, the hole distribution appears to have shifted its profile from a right-skewed to a left-skewed. Absorption at the cathode boundary, coupled with generation in the depletion region surrounding the N-P^- boundary through the unionized acceptor emission process, causes this profile alteration. This process of gradual hole emission from the deep acceptor state, contributes to an enhanced hole density, as shown in Fig. 4.58. The snapshot of the hole profile at 31.59 ns, indicates a much higher density of holes within the P^- region. A more careful study of Fig. 4.58 shows that hole densities on the N-side of the junction at around 1.4-1.5 μm are non-negligible. Clearly, the emission process from the deep acceptor cannot be responsible for such an effect, since there are no acceptor states on the N-side. The increase, can however, be attributed to impact ionization. The possible role of impact ionization, revealed and discussed in case I, is further accentuated through the electron profile at 31.59 of Fig. 4.59. The peak electron density of 2.2×10^{17} cm^{-3} is higher than the value of about 1.8×10^{17} cm^{-3} at 20.31 ns. The results here thus reveal that the process of impact ionization is governed by electrons rather than holes. This is consistent with expectations based on bandstructure considerations, as the smaller effective mass would favor the electrons to gain higher energy from the external field as compared to the hole ensemble. This would consequently increase the probability of successful impact ionization. Also, the threshold energy for an electronics initiated process would be lower than that for

Reproduced with permission of the copyright owner. Further reproduction prohibited without permission.

holes, again based on the disparity between the effective masses.

In this simulation study, the emergence of impact ionization for a deep acceptor level can be understood in terms of the following reasoning. The density of holes is reduced with a deeper level, as the material tends towards a more "intrinsic" specimen. Consequently, the population of minority electrons on the p-side increases. Now impact ionization not only demands the presence of high fields exceeding the threshold value, but also requires the existence of mobile carriers to initiate the process. The high field is always present at or near the N-P^- junction as has ben shown here. However, with deep levels, the density of minority electrons on the P-side is orders of magnitude higher than for the case of shallow acceptors. Consequently, as the minority electrons go past the high fields near the junction, a substantial contribution to the magnitude of impact ionization can occur. Clearly, holes do not play a significant part in impact ionization, since their concentration is actually lowered with a deeper level. Besides, holes in the P^--side would tend to be moving towards the cathode on the right, and *hence in the wrong direction from the high-field region*. Finally, it must be pointed out, the only possible hole assisted impact ionization can occur as a result of minority holes crossing the N-P^- boundary from the N-side. However, the simulation results for cases I-IV have clearly shown the lack of strong impact ionization. This confirms that the electron initiated impact ionization is the dominant process, and will tend to occur in p-regions having deep levels because of an increased minority electron density.

4.4 TWO-DIMENSIONAL RESULTS AND CONTACT INJECTION EFFECTS

Results from two dimensional (2D), time-dependent simulations are presented next. Going to the higher dimension permits detailed probes into effects associated with geometry, shape and size. For example, implicit in the 1D analyses so far, was the assumption that the current flow inside the device is uniform. However, in general, neither the electric field distribution nor that current flow would be uniform, but would depend on the specific

Reproduced with permission of the copyright owner. Further reproduction prohibited without permission.

geometry and contact placement. Sharp, small contacts are expected to enhance local fields, while smoother, bigger geometries should decrease spatial non-uniformities. Some of these geometric effects are studied here and the results discussed through numerical simulations.

4.4.1 FINITE SIZE EFFECTS ON ELECTRIC FIELD DISTRIBUTION

The main focus here is to examine 2D effects on the high voltage current conduction in SiC. The results should be useful for device optimization, and scaling up the voltage hold-off capability of SiC material. For simplicity, a simple metal-SiC-metal (MSM) device structure has been assumed here. Thus, relative to the work described in the previous sections, the n- and p-doped regions were removed to leave only the metallic contacts on the SiC. A 50 Ohm resistance was included in series with the battery. The SiC bulk was assumed to have a square cross-sectional geometry of sides 0.6 μm with contacts lying diagonally across the top and bottom faces. Such a diagonal arrangement was chosen as it maximizes the distance between the anode and the cathode, which is expected to reduce the magnitude of the internal electric fields. This reduction should allow for a higher voltage capability. The 0.6 μm thickness was chosen since is exactly corresponds to that of the intrinsic SiC layer of the NASA Lewis devices.

Results of the 2D electric field distribution for a 120 Volt bias obtained from the time dependent drift-diffusion simulations are shown in Figs. 4.60-4.61. Two different contact lengths were used to probe finite size effects on the field distribution. One was chosen to have a 0.3 μm length to cover half the top and bottom faces, and the other covered 25 percent of the device length. These simulations were carried out at 673 K until 20 ns, a time period sufficiently long for a steady state current value to be reached. A negligible current in the micro-Ampere range was seen to result with negligible space-charge effects inside the semiconductor. The simulation results demonstrate that the 120 Volt bias is below the breakdown threshold, in keeping with experimental observations at NASA Lewis. Due to the

Reproduced with permission of the copyright owner. Further reproduction prohibited without permission.

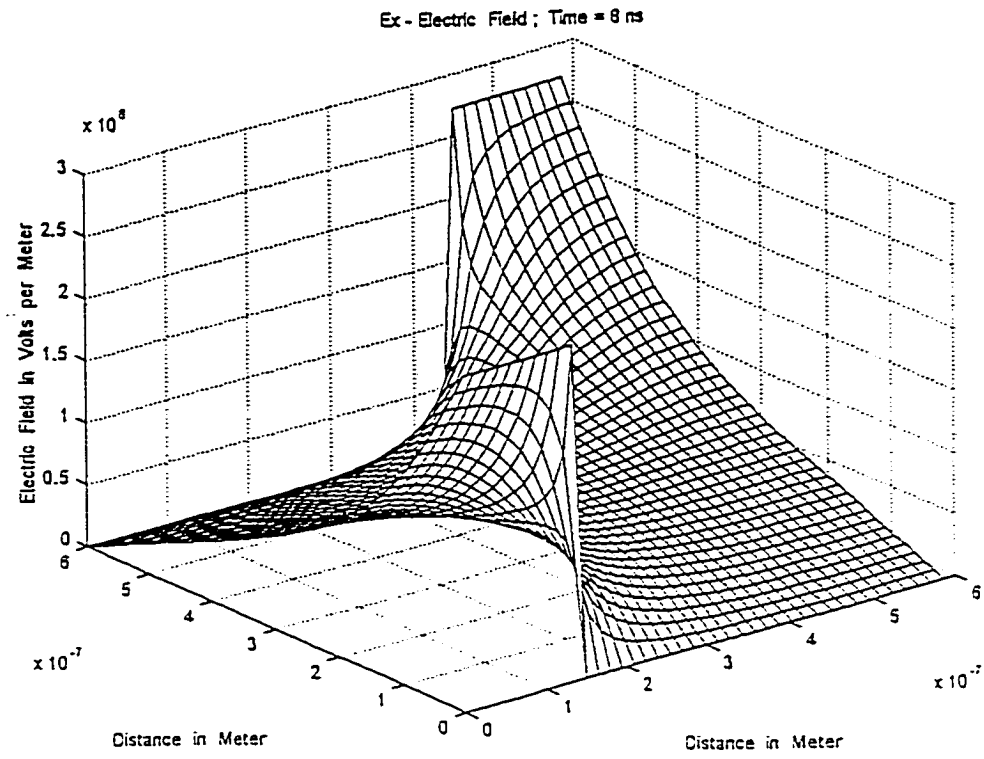

Fig. 4.60(a) The electric field E_x distribution for the smaller contact geometry.

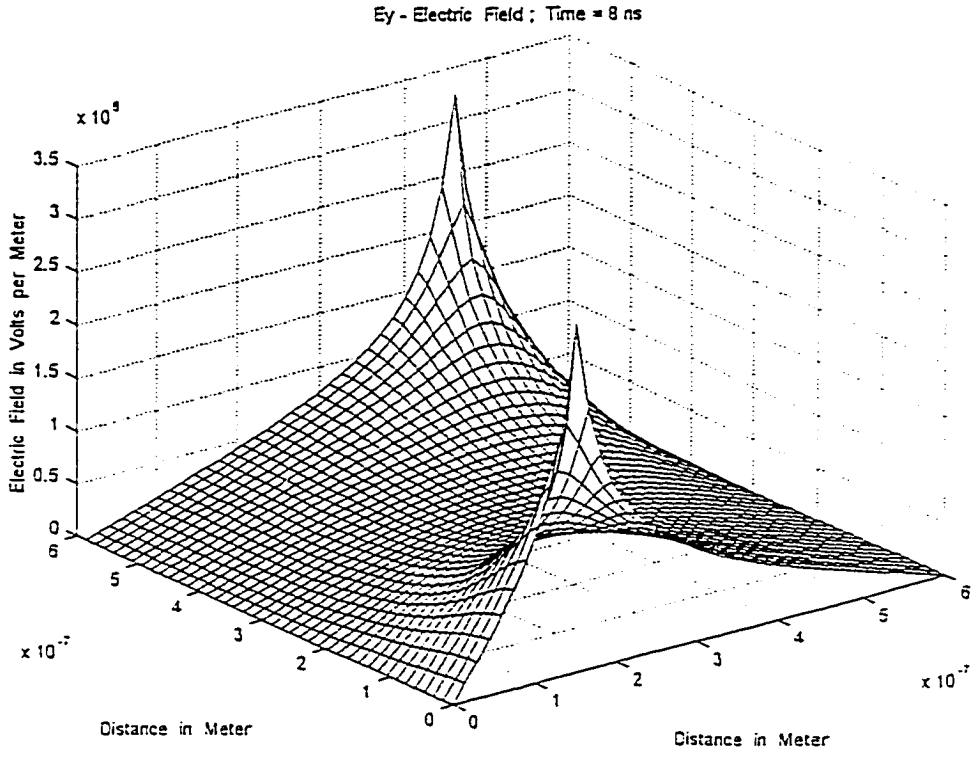

Fig. 4.60(b) The electric field E_y distribution for the smaller contact geometry.

Reproduced with permission of the copyright owner. Further reproduction prohibited without permission.

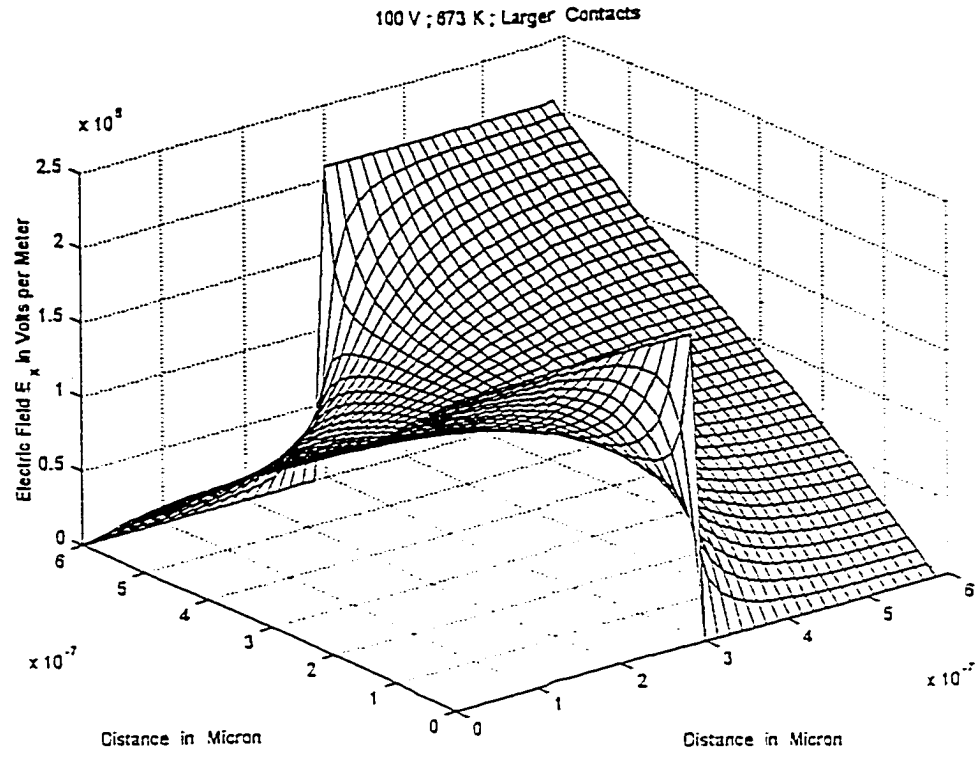

Fig. 4.61(a) The electric field E_x distribution for the larger contact geometry.

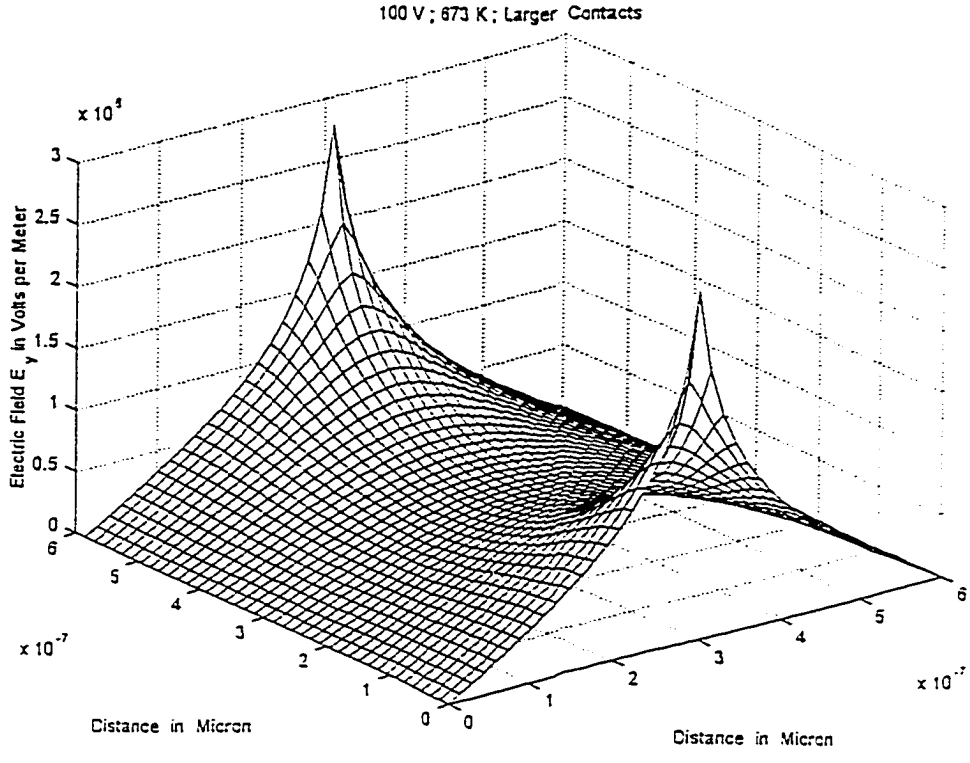

Fig. 4.61(b) The electric field E_y distribution for the larger contact geometry.

Reproduced with permission of the copyright owner. Further reproduction prohibited without permission.

negligible space charge effects, the electric field profiles of Fig. 4.60-4.61 roughly correspond to an electrostatic Laplace solution. The x-field pattern Fig. 4.60(a) for the smaller contacts shows a peak value of about 2.8 MV/cm. The field is mostly concentrated near the two contacts, and is negligible in the two remaining corners on opposite sides. This clearly shows that under a high voltage bias, regions at the contacts would be most likely to fail due to breakdown. The fields along the y-axis for this smaller contact geometry shown in Fig. 4.60(b) show two prominent "spikes." These occur at ends of the contacts and are similar to the field enhancements expected at a sharp boundary. By comparison, the E_x profile for the longer contact in Fig. 4.61(a) is more homogeneous with a lower peak value at 2.2 mV/cm. The y-component peak is also similarly smaller. The important conclusions that follow from these results are : (I) The geometric shape and size of the contacts strongly affect internal field distributions. (II) The field values can be much larger at the contacts than the other areas of the semiconductor bulk. (III) The largest potential for damage appears to be at the contacts. Since carrier tunneling at the contacts is exponentially dependent on the electric-field, a high value would have a significant impact on the stability. Large injection via tunneling could lead to device failures. Also, impact ionization due to the high fields is likely to occur near the contacts.

4.4.2 CURRENT BEHAVIOR IN ABSENCE OF CONTACT TUNNELING

Results of two dimensional analyses for the time dependent current response in the MSM structure are presented next. High external voltages with a 1 ns ramping times were assumed, in keeping with available experiments. For simplicity, the contact tunneling mechanism was deliberately neglected. In the next section, results that include the tunneling process will be presented and compared to this data. In this process, differences between the two situations will be brought out more clearly, and will underscore the role of tunnel injection in the context of high voltage operation.

Reproduced with permission of the copyright owner. Further reproduction prohibited without permission.

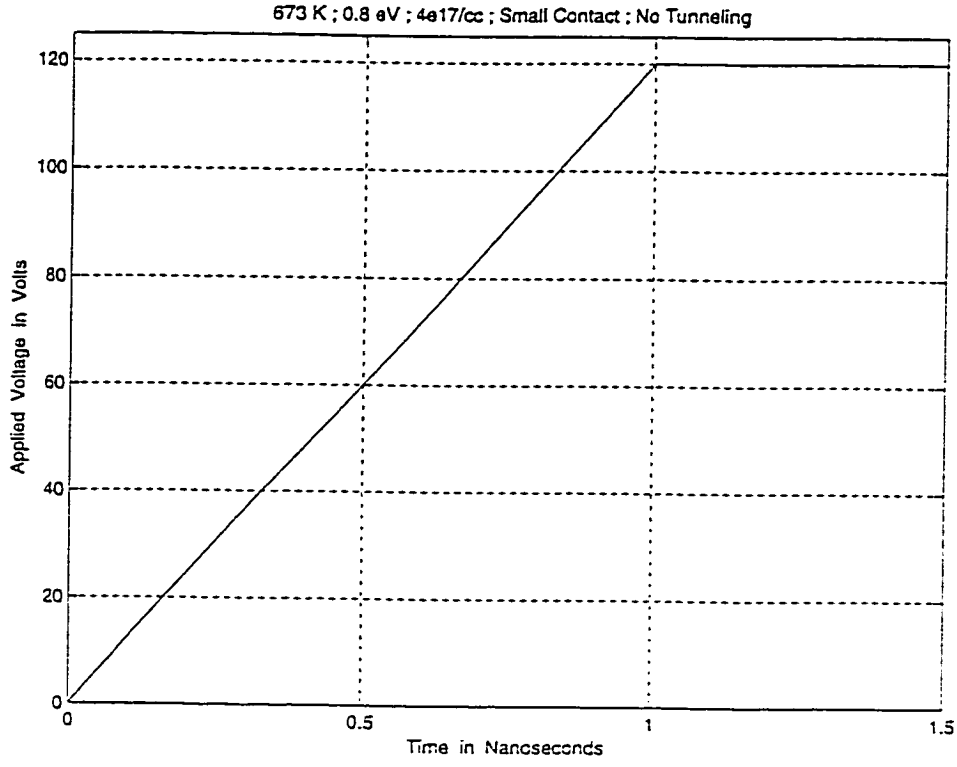

Fig. 4.62(a) Applied voltage waveform at 673 K for the small contact 0.8 eV trap case.

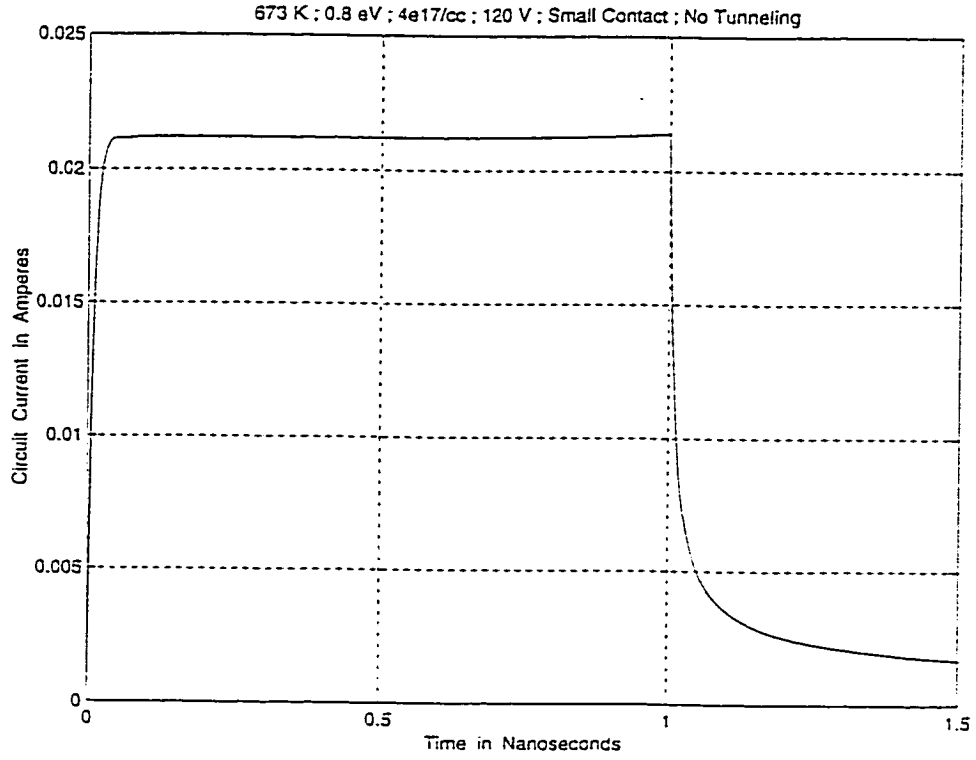

Fig. 4.62(b) Circuit current response at 673 K for the small contact 0.8 eV trap case.

Reproduced with permission of the copyright owner. Further reproduction prohibited without permission.

The 120 Volt external biasing waveform applied to the SiC MSM device in series with the 50 Ohm resistance is shown in Fig. 4.62(a). The simulations were carried out for the small contact geometry of Figs, 4. 60. The trap density was 4 x 10^{17} cm^{-3} at an energy of 0.8 eV, while the donor concentration was chosen to be 2 x 10^{17} cm^{-3}. The resulting current is shown in Fig. 4.62(b). A maximum value of about 22 mA is predicted, and three features are apparent. (A) First, the current is mainly due to the displacement component that exists as long as the external bias is increasing. The displacement current helps build the internal electric fields. As soon as the voltage is held steady at 120 V beyond 1.0 ns, the current begins to decrease monotonically. (B) Second, a slight increase can be detected between 0.5 ns and 1.0 ns. This is due to the gradual trap emptying process which provides additional free carriers to the system. (C) The 120 V bias is insufficient to cause internal breakdown, and the current is seen to decay well into the micro-Ampere range.

At a higher voltage value of 135 V, the MSM structure was observed to be at the threshold of breakdown. The voltage waveform is shown in Fig. 4.63(a), and the current in 4.63(b). The current peak at 24 mA is slightly higher than Fig. 4.62(b) due to higher drift velocity. Though the current decays beyond 1.0 ns, it levels off about 1.35 ns and then exhibits a slow increase. The difference between Figs. 4.62(b) and 4.63(b) is simply in the applied voltage values. Hence, the differing current responses could only be due to internal impact ionization, since the field dependent contact injection mechanism was turned off in these simulations. It also is obvious that the 135 V bias is just beyond the critical breakdown voltage, and the device currents would slowly begin to increase well beyond 1.5 ns. The rather slow rate of current increase beyond 1.35 ns is influenced by the following factors: (I) The relatively small drift velocities v_{dre} and v_{drh}, at this high temperature which lowers the impact ionization term. The impact ionization rate is directly proportional to v_{dr}. (II) The large density (4 x 10^{17} cm^{-3}) of traps assumed in the simulations. With a donor density of 2 x 10^{17} cm^{-3}, only 50 per cent of the traps are filled. This large availability of unfilled trap

Reproduced with permission of the copyright owner. Further reproduction prohibited without permission.

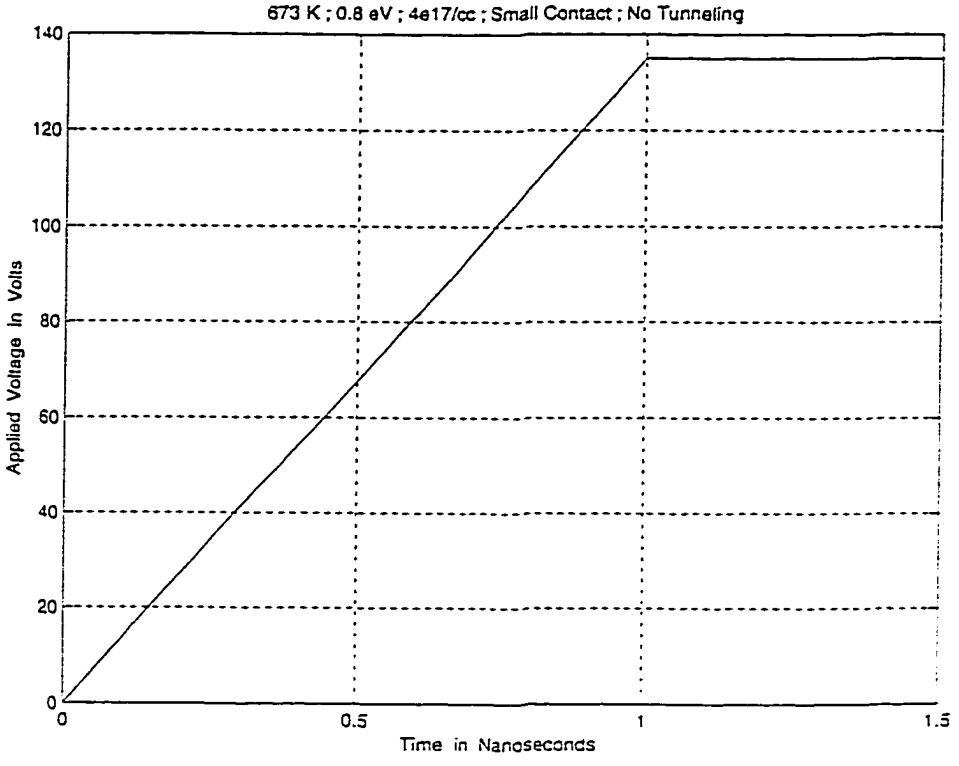

Fig. 4.63(a) Applied voltage waveform at 673 K for the small contact 0.8 eV trap case.

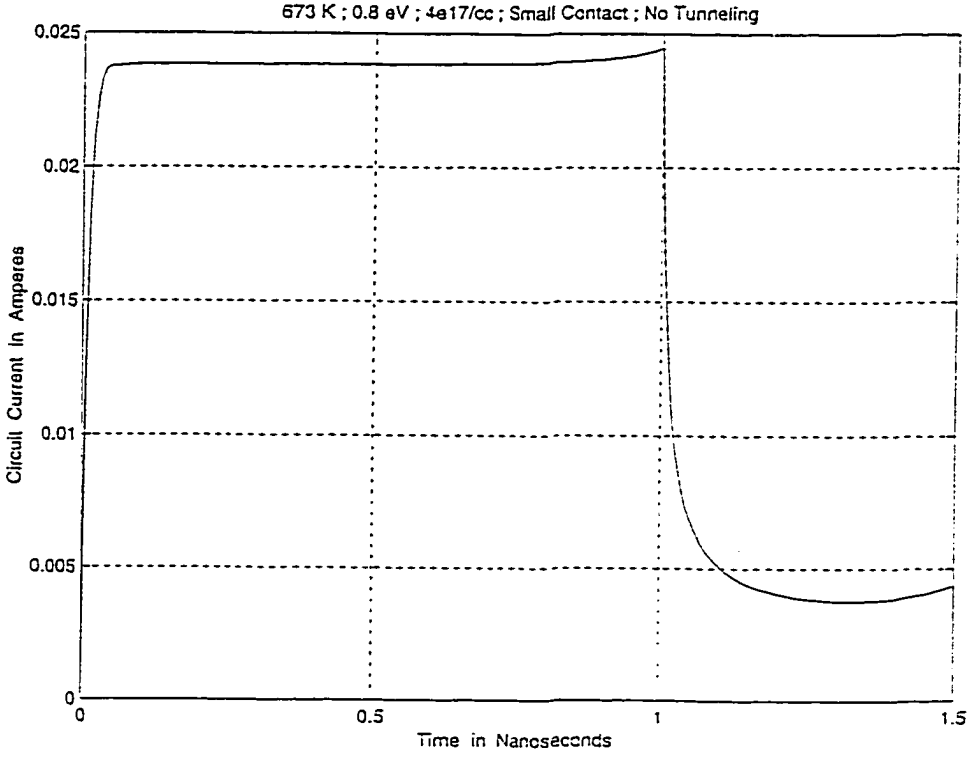

Fig. 4.63(b) Circuit current response at 673 K for the small contact 0.8 eV trap case.

Reproduced with permission of the copyright owner. Further reproduction prohibited without permission.

centers provides a mechanism for continued trapping of the electrons generated through impact ionization. The electron trapping dominates over hole capture due to the larger electron capture cross-section of 10^{-16} cm^{-2}. The cross-section for hole capture was taken to be 10^{-17} cm^{-2}, an order of magnitude lower, in keeping with experimental data.

This breakdown effect is more clearly demonstrated in Figs. 4.64. The voltage waveform is shown in 4.64(a), while the resulting current of Fig. 4.64(b) shoots up beyond a 3.0 Ampere value shortly after the maximum voltage is applied. The 0.2 ns delay between the application of the voltage maxima and the current increase again arises from the internal trap filling. These results which yield breakdown currents in the Ampere range, and threshold values around 135 V are consistent with the NASA experiments.

Similar calculations, without the contact tunneling process, were carried out at 300 K to probe the effects of temperature variation. Figs. 4. 65(a) and 4.65(b) show the 120 V waveform and the corresponding current. Comparing Figs. 4.62(b) and 4.65(b), it becomes clear that the responses are roughly similar, excepting that the current decay beyond 1.0 ns for the lower temperature is significantly faster. This is a two-fold effect associated with electron emission from the 0.8 eV trap, and the temperature dependent carrier drift velocities. At the higher temperature, the emission rate of electrons is significantly higher than at 300 K, which contributes to the gradual conduction current "tail"seen beyond 1.0 ns. Until all of the trapped charges are fully emitted, a continued small current is predicted at 673 K. The rapid fall-off at 300 K represents the rapid sweep out of the mobile electrons with virtually no replenishment via the trap emission. Since the drift velocities are higher at 300 K by almost 50 per cent, the mobile carriers are flushed out from the system faster. In any event, the simulations demonstrate the 120 V bias to be below the breakdown threshold for both temperatures.

At the higher 135 V bias, responses between the 300 K and 673 K temperatures are predicted to be dramatically different. Figs. 4.66(a) and 4.66(b) show the applied voltage and

Reproduced with permission of the copyright owner. Further reproduction prohibited without permission.

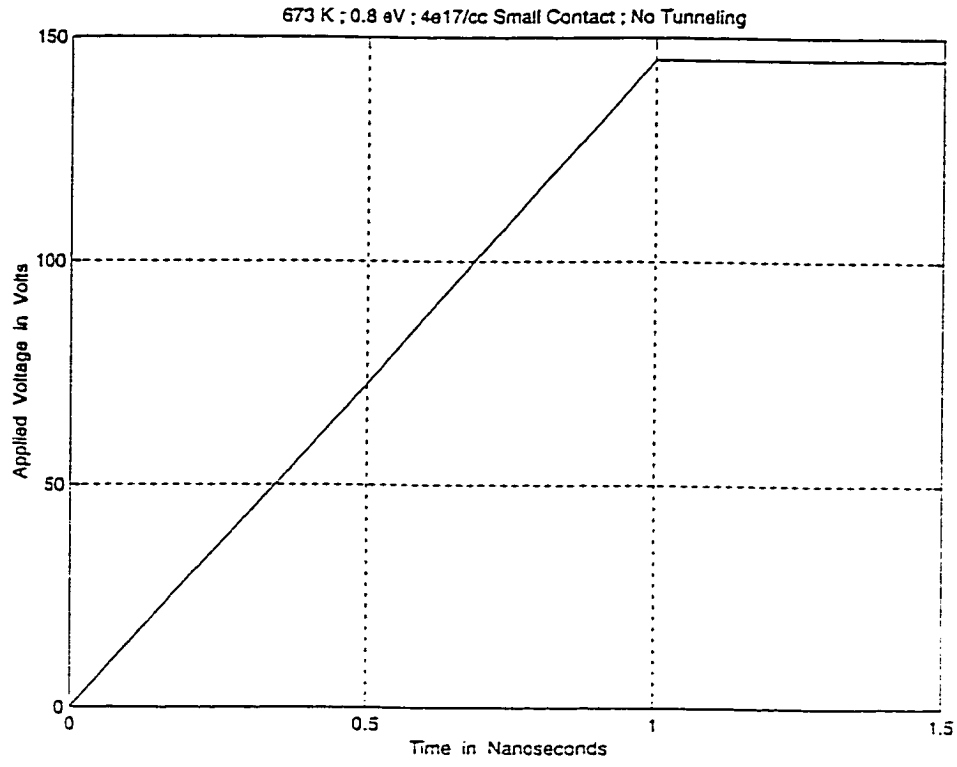

Fig. 4.64(a) Applied voltage waveform at 673 K for the small contact 0.8 eV trap case.

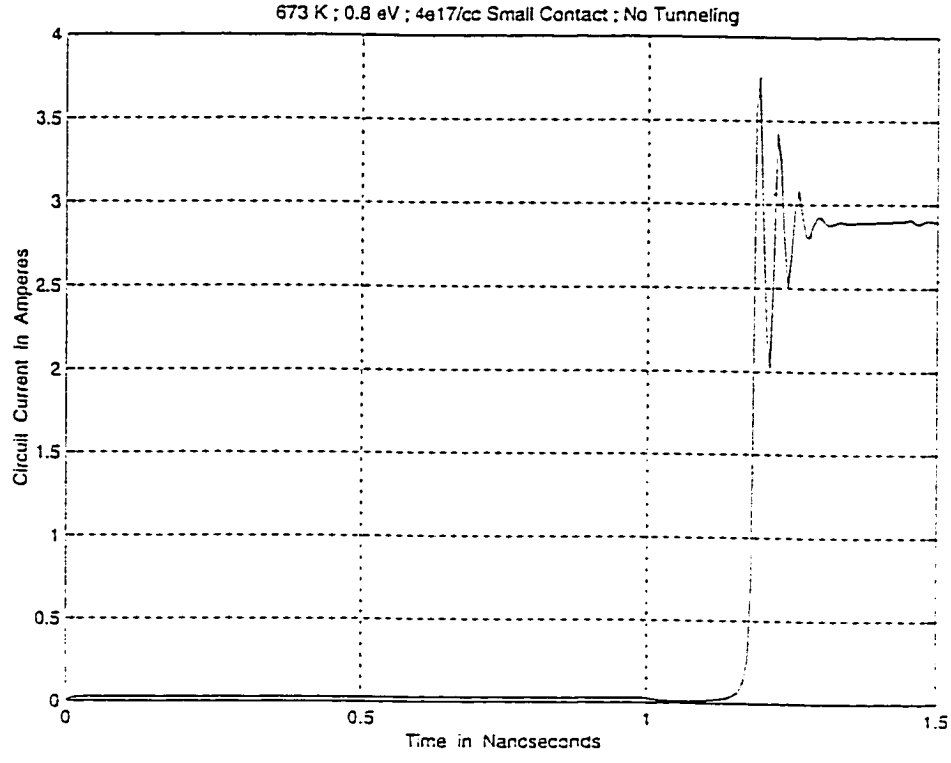

Fig. 4.64(b) Circuit current response at 673 K for the small contact 0.8 eV trap case.

Reproduced with permission of the copyright owner. Further reproduction prohibited without permission.

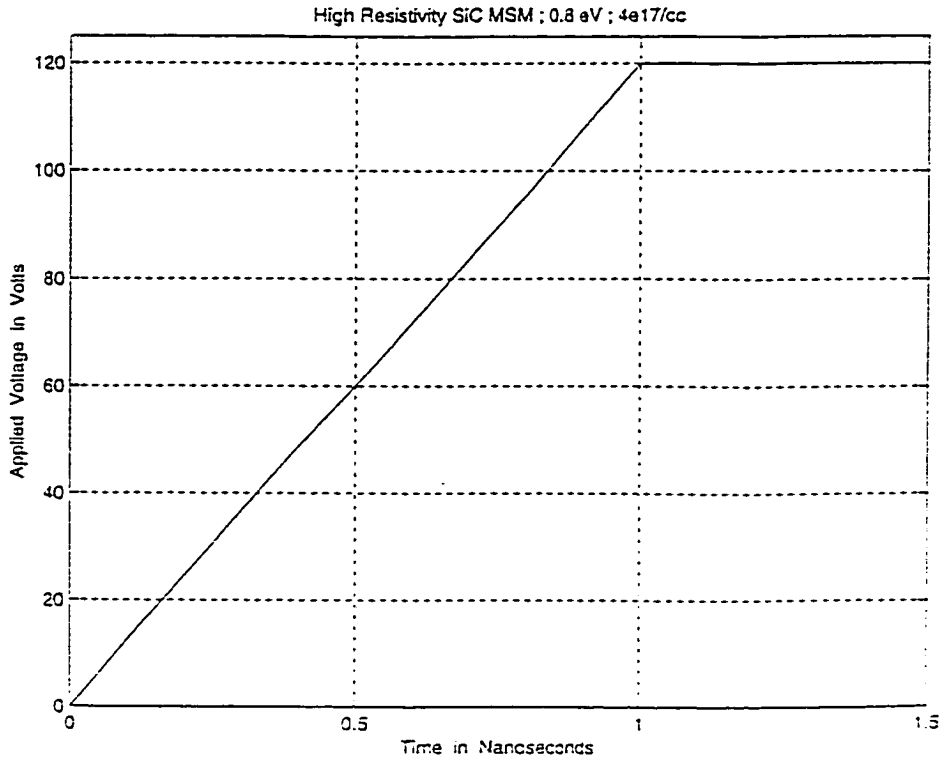

Fig. 4.65(a) Applied voltage waveform at 300 K for the small contact 0.8 eV trap case.

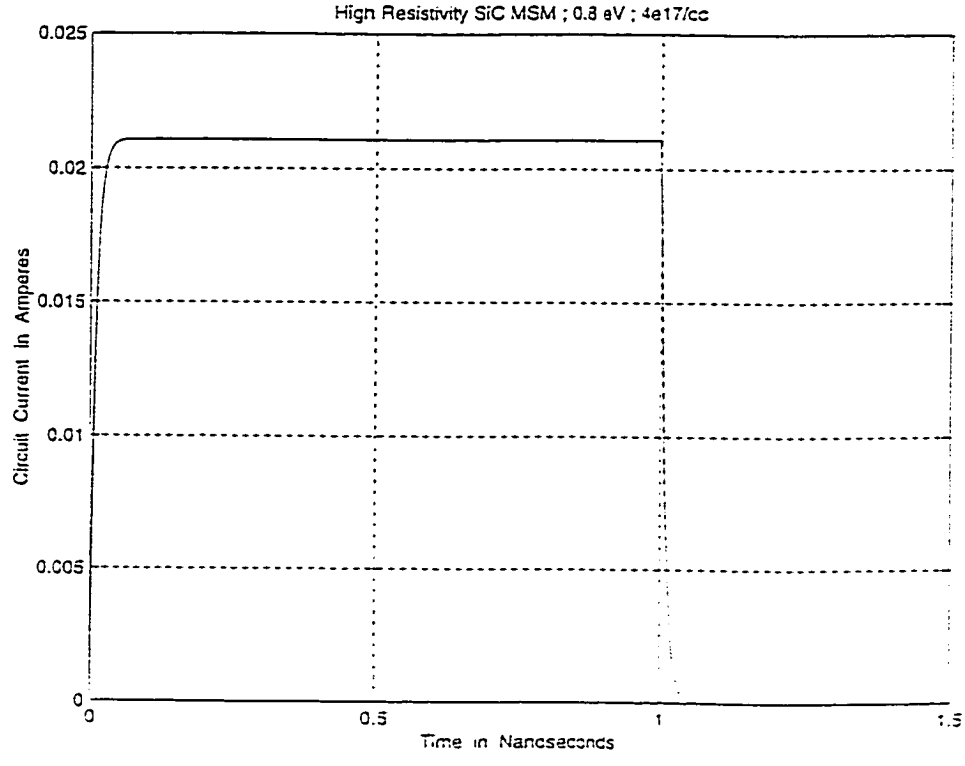

Fig. 4.65(b) Circuit current response at 300 K for the small contact 0.8 eV trap case.

Reproduced with permission of the copyright owner. Further reproduction prohibited without permission.

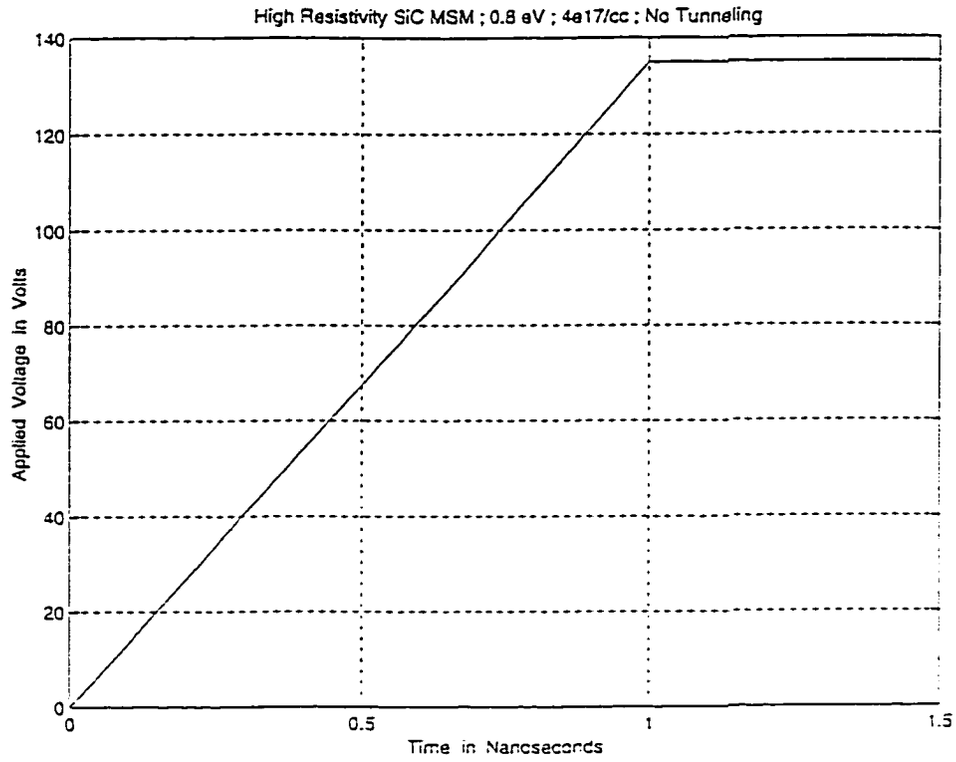

Fig. 4.66(a) Applied voltage waveform at 300 K for the small contact 0.8 eV trap case.

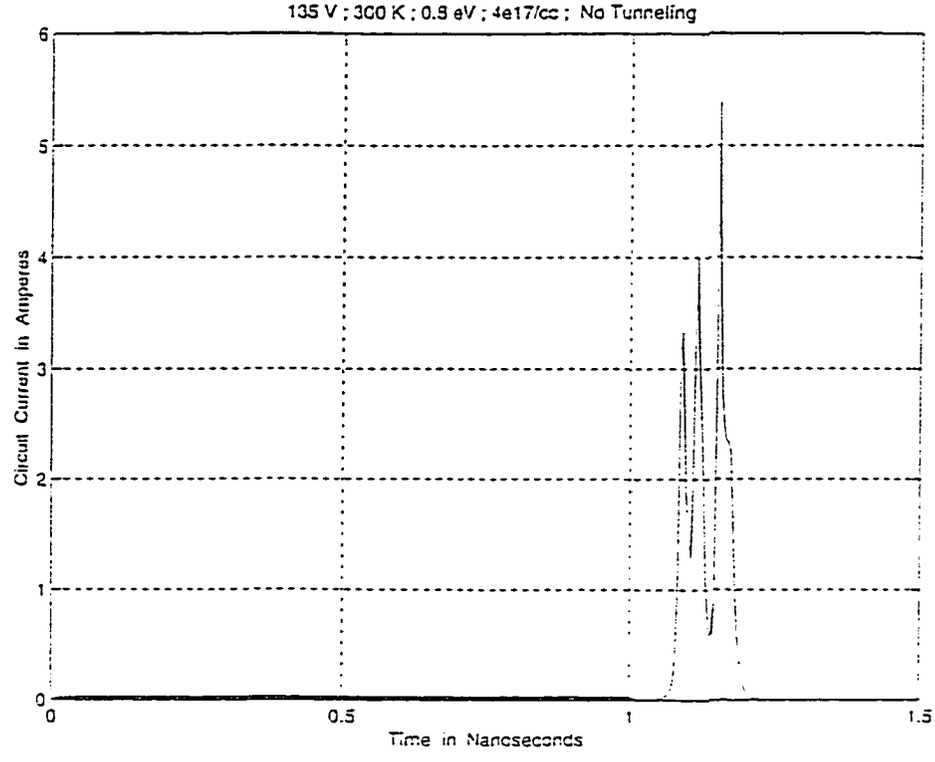

Fig. 4.66(b) Circuit current response at 300 K for the small contact 0.8 eV trap case.

Reproduced with permission of the copyright owner. Further reproduction prohibited without permission.

time dependent circuit current for the 300 K condition. The circuit current up to 1.0 ns is comparable in value to that at 673 K. As the voltage ramp stabilizes to 135 V, the current begins to decay until about 1.08 ns. However, beyond 1.08 ns, a sharp increase in the current followed by an oscillatory response is predicted. Finally, the current decays after about 1.22 ns. This sharp increase in the current arises from internal impact ionization within the bulk SiC. Clearly, the electric fields are large and exceed the ionization threshold. The primary difference in behavior at the two temperatures arises from relative effectiveness of impact ionization, the rate of avalanche growth, and the rate of electron capture into unfilled trap states. At 300 K, both the carrier drift and thermal velocities are higher by about 50 percent. Hence, the impact ionization rate is also correspondingly larger by about 50 percent. Physically, at the lower temperature, the phonon population is smaller leading to weaker carrier-phonon interactions. Hence, the energy loss channel to the phonons is weak at lower temperatures, and a much larger population of high energy carriers can exist. The impact ionization rates are therefore larger, and seed electrons within the bulk SiC quickly lead to a rapid current enhancement. Furthermore, the capture rates which are directly proportional to the thermal velocities, are lower at 300 K. This helps in building up mobile charge more quickly than at 673 K. However, as the field-assisted contact injection mechanism is not considered in these simulations, the supply of mobile charge from the external circuit is minimal. In addition, with increasing current the device voltage drops as a result of the enhanced voltage across the series 50 Ohm resistance. Both of these effects work to quench internal ionization. Consequently, the current is predicted to return to negligible levels as the internal avalanche is flushed out of the system. To this extent then, the potential for instability and rapid current increases is predicted to be higher for the same device at a lower temperature. It is also shown, that with perfect "blocking contacts" such instabilities will not lead to long term breakdown damage.

Finally, to evaluate the role of contact geometry on the current response and

Reproduced with permission of the copyright owner. Further reproduction prohibited without permission.

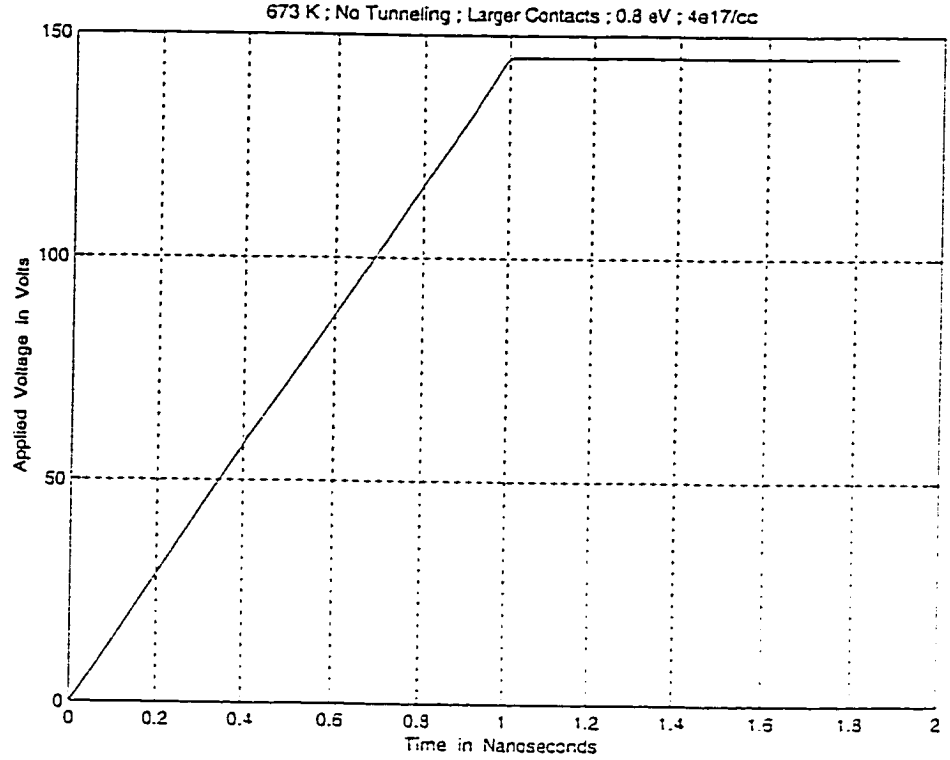

Fig. 4.67(a) Applied voltage waveform at 673 K for the larger contact 0.8 eV trap case.

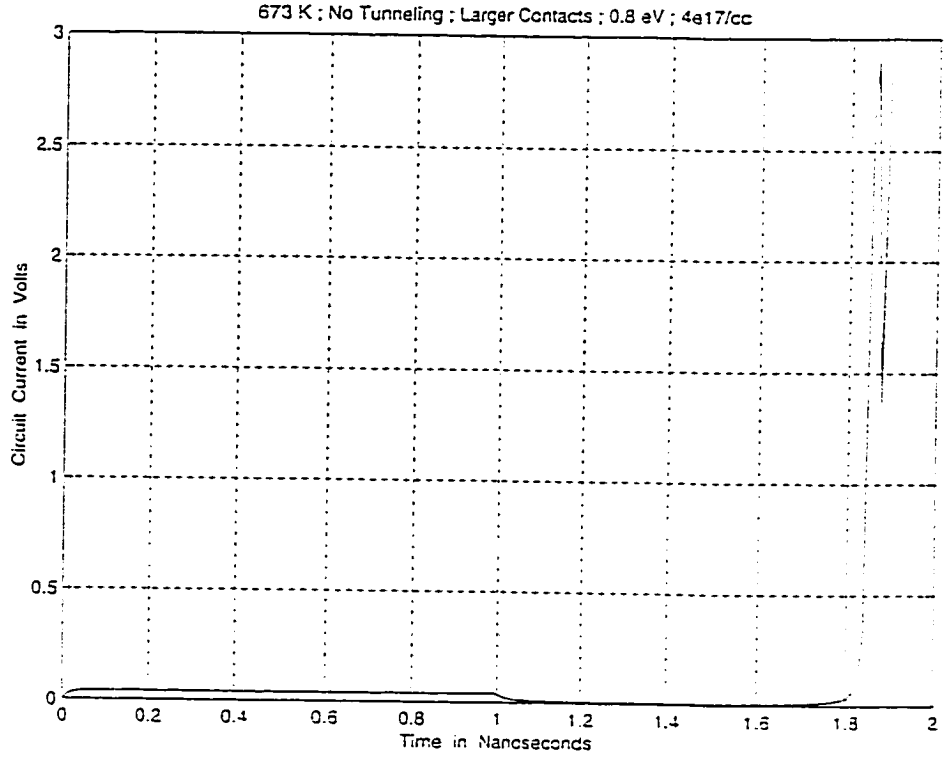

Fig. 4.67(b) Circuit current response at 673 K for the larger contact 0.8 eV trap case.

Reproduced with permission of the copyright owner. Further reproduction prohibited without permission.

breakdown characteristics, simulations were carried out at 673 K for the 145 Volt biasing ramp with larger contacts. A 50 percent contact coverage as considered for Fig.4.61 was assumed. The time dependent voltage and current waveforms are shown in Figs. 4.67. It is evident from the graphs that it takes a relatively long delay of about 0.8 ns for the device current to increase beyond acceptable levels and reach high values. This should be compared with the small contact case shown in Fig. 4.64(b) for which a delay of only 0.2 ns had been predicted. The longer delay simply arises from the lower internal fields which restricts the bulk impact ionization to relatively low levels. From a practical standpoint, it is clear that a larger contact area should be effective in protecting devices and circuits against sudden voltage spikes and short-lived fluctuations. For completeness, the response at 135 Volts with the larger contact geometry is shown in Figs. 4.68. The current of Fig. 4.68(b) should be compared with that of Fig. 4.63(b). Unlike the smaller contact geometry, the current is Fig. 4.68(b) appears to be more stable without any signs of an increase up to 2.5 ns.

4.4.3 CURRENT BEHAVIOR WITH CONTACT TUNNELING

The response of the SiC MSM structures with inclusion of the contact tunneling process is examined next. First, for an 80 Volt bias at 673 K as shown in Fig. 4.69(a), the corresponding circuit current is depicted in Fig. 4.69(b) for the small contact geometry. The current is seen to increase to about 1.6 Ampere with about a 0.2 ns delay after the voltage reaches its maximum value. The device is thus not capable of blocking the 80 Volts, 1.0 ns ramp. This current value of about 1.6 Ampere is in close agreement with the experimental observations of 1.5 Ampere. Clearly, the supply of electrons from the cathode under high field conditions quickly enhances the internal currents and is thus an important mechanism controlling the stability of high voltage operation. Figs. 4.70 show the simulated response to an even higher bias of 100 Volts. Unlike the previous cases, the current is seen to rise dramatically even *before* the end of the 1.0 ns voltage ramp. Clearly, at about an 80 V bias,

Reproduced with permission of the copyright owner. Further reproduction prohibited without permission.

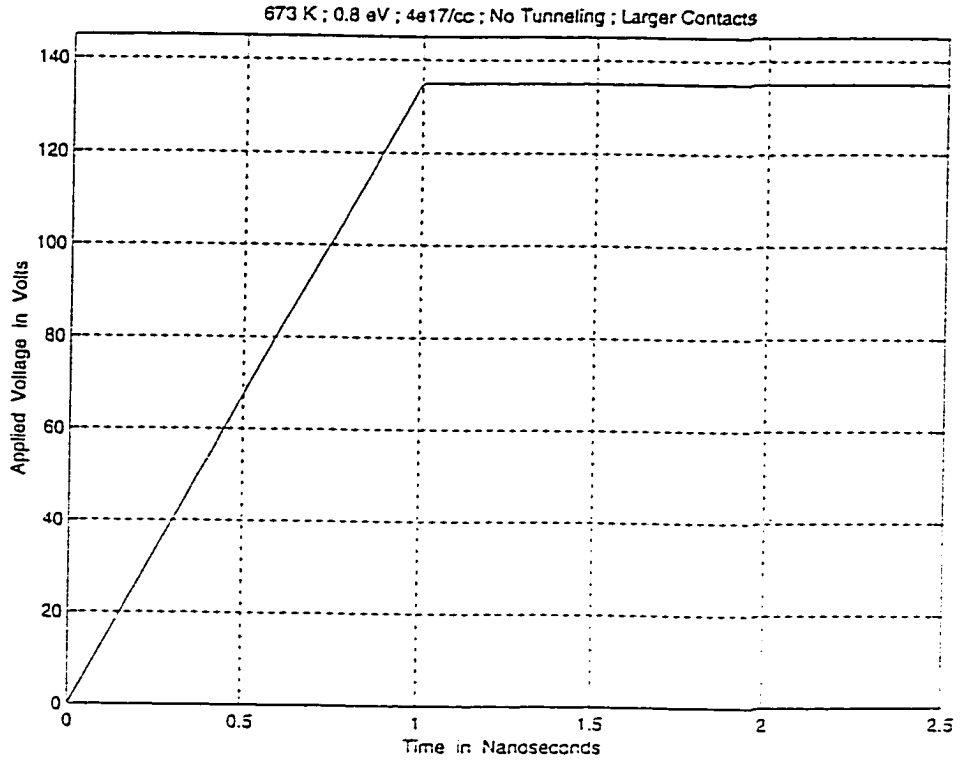

Fig. 4.68(a) Applied voltage waveform at 673 K for the larger contact 0.8 eV trap case.

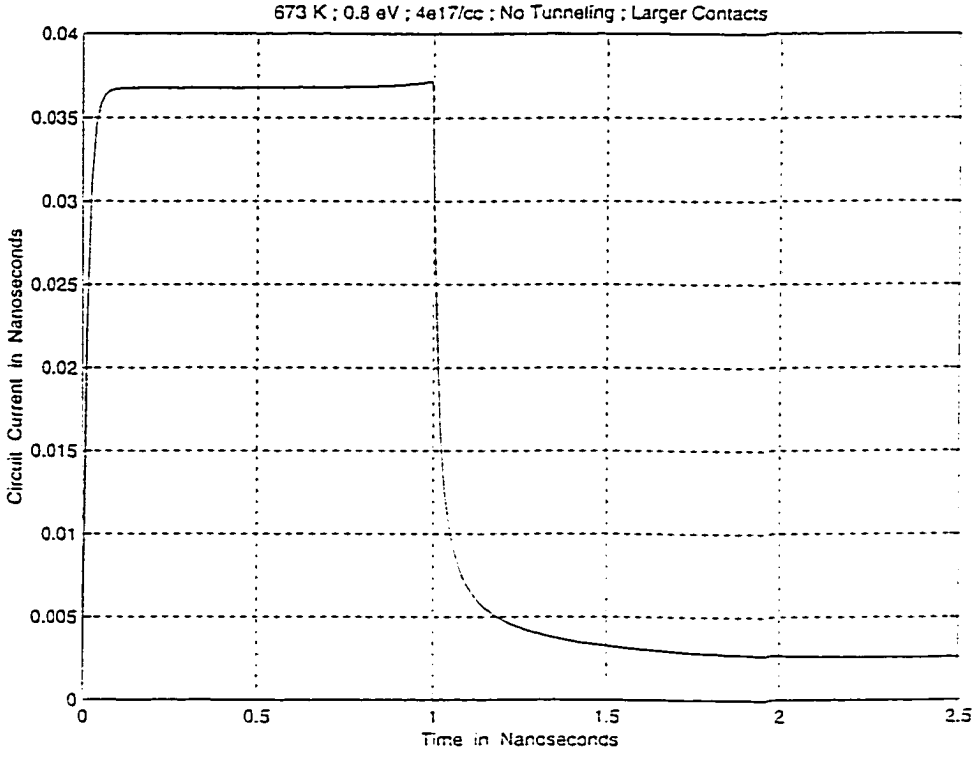

Fig. 4.68(b) Circuit current response at 673 K for the larger contact 0.8 eV trap case.

Reproduced with permission of the copyright owner. Further reproduction prohibited without permission.

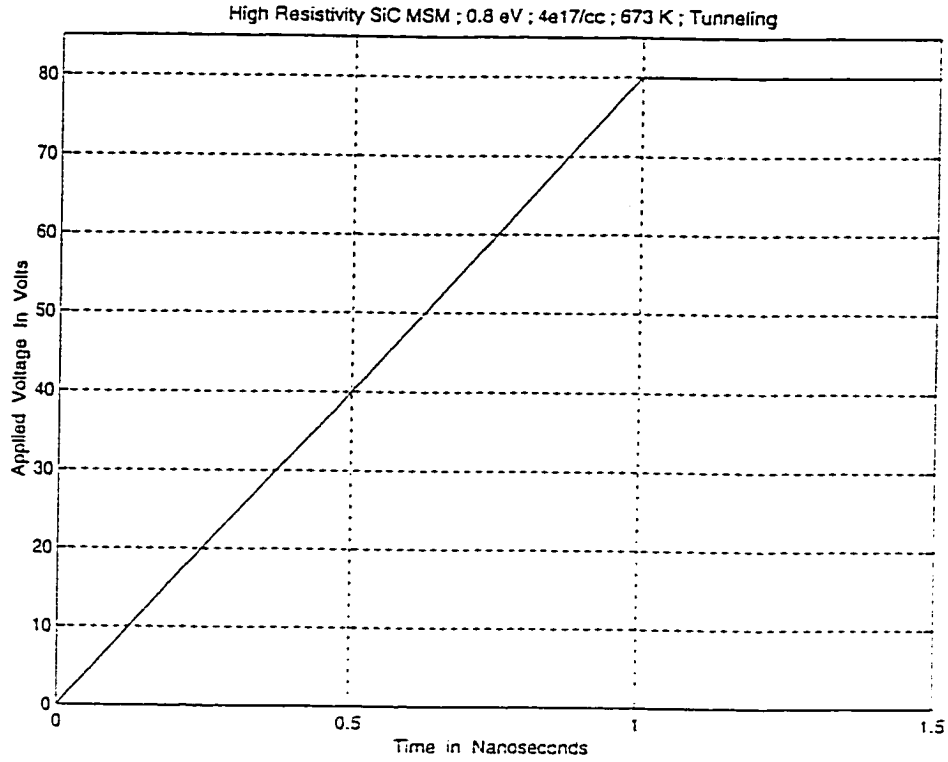

Fig. 4.69(a) Applied voltage at 673 K for small contact 0.8 eV trap case with tunneling.

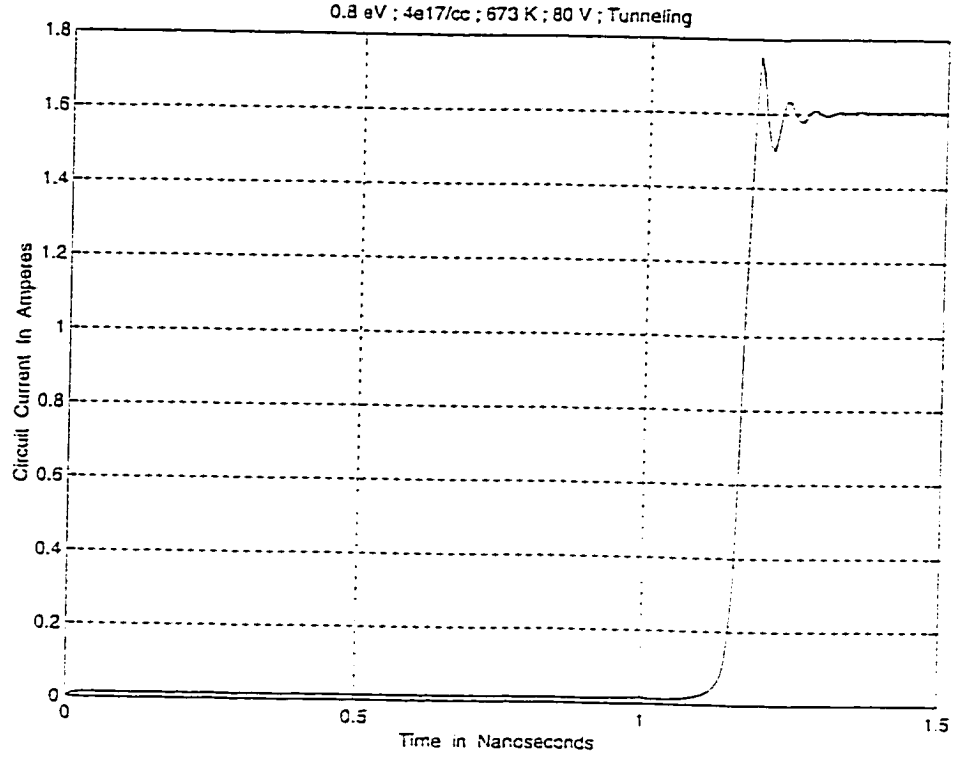

Fig. 4.69(b) Circuit current at 673 K for small contact 0.8 eV trap case with tunneling.

Reproduced with permission of the copyright owner. Further reproduction prohibited without permission.

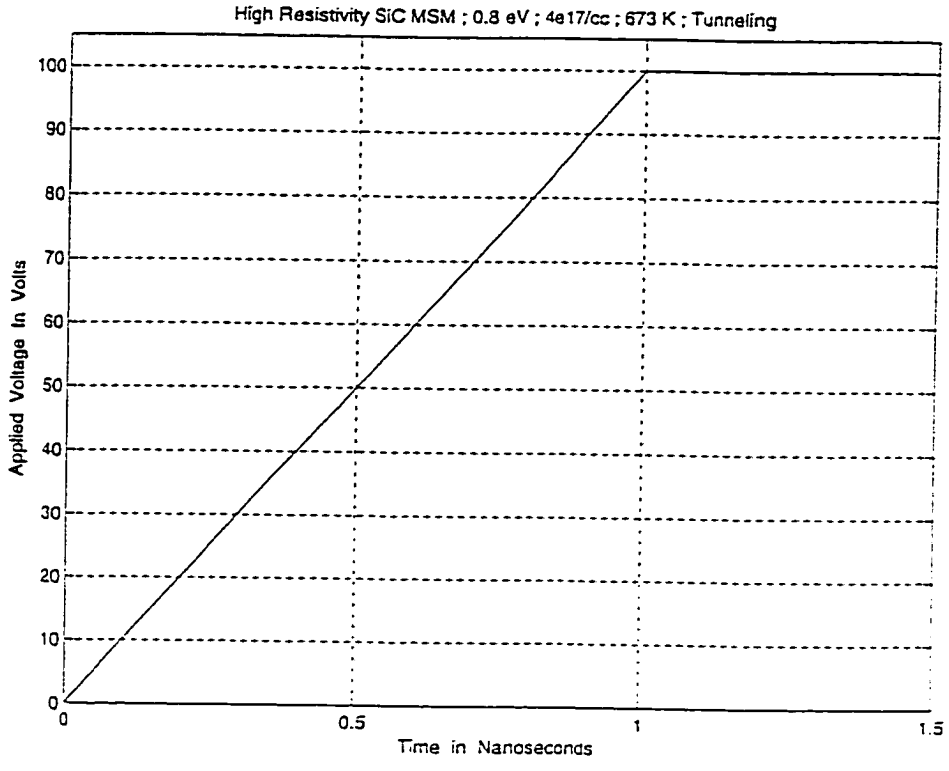

Fig. 4.70(a) Applied voltage at 673 K for small contact 0.8 eV trap case with tunneling.

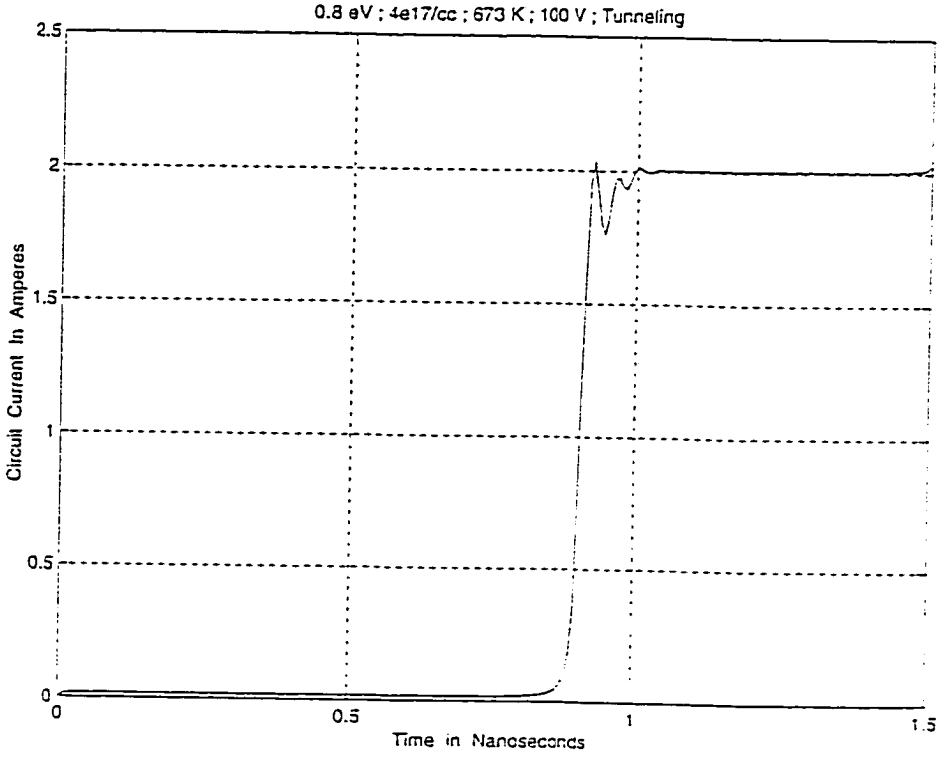

Fig. 4.70(b) Circuit current at 673 K for small contact 0.8 eV trap case with tunneling.

Reproduced with permission of the copyright owner. Further reproduction prohibited without permission.

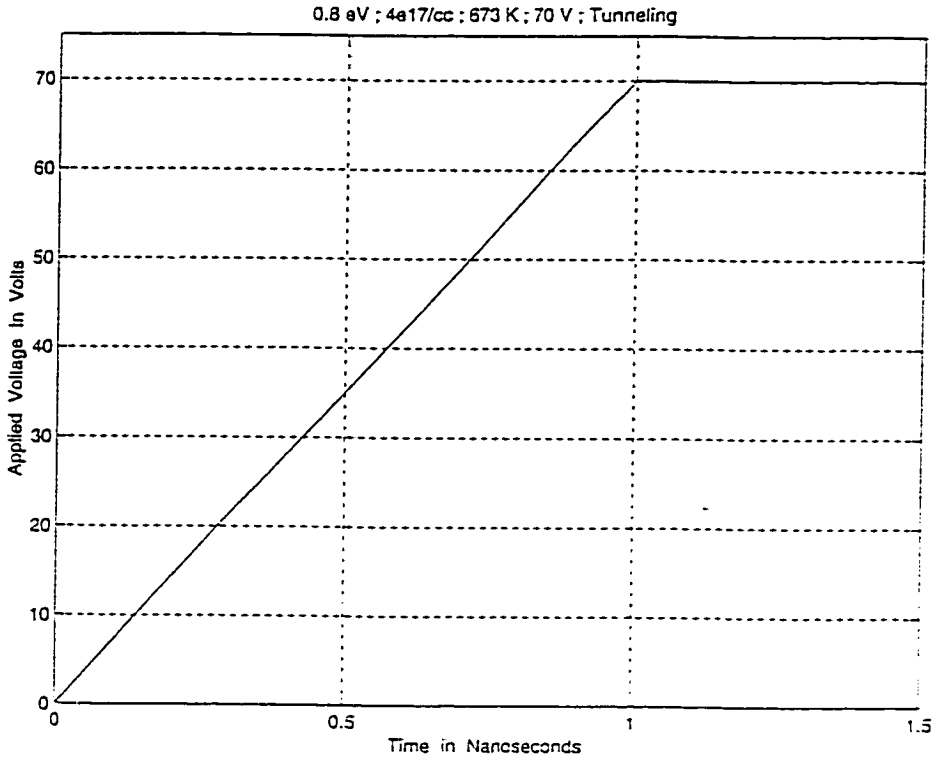

Fig. 4.71(a) Applied voltage at 673 K for small contact 0.8 eV trap case with tunneling.

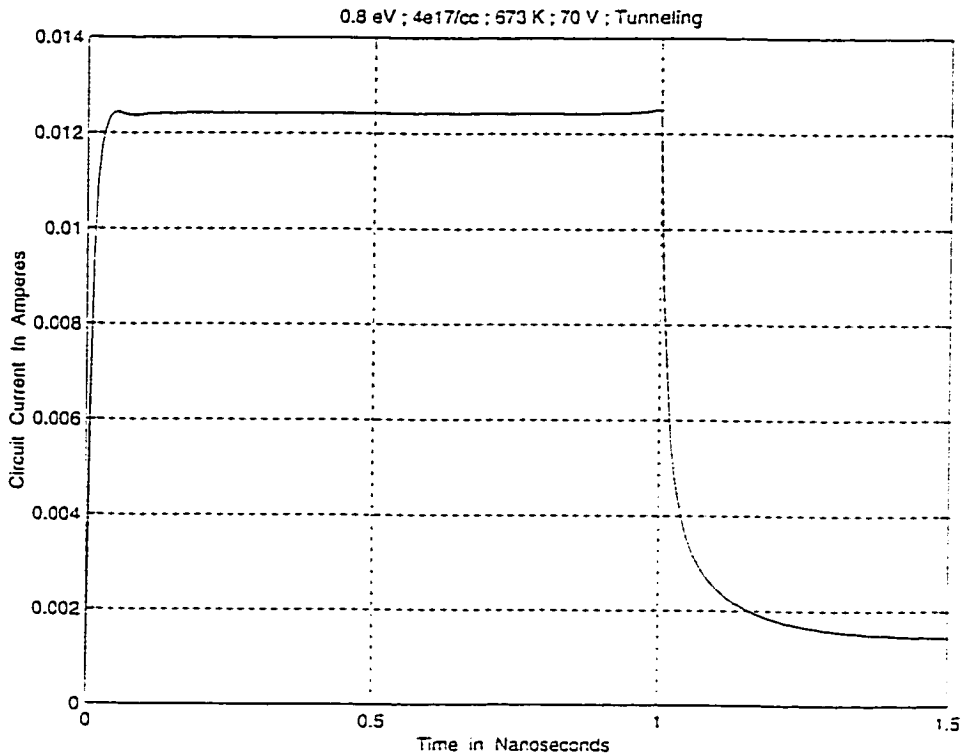

Fig. 4.71(b) Circuit current at 673 K for small contact 0.8 eV trap case with tunneling.

Reproduced with permission of the copyright owner. Further reproduction prohibited without permission.

the electric fields at the contacts are sufficiently large to initiate electron injection. Finally, at the lower 1.0 ns ramp with a 70 Volts maximum bias, the MSM is predicted to hold off the voltage. Figs. 4.71 show the bias and current waveforms. Therefore, for the smaller contact geometry, the hold-off voltage for the 0.6 μm MSM structure with tunneling included is predicted to be about 75 Volts.

The larger area contact geometry is shown to enhance the voltage hold-off capability. This arises primarily due to the lower electric fields at the contacts produced by such larger metallic geometries which work to reduce the field induced carrier tunneling and injection mechanism. For example, Figs. 4.72 show that a 100 Volt ramp can generate excessively large currents, while a 90 Volt bias is relatively stable as in Figs. 4.73. Hence, the hold-off voltage at 673 K has been shown to be increased by over 26 percent from about 75 V for the small contacts to roughly 95 Volts.

4.4.4 ROLE OF DEEP LEVELS

In the above simulations so far, the role of the contact geometry and size, the tunnel injection mechanism and operating temperature have been probed. In all of the calculations, a deep state corresponding primarily to an electron trap 0.8 eV below the conduction band was assumed. However, its role in influencing the current response characteristics was not directly probed. The only affect was an increase in the delay time for current amplification due to the capture of free carriers. Thus, as long as the traps were left unfilled, the rate of current enhancement in response to an external bias was shown to be slow.

A more direct and significant impact of deep levels is now demonstrated. Simulation results will show that deep levels control and change the position of the quasi-Fermi level. Higher trap densities or larger energy levels in an n-type SiC material, will drive the Fermi level further away from the conduction band edge. Since the Fermi levels must align at the semiconductor-metal contact boundary, the above implies that energy difference between the

Reproduced with permission of the copyright owner. Further reproduction prohibited without permission.

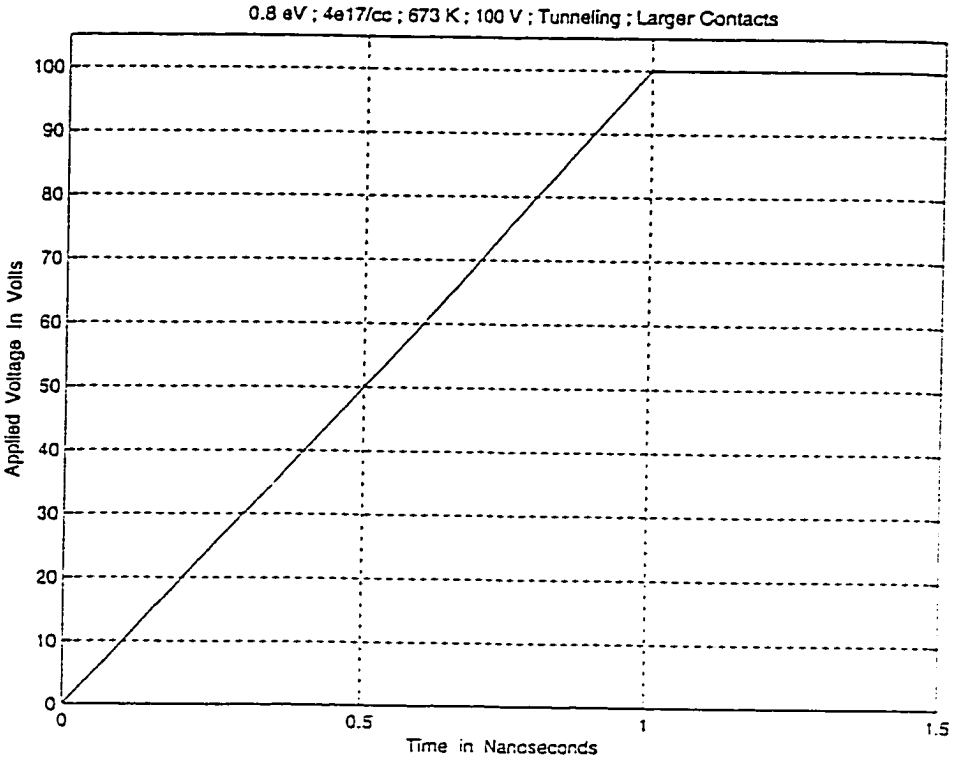

Fig. 4.72(a) Applied voltage at 673 K for small contact 0.8 eV trap case with tunneling.

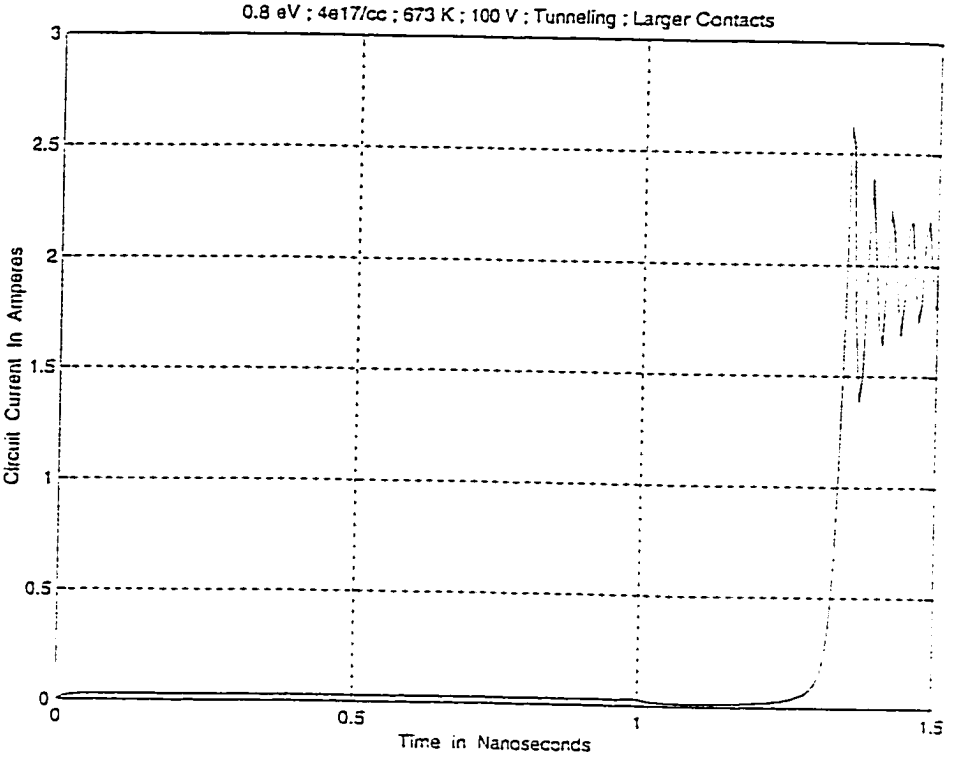

Fig. 4.72(b) Circuit current at 673 K for small contact 0.8 eV trap case with tunneling.

Reproduced with permission of the copyright owner. Further reproduction prohibited without permission.

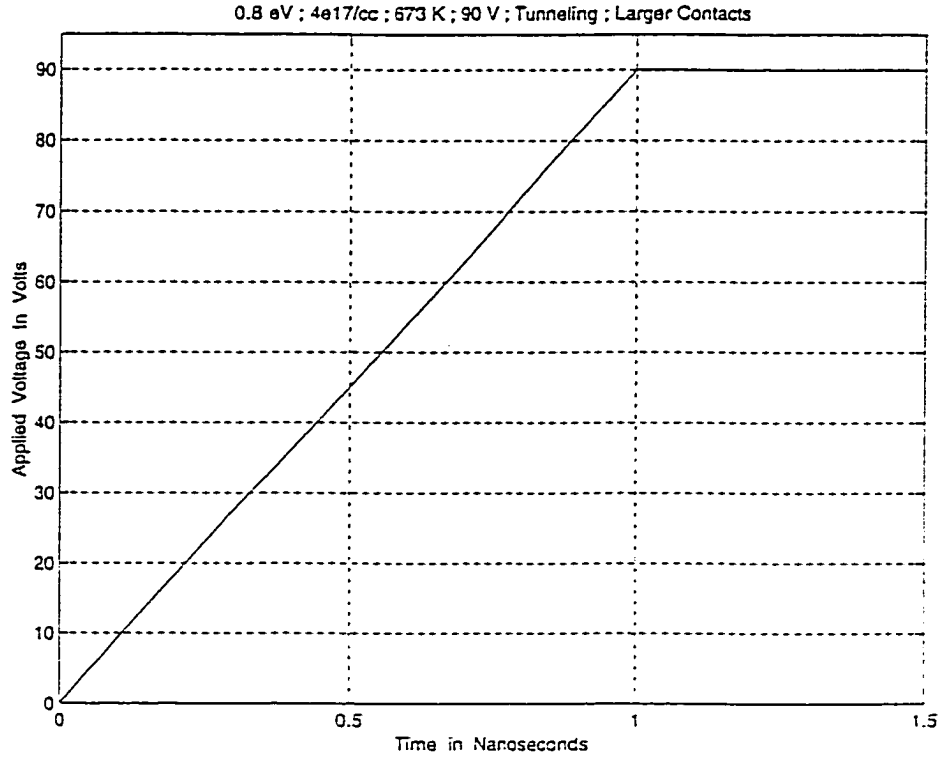

Fig. 4.72(a) Applied voltage at 673 K for larger contact 0.8 eV trap case with tunneling.

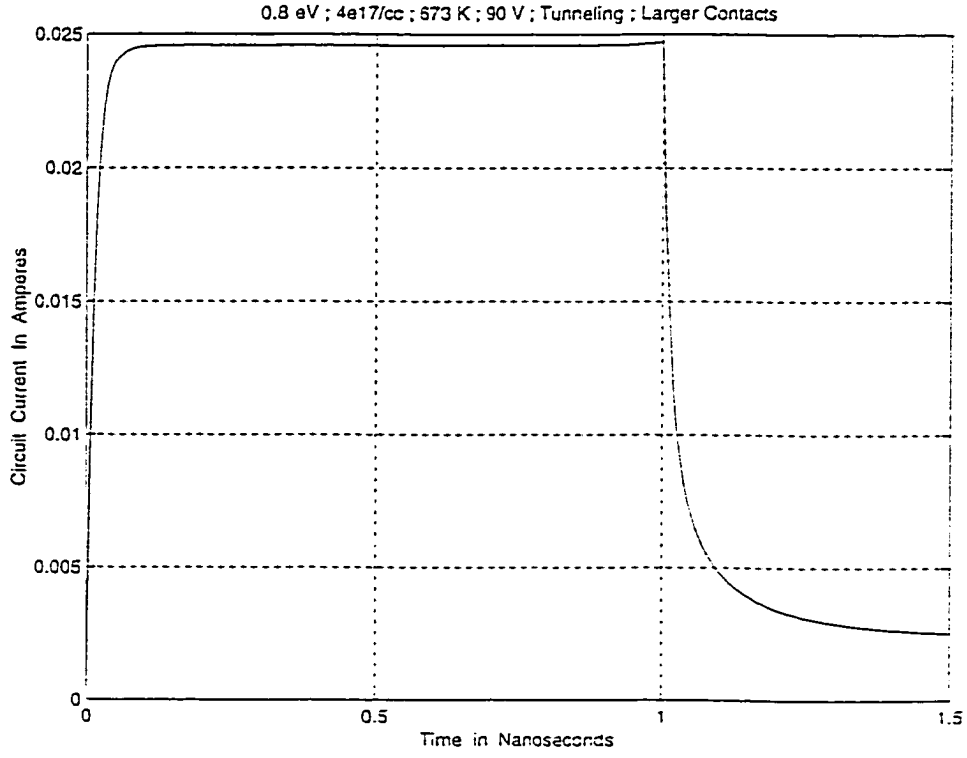

Fig. 4.72(b) Circuit current at 673 K for larger contact 0.8 eV trap case with tunneling.

Reproduced with permission of the copyright owner. Further reproduction prohibited without permission.

semiconductor conduction band edge and the metallic Fermi level will increase. This effectively increases the barrier height for electron injection into the semiconductor. With weaker tunneling and thermionic emission currents, one then expects a gradual shift towards "blocking contact" behavior. This suggests that deeper levels or higher electron trap densities near the cathode region of an n-type SiC material would work to enhance the voltage hold-off capabilities.

Simulations at two different trap energy levels of 0.8 eV and 1.2 eV were carried out at 673K to probe the possibility of such an effect. Figs. 4.74 shows the response to a 100 Volt ramp applied to the SiC MSM structure containing 2×10^{17} cm $^{-3}$ donors and 4×10^{17} cm $^{-3}$ traps 0.8 eV below the conduction band as before. These graphs are the same as those in Fig. 4.72, and the larger contact area was chosen. A sharp current increase and potential device failure is evident. In Fig. 4.75 the same simulations are repeated, but for a 1.2 eV trap level. The current of 4.75(b) is dramatically different. No unstable increases are predicted. This result lends quantitative support for the concept of lower contact injection due to a higher potential barrier at the deeper trap energies.

Similar simulations were carried out for confirmation of the above concept at the lower 300 K temperature. Figs. 4.76 show the results at 300 K with a 0.8 eV trap energy and a 110 Volt bias. An unstable current with fluctuating values reaching 3.0 Amperes is predicted. However, for a much deeper level at 1.2 eV and all other parameters unchanged, a stable behavior was obtained as evident in Fig. 4.77. The current was predicted to rapidly decrease a short time after the 1.0 ns voltage ramp.

Reproduced with permission of the copyright owner. Further reproduction prohibited without permission.

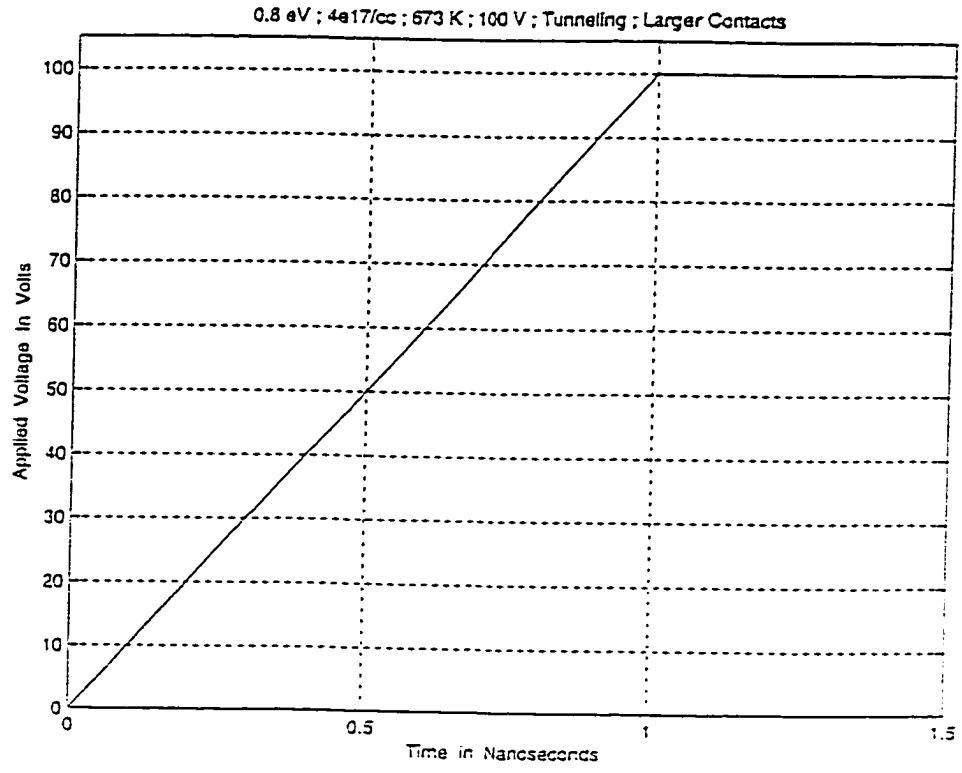

Fig. 4.74(a) Applied voltage at 673 K for large contact 0.8 eV trap case with tunneling.

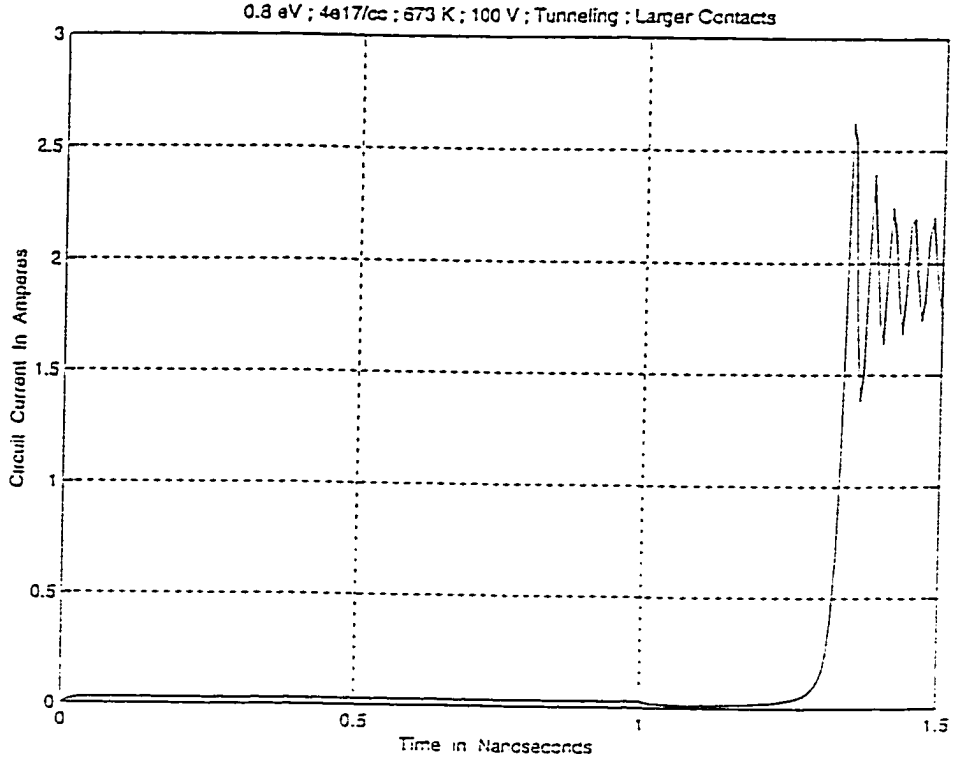

Fig. 4.74(b) Circuit current at 673 K for large contact 0.8 eV trap case with tunneling.

Reproduced with permission of the copyright owner. Further reproduction prohibited without permission.

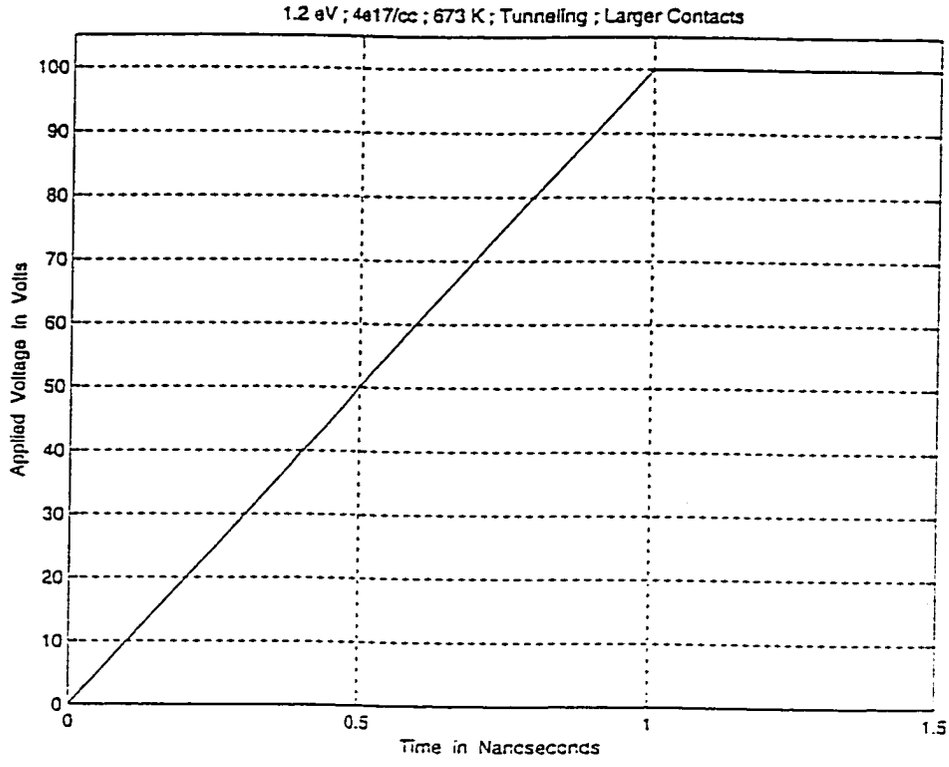

Fig. 4.75(a) Applied voltage at 673 K for large contact 1.2 eV trap case with tunneling.

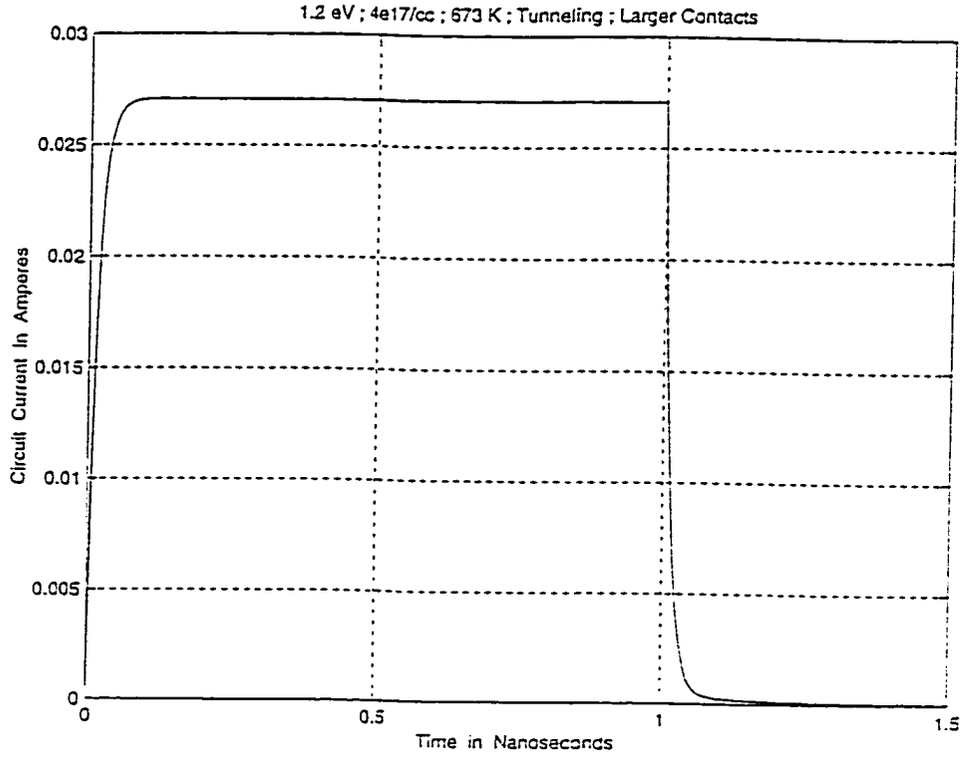

Fig. 4.75(b) Circuit current at 673 K for large contact 1.2 eV trap case with tunneling.

Reproduced with permission of the copyright owner. Further reproduction prohibited without permission.

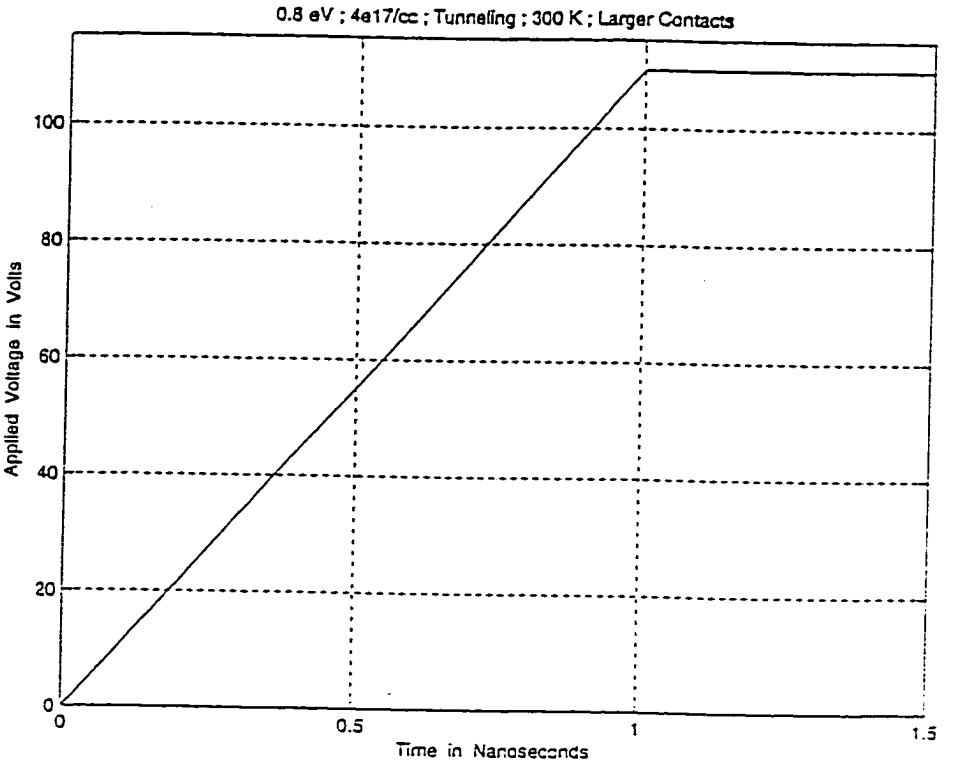

Fig. 4.76(a) Applied voltage at 300 K for large contact 0.8 eV trap case with tunneling.

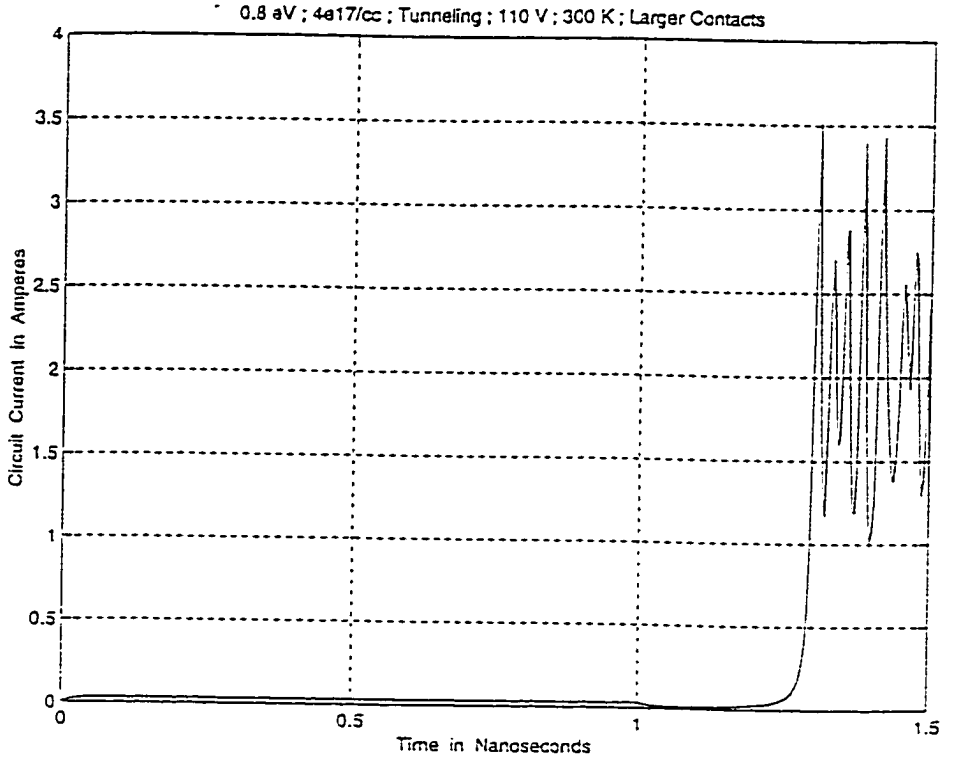

Fig. 4.76(b) Circuit current at 300 K for large contact 0.8 eV trap case with tunneling.

Reproduced with permission of the copyright owner. Further reproduction prohibited without permission.

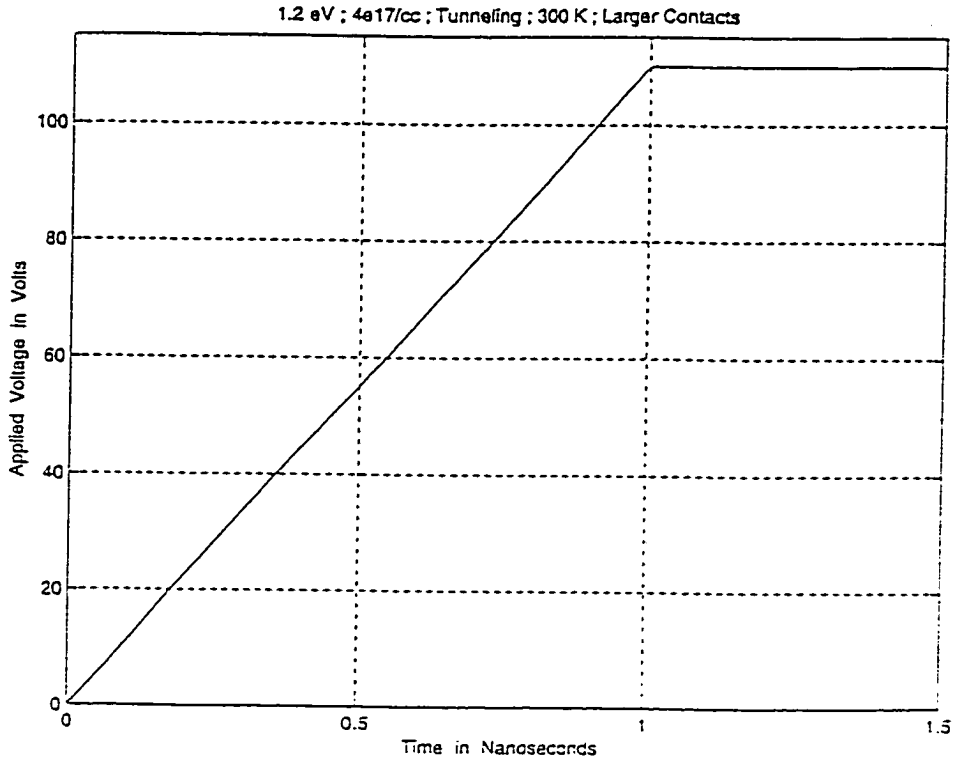

Fig. 4.77(a) Applied voltage at 300 K for large contact 1.2 eV trap case with tunneling.

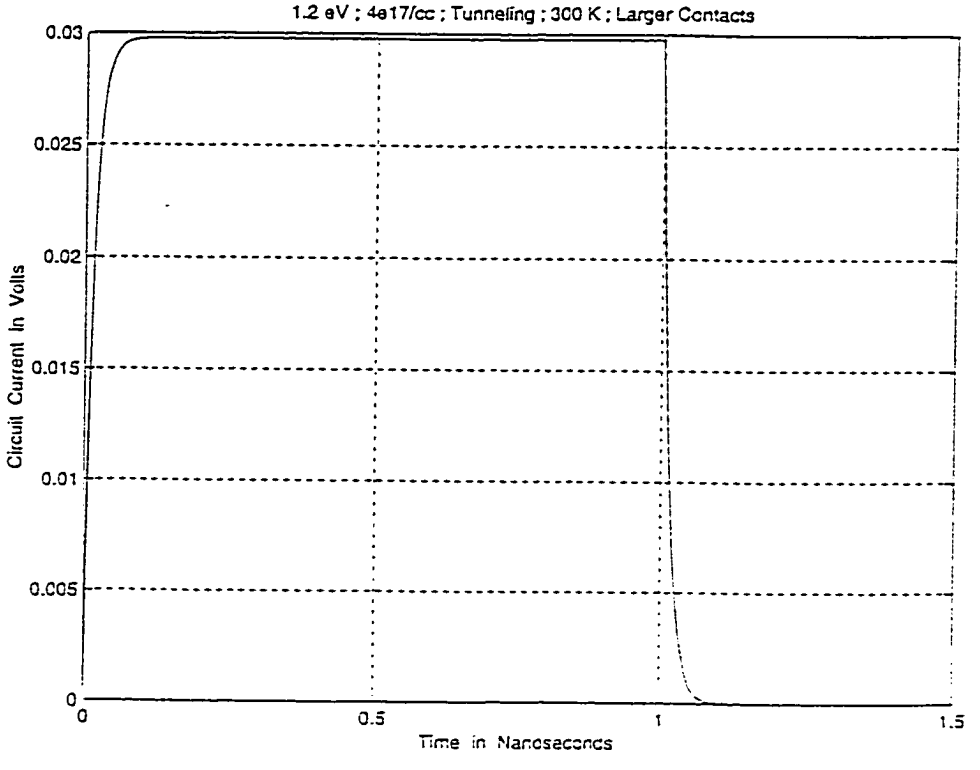

Fig. 4.77(b) Circuit current at 300 K for large contact 1.2 eV trap case with tunneling.

Reproduced with permission of the copyright owner. Further reproduction prohibited without permission.

CHAPTER 5

CONCLUSIONS AND FUTURE RESEARCH

5.1 SUMMARIZING CONCLUSIONS ON SiC WORK

In this research, evaluations of the electrical transport characteristics of SiC were obtained. First principle Monte Carlo simulations were set up to predict the material response for two of the most promising polytypes. Such Monte Carlo simulators are known to be very accurate and do not need any measured electrical data sets as adjustable input parameters. The technique is therefore very useful in studying new material systems for which experimental results are not available *a-priori*. Though the Monte Carlo scheme is well known in the context of semiconductor transport studies and has been applied to many of the commonly used materials, it has not been used much for SiC calculations. The Monte Carlo simulations for SiC that have been developed here are a contribution in this field.

Results of the Monte Carlo calculations seemed to correlate well with some of the experimental data that is becoming available. Both the bulk and quantized inversion layer situations matched the observations well. The trends arising from anisotropy, the temperature and field dependence were shown to be in keeping with qualitative expectations for the new material. The advantages of high voltage operation in terms of superior transport properties over conventional Si and GaAs materials were also quantitatively assessed.

Next, in this research, a one-dimensional simulator for analyzing the electrical response of SiC diode structures was developed based on the drift-diffusion approach. The output and predictions of the Monte Carlo simulator were used for the input transport parameters. The drift-diffusion model based on SiC material parameters was general, and capable of probing effects associated with deep levels, unionized impurity states, high field transport, and internal impact ionization phenomena. The numerical simulator developed was successfully applied to the study of the transient diode characteristics. The diode structure, its parameters and external waveform were deliberately chosen to match those of actual

Reproduced with permission of the copyright owner. Further reproduction prohibited without permission.

devices tested at NASA Lewis for head-to-head comparisons.

A summary of the research highlights and main conclusions of this modeling study is given below:

(i) The 6H- and 4H-polytypes exhibit a significant anisotropy. Hence, in fabricating devices from these materials, care must be taken to position the contacts along specific directions relative to the crystal axis.

(ii) The high field transport behavior of SiC is predicted to be superior to both GaAs and Silicon material. Peak steady state bulk electron drift velocities around 1.5×10^5 m/s have been obtained from Monte Carlo simulations. These are nearly 50 % higher than those in GaAs and about 20 % higher than in silicon.

(iii) Electron mobility which is an important parameter for low field transport was shown to have values around 400 m^2/Vs. are This value is almost a factor of 8 smaller than that for GaAs material. This clearly suggests that SiC cannot be a suitable candidate for low field, small voltage applications, and hence cannot replace GaAs and Si technology in this sector. The speed and frequency response for such low field applications will then be very poor because of the low mobility.

(iv) The high temperature bulk mobility and drift velocity were predicted to be lower than the room temperature value. However, for temperatures as high as 900 K, the reduction in electron mobility was roughly a factor of 2.5. This is not very significant, at least for high field applications since the high field drift velocity at room temperature is predicted to be much higher than the other materials anyway.

(iv) The inversion layer electron mobility for SiC MOSFET devices matched the available experimental predictions rather well. The mobility values were predicted to be around 50 m^2/Vs, and hence much lower than the bulk material. This decrease in the mobility was shown to be the result of additional scattering mechanisms that

Reproduced with permission of the copyright owner. Further reproduction prohibited without permission.

come into affect due to electron confinement within the channel. Specifically, the interface roughness scattering was shown to be significant. The implication is that better processing to improve the quality of the oxide-SiC interface and obtain a smoother surface is absolutely necessary. Unless this is achieved, SiC MOSFETs will not be very useful for microwave and high power, high frequency applications. The poor channel mobility will yield a low cut-off frequency, and hence the frequency response will be limited. Also, in order to decrease interface scattering, the Monte Carlo suggests that small gate voltages will need to be used. But this constraint implies that large signal amplification will be poor. Quite possibly then, MESFETs rather than MOSFETs would be more useful for SiC technology.

(v) Next, based on the drift-diffusion model, deep levels in SiC were shown to play a significant role in the electrical device behavior.

(vi) Deep levels tend to be unionized (or only partially ionized) with emission times that are a strong function of their energy level. Consequently, a deep level present in SiC material, could function as a slow supply channel of mobile carriers after the application of a fast voltage pulse.

(vii) The slow release of majority carriers from deep subband levels in response to a fast voltage pulse is due to the formation and growth of depletion regions. However, the release of majority carriers reduces the electric field away from the depletion region, and enhances it at (and near) the depleted junction.

(viii) Minority carriers across the high field junctions as the depletion region forms and grows in response to an external voltage. The density of minority carriers would be **higher** for impurity states having deep levels. Consequently, the role of minority carrier dominated impact ionization, leading to a possible instability is predicted to be higher in the presence of deep levels.

(ix) Our calculations have shown electrons-initiated impact ionization to be more

Reproduced with permission of the copyright owner. Further reproduction prohibited without permission.

important than the hole process. Consequently, deep levels in p-type material, are predicted to be more critical than deep levels in n-regions. Extrapolating this, one should expect to minimize the possibility of unstable behavior in unipolar devices not containing p-n junctions.

(x) High currents were obtained for devices containing deep levels as compared to those containing shallow energies. As a result, even if device breakdown can be controlled, the "turn-off" process is predicted to be substantially slower for devices containing deep levels.

(xi) High current levels with deep impurities also underscore the potential for a second breakdown due to internal heating.

(xii) Very good quantitative agreement between experimental data and theoretical predictions was obtained with deep levels incorporated into the model. Slow current rise with times stretching over up to almost 100 ns in keeping with experimental data were predicted. This indirectly implies that the actual test devices must have had deep levels. The transient response was also seen to contain "spikes" which originated from a presence of multiple levels with a disparity between their time constants. Such "spikes" were also observed in experiments, and could perhaps serve as a useful probe of the deep levels.

(xiii) From industry's standpoint and for high-voltage, high -temperature applications, the results suggest that successful development of this technology will require the growth and fabrication of good quality material without any deep levels. The operation may not be affected as much by high temperature, as the detrimental effects of high voltage leading to possible avalanching and device breakdown.

(xiv) It was shown that the contact can significantly affect the electrical response behavior. The hold-off voltage could be significantly improved if larger contacts having smoother geometric shapes were used. Also, the process on high-field tunnel

Reproduced with permission of the copyright owner. Further reproduction prohibited without permission.

injection from the contacts was shown to be very detrimental for the stable operation of the SiC devices.

(xv) Finally, the role of deep level impurities was shown to be very significant in controlling potential instabilities. A high trap density would help delay the onset of internal current increases due to carrier capture. Hence, devices containg a high density of deep levels could better survive voltage spikes and transient fluctuations. Also, it was shown that deeper traps would effectively work to increase the potential barrier at the contacts, and reduce carrier injection. Specifically, deeper levels at the cathode of n-SiC and at the anode of p-SiC devices have been predicted to be useful. Conversely, the presence of deep levels at the anode of n-SiC and/or the cathode of p-SiC structure would be detrimental.

The above implies that the best high-voltage results would be obtained not by using reverse biased p-i-n SiC diodes, but rather using MSM structures.

5.2 SCOPE FOR FUTURE RESEARCH

Both microscopic Monte Carlo simulations and drift-diffusion models were developed and applied to the study of electrical behavior in SiC. This constitutes a significant "first-step." The study enabled a number of important conclusions to be made. However, more research work in this direction can be carried out to enhance and improve the present situation. Some of these aspects and the scope for possible future research is given below.

(i) The Monte Carlo codes could be enhanced by including a self-consistent Poisson solver. In the simulations of this research, a constant and uniform electric field was assumed. However, in general, the flow of electrons and holes in an actual device will change the internal electric field distribution and carrier densities. This aspect will, therefore, need the inclusion of a Poisson solver.

Reproduced with permission of the copyright owner. Further reproduction prohibited without permission.

(ii) Electron transport was studied through the Monte Carlo simulations. Electrons were chosen since they are usually more important to current conduction, and make the largest contribution. However, microscopic properties of the holes can also be computed. Hence, holes could be included as a next step, with appropriate information about their effective masses and bandstructure. Unfortunately, some of these input parameters have not been obtained experimentally.

(iii) Full Monte Carlo device simulations could be attempted. This could include both MOSFET and MESFET structures, and high frequency, ac response characteristics.

(iv) The drift-diffusion model which is presently one- and two-dimensional, could be further extended. This could be done to make it possible to simulate spatial non-uniformities, lateral contact geometries, inhomogeneous doping and clustering effects. Possible breakdown due to filamentation could also be simulated.

(v) More complicated voltage shapes and pulse trains could be analyzed by the drift-diffusion model.

Reproduced with permission of the copyright owner. Further reproduction prohibited without permission.

REFERENCES

1. M. Bhatnager and B. J. Baliga, IEEE Trans. Electron. Dev. **40**, 645 (1993).
2. H. Morkoc, S. Strite, G. Geo, M. E. Lin, B. Sverdlov, and M. Burns, J. Appl. Phys. **76**, 1363 (1994).
3. R. J. Trew, J. B. Yen, and P. M. Mock, Proc. IEEE **79**, 598 (1991).
4. S. Strite and H. Morkoc, J. Vac. Sci. Technol. B **10**, 1237 (1992).
5. R. F. Davis, Proc. IEEE **79**, 702 (1991).
6. R. J. Betsch, P. G. McMullin, C. D. Brandt, D. L. Barret, R. G. Sedestecker, R. H. Hopkins, and A. Morese, in Proceedings of the 1991 International Semiconductor Devices Research Symposium, 505 (1991).
7. P. G. Neudeck, D. Larkin, J. E. Starr, J. A. Powell, C. S. Salupo, and L. Matus, IEEE Trans. Electron. Dev. **41**, 826 (1994).
8. J. Crofton, P. Bernes, J. Williams, and J. A. Edmond, Appl. Phys. Lett. **62**, 384 (1993).
9. G. Zeigler, P. Lanig, D. Theis, and C. Weyrich, IEEE Trans. Electron. Dev. **30**, 227 (1983).
10. J. A. Edmond, H. S. Kong, and C. H. Carter, Jr., in Proc. Of Int. Conf. on Amorphous and Crystalline SiC and Other IV-IV Materials, 311, (1991).
11. A. O. Konstantinov, D. P. Litvin, and V. I. Sankin, Sov. Tech. Phys. Lett. **7**, 572 (1981).
12. W. von Muench, P. Hoeck, and E. Pettenpaul, Proc. Int. Electronic Device Meeting, Washington, 337 (1977).
13. W. von Muench and P. Hoeck, Solid-State Electronics, **21**, 479 (1978).
14. M. I. Chaudry, IEEE Electron. Dev. Lett., **12**, 670 (1991).
15. T. Sugii, T. Yamakazi, and T. Ito, Jap. J. Appl. Phys., **30**, 1970 (1991).
16. Y. Tawada, H. Okamoto, and Y. Hamakawa, Appl. Phys. Lett., **39**, 273 (1981).

Reproduced with permission of the copyright owner. Further reproduction prohibited without permission.

17. For example in Silicon Carbide and Related Materials, edited by M. Spencer, R. Devaty, J. Edmond, M. Asif Khan, R. Kaplan, and M. Rahman (IOP, Bristol, 1994).

18. P. Neudeck and J. A. Powell, IEEE Electr. Dev. Lett **15**, 63 (1994).

19. C. Weitzel, J. Palmour, C. H. Carter, K. Moore, K. Nordquist, S. Allen, C. Thero, and M. Bhatnagar, IEEE Trans. Elec. Dev. **ED 43**, 1732 (1996).

20. K. Tsukioka, D. Vasileska, and D. K. Ferry, Phys. B **185**, 466 (1993).

21. M. Ruff, M. Mitlehner, and R. Helbig, IEEE Trans. Electron. Dev. **41**, 1040 (1994).

22. R. P. Joshi, J. Appl. Phys. **78**, 5518 (1995).

23. R. P. Joshi, S. Pathak, and J. A. Mcadoo, J. Appl. Phys. **78**, 1 (1995).

24. S. E. Saddow, C. W. Tipton, and M. Mazzola, J. Appl. Phys. **77**, 318 (1995).

25. P. G. Neudeck and C. Fazi, J. Appl. Phys. **80**, 1219 (1996).

26 V. Tsvetkov, S. T. Allen, H. S. Kong, and C. Carter, in Proc of Int. Conf. on SiC and Related Materials, 577 (1995).

27. H. G. Junginger, and W. van Haeringen, Phys. Stat. Sol. **37**, 709 (1970).

28. N. T. Son, W. M. Chen, O. Kordina, A. O. Konstantinov, B. Monemar, and E. Janzen, Appl. Phys. Lett. **66**, 3210 (1995).

29. M. Schadt, G. Pensl, R. P. Devaty, W. J. Choyke, R. Stein, and D. Stephani, Appl. Phys. Lett. **65**, 3120 (1994).

30. W. Suttrop, G.Pensl, W. J. Choyke, A. Dornen, S. Leibenzeder, R. Stein, Amporphous and Crystalline Silicon Carbide, IV Proc. of the 4th International Conference, 129 (1991).

31. W. J. Schaffer, G. H. Negley, K. G. Irvine, and J. W. Palmour, Mat. Res. Soc. Symp. Proc. **339**, 595 (1994).

32. L. G. Matus, J. A. Powell, and C. S. Salupo, Appl. Phys. Lett. **59**, 1770 (1991).

33. W. von Muench and I. Pfaffeneder, J. Appl. Phys. **48**, 4831 (1977).

Reproduced with permission of the copyright owner. Further reproduction prohibited without permission.

34. V. I. Levin, Y. M. Tairov, M. G. Travazhdyan, F. Tsvetkov, and M. A. Chernov, Sov. Phys. Tzv **14**, 830 (1978).

35. Y. M. Tairov and R. Tsverkov, J. Cryst. Growth **52**, 146 (1981).

36. M. Ikeda, T. Hayakawa, Z Yamagiva, H. Matsunami, and T. Tanaka, J. Appl. Phys. **50**, 8215 (1979).

37. A. Suzuki, H. Ashida, N. Furui, K. Mameno, and H. Matsunami, Jpn. J. Appl. Phys. **21**, 579 (1982).

38. C. D. Fung, and J. J. Kopanski, Appl. Phys. Lett. **45**, 757 (1984).

39. B. E. Deal, and A. Z. Grove, J. Appl. Phys. **36**, 3770 (1965).

40. W. Z. Pan, and A. J. Steckl, J. Electrochem. Soc. **137**, 212 (1993).

41. G. Pensl, and W. J. Choyke, Physica B **185**, 264 (1993).

42. M. Ghezzo, D. M. Brown, E. Bowney, J. Kretchmer, W. Hennessy, D. L. Polla, and H. Bakhru, IEEE Electron. Dev. Lett. **13**, 639 (1992).

43. G. Kelner, Z. Binari, M. Sur, and J. W. Palmour, Electron. Dev. Lett. **27**, 1038 (1991).

44. T. Kimoto, T. Urushidani, S. Kobayashi, H. Matsunami, IEEE Electron. Dev. Lett. **14**, 548 (1993).

45. B. J. Baliga, Amorphous and Crystalline SiC, Proc.. of the 4th International Conferrence, 305 (1992).

46. S. Karmann, W. Suttrop, A. Schoner, M. Schadt, C. Haberstroh, F. Engelbrecht, R Helbig, G. Pensl, R. A. Stein, and S. Leibenzeder, J. Appl. Phys. **72**, 5437 (1992).

47. W. J. Schaffer, H. S. Kong, G. H. Negley, and J. Palmour, Inst. Phys. Conf. Ser. **137**, (IOP Publishing Ltd., N. York, 1994), Chap. 3, pp. 155-159.

48. W. J. Schaffer, G. H. Negley, K. Irvine, and J. W. Palmour, in *Diamond, Silicon Carbide and Nitride Wide Bandgap Semiconductors*, edited by C. H. Carter, G. Gildenblat, S. Nakamura, and R. Nemanich, MRS Proc. No. 339 (Materials Research

Reproduced with permission of the copyright owner. Further reproduction prohibited without permission.

Society, Pittsburgh, 1994).

49. L. A. Lipkin and J. W. Palmour, J. Electr. Mater. **25**, 909 (1996).

50. M. Bhatnager, P. McLarty, and B. J. Baliga, IEEE Electron Dev. Lett. **13**, 501 (1992).

51. J. W. Palmour, J. A. Edmond, H. S. Kong, C. H. Carter Jr., IECEC-93 Proceedings of the 28th Intersocity Energy Conversion Engineering Conference **1**, 249 (1993).

52. G. Kelnev, Z. Binari, K. Sleger, and H. Kong, IEEE Electron. Dev. Lett. **8**, 428 (1987).

53. J. W. Palmour, C. H. Carter, C. Weitzel, and K. J. Nordquist, "Diamond, SiC and Nitride Wide Bandgap Semiconductors", Proc. Materials Research Society Conference 302, (1994).

54. J. W. Palmour, J.A. Edmond, H. S. Kong, and C. H. Carter Jr., Physica B **185**, 416 (1993).

55. J. A. Edmond, H. S. Kong, and C. H. Carter Jr., Physica B **185**, 453 (1993).

56. D. M. Brown, E.T. Bowney, M. Ghezo, J. W. Kretchner, R. J. Saia, Y. S. Liu, J. A. Edmond, G. Gati, J. M. Pimbley, and W. E. Schneider, IEEE Trans. Electron. Dev. **40**, 325 (1993).

57. C. Raymond, C. Richier, P. N. Brounkov, F. Ducroquet, G. Guillot, L. M. Porter, R. F. Davis, and T. B. Jaussandc, Mat. Sci. and Engg. **B29**, 122 (1995).

58. R. B. Campbell, and H. C. Chang, Solid-State Electron **63**, 949 (1967).

59. P. Neudeck, D. Larkin, J. A. Powell, L. G. Matus, and C. Salupo, Appl. Phys. Lett. **64**, 1386 (1994).

60. S. Tiwari, in *Compound Semiconductor Devices*, (Academic Press, N. York, 1992).

61. M. Kurata, in *Numerical Analysis of Semiconductor Devices*, (D. C. Heath, MA, 1985).

62. C. Jacobani and P. Lugli, in *The Monte Carlo Method for Semiconductor Device Simulation*, (Springer-Verlag, Wien, 1989).

Reproduced with permission of the copyright owner. Further reproduction prohibited without permission.

63. N. T. Son, O. Krdina, A. O. Konstantinov, W. M. Chen, E. Sorman, B. Monemar, and E. Janzen, Appl. Phys. Lett. **65,** 3209 (1994).

64. C. Jacoboni and L. Reggiani, Rev. Mod. Phys. **55**, 645 (1983).

65. E. M. Conwell, Solid State Phys. **6**, 109, (1967).

66. H. G. Reik and H. Risken, Phys. Rev. **126**, 1737 (1962).

67. H. Budd, J. Phys. Soc. Japan **21**, 420 (1966).

68. T. Kurosawa, J. Phys. Soc. Japan **21**, 424 (1966).

69. W. Fawcett, in *Electron in Crystalline Solids* (International Atomic Energy Agency, Vienna, 1973).

70. A. D. Boardman, in *Physics Programs*, edited by A. D. Boardman (Wiley, New York, 1980).

71. A. D. Broadman, W. Fawcett and H. D. Rees, Solid State Commun. **6**, 305 (1968).

72. W. Fawcett, A. D. Broadman and S. Swain, J. Phys. Chem. Sol. **13**, 1963 (1970).

73. G. L. Bir and G. E. Pikus, in *Symmetry and Strain-Induced Effects in Semiconductors*, edited by D. Louvish (Wiley, New York, 1974).

74. B. K. Ridley, in *Quantum Processes Semiconductors* (Oxford University Press, 1982).

75. E. M. Conwell and V. F. Weisskopf. Phys. Rev. **77**, 388 (1950).

76. H. Brooks and C. Herring, Phys. Rev. **83**, 879 (1951).

77. F. Stern, CRC Critical Rev. in Solid State Science **4**, 499 (1974); F. Stern and W. E. Howard, Phys. Rev. **163**, 816 (1967).

78. T. Ando, A. B.Fowler, and F. Stern, Rev. Mod. Phys. **54**, 437 (1982).

79. K. Masaki, K. Taniguchi, C. Hamaguchi, and M. Iwase, Jap. J. Appl. Phys. **30**, 2734 (1991).

80 T. Ando, J. Phys. Soc. Jpn. **43**, 1616 (1977).

81. P. Price, Ann. Phys. **133**, 217 (1981).

Reproduced with permission of the copyright owner. Further reproduction prohibited without permission.

82. F. Gamiz, J. Roldan, J. Lopez-Villanueva, and J. Carceller, J. Appl. Phys. **69**, 2219 (1996).

83. S. Selberherr, in *Analysis and Simulation of Semiconductor Devices*, (Springer-Verlag, Wien, 1984).

84. R. G. Humphreys, D. Bimberg, and W. J. Choyke, Solid State Commun. **39**, 163 (1981).

85. J. R. Zhou, D. Vasileska, and D. K. Ferry, Solid State Electronics **36**, 1289 (1993).

86. O. Madelung, in *Physics of Group IV and III-V Compounds*, Group III, Vol. 17a, Landolt-Bornstein *New Series* (Springer-Verlag, Berlin, 1981).

87. P. J. Price, in *Semiconductors and Semimetals*, edited by R. K. Willardson and A. C. Beer (Academic, N. York, 1979), Vol. 14, p.249.

88. F. Reif, *Fundamentals of Statistical and Thermal Physics* (McGraw-Hill, N. York, 1965).

89. F. Gamiz, J. B. Roldan, J. A. Lopez-Villanueva, and J. E. Carceller, Appl. Phys. Lett. **69**, 2219 (1996); J. B. Roldan, F. Gamiz, J. A. Lopez-Villanueva, and P. Cartujo, J. Electr. Materials **26**, 203 (1997).

90. T. Ando, A. B. Fowler, and F. Stern, Rev. Mod. Phys. **54**, 437 (1982).

91. A. G. Sabnis and J. T. Clemens, IEDM Tech. Digest, 18 (1979).

92. S. M. Goodnick, D. K. Ferry, C. W. Wilmsen, Z. Lilienthal, D. Fathy, and O. L. Krivanek, Phys. Rev. B **32**, 8171 (1985).

93. S. Yamakawa, H. Ueno, K. Taniguchi, C. Hamaguchi, K. Miyatsuji, K. Masaki, and U. Ravaioli, J. Appl. Phys. **79**, 911 (1996).

94. D. Vasileska and D. K. Ferry, IEEE Trans. Elec. Dev. **ED-44**, 1997.

95. F. F. Fang and W. E. Howard, Phys. Rev. Lett. **16**, 797 (1966).

96. D. K. Ferry, Phys. Rev. B **14**, 1605 (1976).

Reproduced with permission of the copyright owner. Further reproduction prohibited without permission.

VITA

Sanjay Pathak

297 Kingbird Ct
ThreeBridges
NJ 08887 USA

Education:

Ph.D. Electrical Engineering, Old Dominion University, Norfolk VA
M.Tech. Material Science, Indian Institute of Technology Kanpur, India
B.Tech. Electrical Engineering, G.B. Pant University, Pantnager, India

Professional Experience:

Project Leader, GCI, Parsippany NJ (June 97 - Present)
Involved in leading a design team to develop Document management Solution for Johnson and Johnson, NJ.

Computer Programmer, ADI, Herendon VA (Jan 97 - May 97)
Involved in development of a computer system for IBM to facilitate educational courses over the Internet.

Research Associate, Astropower Inc., Newark DE. (Jun 96 - Dec 96)
Developing low defect density large area SiC material by lateral epitaxial overgrowth. Crystal growth of beta-SiC over <100> and <111> silicon substrate and various masks like silicon dioxide, tungsten, silicon oxinitride etc. are performed and characterized using SEM, TEM and XRD.

Research Assistant, Old Dominion University, Norfolk VA. (Jan 94 - May 96)
Simulation of wide band-gap semiconductor (SiC) devices for their high electric field and high temperature behavior. Study of Deep levels characteristics for SiC n+np diode.

Simulation and optimization of Low-temperature GaAs MSM phtodiode. Optimization and design of reflection coating of AlGaAs-GaAs back layer for the maximum reflection to enhance the sensitivity of photodiode.

Publications:

"Simulation for the dynamic response of Single-Transit SiC IMPATTs", R. P. Joshi and Sanjay Pathak, Proceedings IEE Southeastcon'95, Mar 26-29, 1995 Raleigh NC.

"Hot-electron and thermal effects on the dynamic characteristics of single-transit SiC impact-ionization avalanche transit-time diodes" R. P. Joshi and Sanjay Pathak and J.A. Mcadoo, J. Appl. Phys. 78(5), 1 Sept 1995

The word processor for this thesis was Dr. Sanjay Pathak

Reproduced with permission of the copyright owner. Further reproduction prohibited without permission.

IMAGE EVALUATION TEST TARGET (QA-3)

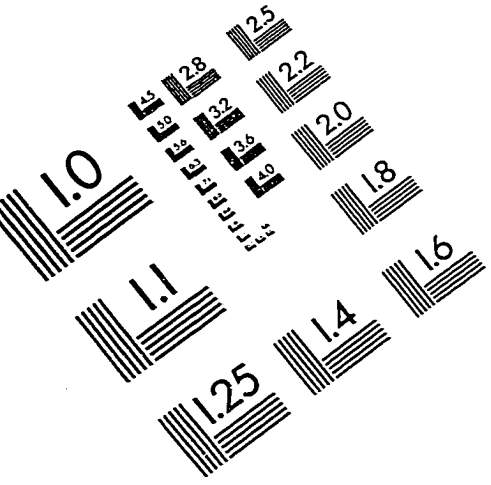

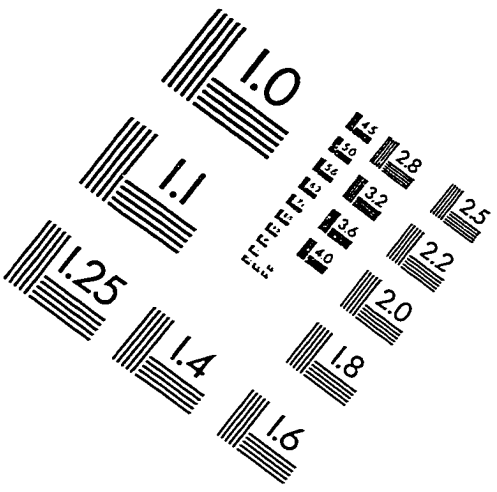

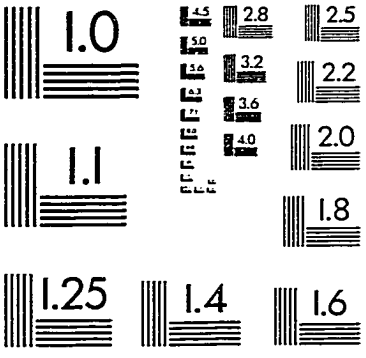

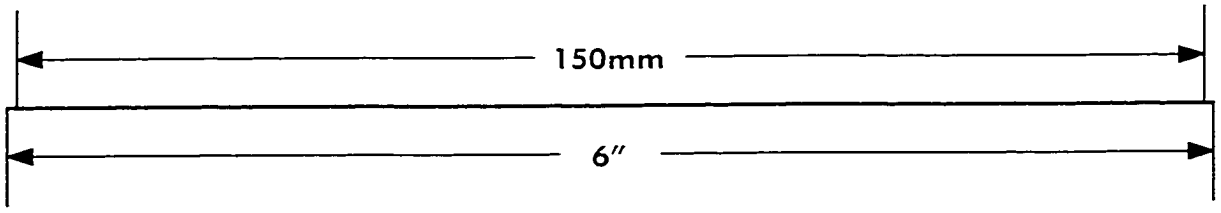

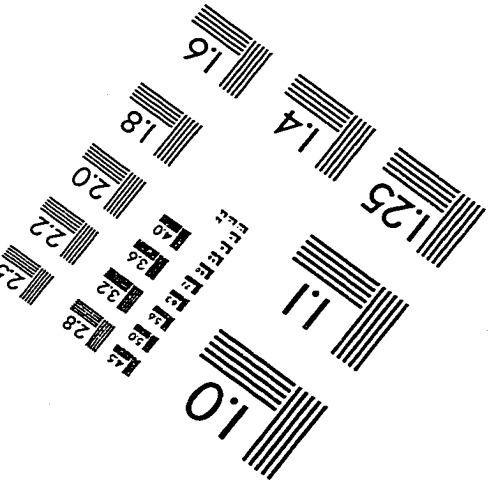

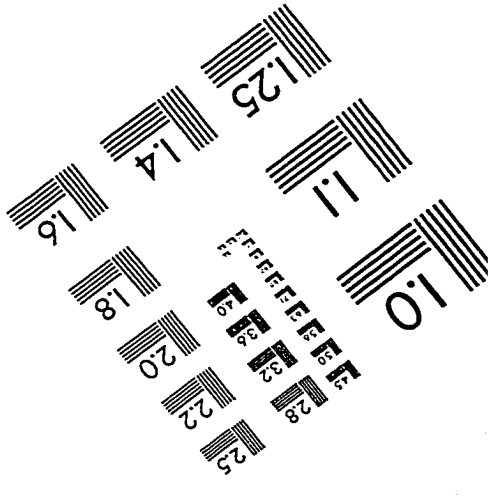

APPLIED IMAGE, Inc
1653 East Main Street
Rochester, NY 14609 USA
Phone: 716/482-0300
Fax: 716/288-5989

© 1993, Applied Image, Inc., All Rights Reserved

Reproduced with permission of the copyright owner. Further reproduction prohibited without permission.